Exploring the Photophysics of Magnetically Doped Semiconductor Nanocrystals

Christian Soren Erickson

A dissertation
submitted in partial fulfillment of the
requirements for the degree of

Doctor of Philosophy

University of Washington
2021

Reading Committee:
Daniel Gamelin, Chair
Brandi Cossairt
Phillip Reid

Program Authorized to Offer Degree:
Chemistry

University of Washington

Abstract

Exploring the Photophysics of Magnetically Doped Semiconductor Nanocrystals

Christian Soren Erickson

Chair of the Supervisory Committee:
Professor Daniel R. Gamelin
Department of Chemistry

The inclusion of dopant ions in semiconductor materials provides a useful pathway to add optical, electronic, and magnetic functionality which in turn enable the creation of numerous real-world technologies. Magnetic dopants are of particular interest due to their potential impact in future spintronics and quantum computing applications. Recent advancement in the synthesis of magnetically doped colloidal nanocrystals (NC) have allowed researchers to begin studying the intersection of semiconductors and magnetism in the quantum confined limit where magnetic exchange interactions are dramatically enhanced. The most interesting phenomena resulting from these magnetic exchange interactions is photo-generated magnetic ordering, known as an excitonic magnetic polaron (EMP), observed in Mn^{2+} doped II-VI materials. This thesis focuses on the recent spectroscopic observation and analysis of (EMPs) at the single NC level. The unprecedent insight gained at the single particle level allows us to experimentally confirm a longstanding EMP hypothesis that crystal anisotropy is a significant factor in by the total EMP stabilization and its orientation. Overall, this work highlights the importance of understanding anisotropic distortions to magneto-optic properties and will help to identify synthetic pathways to take advantage of the relationship between NC anisotropy and magnetic behavior.

Acknowledgements

I would like to first thank Prof. Daniel Gamelin for initially welcoming me into his group as an undergraduate researcher many years ago and starting me on the path of personal scientific development. Had it not been for that first experience with research and semiconductor nanocrystals my PhD journey would have never nucleated. Next, I would like to thank Prof. David Patrick for giving me the freedom and trust to continue to study nanocrystals in his lab at Western and for showing me the value of concentrating your research toward big picture ideas. I would like to thank Daniel again for collaborating with Prof. Patrick and I while I was working at Western and for helping in my transition back to his lab at UW. During my time in his lab as a graduate student I have faced several challenges from broken instruments, a screwdriver in the magnet, uncooperative syntheses, multiple collaborations, and Daniel has been incredibly supportive in guiding me to a PhD. Thank you for involving me in the numerous interdisciplinary collaborations and for giving me the freedom to pursue the ideas I thought were cool.

Next, I would like to thank my committee members. Prof. Phil Reid, since being an undergraduate student in your physical chemistry lab course I have valued your perspective on scientific learning and research. Prof. Brandi Cossairt, thank you for being a part of every one of my graduate exam committees, I have appreciated your enthusiasm and valued the feedback that you have given to my work. Prof. Vince Holmberg, thank you for taking time to listen to my research and for insightful comments and expert management of the MEMC IRG-1research talks.

The Gamelin group has been attached to every part of my scientific research career for the great part of a decade. I had the wonderful opportunity to be a part of the group as an undergrad, external collaborator, graduate student, and visiting student. During this incredible time, I have been able to work with many amazing scientists. Alas, nearly 10 years is far too short a time to live among such excellent and admirable people. I don't know half of you half as well as I should like, and I like less than half of you half as well as you deserve. I have things to finally do, and I've put this graduation off for far too long. In an effort to bid grad school a fond farewell I would like to thank the many members of the group who bear some responsibility for my PhD. Dr. Vlad Vlaskin, thank you for first introducing me the world of nanoparticles, dopants, scientific philosophy, and for devoting time to an untrained, curious undergrad. Vlad taught me everything I needed to know about synthesis, and I will always be indebted to his mentorship and scientific achievements. I would like to thank Troy Kilburn for helping me get my foot in the door of undergraduate research, his thoughts about the meaning of scientific research, sharing the 218 office and a love for the Sounders and US soccer, and for sharing many pints of beer at Big Time. Dr. Liam Bradshaw, thank you for agreeing to collaborate with me on the LSC project and for helping me to settle into grad school. My introduction to Dr. Charlie Barrows occurred when he was first-year graduate student that I was helping in the early stages of diffusion doping. Subsequently, when I returned to the group Charlie became a grad school mentor and friend who taught me the ins-outs of new and improved diffusion doping and personal scientific growth. Thank you for being the trailblazer to many of my projects and for your willingness to answer all kinds of questions. Dr. Arianna Marchioro, I am endlessly thankful for your mentorship in spectroscopy, thank you for your help in getting so many projects off the ground. Dr. Patrick Whitham, thank you for teaching me how to deal with EH&S and for sharing your baking. Thank you, Prof. Carl Brozek, for your guidance through difficult stages of grad school, I will miss our lunch walks and I will continue to follow your exciting progress at Oregon. Dr. Michael De Siena, I admire your experimental efficiency, thank you for challenging me to make the best argument

and for taking time to begrudgingly teach me about things. Dr. Jose Araujo, thank you for the birthday beer crawls, for your support when nothing ever works, for sharing the 218 office, and for always being willing to help when needed in lab. Thank you, Mori Taylor, I admire your enthusiasm and your drive to continue learning, thank you for working on the diffusion doping project, for allowing me to grow into a mentor role, and for our many discussions that had nothing to do with science. Dr. Kim Hartstein, thank you for lending your empathetic ear to the struggles of grad school and for giving me the opportunity to contribute to your research. I admire your ability to create a global community with your science. Dr. Heidi Nelson, thank you for showing me how to use the magnet and for answering my many questions about Cu^{+} and EMPs. Dr. Matt Crane, I admire your endless curiosity and your insightful research advise, thank you for teaching me through numerous spectroscopy problems. Tyler Milstein, I admire your ability to completely immerse yourself into a hobby or research area and then quickly change directions. Thank you for sharing memes, stock tips, jokes, and nanocrystals. Ted Cohen, I greatly appreciated that you continued on the LSC project and that you were able to teach me valuable coding skills, I hope that I get another chance to sail with you. Diana Roh, I admire your determination to complete a research project or a marathon and your ability to speak your mind, thank you for laughing at my jokes and for sharing your cat pictures. Atch Gopalan, thank you for taking time to chat about soccer and for your willingness to grab a pint. Kelly Walsh, I am enormously grateful of your help with diffusion doping, the magnet, and lab safety, thank you for taking over on so many of my group roles and helping the lab manage to get through COVID. Laura Jacoby, thanks for coming to me for advice/questions, and for helping me to learn coding skills. Thank you, Kimo Pressler, for helping me transition to the world of 2-D magnetism, I'm excited to see all the awesome nanocrystals you'll make in the not-so-distant future.

Thank you Prof. Gerd Bacher for your wonderful mentorship while sharing the CHB 218 office with me. I do not think I would have finished graduate school had I not been given the opportunity to interact with you on daily basis. Thank you for inviting me to study in your lab and making me feel welcome in Duisburg. Dr. Rachel Fainblat, thank-you for all your help in the basement, especially for helping me fix the MCD and most especially sharing in the experience of putting a screwdriver through the magnet. Thank for all of your mentorship of the single particle collaboration and for supporting my stay in Duisburg. Dr. Severin Lorenz, I will forever appreciate the single particle spectroscopy that you did on the EMP samples, thank you for all of your exceptional work and for making my summer in Duisburg memorable.

I would like to thank my family for all of their love and encouragement for the last 28 years, without their support I would not have been able to achieve this accomplishment. I appreciate that you have always pushed me to pursue school, even at the expense of not yet having a real job. Thank-you for asking me questions about my work, for teaching me my earliest math and science lessons, supporting my many school activities (academic or otherwise), and for making me feel close despite the great distance between us. Jon, thank you for getting me out of the lab, for helping me explore brewing, and for being a supportive younger brother. Jon and Nancy Garvin, thank you for your love and support throughout my entire school career and for proving me with a home-away from home in Lake Stevens.

Emily Garvin, you are truly my better half. Thank you for going with me on my grad school journey and for making this part of our lives so fun and memorable. I have always appreciated and continue to depend on your daily love, encouragement, and support. I admire your thoughtfulness, tenacity, creativity, humor, curiosity, and independence. Thank you for making my Ph.D possible, I'm really excited to see where we go from here.

Table of Contents

List of Figures

Chapter 1: Accessing Excitonic Magnetic Polarons with Doped Semiconductor Nanocrystals

1.1.Overview

The introduction of magnetic dopants to semiconductor nanocrystals (NCs) provides a platform to not only impart entirely new magnetic functionality to semiconductor materials but also to study the intersection of magnetism and semiconductor physics. Understanding gained from the study of dilute magnetic semiconductors (DMSs) will support spin manipulation techniques related to quantum computing technologies. Significant strides have recently been made in the synthesis DMS NCs, though further development of magnetic exchange interactions in these materials is still needed to make an impact in this technology space. This Chapter summarizes the underlying physical phenomena responsible for robust magnetic exchange interactions, highlights key synthetic contributions to the field of magnetically doped NCs, and discusses the emergence of NC excitonic magnetic polarons (EMPs). Investigations of NC EMPs provide evidence supporting a longstanding hypothesis that NC anisotropy is a major contributor to both the magnitude and directionality of excited state magneto-optical behavior. Insight gained at the single particle level significantly advances the field of NC EMPs and suggests further exploration of the relationship between NC anisotropy and photo-induced magnetism.

1.2 Introduction

Semiconductors underpin the vast technological space that defines the modern world and have been the guiding force of the past two centuries of scientific development at the intersection of materials chemistry, optical spectroscopy, and applied physics. Complete understanding of the structure-function relationship between a semiconductor's composition and its electronic, magnetic, and optical properties is fundamentally important to those three fields. The origin of this understanding is a fabric of materials synthesis expertise, honed over iteration, and precise experimental insight, focused by theory. Recent advances in materials synthesis and characterization have given chemists exceptional control over the composition, crystal structure, shape, and most importantly control over the material's size at the nanometer scale.[1-4] Early

synthetic methods for nanometer scale CdSe semiconductor crystals with narrow size distributions revealed that careful adjustment of size of nanocrystals would result in a change in the material's optical properties.[5,6] At this scale classical physics can no longer describe observed phenomena and quantum mechanics must take precedence. In this quantum mechanical framework, the exciton, which is an electron/hole pair generated by the absorption of a photon, becomes like the classic quantum mechanics case study of a particle in a box, with a Hamiltonian described by the nanoparticle's size, shape, and composition. Consequently, the energy of the exciton (particle) is partly determined by the confinement potential of the nanocrystal radius (box size).

In addition to the affirmation of quantum mechanical theory, this observation yields two incredible results. First that the properties of semiconductors at the nano scale are fundamentally different from their bulk counterparts, opening opportunities for applications that could not be realized using bulk materials.[1-6] Second, that controlling the particle size provides a degree of tunability to engineer the material's properties to the specific needs of a given application. Combined, these two results have sparked considerable research attention, creating the field of semiconductor nanocrystals as we know it today, because of their potential impact to a vast number of vital industries such as solar energy harvesting, information processing, bioimaging, solid state lighting, and many others.[7-13] Many more potential applications and research directions could still be opened as semiconductor nanocrystal community investigates new ways to tune the properties the material properties.

Another method to impart additional tunabilty or even to add entirely new functionality to the existing semiconductors is the incorporation of impurity defects or dopants.[14-18] Historically the incidental incorporation of impurity defects was problematic to a field attempting to investigate and utilize pure semiconductor materials.[19] However, the intentional incorporation of dopant atoms can, for example, impart new photoluminescence pathways allowing for the development of phosphor materials such as the ruby laser.[20] Incorporation of dopants with unpaired electrons, also known as spins, can impart magnetic functionality where the individual spins can be detected and manipulated to perform logic, communications, and storage functions in spin-based devices.[21-25] Semiconductors doped with transition metal atoms form a family of materials known as dilute magnetic semiconductors (DMS).[26] DMSs are particularly attractive for spin-based applications because their properties derive from a combination of the magnetic dopant and the host

semiconductor.[21-25] Spin exchange interactions between the host semiconductor charge carriers and the dopant's unpaired spins have led to the observation of a variety of magneto-optical phenomena such as "whopping" Zeeman splittings,[27,28] magnetically tunable lasing,[29] giant Faraday rotations,[30-32] and the most notable yet discovered: the optical generation of a magnetically ordered excited state, known as an excitonic magnetic polaron (EMP).[33-46]

Localization of the semiconductor carriers within the quantum confinement potential of a nanocrystal or other nanostructured material enhances the spin exchange interactions with the dopant spins due to the increased spatial overlap between the carrier wavefunctions and the dopant spins.[47-49] Consequently, DMS nanomaterials have received considerable attention for attaining the maximum possible magnetic response.[14,15,50-54] This attention has revealed that incorporating dopants into these nanomaterials is a unique synthetic challenge absent in bulk materials and that DMS nanomaterials provide the opportunity to study effects or applications that cannot be accessed at the bulk semiconductor level.[55] This chapter will serve as an introduction to the synthesis and spectroscopy of magnetically doped semiconductor nanocrystals with specific attention paid to the EMP phenomena observed in these nanocrystals. We begin with a discussion of the spectroscopic signatures of transition metal dopants in II-VI semiconductors and how magneto-optical spectroscopies can inform our understanding of the magnetic exchange interactions. Next, we will discuss the roles of the nanocrystal size, shape, and surface as well as the distribution of dopant ions as they relate to materials magnetic and optical properties. Then we will review the history of doped nanocrystal synthesis and the methods employed to achieve well controlled doping of high-quality particles. Finally, we will highlight the recent progress toward understanding the formation and dynamics of the EMP excited state in colloidal nanocrystals.

1.3 New properties from transition metal dopants

The general purpose of doping is either to enhance an inherent property of the pure material that you are adding the dopant into or add a new property to the material. Dopants, when incorporated into II-VI materials, can add a mixture new electronic, luminescent, and magnetic properties. Depending on the nature of the dopant, certain characteristic features are observed and investigated to fully understand how the dopant is changing the properties of the host semiconductor. We will focus on the cases of luminescent and magnetic dopants.

1.3.1 Luminescent dopants. When luminescent dopants are introduced, the host semiconductor can be used as an optical sensitizer of electronic states within its band gap introduced by well-known luminescent dopants like Mn^{2+} or Cu^{+}, known as activators.[11, 56] Photoexcitation of the host semiconductor promotes an electron from the valance band to the conduction band creating an electron-hole pair, an excited state known as an exciton. In undoped materials, this exciton may relax radiatively via emission of a band-edge photon following electron-hole pair recombination, or non-radiatively via energy transfer to a defect site, coupling to lattice vibrations, or multicarrier processes such as Auger recombination.[1-3]

Luminescent dopants open new relaxation pathways for the exciton which must compete with the native relaxation pathways that are observed in undoped materials.[14-19] Certain luminescent dopants like Mn^{2+} introduce discrete *d-d* states to the electronic structure of the host semiconductor.[14-16] If energy transfer to these dopants can out compete the other relaxation processes, then the energy of the exciton will be used to excite the internal *d-d* transition localized around the dopant. This state will then relax according to the selection rules and processes specific to that localized *d-d* state. In the case of Mn^{2+}, it possesses a d^5 electron configuration resulting in the characteristic spin and parity forbidden lowest energy (~2.2 eV) *d-d* transition $^4T_1 \rightarrow {}^6A_1$.[14-16] When Mn^{2+} is doped into II-VI materials with bandgaps greater than ~2.2 eV, such as ZnS, ZnSe, or CdS, this *d-d* level is energetically positioned within the band gap.[16] Photoexcitation of these materials results in rapid energy transfer from the delocalized excitonic excited state to the $^4T_1$ excited state localized on one of the Mn^{2+} dopants, mediated by higher-lying vibronic levels.[16] Since the recombination from this state is both spin and parity forbidden, the photoluminescence lifetime is on the order of 100's μs to ms long. The characteristic efficient energy transfer, long PL lifetime, and orange color are key signatures of Mn^{2+} luminescence in the many commercial phosphors based on this dopant.[19]

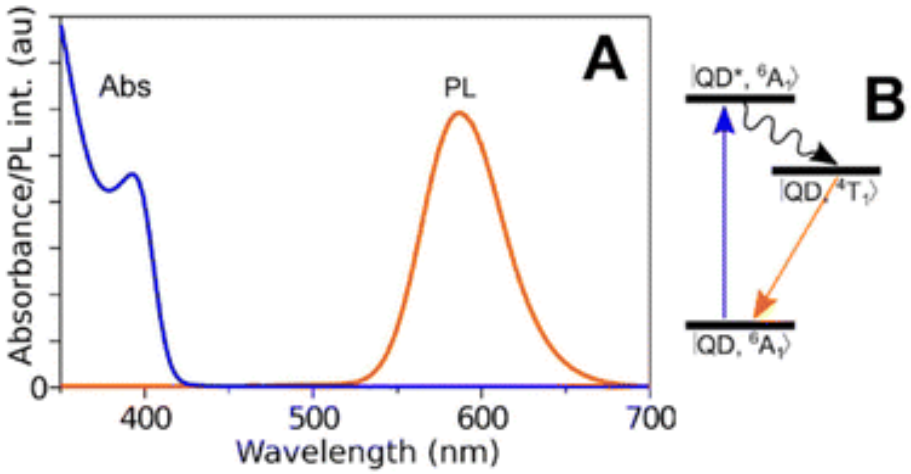

Figure 1.1 Photoluminescence in Mn^{2+} doped ZnSe/ZnS NCs. (A) Absorption and photoluminescence spectra of colloidal Mn^{2+}-doped ZnSe/ZnS QDs. (B) Schematic description of luminescence sensitization in Mn^{2+}-doped QDs. Photon absorption by the doped quantum dot in its ground state ($|QD,{}^6A_1\rangle$) gives the excited quantum dot ($|QD^*,{}^6A_1\rangle$). Energy rapidly localizes to excite Mn^{2+} within the QD ($|QD, {}^4T_1\rangle$), which then emits with a high quantum yield. Radiative processes are indicated as straight lines and nonradiative processes as wavy lines. Adapted with permission from reference 56.

When Mn^{2+} is doped into II-VI materials with bandgaps less than ~2.2 eV, such as bulk CdSe or CdTe, the $^4T_1$ excited state is energetically outside the band gap.[16] In these materials, energy transfer to Mn^{2+} is not possible because thermalization to the lower lying excitonic excited state is orders of magnitude faster than any possible energy transfer mechanism. However, when materials like CdSe are quantum confined, as they are in NCs, the energy of its lowest excitonic excited state can be tuned to be greater than the ~2.2 eV Mn^{2+} $^4T_1$ excited state.[57-61] In very small CdSe with large band gap energies, sensitized Mn^{2+} luminescence is observed.[16, 61] For intermediate sizes of CdSe NCs, the excitonic excited state of the CdSe can be tuned just above the energy of the Mn^{2+} $^4T_1$ excited state.[61] When these two states are close in energy a thermal equilibrium is achieved between the two excited state populations and emission is observed from both states.[61] At low temperatures, only Mn^{2+} $^4T_1$ excited state emission is observed because the excited state population does not have the requisite amount of thermal energy to repopulate the higher lying excitonic state.[61] At high temperatures, only excitonic photoluminescence is observed because there is sufficient thermal energy to populate the excitonic state and because excitonic

radiative recombination probability is on the order of 10^4 times greater than the probability of the spin and parity forbidden Mn^{2+} $^4T_1 \rightarrow {}^6A_1$ transition.[16, 61] Carefully tuning the excitonic excited state in related to the $^4T_1$ excited state will alter the energetic spacing between the two levels resulting a change in the temperature requires for the two excited state populations to reach equilibrium.[57-61] The relationship between the CdSe NC size and the observation of Mn^{2+} *d-d* emission is depicted in Figure 1.2 below.

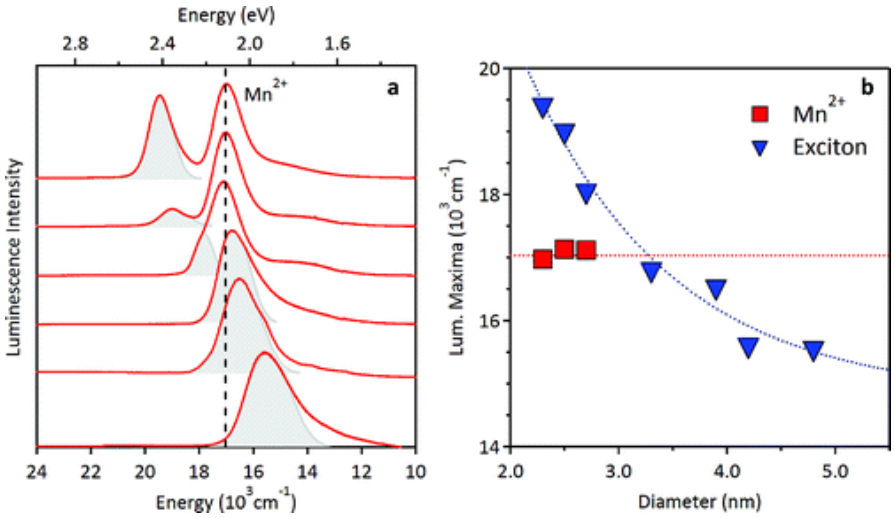

Figure 1.2 Size dependent photoluminescence in Mn^{2+}: CdSe NCs. Mn2+: CdSe quantum dot photoluminescence as a function of nanocrystal diameter. (a) Low-temperature (5 K) photoluminescence spectra of a series of Mn^{2+}: CdSe quantum dots with d = 2.3, 2.5, 2.7, 3.3, 3.9, and 4.2 nm (top to bottom). The vertical broken line shows the energy of the Mn^{2+} $^6A_1 \leftarrow {}^4T_1$ luminescence (maximum: 17200 cm^{-1}, or 2.11 eV), observed only in the smallest samples. (b) Energies of the Mn2+ 4T1 and CdSe excitonic photoluminescence maxima plotted vs Mn^{2+}:CdSe nanocrystal diameter. Adapted with permission from reference 61.

1.3.2 Magnetic Dopants. Magnetic transition metal dopants constitute any dopant that possess unpaired electrons when substituted for the host cation, and in II-VI semiconductor materials these dopants include Co^{2+}, Fe^{2+}, and Mn^{2+}.[49-54] The unpaired spins in the dopants *d* orbitals can introduce new magnetic properties to the host semiconductor through magnetic exchange interactions which are mediated through several orbital pathways involving the orbitals that comprise the host's conduction and valence bands.[62] In the case of CdSe and similar II-VI materials these bands are largely characterized by predominantly empty Cd (or other cation) *s*

orbitals in the conduction band and predominantly filled Se (or other anion) *p* orbitals in the valence band.[62] Owing to the nature of these orbitals, the exchange interactions are known as *sp-d* exchange interactions.[62] In materials where these exchange interactions are strong, magnetic behavior is manifested in the electronic transitions of the host semiconductor exhibiting large excitonic Zeeman splittings among other effects.[28]

1.3.3 Sp-d Exchange. The coupling between the delocalized carriers in the host semiconductor bands and the localized unpaired dopant *d* electrons is the primary feature that defines DMS materials.[49] Since Mn^{2+} is the most studied dopant in the DMS material literature, and because it is responsible for the EMP phenomena that will discussed in more detail later we will use it as an example to describe *sp-d* exchange interactions. Magnetic exchange coupling.is mediated by electron exchange in orbital pathways between a Mn^{2+} dopant and the host CdSe bands. Electrons localized on the Mn^{2+} *d* orbitals can fill empty orbitals in the valence band, likewise electrons in the valence band can fill empty orbitals of the Mn^{2+} dopant. Similarly, electrons in the conduction band may fill empty dopant orbitals. Though typically labeled as *s-d* exchange the interactions with the conduction band electrons and dopant orbitals are dominated by ferromagnetic kinetic exchange largely involving the Mn^{2+} 4*s* orbitals, though some weak *anti*-ferromagnetic kinetic *s-d* exchange interactions are also present.[62] On the other hand, exchange with the valence band holes are dominated by *anti*-ferromagnetic kinetic exchange.[49,62]

These *s-d* and *p-d* exchange interactions have characteristic exchange energies that are related to the exchange constants $N_0\alpha$ and $N_0\beta$, respectively.[49] The exchange energy between the valence band holes and Mn^{2+} dopants is on the order of 4-5 times stronger than with the conduction band electrons due to a combination of symmetry restriction on *s-d* interactions and the hybridization of the Mn^{2+} 3*d* orbitals with the anion *p* orbitals that comprise the valence band.[62,63] Similar exchange pathways exist for other magnetic dopant and host semiconductor, though each combination of dopant and host have unique values for $N_0\alpha$ and $N_0\beta$.[49] The exchange energy also depends on the extent of the charge carrier-dopant wavefunction overlap.[47] Dopants closest to the center of these wavefunctions have the greatest impact on the total exchange interaction, and their influence diminishes as the probability distribution of the wavefunction goes to zero.[47] For this reason, DMS materials are typically engineered to produce the greatest possible overlap between the charge carrier wavefunctions and the dopant ion distributions. NCs are especially useful in this

regard because the quantum confined wavefunction increases the overall overlap integral due to the significantly reduced wavefunction tunneling outside of the NC.[49-55] Furthermore, because the wavefunction probability distribution can be tuned with the size of the NC some of the magnetic properties also take-on a size dependence.[47]

At zero external magnetic field the exchange interactions can lead to several magnetic phenomena such as EMP formation.[33-46] When a semiconductor is placed into a magnetic field the spin degeneracy of its excitonic levels is split in energy according to the well-studied Zeeman effect. Equation 1 (shown below) describes the contributions to the total Zeeman splitting energy as a sum of the intrinsic contribution of the host semiconductor (ΔE_{int}), and the contribution from Mn^{2+} derived *sp-d* exchange interactions (ΔE_{sp-d}).[28]

$$\Delta E_Z = \Delta E_{int} + \Delta E_{sp-d} = g_{int}\mu_B B + x_{eff}\gamma N_0(\alpha - \beta)\langle S_z\rangle \qquad \text{Eq 1.1}$$

While the intrinsic term only depends on the intrinsic g value of the host exciton (generally ~1), the Bohr magneton (μ_B), and the applied magnetic field, *B*, the exchange term is more complex. The giant Zeeman effect that is observed in DMS materials depends on a combination of the effective dopant concentration, x_{eff}, the exciton-dopant wavefunction overlap term, γ, the exchange parameter, $N_0(\alpha - \beta)$, and the spin expectation value, $\langle S_z\rangle$.[28] In this analysis, the dopant concentration is considered "effective" because Mn^{2+} and other similar dopants will typically form antiferromagnetic dimers and other clusters with reduced total magnetization.[64] Assuming a statistical formation of these dimers and clusters based upon the geometry of the host crystal lattice and a given total dopant concentration one can relate the effective dopant concentration to the total concentration.[64] Since the overlap integral cannot be directly measured it is usually taken to be 1 unless knowledge about the dopant distribution or electronic structure of the host semiconductor would suggest that it should be reduced, γ=1 for a uniform Mn^{2+} distribution. The spin expectation value, $\langle S_z\rangle$, is defined by the Brillouin function (Equation 1.2), and describes the magnetization of a Curie paramagnet of a given spin, S, and gyromagnetic ratio, g_{TM}, along the magnetic field direction, *z*, at the experimental temperature, *T*, and applied magnetic field, *B*.[28] Using the sign convention of Piepho and Schatz, $S = -5/2$,[65] for Mn^{2+} and the exchange parameters $N_0(\alpha - \beta)$ are positive.[28]

$$S_z = \frac{2S+1}{2}coth\left(\frac{2S+1}{2}\frac{g_{Mn}\mu_B B}{k_B T}\right) - \frac{1}{2}coth\left(\frac{g_{Mn}\mu_B B}{k_B T}\right) \qquad \text{Eq 1.2}$$

ΔE_{sp-d} opposes the relatively weak ΔE_{int} and is strongly temperature dependent since it follows the temperature dependence of the paramagnetic dopant Mn^{2+}.[28, 66] At sufficiently low temperatures, and sufficiently large values of x_{eff}, ΔE_{sp-d} dominates the total Zeeman splittings in Mn^{2+} doped DMS materials.[28] In the limit of small magnetic fields (before dopant magnetization begins to saturate), ΔE_Z is linearly dependent on the external magnetic field and it can be approximated with an effective *g*-factor using the following equation:

$$\Delta E_Z \approx g_{eff}\mu_B B \qquad \text{Eq. 1.3}$$

1.3.4 Magneto-Optical Spectroscopy. While there are a variety of spectroscopic and analytical techniques can detect the incorporation of a dopant inside a host semiconductor lattice, most of these techniques do not provide any information about the nature or extent of the magnetic exchange interactions that may be occurring in DMS materials.[67, 68] Optically detected magnetic resonance and electron paramagnetic resonance provide clear signatures of a specific dopant within a nanocrystal lattice and depending on the dopant concentration can determine properties of the dopant such as its the general location or coordination environment, though these can lose sensitivity when the dopant concentration is larger than ~1%.[69-71] Further than measuring just the presence of a dopant in the lattice, polarized spectroscopies such as magnetic circular dichroism (MCD),[28] magnetic circularly polarized photoluminescence (MCPL),[16] and Faraday rotation[30-32] can provide a wealth of information about the characteristic *sp-d* exchange interactions in DMS materials by directly probing the host semiconductor's electronic transitions in a magnetic field.[28]

MCD spectroscopy probes the differential absorption of left and right circularly polarized light in an applied magnetic field and it is a particularly useful tool to investigate the magneto-optical response of magnetically doped materials.[28] The application of the magnetic field splits an initially spin degenerate state into its separate M_J levels according to the Zeeman affect.[28] The simplest version of this splitting is depicted in Figure 1.3. MCD utilizes that difference in the selection rules for the absorption of polarized light to probe the splitting between these states. Under zero applied magnetic field, the absorptive transition from ground to excited state is equally allowed for both right and left circularly polarized light. Following application of the magnetic field, each of the M_J levels is then separated in energy and is only accessible via the polarization of light allowed for that transition: σ^+, right circular polarized light, for the $\Delta M_J = -1$ transition and σ^-, left circular polarized light, for the $\Delta M_J = +1$ transition. Due to the energetic splitting

between these two levels, the MCD signal, plotted as the difference between the absorption of left and right circularly polarized light, is manifested as a derivative shape with a negative leading edge (using the sign convention of Piepho and Schatz).[65] The example shown in Figure 1.3 is generally classified as an A term MCD signal, where the magnetic field is only splitting the spin degeneracy of the excited state. Other MCD signals that may be present include a field induced splitting of the ground state, C term, and a field induced mixing of states, B term, though these signals do not feature prominently in the MCD spectra of DMS materials.[65] The Zeeman splitting occurs in all the excitonic transitions observed in CdSe and each of these transitions have their own intrinsic Zeeman splitting behavior.[49] Incorporating a dopant, such as Mn^{2+} to the CdSe NC alters both the sign and magnitude of the observed Zeeman splitting.[28] Collectively the MCD spectrum of the excitonic transitions reveals the combined ground state magneto-optical response of the material. While disentangling the contributions from each individual transition is possible and informative, analysis of the lowest energy feature is typically sufficient to determine the magnitude of the dominant *sp-d* exchange interactions.[72]

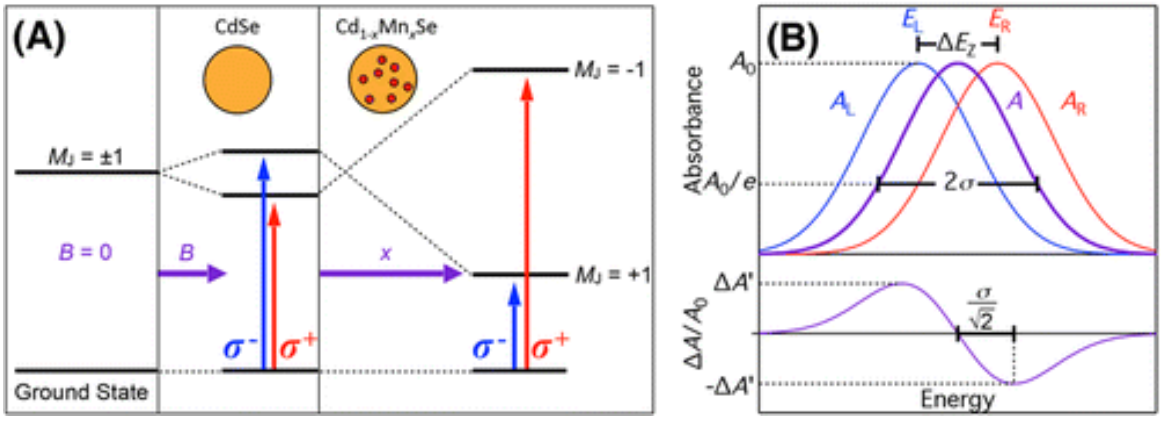

Figure 1.3 A-term MCD splitting. (A) Excitonic Zeeman splittings in undoped and Mn^{2+}-doped CdSe QDs, as probed by absorption and MCD spectroscopies. Application of an external magnetic field (B) splits the first bright excitonic state by the Zeeman energy, ΔE_Z. The sp–d exchange inverts and enhances this splitting, yielding a "giant" excitonic Zeeman splitting. (B) Illustration of the excitonic Zeeman splitting as probed by absorption (top) and MCD (bottom) experiments. The key parameters used for quantitative spectral analysis are illustrated. Adapted with permission from reference 28.

Measuring the temperature-dependent excitonic Zeeman splitting reveals the influence of thermal effects, specifically the ease of aligning an ensemble of paramagnets who's thermally assisted fluctuations are suppressed at low temperature, on the magneto-optical behavior of Mn^{2+} doped CdSe.[28, 66] Additionally, in the limit of low dopant concentration, the variable temperature MCD signal demonstrates the competition between the oppositely signed intrinsic and exchange derived Zeman splitting energies as demonstrated in Figure 1.4.[66]

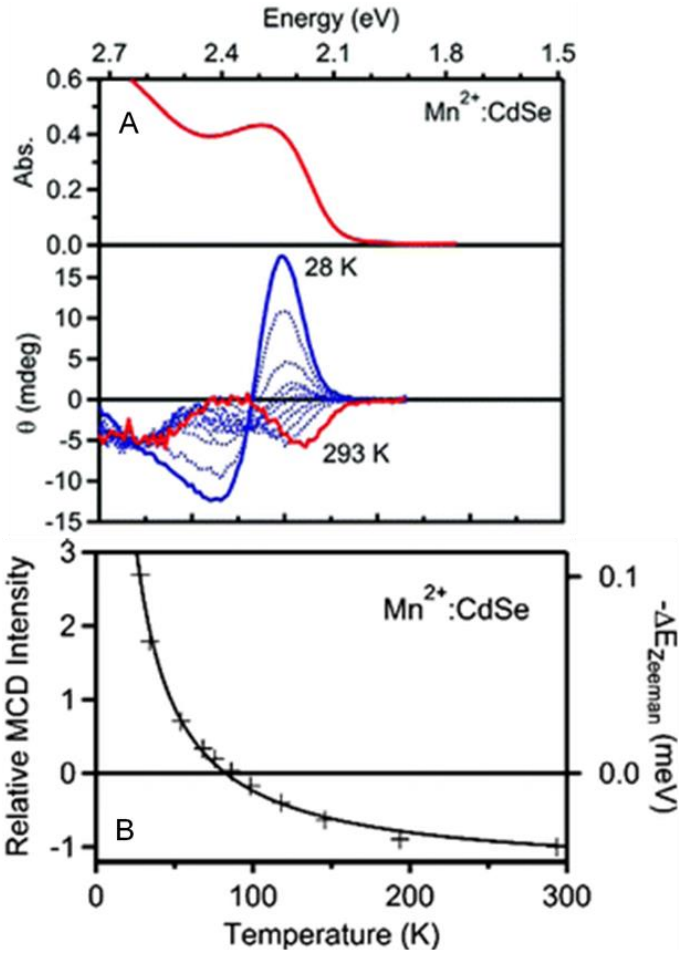

Figure 1.4 Temeperature dependent MCD of Mn^{2+} doped CdSe. (A) Representative absorption and variable temperature MCD spectra of colloidal 0.5% Mn^{2+} doped CdSe collected at 0.63T. The bold red and blue MCD spectra represent the highest and lowest temperatures, respectively. (B) Temperature dependence of the MCD signal intensities in panel A, normalized at room temperature. The plus signs are the integrated MCD intensities of the lowest-energy feature for the exciton. The solid line are fits to the data using equations 1.1-1.2. The right axes show the corresponding excitonic Zeeman splittings. Adapted with permission from reference 66.

Typically, the Zeeman splitting is measured in the low temperature limit where ΔE_{sp-d} dominates the contribution from ΔE_{int} due to the inverse temperature dependence of S_Z, therefore contributions from ΔE_{int} are ignored.[28] When dopant concentrations are large, the observed excitonic Zeeman splitting at low temperature (<2 K) can be on the order of 100+ meV at magnetic saturation. with g_{eff} values exceeding 1000.[28, 52] The contribution from the *sp-d* exchange interactions to the excitonic Zeeman splitting in these highly doped materials is large enough to maintain the sign of the MCD signal even at room temperature.[28,52]

1.4 Synthetic Advancements in Magnetically Doped Nanocrystals

Following the emergence of reproducible synthetic procedures for colloidal NCs,[4-6] the DMS community quickly attempted to find a suitable method for doping these structures due to their interest in investigating the effects of increased quantum confinement on the magnetic exchange interactions.[14] The magnitude of these interactions was predicted to be substantially increased in the quantum confined limit that small particles afforded.[47] Additionally, the processability of colloidal solutions would vastly simplify future device integration.[3, 4, 6, 7, 11] The solubility of Mn^{2+} and other similar dopants in bulk materials,[26] suggested that the incorporation of these dopants in NCs would be relatively straightforward. However, early attempts to make doped CdSe, ZnSe, and other similar NCs with Mn^{2+} resulted in dopant concentrations below 1%, resulting in a large fraction of the NCs with no dopant ions at all.[55] This initial difficulty even led some to conclude that dopants such as Mn^{2+} in CdSe could never be incorporated in large quantities.[55] At the time, differences between dopant and host diffusivity, reactivity, and ligand affinity were not fully appreciated as groups were attempting to introduce dopants simultaneously with NC nucleation and growth. Ultimately, the large surface to volume ratio found in colloidal NCs coupled with energetic favorability of the formation of ligated dopant ions over dopant-anion bond formation in the host NCs led to poor rates of dopant inclusion.[52,55]

Alongside early attempts to incorporate dopants during the NC nucleation and growth stages several research groups were beginning to demonstrate the versatile control of post synthetic cation exchange.[73-75] Early reports showed that NCs shelled with a secondary semiconductor material, such as CdSe shelled with ZnSe, would undergo rapid alloy formation, indicating that cations inside NCs were mobile.[76] Using purified, pre-made NCs researchers could demonstrate that when the cation of their choice is introduced and when the chemical potential of both cations

in the solution as well as in the NCs are carefully tuned that they could drive systematic cation exchange reactions.[73-75] This versatile, often reversible, approach could produce large dopant concentrations, well controlled alloy formation, and core/shell interfaces.[77-79] The primary caveat of this approach, however, was that only dopants with high diffusivity and bond formation energies competitive with those of the host cation could be utilized.[73-79] Though cation exchange could not be used to incorporate poorly diffusing dopants such as Mn^{2+}, it could be used to partially explain why Mn^{2+} incorporation was so difficult. Since cations in the NC lattice were mobile during the NC growth phase, solution mediated cation exchange processes could rapidly cycle cations from NC interior and surface to the solution completing a cycle of self-purification where weakly bound dopants would be expelled.

Identifying the role of specific ligands interactions with the dopant ions proved to be the most fruitful step towards robust doped NC synthesis. Larger dopant concentrations were achieved using cluster thermolysis reactions, where clusters of ten or fewer semiconductor units are thermally decomposed in mildly coordinating conditions.[50, 80-84] The advantage this synthetic procedure has over more typical "hot-injection" procedures is that the NC nucleation and growth phases are significantly stretched in time allowing researchers to monitor the slow incorporation of dopant ions as the NCs reach their stable final size.[50, 80-84] This method was first developed using Co^{2+} dopants in CdS NCs, where characteristic shifts in the Co^{2+} ligands field absorption were especially useful.[50, 84] This absorption signal could indicate differences between surface coordinated Co^{2+} that were partially bound by amine-based ligands and Co^{2+} that was completely coordinated by lattice S^{2-}.[50, 84] Adapting this synthesis for Mn^{2+} in ZnSe and CdSe revealed that the harder Lewis acid, Mn^{2+}, would be less likely to remain in the NC when cation exchange was possible. Moving to less coordinating solvents, reducing the amount of cation coordinating ligand and increasing the amount of free anion in solution proved to be particularly useful solutions for the differences between these two dopants in the cluster synthesis and were carried forward to future syntheses.

Though the cluster method was able to achieve record Mn^{2+} concentrations in NCs, it was also plagued by poor control over the NC size, shape, and morphology and efforts to circumvent these issues were usually met with losses in the NC monodispersity or in the dopant concentration. For this reason, the Gamelin group took inspiration from NC cation exchange processes and used

the observations gained from the cluster synthesis to develop a new synthetic procedure known as "diffusion doping".[52] In this method, pre-made CdSe NCs are combined with excess Se^{2-} and Mn^{2+} at elevated temperature and allowed to react over a period of time between 10's of minutes to several hours.[52, 85] During the reaction, Se^{2-} is first deposited onto the NC surface, reducing the chemical potential of cations in the NCs by creating cation vacancies. Excess Mn^{2+} in solution, combined with minimal cation coordinating ligands, increases the chemical potential of cations in solution. Combined, these changes in chemical potential create a driving force for the dopant Mn^{2+} ions to diffuse into the volume of the NCs. Over the course of several hours the dopant concentration and magnetic exchange interactions first sharply rise and then stabilize as the dopants are thermodynamically distributed through the NC. Mn^{2+} concentration exceeding 35% can be easily achieved using this method. Diffusion doping is a major milestone in the preparation of DMS nanomaterials for several reasons. First, the NC ensemble size distribution, shape, and morphology are all maintained during the course of the reaction. Second, the Mn^{2+} dopant concentration can be stoichiometrically controlled with the amount of anion added to the reaction mixture. Finally, this reaction can be adapted to incorporate similar dopants like Fe^{2+} and Co^{2+} into the broad family of II-VI NCs. The unprecedented level of control afforded by diffusion doping has opened new avenues to explore the effects of *sp-d* exchange interactions in DMS NCs and has already yielded the largest Zeeman splittings and g values reported to date.[28]

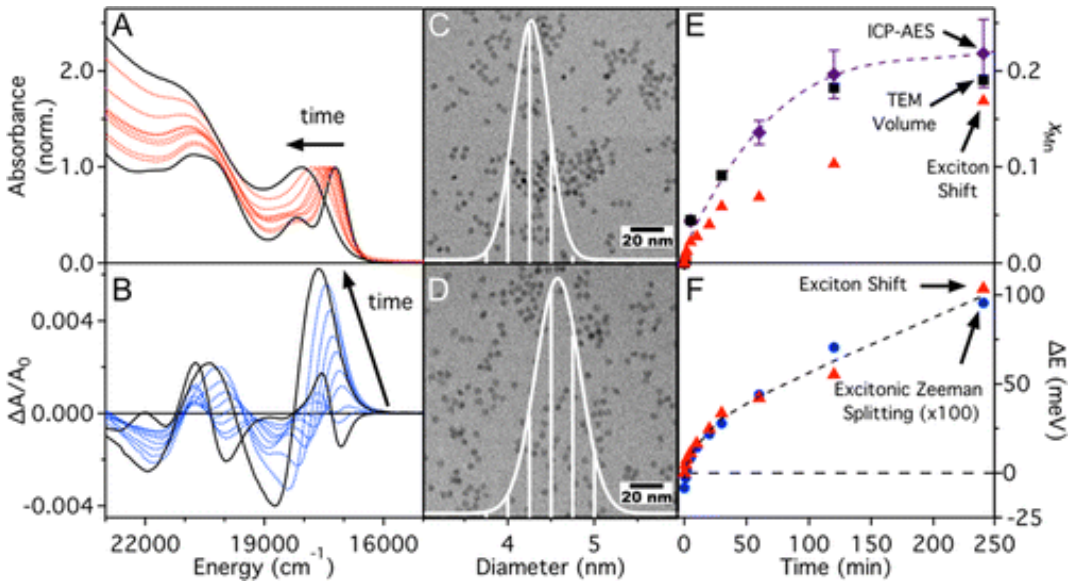

Figure 1.5 Spectroscopic signatures of diffusion doping. (A) Room-temperature absorption spectra of reaction aliquots taken at different times during wz-CdSe nanocrystal diffusion doping at 300 °C, normalized at the first excitonic maximum. (B) Corresponding MCD spectra showing a sign inversion and signal growth with increased reaction time, indicative of growing sp–d exchange coupling strengths. TEM image and corresponding diameter histogram from analysis of undoped CdSe precursor nanocrystals (C), and of $Cd_{1-x}Mn_xSe$ nanocrystals after diffusion doping (D). (E) Mn^{2+} concentration (x_{Mn}) determined by ICP-AES (purple tilted squares, with error bars from three measurements of each aliquot), analysis of nanocrystal volumes from TEM (black squares), and analysis of the excitonic absorption energy shifts (red triangles). (F) Excitonic absorption energy shifts (red triangles, from analysis of panel A data) and excitonic Zeeman splittings (blue circles, from analysis of panel B data, multiplied by 100) plotted vs the diffusion-doping time. Adapted with permission from ref 52.

1.5 Excitonic Magnetic Polarons

The most remarkable phenomena related to the DMS exchange interactions is the photo-induced formation of a magnetically ordered state known as the EMP.[33-46] EMPs occur when simultaneous coupling between individual dopants and the spins of the carriers induces a ferromagnetic alignment of the dopant spins within the volume of the semiconductor exciton in the absence of an external magnetic field.[33-46] Magnetic ordering is accompanied by a splitting of the excitonic spin states and a stabilization of the exciton of tens to hundreds of meV in some

cases.[43] Similar to the EMP, the bound magnetic polaron, was initially observed in bulk materials, the magnitude of the sp-d exchange interactions that govern magnetic alignment can be enhanced by localizing the volume of the semiconductor carrier wavefunctions within the confinement potential associated with defects or material interfaces.[33-36] Recent advances in colloidal nanocrystal synthesis have led to even an even greater degree of confinement than is afforded in quantum-well or other self-assembled structures.[52, 54] Using high quality doped semiconductor nanocrystals researchers have demonstrated substantially larger EMP stabilization energies than the previous self-assembled systems,[43] integration with electronic devices,[86] and with their greater degree of synthetic tunability,[52, 54] nanocrystal EMPs have enabled the testing of longstanding hypotheses related to anisotropy,[43, 87] and dopant spin dynamics.[46, 87]

1.5.1 General Characterization. In general, an EMP may only be formed when the photo-induced energetic stabilization of the exciton is large enough to suppress the statistical magnetic fluctuations of the dopant spins which oppose the net alignment of the EMP.[33-46] Since the dopant spins are Curie paramagnets and the statistical fluctuations are driven by the system's available thermal energy, EMPs have typically only been observed at very low temperatures.[33-46] Additionally, the excitonic excited state lifetime, τ_{Ex}, must exceed the EMP formation time, τ_{mp}, so that the EMP can form before the exciton decays. For most samples, under steady-state excitation conditions, the variable temperature photoluminescence can be used as a reliable method to determine the equilibrium EMP energy, E_{mp}, as shown in Figure 1.6.[33-46] Temperature dependence of the EMP semiconductor band gap is well described by a combination of the typical Varshni temperature dependence and a low temperature Brillouin-like contribution:

$$E_g(T) = E_0(T) - E_{mp}(T) = E_0(T) - \frac{1}{2} x_{eff} \gamma N_0 (\alpha - \beta) B_{5/2}\left(\frac{5\mu_B g_{Mn} B_{eff}}{2k_B(T+T_0)}\right) \qquad (1.4)$$

where $E_0(T)$ is the intrinsic temperature dependent Varshni behavior, $B_{5/2}$ is the Brillouin function (see Eq 1.2) for spin S=5/2, $N_0\alpha$ and $N_0\beta$ are the well-known exchange parameters for the electron and hole respectively.[26] Together T_0 and x_{eff} are parameters which consider the effective Mn^{2+} concentration that is created by the antiferromagnetic interactions of neighboring Mn^{2+} ions in the form of either Mn-Mn dimers or larger cluster species that have a reduced spin contribution. While T_0 is a phenomenological parameter between 0-5 K, that is typically taken from previous literature reports,[45] the effective Mn^{2+} concentration, x_{eff} relies on the quantification of the total Mn^{2+}

concentration and assumptions about Mn^{2+} distribution and the extent to which clusters of Mn^{2+} reduce the expected spin density.[64] The coefficient γ is a correction term that describes the spatial overlap of the confined exciton wavefunction with the dopant ions. γ is typically assumed to be 1 for a homogenous distribution of dopants.[64] Varshni behavior, $E_0(T)$, is extracted by either fitting the temperature dependent absorbance spectra, high temperature photoluminescence spectra, or photoluminescence of an appropriate undoped control sample.[46] Finally, the sp-d exchange coupled exciton-Mn^{2+} system is collectively treated as a paramagnet with an effective internal exchange field, B_{mp}, by fitting the E_{mp} (T) to a S=5/2 Brillouin function (which depends on the Bohr magneton, μ_B, the Mn^{2+} Landé g factor, g_{Mn}, and Boltzmann thermalization), B_{eff} can be extracted.[33-46]

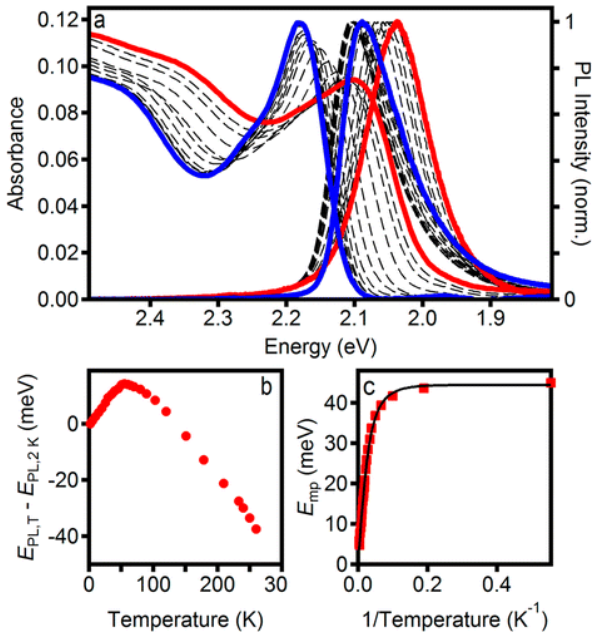

Figure 1.6 Steady-state spectroscopic signatures of EMP formation. (A) Variable-temperature absorption and photoluminescence spectra of colloidal $Cd_{0.87}Mn_{0.13}Se$ QDs ($d \sim 4.5$ nm) recorded between 5 K (blue) and 280 K (red) at zero magnetic field. (B) Temperature dependence of the PL peak energy plotted relative to the PL energy at $T = 2$ K. (C) Temperature dependence of the EMP energy obtained from the absorption and PL energies. The linear increase in the EMP energy at high temperatures reflects Curie paramagnetism. The plateau at low temperature reflects saturation of the nanocrystal magnetization. The solid line is a fit to the Brillouin function of Eq 1.2 using $S = 5/2$ and $g_{Mn} = 2.00$, which yields $B_{eff} = 17$ T for the exchange field acting on the Mn^{2+} spins in the QDs. Adapted from permission from ref 46.

EMPs that were observed in many of the earlier self-assembled QD and quantum well structures were typically limited to rather small exchange fields (B_{mp} < ~3-4T) which were insufficient to achieve magnetic saturation at all but the lowest temperatures.[33-42] The confinement afforded to colloidal $Cd_{1-x}Mn_xSe$ QDs have demonstrated exchange fields that exceed 40T when estimated at short times, and additional contributions from a secondary EMP relaxation occurring over longer times suggest that effective fields as large as 100T may also be possible.[43] The EMP phenomena, depicted schematically in Figure 1.7, can be better understood by temporally subdividing it into three distinct dynamical phases for closer examination.[46] Analyzing these phases; initial formation, subsequent stabilization, and long-term relaxation, separately, allows us to highlight the specific role that each sub-phenomenon such as dopant fluctuations, carrier lifetime, sp-d exchange, local anisotropy, or spin procession play in the overall EMP evolution.[33-45] Additionally, these phases also provide natural divisions between the various material characterization techniques and data analysis used to study EMP formation and dynamics.

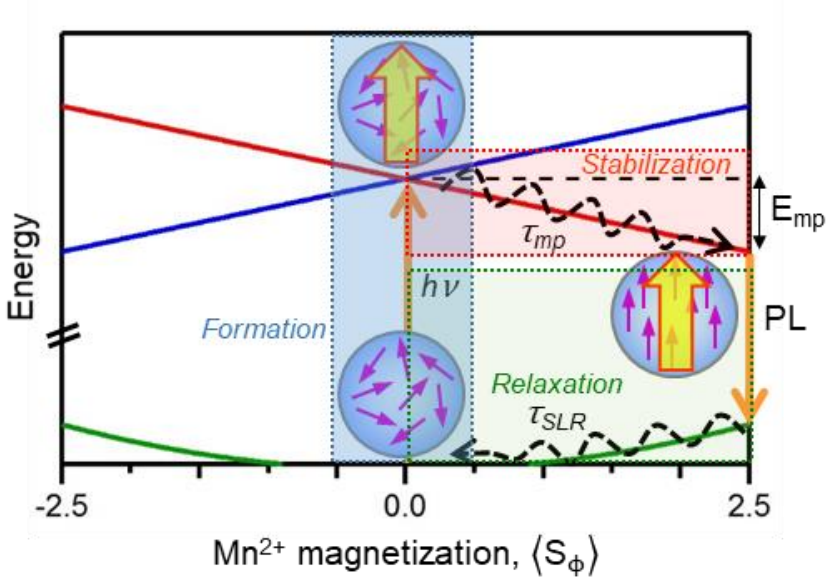

Figure 1.7 EMP magnetic coordinate diagram. Single-magnetic-coordinate diagram describing EMP formation, stabilization, and relaxation in a DMS QD along the internal magnetic direction φ at zero applied magnetic field (B_{app}=0). Red and blue lines represent the Zeeman split sub-levels of the excitonic excited state. Green line reflects the energy of the system, following recombination, as the Mn^{2+} ions aligned by the EMP undergo spin-lattice relaxation. Adapted from permission from ref 46.

1.5.2 EMP Formation. Initial EMP formation, depicted as the blue region of Figure 1.7, occurs as the exciton is generated following the absorption of a photon by the host semiconductor NC. Before photoexcitation, and with no applied magnetic field, this ensemble of spins has no net magnetization along any particular direction, (corresponding to the spin expectation value S_ϕ of 0 on the x-axis of Figure 1.7, and the cartoon QD at the bottom), however the dopant spins do fluctuate randomly in time.[46] At the moment of photoexcitation, these statistical magnetic fluctuations of the dopant spin ensemble cause a small shift of S_ϕ from 0, generating a non-zero magnetization in a random direction (either direction on the x-axis of Figure 1.7, depending on the spin of the system relative to an arbitrary observation axis). Along this initial direction, the electron and hole of the exciton, and their respective spins, start to interact via exchange coupling with the ensemble of dopant spins thereby stabilizing the exciton. In the low temperature limit, this stabilization continues to grow in magnitude as more of the dopant spins align with the spin of the exciton either until the system reaches magnetic saturation or the exciton decays via emission of a photon. Ultimately, at $B_{app} = 0$, the EMP creates a large net magnetization of the spin sub-lattice like those observed when the Zeeman sub-levels are split by the application of an external magnetic field.

Given that EMP formation results in a time resolved energetic stabilization of the exciton, time resolved photoluminescence spectroscopy (TRPL) can be used to confirm the presence of an EMP, measure its formation time, and determine the magnitude of EMP stabilization. A dynamic redshift of the excitonic TRPL energy is characteristic of EMP formation, and reports on the magnetization of the dopant spins with the exchange field of the exciton as seen in Figure 1.7A. This redshift is usually observed quite rapidly, significantly faster (~200 ps) than the excitonic PL decay (~5 ns), due to efficient Mn^{2+}-Mn^{2+} spin-spin interactions at the concentrations required to generate an EMP,[88] and possibly due to accelerated spin-lattice relaxation in the presence of the charge carriers.[89-91] The EMP formation time, τ_{MP}, is dependent on the dopant concentration and temperature.[33-42] Due to the concentration dependent spin-spin interactions that mediate EMP formation, magnetic alignment may take between ~100 ps (for x >10%) and several ns (for x ~1%) meaning that in low doping limit EMP formation may be halted by recombination before alignment can be achieved.[33-42] Though no specific Mn^{2+} concentration is required to achieve EMP formation, it is easier to observe Mn^{2+} are relatively large (>5%).

Analysis of the Mn^{2+} fluctuations and their initial influence on the magnetic exchange interactions at the moment of photoexcitation is an important consideration for EMP formation. Statistical fluctuations of Mn^{2+} spins are responsible for emission line width broadening at low temperatures, and they stem from the statistical variation of the occupation of the six possible spin projections ($s_z = \pm 5/2, \pm 3/2, \pm 1/2$) that are available for each individual Mn^{2+} ion (S = 5/2). In the limit of a single dopant, each of these six spin projections can couple with the exciton of a single NC to produce six emission lines of equal intensity separated by in energy by the *sp-d* exchange interaction. In NCs with many Mn^{2+} dopants, the fluctuations of these spin projections result in the random fluctuations in the total magnetization of the population of Mn^{2+} ions. Because the occupation of the Mn^{2+} spin projections are thermodynamic in origin, reducing the temperature suppresses these fluctuations, consequently easing EMP formation at low temperatures. This reduction of the magnetic fluctuations is evident in the variable temperature emission linewidth under no applied magnetic field, and a similar reduction in line widths observed at low temperature with a magnetic field or in the presence of the exchange field of an EMP.

External magnetic fields hasten the formation of the EMP by suppressing the magnetic fluctuations and partially pre-aligning the dopants along the magnetization axis depicted in Figure 1.7. This effect is clearly seen in the difference between t = 0 and t = 0.8 ns as a function of the applied magnetic field in the time resolved magnetic circularly polarized photoluminescence (MCPL) depicted in Figure 1.8B. MCPL, which is plotted as the polarization ratio, $\Delta I/I = (I_L - I_R)/(I_L + I_R)$, where I_L and I_R are the integrated intensities of left and right circularly polarized excitonic emission respectively, reflects the spin polarization that is generated by the *sp-d* exchange interactions in the excited state. In the presence of an external filed, the total change in the tr-MCPL is greatly reduced owing to significant alignment of the Mn^{2+} dopants at t = 0 ns and the suppression of Mn^{2+} fluctuations. Given the observed Zeeman splittings measured by MCD (red circles in Figure 1.8), the experimental MCPL polarization ratios fall well short of expected MCPL behavior (100% polarization by ~0.4T at this temperature) based solely on Boltzmann population of the Zeeman sub-levels. Including the contribution from temperature dependent magnetic fluctuations does more accurately predict the MCPL behavior at high temperatures but fails to account for the observed trends at low temperature, this deviation will be addressed in the next section.

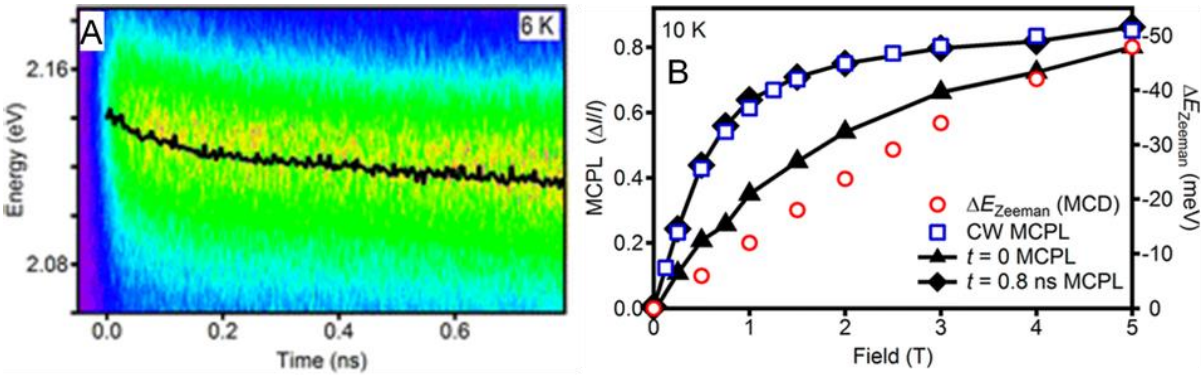

Figure 1.8 Time-resolved photoluminescence depicting EMP formation and its relation to steady-state measurements. (**A**) Streak-camera image of PL from $Cd_{0.87}Mn_{0.13}Se$ QDs. The solid line traces the peak emission energy, which redshifts due to EMP formation. (**B**) Field dependence of ΔE_{Zeeman} from MCD, CW-MCPL ratio, MCPL ratio at t = 0, and MCPL ratio at t = 0.8 ns. The field dependence of the MCPL ratio at t = 0, before EMP formation, resembles the field dependence of ΔE_{Zeeman} from MCD. The field dependence of the MCPL ratio at t = 0.8 ns, after EMP formation, resembles the field dependence of the CW-MCPL. The change in the TR-MCPL ratio from t = 0 to t = 0.8 ns reflects the change in Mn^{2+} magnetization during EMP formation. Adapted from permission from ref 46.

1.5.3 EMP Stabilization. After the initial formation of the EMP, Mn^{2+} ions continue to interact with and contribute to the stabilizing exciton until magnetic saturation is reached, or if recombination of the exciton occurs. In this limit the disordering force of the magnetic fluctuations are in equilibrium with the stabilization of exciton by the EMP exchange field. The application of an external magnetic field will only change the total Mn^{2+} alignment if the initial B_{eff} generated by the EMP was not strong enough to fully saturate the Mn^{2+} spins. For this reason, many consider EMP formation to be suppressed under applied magnetic fields because the relative contribution to the total Mn^{2+} alignment from the EMP under these conditions is reduced relative to case of no applied field. The maximum possible EMP stabilization is achieved when the product of $\frac{1}{2} x_{eff} \gamma N_0 (\alpha - \beta) B_{5/2}\left(\frac{5\mu_B g_{Mn} B_{eff}}{2k_B(T+T_0)}\right)$ from eq. 1.4 is maximized. Here x_{eff}, and B_{eff} are the only non-constant controllable variables to tune the EMP stabilization energy. Mn^{2+}-Mn^{2+} anti-ferromagnetic interactions in dimers and clusters limit the total magnetization to an "effective" Mn^{2+} concentration with a maximum of ~4.5%. Provided that there is complete overlap between

the exciton wavefunction and the distribution of Mn^{2+} ions is uniform all of these "effective" Mn^{2+} will contribute to the EMP stabilization. The exchange field, B_{eff}, is described by eq 1.5:

$$B_{eff} \approx \frac{|N_0\alpha - \beta|}{2\mu_B g_{Mn}} \cdot \frac{1}{N_0 V_{ex}} \qquad \text{Eq. 1.5}$$

where N_0 and V_{ex} are the cation density and excitonic volume respectively. Since B_{eff} is inversely dependent on the volume of the excitonic wavefunction reducing the volume of NC will result in larger values of B_{eff}. Though, in theory, this volume could be arbitrarily small, the energy transfer from the CdSe excitonic exited state to the Mn^{2+} $^4T_1$ *d-d* level (discuss in section 1.3.1) provides the lower limit to the NC size where the excitonic excited state is retained and EMP formation can occur. The Brilluoin function describes the temperature and field dependent saturation behavior and ranges from 0 to 1. When the Brillouin function is evaluated at larger values of B_{eff} in eq 1.4 the EMP can more easily reach magnetic saturation at greater temperatures and therefore the magnitude of the EMP stabilization is maximized. Typically, the total EMP stabilization energy in determined by fitting the variable temperature emission energy maximum to eq. 1.4 or by taking the difference between the photoluminescence energies at the moment of excitation and the maximum redshift following EMP formation. EMP stabilization energy may also be estimated as half of the excitonic Zeeman splitting (see Figure 1.7).

Recent development of colloidal DMS NCs has allowed for the investigation of EMP is the small volume limit. Additionally, due to the confined wavefunctions in NCs, the excited state lifetimes are significantly longer then bulk and epitaxial systems where the investigation of EMP stabilization was limited due the relative short-lived excitonic excited state lifetime (< 1ns). In the earliest report on colloidal NC EMPs a substantial stabilization (>100 meV) of the exciton was observed in the cw-photoluminescence corresponding to B_{eff} ~ 75T. The largest exchange fields that had been observed previously were on the order of ~3.5 T in epitaxial NCs. Additionally, the observed EMP stabilization was much greater than the predicted stabilization based on an isotropic description of EMP behavior (Eq. 1.4). Investigation of the TRPL of this photoluminescence, shown in Figure 1.9, revealed that the photoluminescence energy continued to shift long after the typically EMP formation timeframe (~100ps) and continued on the ns time scale.

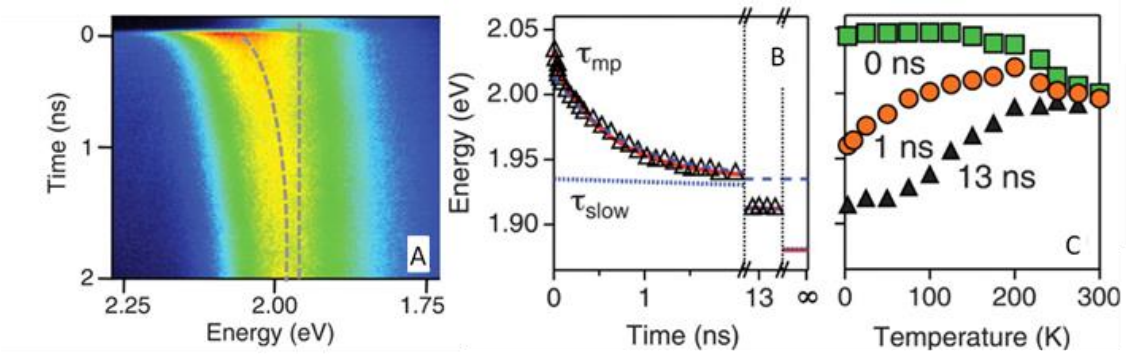

Figure 1.9 Time-resolved photoluminescence depicting EMP relaxation on an extended time scale. (**A**) TRPL spectra for d = 5.0 nm 4.2% Mn^{2+}:CdSe. The vertical dashed line indicates the PL energy 13 ns after the laser pulse. (**B**) 5-K PL energy maximum versus time for the same Mn^{2+}:CdSe QDs, The PL energy converges to that observed in continuous-wave measurements (1.88 eV, $t = \infty$). The red line shows a fitted tri-exponential decay (τ_1 = 10 ps, τ_2 = 570 ps, τ_3 = 20 ns) for illustration. Vertical dotted lines indicate timeline discontinuities. (**C**) Mn^{2+}:CdSe QD PL maximum versus temperature, measured ~0, 1, and 13 ns after the laser pulse. Adapted from permission from ref 43.

The additional excitonic stabilization observed in the cw-photoluminescence of doped NC EMPs and in the long-term (> 1 ns) TRPL, after EMP formation has already occurred, cannot be accounted for based on an isotropic description of the EMP phenomena or any contribution from magnetic fluctuations. Furthermore, the lack of complete MCPL polarization despite very large excitonic Zeeman splittings at low temperature is also difficult to reconcile with established EMP physical understanding. These experimental observations appear to suggest that EMP orientation and stabilization is not entirely dependent on solely Mn^{2+} magnetization at the moment of photoexcitation. One effective explanation for these experimental observables is the presence of excitonic anisotropy that may alter the direction and magnitude of the *sp-d* exchange interactions. In both 2D DMS quantum wells,[92] and polaron formation in bulk hexagonal Mn^{2+} CdSe,[93] the presence of significant hole effective-mass anisotropy was used to describe the observed EMP behavior. This effective mass anisotropy is manifested in anisotropic g values that would give the exciton a preferred orientation. Such a preferred orientation would distort the EMP energetic landscape along the preferred direction, introducing a new force that contributes to the total stabilization of the EMP. Additionally, the shape anisotropy present in strongly confined NCs likely enhances this preferred orientation.[94, 95] This anisotropy hypothesis is best demonstrated

using a 3-D distorted potential energy surface, shown in Figure 1.10, where the magnetic coordinate diagram from figure 1.7 is extened to include rotation of the magnetization into an arbitrary direct. Figure 1.10 depicts the upper and lower excitonic Zeeman surfaces for the simplest an axially anisotropic deviation from the isotropic limit illustrating the appearance of an energetic barrier to magnetic reorientation. Additional warping of this energy landscape is also expected to arise from NC crystal sturcture, local surface dipoles, or low-symmetry shapes and faceting. In the ensemble, these colloidal DMS NCs show a powder distribution of their individual anisotropies.

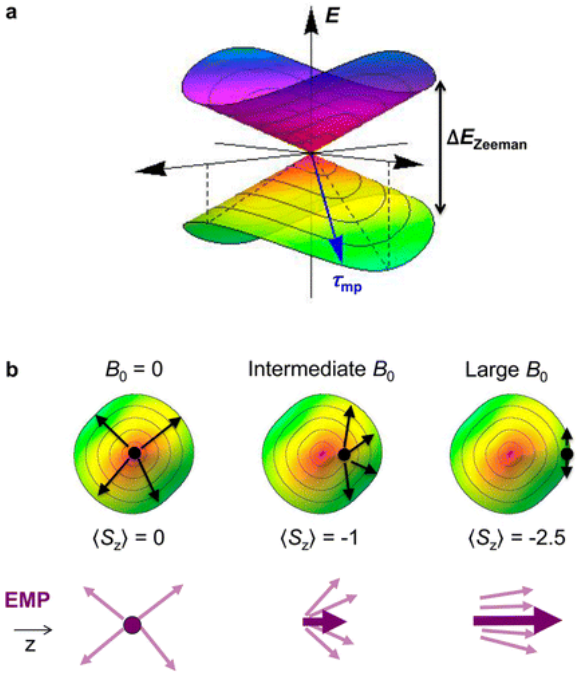

Figure 1.10 Multidimensional EMP magnetic coordinate diagram. (**A**) Multidimensional magnetic-coordinate diagram describing the excitonic Zeeman splitting of an axially distorted $Cd_{1-x}Mn_xSe$ QD. The potential energy surface is warped by anisotropic effects, which introduce barriers to EMP rotation in an external magnetic field. Concentric contour lines represent increments of $\langle S_\phi \rangle = 1/2$. (**B**) Illustration of the effect of increasing B_0 (left to right) on EMP formation on the lower Zeeman potential energy surface. The black circles indicate the initial Mn^{2+} magnetization ($M(B_0)$), the thin arrows indicate various EMP formation trajectories, and the thick arrows indicate the net EMP projection onto the laboratory *z* axis, which parallels B_0. Adapted from permission from ref 46

Under no applied magnetic field random magnetic fluctuations ensure that EMPs form in random directions in the ensemble of QDs, yielding energetic stabilization of the exciton but zero

net polarization due to the averaging over all possible EMP orientations. When an external field is applied the magnetization is displaced from the center of the potential energy surface, yielding ensemble EMP formation along the direction of the applied field B_0 as shown in Figure 1.10B (intermediate B_0). Fluctuations of the dopant spins are not completely suppressed under intermediate applied magnetic field and therefore cause EMPs to form misaligned within a cone around the applied field direction, perturbed by the surface of the potential energy surface. EMPs initially formed off axis may then slowly stabilize through a reorientation process along the EMP potential energy surface. At large B_0 and low temperature, the dopants are fully magnetized prior to photoexcitation, and the ensemble of EMPs is maximally stabilized with minimal formation time. In this limit, some EMPs are still not fully aligned with B_0 due to the additional force of the anisotropic potential energy surface pinning the orientation of the EMP along a distribution of individual internal anisotropy axes across the ensemble of NCs. Overall, EMP orientation and stabilization in colloidal DMS NCs is influenced by external magnetic fields, fluctuations of the dopant spin projections, and an internal axis likely stemming from anisotropy due to uniaxial crystal structure.

Measurements on the single particle level have had an important impact on the field of colloidal NCs because they are able to remove the obscurity that results from averaging over distributions of NC size, shape, orientation, quantum yield etc. found in measurements of NC ensembles.[96-99] In a limited number of cases single particle spectroscopy has been used to investigate colloidal doped NCs, largely focusing on the luminescence of internal dopant ligand field transitions,[100, 101] blinking behavior,[102-104] and fine structure effects caused by individual dopants.[105] Single NC spectroscopy has been used in the investigations of epitaxially grown DMS materials,[106, 107] with demonstrations of both EMP formation[39] and magnetic fluctuations[61] in a highly anisotropic system characterized by strong quantum confinement along the growth axis. Using single particle spectroscopy at low temperature and under an applied magnetic field, researchers were recently able to investigate EMPs in colloidal NC with uniaxially dominated exchange interactions caused by the hexagonal crystal structure. A distinct shift in energy with temperature and applied magnetic field, combined with a characteristic change in the photoluminescence line width is observed for a series of individual NCs. Single particle observations in a 3-D vector magnetic field demonstrate unambiguous signatures of anisotropy effects on both the direction and stability of EMP formation. EMP formation ins these single

particles can be stabilized (increase of EMP binding energy) or destabilized (decrease of EMP binding energy), by varying the angle between the external magnetic field and an internal anisotropy axis of the nanocrystals. These results are addressed in detail in Chapters 2 & 3.

1.5.4 EMP Relaxation. Following recombination, the dopant spins in the ground state relax back to zero net magnetization, described by the green region of Figure 1.7, on the time scale defined by Mn^{2+} spin lattice recombination time, τ_{SLR}, in the absence of any charge carriers. The spin lattice relaxation time can vary by several orders of magnitude depending on the Mn^{2+} concentration and is largely dominated by a combination of Mn^{2+}-Mn^{2+} dipolar coupling, hyperfine interactions with protons (^1H) on the NC surface,[108] and phonons originating from either the lattice or the surface ligands.[109] If the rate of photoexcitation is faster the spin lattice relaxation time it is possible to generate an EMP using the partially aligned Mn^{2+} spin from a previous photoexcitation event, and after several photoexcitation and emission cycles build-up substantial magnetization.[110] This process results in the appearance of an ultra-long spin memory of the individual NCs and may be an interesting avenue of manipulate EMPs in future spintronics applications.

1.6 Summary

The synthesis of DMS NCs with tunable concentrations of magnetic impurities and well controlled optical properties represents a great achievement in nanoscience. Our ability to access these materials supports fundamental research and potential technological applications at the intersection of semiconductor and magnetism. This Chapter summarizes the fundamental physics behind the *sp-d* exchange interactions that are responsible for a number of magneto-optical phenomena is DMS materials, and most importantly responsible for photo-induced magnetism that occurs in EMPs. Significant enhancement of the EMP stabilization energy is observed in colloidal NCs and is assigned to anisotropic stabilization of the EMP excited state. Temperature and magnetic field-dependent single particle photoluminescence spectroscopy was used to unravel the formation of EMPs in individual NCs for the first time and these experiments provide unique insights into the role of anisotropy in EMP formation and magnetic fluctuations. The findings here of anisotropic stabilization and orientation of EMPs within DMS NCs impact the understanding of the stability and magneto-optical properties of such materials, which in turn has ramifications for how to further improve the synthesis of these materials and their incorporation into future spintronic technologies.

1.7 References

1. Talapin, D. V.; Lee, J.-S.; Kovalenko, M. V.; Shevchenko, E. V., Prospects of Colloidal Nanocrystals for Electronic and Optoelectronic Applications. *Chem. Rev.* **2010,** *110*, 389-458.
2. V.I. Klimov (Ed.), Nanocrystal Quantum Dots, second ed., CRC Press: Boca Raton, FL, 2010.
3. Smith, A. M.; Nie, S. Semiconductor Nanocrystals: Structure, Properties, and Band Gap Engineering. *Acc. Chem. Res.* **2010**, *43*, 190-200.
4. Kovalenko, M. V.; Manna, L.; Cabot, A.; Hens, Z.; Talapin, D. V.; Kagan, C. R.; Klimov, V. I.; Rogach, A. L.; Reiss, P.; Milliron, D. J.; Guyot-Sionnest, P.; Konstantatos, G.; Parak, W. J.; Hyeon, T.; Korgel, B. A.; Murray, C. B.; Heiss, W., Prospects of Nanoscience with Nanocrystals. *ACS Nano* **2015,** *9*, 1012-1057.
5. Brus, L Electronic wave functions in semiconductor clusters: experiment and theory. *J. Phys. Chem.* **1986**, *90*, 2555–2560.
6. Murray, C. B.; Norris, D. J.; Bawendi, M. G. Synthesis and characterization of nearly monodisperse CdE (E=Sulfur, Selenium, Tellurium) semiconductor nanocrystallites. *J. Am. Chem. Soc*. **1993**, *115*, 8706.
7. Bruchez, M.; Moronne, M.; Gin, P.; Weiss, S.; Alivisatos, A. P., Semiconductor Nanocrystals as Fluorescent Biological Labels. *Science* **1998,** 281, 2013.
8. Hillhouse, H. W.; Beard, M. C., Solar cells from colloidal nanocrystals: Fundamentals, materials, devices, and economics. *Curr. Opin. Colloid In.* **2009,** *14*, 245-259.
9. Talapin, D. V.; Steckel, J., Quantum dot light-emitting devices. *MRS Bulletin* **2013,** *38*, 685-691.
10. Runnerstrom, E. L.; Llordes, A.; Lounis, S. D.; Milliron, D. J., Nanostructured electrochromic smart windows: traditional materials and NIR-selective plasmonic nanocrystals. *Chem. Commun.* **2014,** *50*, 10555-72.
11. Bradshaw, L. R.; Knowles, K. E.; McDowall, S.; Gamelin, D. R., Nanocrystals for Luminescent Solar Concentrators. *Nano Lett.* **2015,** *15*, 1315-1323.
12. Yoon, H. C.; Oh, J. H.; Ko, M.; Yoo, H.; Do, Y. R., Synthesis and Characterization of Green Zn–Ag–In–S and Red Zn–Cu–In–S Quantum Dots for Ultrahigh Color Quality of Down-Converted White LEDs. *ACS Appl. Mater. & Interf.* **2015,** *7*, 7342-7350.
13. Protesescu, L., Yakunin, S., Bodnarchuk, M. I., Krieg, F., Caputo, R., Hendon, C. H., Ynag, R. X., Walsh, A., Kovalenko, M. V. Nanocrystals of Cesium Lead Halide Perovskites ($CsPbX_3$, X = Cl, Br, and I): Novel Optoelectronic Materials Showing Bright Emission with Wide Color Gamut *Nano Lett.* **2015**, 15, 3692–3696.
14. Norris, D. J.; Yao, N.; Charnock, F. T.; Kennedy, T. A., High-Quality Manganese-Doped ZnSe Nanocrystals. *Nano Lett.* **2000**, *1***,** 3-7.
15. Norris, D. J.; Efros, A. L.; Erwin, S. C. Doped Nanocrystals. *Science*, **2008**, *319*, 1776.
16. Beaulac, R.; Archer, P. I.; Gamelin, D. R. Luminescence in Colloidal Mn^{2+}-Doped Semiconductor Nanocrystals. *J. Solid State Chem.* **2008**, *181*, 1582-1589.
17. Milstein, T. J.; Kroupa, D. M.; Gamelin, D. R. Picosecond Quantum Cutting Generates Photoluminescence Quantum Yields Over 100% in Ytterbium-Doped $CsPbCl_3$ Nanocrystals. *Nano Lett.* **2018**, *18*, 3792-3799.
18. Cohen, T.A.; Milstein, T.J.; Kroupa, D.M.; MacKenzie, J.D.; Luscombe, C.; Gamelin, D.R. Quantum-Cutting Yb^{3+}-Doped Perovskite Nanocrystals for Monolithic Bilayer Luminescent Solar Concentrators. *J Mat. Chem. A* **2019**, *7*, 9279-9288.

19. Fundamentals of Phosphors. CRC Press: Boca Raton, 2006.
20. Maiman, T. H. Stimulated Optical Radiation in Ruby. *Nature*. **1960**, *187*, 493-494.
21. Fiederling, R.; Keim, M.; Reuscher, G.; Ossau, W.; Schmidt, G.; Waag, A.; Molenkamp, L. W. Injection and Detection of a Spin-Polarized Current in a Light- Emitting Diode. *Nature* **1999**, *402*, 787–790.
22. Ohno, H.; Matsukura, F.; Omiya, T.; Akiba, N. Spin-Dependent Tunneling and Properties of Ferromagnetic (Ga,Mn)As. *J. Appl. Phys.* **1999**, *85*, 4277–4282.
23. Ohno, Y.; Young, D. K.; Beschoten, B.; Matsukura, F.; Ohno, H.; Awchalom, D. D. Electrical Spin Injection in a Ferromagnetic Semiconductor Heterostructure. *Nature* **1999**, *402*, 790–792.
24. Awschalom, D. D.; Flatté, M. E. Challenges for Semiconductor Spintronics. *Nat.Phys.* **2007**, *3*, 153–159.
25. Dietl, T.; Ohno, H. Dilute Ferromagnetic Semiconductors: Physics and Spintronic Structures. *Rev. Mod. Phys.* **2014**, *86*, 187–251.
26. Gaj, J. A.; Kossut, J. *Introduction to the Physics of Diluted Magnetic Semiconductors*. Springer: Berlin, 2010; Vol. 144.
27. Aggarwal, R. L.; Jasperson, S. N.; Stankiewicz, J.; Shapira, Y.; Foner, S.; Khazai, B.; Wold, A. Magnetoreflectance at the Band Edge in $Cd_{1-x}Mn_xSe$. *Phys. Rev. B* **1983**,*28*, 6907–6913.
28. Barrows, C. J.; Vlaskin, V. A.; Gamelin, D. R. Absorption and Magnetic Circular Dichroism Analyses of Giant Zeeman Splittings in Diffusion-Doped Colloidal $Cd_{1-x}Mn_xSe$ Quantum Dots. *J. Phys. Chem. Lett.* **2015**, *6*, 3076-3081.
29. Isaacs, E. D. Magnetically tunable diluted magnetic semiconductor (Cd, Mn)Te quantum well laser. *Appl. Phys. Lett.*, **1986**, *48*, 275-277.
30. Bartholomew, D. U.; Furdyna, J. K.; Ramdas, A. K. Interband Faraday-Rotation in Diluted Magnetic Semiconductors: Zn1–*x*Mn*x*Te and Cd1–*x*Mn*x*Te. *Phys. Rev. B* **1986**, *34*, 6943–6950.
31. Yasuhira, T.; Uchida, K.; Matsuda, Y. H.; Miura, N.; Twardowski, A. Magnetic and Non-Magnetic Faraday Rotation in ZnMnSe in High Magnetic Fields. *Semicond. Sci. Technol.* **1999**, *14*, 1161–1164.
32. Yasuhira, T.; Uchida, K.; Matsuda, Y. H.; Miura, N.; Twardowski, A. Giant Faraday Rotation Spectra of $Zn_{1-x}Mn_xSe$ Observed in High Magnetic Fields Up To 150 T. *Phys. Rev. B* **2000**, *61*, 4685–4688.
33. Golnik, A.; Ginter, J.; Gaj, J. A. Magnetic Polarons in Exciton Luminescence of $Cd_{1-x}Mn_xTe$. *J. Phys. C.: Sol. State Phys.* **1983**, *16*, 6073–6084.
34. Harris, J. H.; Nurmikko, A. V. Formation of the Bound Magnetic Polaron in (Cd,Mn)Se. *Phys. Rev. Lett.* **1983**, *51*, 1472–1475.
35. Awschalom, D. D.; Warnock, J.; von Molnár, S. Low Temperature Magnetic Spectroscopy of a Dilute Magnetic Semiconductor. *Phys. Rev. Lett.* **1987**, *58*, 812–815.
36. Mackh, G.; Ossau, W.; Yakovlev, D. R.; Waag, A.; Landwehr, G.; Hellmann, R.; Göbel, E. O. Localized Exciton Magnetic Polarons in $Cd_{1-x}Mn_xTe$. *Phys. Rev. B* **1994**, *49*, 10248.
37. Oka, Y.; Shen, J.; Takabayashi, K.; Takahashi, N.; Mitsu, H.; Souma, I.; Pittini, R. Dynamics of Excitonic Magnetic Polarons in Nanostructure Diluted Magnetic Semiconductors. *J. Lumin.* **1999**, 83-84, 83–89.
38. Kavokin, K. V.; Merkulov, I. A.; Yakovlev, D. R.; Ossau, W.; Landwehr, G. Exciton Localization in Semimagnetic Semiconductors Probed by Magnetic Polarons. *Phys. Rev. B: Condens. Matter Mater. Phys.* **1999**, *60*, 16499–16505.

39. Maksimov, A. A.; Bacher, G.; McDonald, A.; Kulakovskii, V. D.; Forchel, A.; Becker, C. R.; Landwehr, G.; Molenkamp, L. W. Magnetic Polarons in a Single Diluted Magnetic Semiconductor Quantum Dot. *Phys. Rev. B: Condens. Matter Mater. Phys.* **2000**, *62*, R7767–R7770.
40. Seufert, J.; Bacher, G.; Scheibner, M.; Forchel, A.; Lee, S.; Dobrowolska, M.; Furdyna, J. K. Dynamical Spin Response in Semimagnetic Quantum Dots. *Phys. Rev. Lett.* **2001**, *88*, 027402.
41. Dorozhkin, P. S.; Chernenko, A. V.; Kulakovskii, V. D.; Brichkin, A. S.; Maksimov, A. A.; Schoemig, H.; Bacher, G.; Forchel, A.; Lee, S.; Dobrowolska, M.; et al. Longitudinal and Transverse Fluctuations of Magnetization of the Excitonic Magnetic Polaron in a Semimagnetic Single Quantum Dot. *Phys. Rev. B: Condens. Matter Mater. Phys.* **2003**, *68*, 195313.
42. Zaitsev, S. V.; Schömig, H.; Forchel, A.; Bacher, G. Magnetooptics and Dynamics of a Magnetic Polaron in Semimagnetic CdSe/ZnMnSe Quantum Dots. *JETP Lett.* **2007**, *85*, 323–327.
43. Beaulac, R.; Schneider, L.; Archer, P. I.; Bacher, G.; Gamelin, D. R. Light-Induced Spontaneous Magnetization in Doped Colloidal Quantum Dots. *Science* **2009**, *325*, 973–976.
44. Sellers, I. R.; Oszwazdowski, R.; Whiteside, V. R.; Eginligil, M.; Petrou, A.; Zutic, I.; Chou, W.-C.; Fan, W. C.; Petukhov, A. G.; Kim, S. J.; et al. Robust Magnetic Polarons in Type-II (Zn,Mn)Te/ZnSe Magnetic Quantum Dots. *Phys. Rev. B: Condens. Matter Mater. Phys.* **2010**, *82*, 195320.
45. Kłopotowski, Ł.; Cywinski, Ł.; Wojnar, P.; Voliotis, V.; Fronc, K.; Kazimierczuk, T.; Golnik, A.; Ravaro, M.; Grousson, R.; Karczewski, G.; Wojtowicz, T.; Magnetic Polaron Formation and Exciton Spin Relaxation in Single $Cd_{1-x}Mn_xTe$ Quantum Dots. *Phys. Rev. B: Condens. Matter Mater. Phys.* **2011**, *83*, 081306.
46. Nelson, H. D.; Bradshaw, L. R.; Barrows, C. J.; Vlaskin, V. A.; Gamelin, D. R. Picosecond Dynamics of Excitonic Magnetic Polarons in Colloidal Diffusion-Doped $Cd_{1-x}Mn_xSe$ Quantum Dots. *ACS Nano* **2015**, *9*, 11177–11191.
47. Bhattacharjee, A. K.; Pérez-Conde, J. Confinement-Induced Enhancement of Spin Interaction in Mn-Doped II–VI Semiconductor Nanocrystals. *Phys. Stat. Sol. (B)* **2004**, *241*, 672–675.
48. Bacher, G.; Schömig, H.; Scheibner, M.; Forchel, A.; Maksimov, A. A.; Chernenko, A. V.; Dorozhkin, P. S.; Kulakovskii, V. D.; Kennedy, T.; Reinecke, T. L. Spin-Spin Interaction in Magnetic Semiconductor Quantum Dots. *Phys. E.*, **2005**, *26*, 37–44.
49. Henneberger, F.; Puls, J. Diluted Magnetic Quantum Dots. In Introduction to the Physics of Diluted Magnetic Semiconductors; Kossut, J., Gaj, J. A., Eds.; Springer Series in Materials Science 144; Springer-Verlag: Berlin, 2010; pp 161-190.
50. Archer, P. I.; Santangelo, S. A.; Gamelin, D. R. Direct Observation of sp–d Exchange Interactions in Colloidal Mn^{2+}- and Co^{2+}-Doped CdSe Quantum Dots. *Nano Lett.* **2007**, *7*, 1037–1043.
51. Fainblat, R.; Frohleiks, J.; Muckel, F.; Yu, J. H.; Yang, J.; Hyeon, T.; Bacher, G. Quantum Confinement-Controlled Exchange Coupling in Manganese(II)-Doped CdSe Two-Dimensional Quantum Well Nanoribbons. *Nano Lett.* **2012**, *12*, 5311–5317.
52. Vlaskin, V. A.; Barrows, C. J.; Erickson, C. S.; Gamelin, D. R. Nanocrystal Diffusion Doping. *J. Am. Chem. Soc.* **2013**, *135*, 14380−14389.

53. Muckel, F.; Yang, J.; Lorenz, S.; Baek, W.; Chang, H.; Hyeon, T.; Bacher, G.; Fainblat, R. Digital Doping in Magic-Sized CdSe Clusters. *ACS Nano* **2016**, *10*, 7135–7141.
54. Barrows, C. J.; Chakraborty, P.; Kornowske, L. M.; Gamelin, D. R. Tuning Equilibrium Compositions in Colloidal Cd1–*x*Mn*x*Se Nanocrystals Using Diffusion Doping and Cation Exchange. *ACS Nano* **2016**, *10*, 910–918.
55. Erwin, S. C.; Zu, L.; Haftel, M. I.; Efros, A. L.; Kennedy, T. A.; Norris, D. J., Doping semiconductor nanocrystals. *Nature*, **2005**, *436*, 91-94.
56. Erickson, C. S.; Bradshaw, L. R.; McDowall, S.; Gilbertson, J. D.; Gamelin, D. R.; Patrick. D. L. Zero-Reabsorption Doped-Nanocrystal Luminescent Solar Concentrators. *ACS Nano* **2014,** *8*, 3461-3467.
57. McLaurin, E. J.; Bradshaw, L. R.; Gamelin, D. R. Dual-Emitting Nanoscale Temperature Sensors. *Chem. Mater.*, **2013**, *25*, 1283-1292.
58. McLaurin, E. J.; Fataftah, M. S.; Gamelin, D. R. One-step synthesis of alloyed dual-emitting semiconductor nanocrystals. *Chem. Commun.*, **2013**, *49*, 39–41.
59. McLaurin, E. J.; Vlaskin, V. A.; Gamelin, D. R. Water-Soluble Dual-Emitting Nanocrystals for Ratiometric Optical Thermometry. *J. Am. Chem. Soc.*, **2011**, *133*, 14978–14980.
60. Vlaskin, V. A.; Janßen, N.; van Rijssel, J.; Beaulac, R.; Gamelin, D. R. Tunable Dual Emission in Doped Semiconductor Nanocrystals. *Nano Letters*, **2010**, *10*, 3670–3674.
61. Beaulac, R.; Archer, P. I.; Liu, X.; Lee, S.; Salley, G. M.; Dobrowolska, M.; Furdyna, J. K.; Gamelin, D. R. Spin-Polarizable Excitonic Luminescence in Colloidal Mn^{2+}-Doped CdSe Quantum Dots. *Nano Letters*, **2008**, *8*, 1197-1201.
62. Beaulac, R.; Feng, Y.; May, J. W.; Badaeva, E.; Gamelin, D. R.; Li, X. Orbital Pathways for Mn^{2+}-Carrier *sp-d* Exchange in Magnetic Semiconductor Quantum Dots. *Phys. Rev. B*, **2011**, *84*, 195324.
63. Beaulac, R.; Gamelin, D. R. Two-Center Formulation of Mn^{2+}–Electron *s–d* Exchange Coupling in Bulk and Quantum-Confined Diluted Magnetic Semiconductors. *Phys. Rev. B* **2010**, *82*, 224401.
64. Shapira, Y.; Foner, S.; Ridgley, D. H.; Dwight, K.; Wold, A. Technical Saturation and Magetization Steps in Diluted Magnetic Semiconductors: Predictions and Observations *Phys. Rev. B: Condens. Matter Mater. Phys.* **1984**, *30*, 4021– 4023.
65. Piepho, S. B.; Schatz, P. N. *Group Theory in Spectroscopy with Applications to Magnetic Circular Dichroism*. Wiley: New York, 1983.
66. Schimpf, A. M.; Gamelin, D. R. Thermal Tuning and Inversion of Excitonic Zeeman Splittings in Colloidal Doped CdSe Quantum Dots. *J. Phys. Chem. Lett.* **2012**, *3*, 1264–1268.
67. Bryan, J. D.; Gamelin, D. R. Doped Semiconductor Nanocrystals: Synthesis, Characterization, Physical Properties, and Applications. *Prog. Inorg. Chem.* **2005**, *54*, 47–126.
68. Ladizhansky, V.; Vega, S. Doping of CdS Nanoparticles by Co^{2+} Ions Studied by NMR. *J. Phys. Chem. B* **2000**, *104*, 5237–5241.
69. Hoffman, D. M.; Meyer, B. K.; Ekimov, A. I.; Merkulov, I. A.; Efros, A. L.; Rosen, M.; Couino, G.; Gacoin, T.; Boilot, J. P. Giant Internal Magnetic Fields in Mn Doped Nanocrystal Quantum Dots. *Solid State Commun.* **2000**, *114*, 547–550.
70. Norris, D. J.; Yao, N.; Chamrock, F. T.; Kennedy, T. A. High-Quality Manganese-Doped ZnSe Nanocrystals. *Nano Lett.* **2001**, *1*, 3–7.

71. Zheng, W.; Wang, Z.; Wright, J.; Goundie, B.; Dalal, N. S.; Meulenberg, R. W.; Strouse, G. F. Probing the Local Site Environments in Mn:CdSe Quantum Dots. *J. Phys. Chem. C* **2011**, *115*, 23305–23314.
72. Fainblat, R.; Muckel, F.; Barrows, C. J.; Vlaskin, V. A.; Gamelin, D. R.; Bacher, G. Valence-Band Mixing Effects in the Upper-Excited-State Magneto-Optical Responses of Colloidal Mn^{2+}-Doped CdSe Quantum Dots. *ACS Nano* **2014**, *8*, 12669-12675.
73. Son, D. H.; Hughes, S. M.; Yin, Y.; Alivisatos, A. P. Cation Exchange Reactions in Ionic Nanocrystals. *Science* **2004**, *306*, 1009–1012.
74. de Mello Donegá, C. Synthesis and Properties of Colloidal Heteronanocrystals. *Chem. Soc. Rev.* **2011**, *40*, 1512–1546.
75. Beberwyck, B. J.; Surendranath, Y.; Alivisatos, A. P. Cation Exchange: A Versatile Tool for Nanomaterials Synthesis. *J. Phys. Chem. C* **2013**, *117*, 19759–19770.
76. Zhong, X.; Han, M.; Dong, Z.; White, T. J.; Knoll, W. Composition-Tunable ZnxCd1-xSe Nanocrystals with High Luminescence and Stability *J. Am. Chem. Soc.* **2003**, 125, 8589-8594.
77. Rivest, J. B.; Jain, P. K. Cation Exchange on the Nanoscale: An Emerging Technique for New Material Synthesis, Device Fabrication, and Chemical Sensing. *Chem. Soc. Rev.* **2013**, *42*, 89–96.
78. Gupta, S.; Kershaw, S. V.; Rogach, A. L. 25th Anniversary Article: Ion Exchange in Colloidal Nanocrystals. *Adv. Mater.* **2013**, *25*, 6923–6944.
79. De Trizio, L.; Manna, L. Forging Colloidal Nanostructures via Cation Exchange Reactions. *Chem. Rev.* **2016**, *116*, 10852–10887.
80. Dance, I. G.; Choy, A.; Scudder, M. L. Syntheses, properties, and molecular and crystal structures of $(Me_4N)_4[E_4M_{10}(SPh)_{16}]$ (E = sulfur or selenium; M = zinc or cadmium): molecular supertetrahedral fragments of the cubic metal chalcogenide lattice *J. Am. Chem. Soc.* **1984**, 106, 6285-6295.
81. Cumberland, S.L.; Hanif, K.M.; Javier, A.; Khitrov, G.A.; Strouse, G.F.; Woessner, S.M.; Yun, C.S. Inorganic Clusters as Single-Source Precursors for Preparation of CdSe, ZnSe, and CdSe/ZnS Nanomaterials *Chem. Mater.*, **2002**, *14*, 1576-1584.
82. Magana, D.; Perera, S. C.; Harter, A. G.; Dalal, N. S.; Strouse, G. F. Switching-on Superparamagnetism in Mn/CdSe Quantum Dots *J. Am. Chem. Soc.* **2006**, *128*, 2931-2939.
83. Patrick T. K. Chin, Jan W. Stouwdam, and Rene A. J. Janssen. Highly Luminescent Ultranarrow Mn Doped ZnSe Nanowires *Nano Lett.* **2009,** 9, 745.
84. Norberg, N. S.; Parks, G. L.; Salley, G. M.; Gamelin, D. R. Giant Excitonic Zeeman Splittings in Colloidal Co^{2+}-Doped ZnSe Quantum Dots. *J. Am. Chem. Soc.*, **2006**, *128*, 13195-13203.
85. Barrows, C. J.; Chakraborty, P.; Kornowske, L. M.; Gamelin, D. R. Tuning Equilibrium Compositions in Colloidal $Cd_{1-x}Mn_xSe$ Nanocrystals Using Diffusion Doping and Cation Exchange. *ACS Nano* **2016**, *10*, 910-918.
86. Muckel, F.; Barrows, C. J.; Graf, A.; Schmitz, A.; Erickson, C. S.; Gamelin, D. R.; Bacher, G. Current-induced magnetic polarons in a colloidal quantum-dot device. *Nano Lett.* **2017**, *17*, 4768-4773.
87. Lorenz, S.; Erickson, C.S.; Riesner, M.; Gamelin, D.R.; Fainblat, R.; Bacher, G. Directed Exciton Magnetic Polaron Formation in a Single Colloidal Mn^{2+} CdSe/CdS Quantum Dot. *Nano Lett.*, **2020**, *20*, 1896-1906.

88. Dietl, T.; Peyla, P.; Grieshaber, W.; Merle d'Aubigné, Y. Dynamics of Spin Organization in Diluted Magnetic Semiconductors *Phys. Rev. Lett.* **1995**, *74*, 474– 477
89. Scherbakov, A. V.; Yakovlev, D. R.; Akimov, A. V.; Merkulov, I. A.; König, B.; Ossau, W.; Molenkamp, L. W.; Wojtowicz, T.; Karczewski, G.; Cywinski, G.Acceleration of the Spin-Lattice Relaxation in Diluted Magnetic Quantum Wells in the Presence of a Two-Dimensional Electron Gas *Phys. Rev. B: Condens. Matter Mater. Phys.* **2001**, *64*, 155205.
90. Kneip, M. K.; Yakovlev, D. R.; Bayer, M.; Maksimov, A. A.; Tartakovskii, I. I.; Keller, D.; Ossau, W.; Molenkamp, L. W.; Waag, A. Spin-Lattice Relaxation of Mn Ions in ZnMnSe/ZnBeSe Quantum Wells Measured under Pulsed Photoexcitation *Phys. Rev. B: Condens. Matter Mater. Phys.* **2006**, *73*, 045305.
91. Schimpf, A. M.; Rinehart, J. D.; Ochsenbein, S. T.; Gamelin, D. R. Charge-State Control of Mn^{2+} Spin Relaxation Dynamics in Colloidal *n*-Type $Zn_{1-x}Mn_xO$ Nanocrystals *J. Phys. Chem. Lett.* **2015**, *6*, 1748– 1753.
92. Fiederling, R.; Yakovlev, D. R.; Ossau, W.; Landwehr, G.; Merkulov, I. A.; Kavokin, K. V.; Wojtowicz, T.; Kutrowski, M.; Grasza, K.; Karczewski, G.Exciton Magnetic Polarons in (100)- and (120)-Oriented Semimagnetic Digital Alloys (Cd,Mn)Te *Phys. Rev. B: Condens. Matter Mater. Phys.* **1998**, *58*, 4785– 4792.
93. Scalbert, D.; Cernogora, J.; Benoit à la Guillaume, C.; Nawrocki, M. Bistability of Magnetic Polarons Bound to Acceptors in a Wurtzite Semimagnetic Semiconductor *Phys. Rev. B: Condens. Matter Mater. Phys.* **1988**, *38*, 13246– 13256.
94. Výborný, K.; Han, J. E.; Oszwałdowski, R.; Žutić, I.; Petukhov, A. G. Magnetic Anisotropies of Quantum Dots Doped with Magnetic Ions *Phys. Rev. B: Condens. Matter Mater. Phys.* **2012**, *85*, 155312.
95. Peng, B.; May, J. W.; Gamelin, D. R.; Li, X. Effects of Crystallographic and Shape Anisotropies on Dopant-Carrier Exchange Interactions in Magnetic Semiconductor Quantum Dots. *J. Phys. Chem. C* **2014**, *118*, 7630–7636.
96. Nirmal, M.; Dabbousi, B. O.; Bawendi, M. G.; Macklin, J. J.; Trautman, J. K.; Harris, T. D.; Brus, L. E. Fluorescence Intermittency in Single Cadmium Selenide Nanocrystals. *Nature* **1996**, *383*, 802– 804.
97. Chen, Y.; Vela, J.; Htoon, H.; Casson, J. L.; Werder, D. J.; Bussian, D. A.; Klimov, V. I.; Hollingsworth, J. A. "Giant" Multishell CdSe Nanocrystal Quantum Dots with Suppressed Blinking. *J. Am. Chem. Soc.* **2008**, *130*, 5026– 5027.
98. Schlegel, G.; Bohnenberger, J.; Potapova, I.; Mews, A. Fluorescence Decay Time of Single Semiconductor Nanocrystals. *Phys. Rev. Lett.* **2002**, *88*, 137401
99. Neuhauser, R. G.; Shimizu, K. T.; Woo, W. K.; Empedocles, S. A.; Bawendi, M. G. Correlation between Fluorescence Intermittency and Spectral Diffusion. *Phys. Rev. Lett.* **2000**, *85*, 3301– 3304
100. Hazarika, A.; Layek, A.; De, S.; Nag, A.; Debnath, S.; Mahadevan, P.; Chowdhury, A.; Sarma, D. D. Ultranarrow and Widely Tunable Mn^{2+}-Induced Photoluminescence from Single Mn-Doped Nanocrystals of ZnS-CdS Alloys. *Phys. Rev. Lett.* **2013**, *110*, 267401.
101. Parobek, D.; Roman, B. J.; Dong, Y.; Jin, H.; Lee, E.; Sheldon, M.; Son, D. H. Exciton-to-Dopant Energy Transfer in Mn-Doped Cesium Lead Halide Perovskite Nanocrystals. *Nano Lett.* **2016**, *16*, 7376– 7380.
102. Ishizumi, A.; Kanemitsu, Y. Blinking Behavior of Surface-Defect and Impurity Luminescence in Nondoped and Mn^{2+}-Doped CdS Nanocrystals. *J. Phys. Soc. Jpn.* **2009**, *78*, 083705.

103. Zhang, Y.; Gan, C.; Muhammad, J.; Battaglia, D.; Peng, X.; Xiao, M. Enhanced Fluorescence Intermittency in Mn-Doped Single ZnSe Quantum Dots. *J. Phys. Chem. C* **2008**, *112*, 20200– 20205.
104. Whitham, P. J.; Knowles, K. E.; Reid, P. J.; Gamelin, D. R. Photoluminescence Blinking and Reversible Electron Trapping in Copper-Doped CdSe Nanocrystals. *Nano Lett*. **2015**, *15*, 4045– 4051.
105. Fainblat, R.; Barrows, C. J.; Hopmann, E.; Siebeneicher, S.; Vlaskin, V. A.; Gamelin, D. R.; Bacher, G. Giant Excitonic Exchange Splittings at Zero Field in Single Colloidal CdSe Quantum Dots Doped with Individual Mn^{2+} Impurities. *Nano Lett*. **2016**, *16*, 6371– 6377.
106. Besombes, L.; Léger, Y.; Maingault, L.; Ferrand, D.; Mariette, H.; Cibert, J. Probing the Spin State of a Single Magnetic Ion in an Individual Quantum Dot. *Phys. Rev. Lett*. **2004**, *93*, 207403.
107. Léger, Y.; Besombes, L.; Maingault, L.; Mariette, H. Valence-Band Mixing in Neutral, Charged, and Mn-Doped Self-Assembled Quantum Dots. *Phys. Rev. B: Condens. Matter Mater. Phys.* **2007**, *76*, 045331.
108. Schimpf, A. M.; Ochsenbein, S. T.; Gamelin, D. R. Surface Contributions to Mn^{2+} Spin Dynamics in Colloidal Doped Quantum Dots. *J. Phys. Chem. Lett*. **2015**, *6*, 457-463.
109. Moro, F., Turyanska, L., Granwehr, J., Patanè, A. Spin manipulation and spin-lattice interaction in magnetic colloidal quantum dots. *Phys. Rev. B.*, **2014**, *90*, 205428.
110. Gurung, T., Mackowski, S., Karczewski, G., Jackson, H. E., Smith, L.M. Ultralong spin memory of optically excited single magnetic quantum dots. *Appl. Phys. Lett*. **2008** *93*, 153114

Chapter 2: Directed Exciton Magnetic Polaron Formation in a Single Colloidal Mn^{2+}:CdSe/CdS Quantum Dot

2.1 Overview

One of the most prominent signatures of transition metal doping in colloidal nanocrystals is the formation of charge carrier induced magnetization of the dopant spin sublattice, called exciton magnetic polaron (EMP). Understanding the direction of EMP formation, however, is still a major obstacle. Here, we present a series of temperature-dependent photoluminescence studies on single colloidal Mn^{2+}:CdSe/CdS core/shell quantum dots (QDs) performed in a vector magnetic field providing unique insight into the interaction between individual excitons and numerous magnetic impurities. The energy of the QD emission and its full width at half maximum (FWHM) are controlled by the interplay of EMP formation and statistical magnetic fluctuations, in excellent agreement with theory. Most important, we give the first direct demonstration that anisotropy effects – hypothesized for more than a decade – dominate the direction of EMP formation. Our findings reveal a pathway for directing the orientation of optically induced magnetization in colloidal nanocrystals.

2.2 Introduction

Recent advances in chemical synthesis enable the design of tailored, high-quality nanocrystals with small size dispersions, a wide variety of shapes, and complex geometries.[1,2] One of the most enduring challenges in this field has been the use of controlled doping, *i.e.* replacing individual atoms in the crystal matrix by impurities, to control the physical properties of such nanocrystals.[3–6] Dopants may act as emission centers, affecting the luminescence of the host material.[7–16] Introducing open-shell transition metal ions such as cobalt or manganese into non-magnetic semiconductors endows the host nanocrystals with magnetic functionalities.[17–25] Exchange interactions between the localized magnetic moments of the dopants' *d* electrons and the magnetic moments of the delocalized charge carriers (*s*-type electrons and *p*-type holes) result in

giant magneto-optical responses.[26,27] This development was boosted by the prediction of huge exchange fields in colloidal quantum dots (QDs),[28] making room temperature applications feasible. Indeed, giant Zeeman splittings have been observed up to room temperature in various colloidal nanocrystals.[6,29,30] Among the most intriguing consequences of the pronounced *sp-d* exchange interactions is the spontaneous alignment of the dopant magnetic moments mediated by photogenerated charge carriers in the host QDs[31–34], the so-called exciton magnetic polaron (EMP) formation. In colloidal QDs, these EMPs have been demonstrated to be stable up to room temperature[31] and even accessible by electrical charge carrier injection.[35] Another fundamental consequence of the finite number of magnetic dopants inside a colloidal QD is the occurrence of thermodynamic spin fluctuations, modifying, *e.g.*, EMP formation[32] and carrier spin dynamics.[33]

Until now, EMP formation in doped nanocrystals has only been investigated in nanocrystal ensembles,[31–34] where unavoidable inhomogeneous broadening effects cover fundamental physical properties due to distributions of nanocrystal shape, size, composition, and orientation within the ensemble. As an example, anisotropic EMP formation has been theoretically predicted[36,37] and used to explain long relaxation times of optically excited EMPs in Mn^{2+}-doped CdSe QDs[31,32] - but such anisotropy has never been directly observed experimentally.

In a very limited number of cases, experiments on transition metal doped colloidal nanocrystals have been extended to single QD studies, mostly focusing on the luminescence of the internal dopant ligand field transition[12,38] and its intermittency[39–41]. In addition, fine structure effects of excitonic luminescence caused by individual Mn^{2+} dopants in single nanocrystals have been addressed.[42] This limited body of experimental literature is quite surprising in two aspects. First, single nanocrystal spectroscopy gave valuable input for the research on undoped semiconductor nanocrystals, *e.g.*, by revealing luminescence blinking caused by a statistical redistribution of charge carriers,[43,44] their impact on radiative recombination dynamics,[45] and spectral diffusion,[46] as well as the control of these effects *via* core/shell architectures.[47] In addition, electric field induced Stark shifts,[48] fine structure splitting due to *s-p* exchange,[49] and their tuning in a magnetic field,[50] or multiexciton emission[51,52] have been studied, among others. Second, single QD spectroscopy has been applied to epitaxially grown semiconductors doped with transition metals, demonstrating coupling between excitons and individual dopants[53–56] and revealing EMP formation[57–60] as well as spin fluctuations[57,61–63] in a highly anisotropic system characterized by strong quantum confinement along the growth axis and a rather weak one perpendicular to it.

In this work, we present magneto-photoluminescence (PL) spectroscopy studies of EMP formation in single colloidal Mn^{2+}:CdSe/CdS QDs with wurtzite crystal structure (see Figure A.2). Statistical fluctuations of the Mn^{2+} magnetization are found to be the source of a pronounced broadening of single QD emission linewidth at low temperatures. A distinct shift in energy with temperature and magnetic field, combined with a characteristic change in full width at half maximum (FWHM), is observed for a series of individual QDs. The uniquely detailed set of data gained for single QDs is described well by a theoretical model considering the interplay of EMP formation and thermodynamic spin fluctuations. Most interesting, unambiguous signatures of anisotropy effects on both the direction and stability of EMP formation and on statistical fluctuations of the Mn^{2+} spins are found. By applying a 3D vector magnetic field, we demonstrate that EMP formation can be manipulated, *i.e.*, stabilized (increase of EMP binding energy) or destabilized (decrease of EMP binding energy), by varying the angle between the external magnetic field and a dominant anisotropy axis of the nanocrystals. This EMP stabilization and destabilization in addition affects thermodynamic spin fluctuations visualized by a corresponding decrease and increase of the excitonic linewidth, respectively.

3.3 Results and Discussion

Mn^{2+}-doped CdSe/CdS nanocrystals (core diameter: 5.8 nm, total diameter: 11.9 nm) with an average dopant concentration of $x_{\mathrm{Mn}} = 0.9\%$ were synthesized for single QD experiments. Undoped CdSe/CdS QDs with similar core/shell structure were prepared as a reference (see SI for further information). Both samples use giant CdS shells to minimize the overlap of the hole wave function with surface trap states, while attracting the electron *via* Coulomb interaction close to the core. Surface traps are often reported to induce PL intermittency and spectral diffusion.[46,47,64] Details about sample fabrication for spatially resolved PL experiments can be found in the SI.

Figure 2.1 depicts the temperature dependent PL spectra of (a) a single undoped CdSe/CdS QD and (b) a single Mn^{2+}-doped CdSe/CdS QD (QD #1). The PL of the undoped QD exhibits a narrow zero phonon line (ZPL) with a FWHM of 1.1 meV (limited by the spectral resolution of our experimental setup), in agreement with literature values for comparable excitation intensities of ≤ 10 Wcm^{-2}.[65] A weak phonon replica, related to the simultaneous emission of a longitudinal optical (LO) phonon, is observed red shifted by 26.5 meV from the ZPL, as commonly reported in the literature.[66,67] The ZPL shows an increase of the FWHM and a red shift with increasing temperature, the latter being characteristic for the temperature dependence of the band edge

emission in most semiconductors.[68] In contrast, the Mn^{2+}:CdSe/CdS single QD exhibits a significantly broadened ZPL with a FWHM of 6.3 meV at 4 K. Interestingly, the phonon replica is shifted by 27.3 meV with respect to the ZPL and exhibits higher intensity compared to the undoped reference QD. This difference may indicate enhanced coupling between the LO phonon and the exciton, possibly related to the introduction of lattice distortions because of the doping and/or the specific shape of the nanocrystals (see Figure A1). Most important, the energy shift with temperature observed in the doped QD strongly deviates from its undoped counterpart, showing a blue shift between 4 K and 40 K followed by a red shift when the temperature is further increased. In addition, a significant change of the emission linewidth is observed with raising temperature.

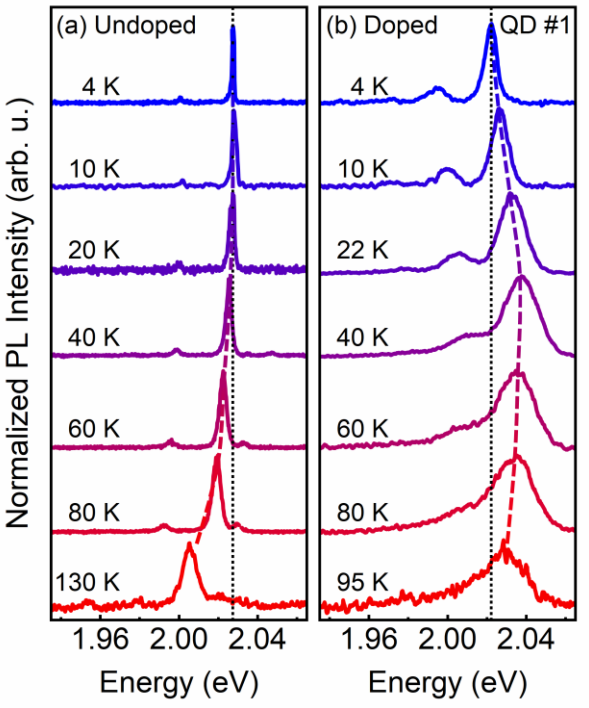

Figure 2.1 Temperature dependent single particle photoluminescence spectra. Photoluminescence spectra of (a) an undoped CdSe/CdS single QD and (b) a single Mn^{2+}:CdSe/CdS doped QD (QD #1) at different temperatures. Dashed lines serve as a guide to the eye to indicate the shift of the emission maximum. Dotted lines mark the energy position of the ZPL at T = 4 K.

To investigate the temperature dependent shift of the PL energy, ΔE_{PL}, of the single QDs more thoroughly, the peak energy values are extracted from the data in Figure 2.1 and summarized in Figure 2.2 (a). The undoped CdSe/CdS QD is discussed first to establish a reference for the

intrinsic contributions to $\Delta E_{\mathrm{PL}}(T)$, known as Varshni shift. To preclude statistical variations for the undoped reference, four individual undoped QDs were measured. The averaged data are displayed as gray dots in Figure 2.2 (a).

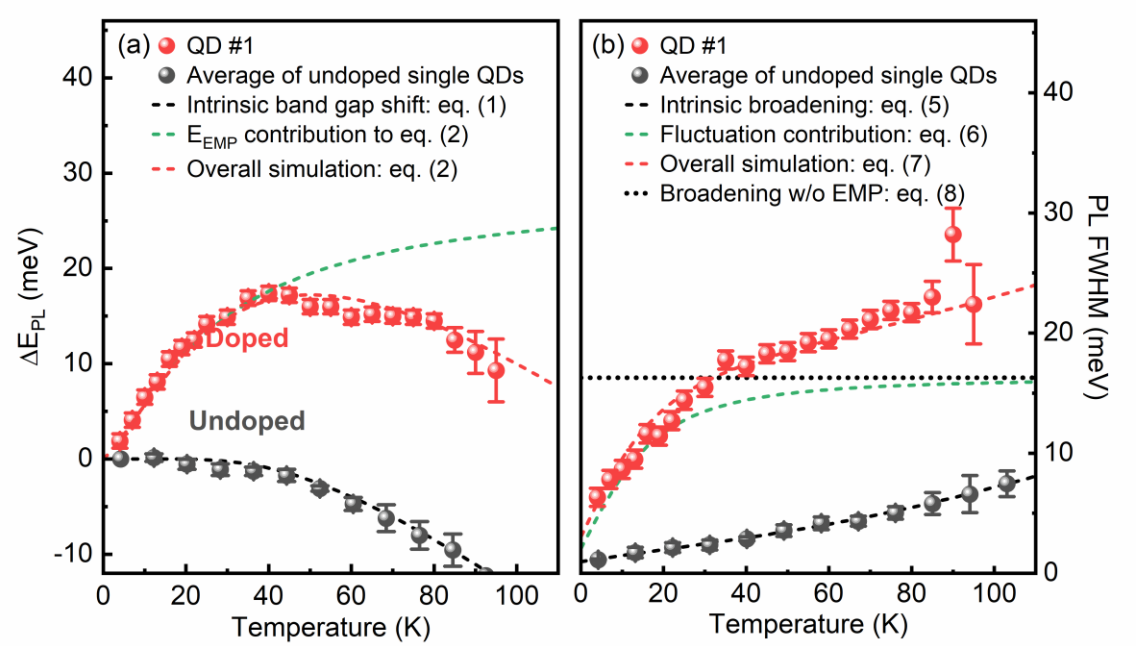

Figure 2.2 Compiled temperature dependence of single particle photoluminescence maxima and linewidth. (a) Temperature-dependent PL shift $\boldsymbol{\Delta E_{\mathrm{PL}}}$ of QD #1 (red) and undoped single QDs (gray, averaged over four QDs). The dashed gray line indicates the fit of the data of undoped QDs to eq. (2.1). The dashed red line shows the simulated overall shift for QD #1 described by eq. (2.2). The green dashed curve illustrates the EMP contribution to eq. (2.2). (b) ZPL FWHM of QD #1 (red), compared to the average of four undoped single QDs (gray). The data of undoped single QDs were fitted using eq. (2.5) (black dashed curve). The red dashed curve shows the simulation result for QD #1, using eq. (2.7) with the same parameters as used in (a). The contribution of the fluctuation broadening according to eq. (2.6) is shown by the green dashed line. The high temperature limit, *i.e.* neglecting EMP formation, is calculated according to eq. (2.8) and indicated as a black dotted line. The data of QD #1 in (a) and (b) were fitted simultaneously to eqs. (2.2) and (2.7), using $\boldsymbol{N_0}$ = 17.82 nm^3,[69] $\boldsymbol{N_0\alpha}$ = 0.23 eV,[70] $\boldsymbol{N_0\beta}$ = - 1.27 eV.[70]

The temperature dependent shift of the band gap for undoped semiconductors is commonly ascribed to a mixture of crystal volume expansion (minor influence) and electron – phonon

interaction (major influence).[68] It is usually fit to fully empirical[68] or semi–empirical formulae, as introduced by O'Donnell and Chen:[71]

$$W_{\mathrm{g,intrinsic}}(T) = W_{\mathrm{g,intrinsic}}(0\ \mathrm{K}) - 2 \cdot S_{\mathrm{OC}} \cdot \langle \hbar\omega \rangle \cdot \frac{1}{\exp\left(\frac{\langle \hbar\omega \rangle}{k_B T}\right) - 1} \tag{2.1}$$

Hereby, $\Delta W_{\mathrm{g,intrinsic}}(T) = W_{\mathrm{g,intrinsic}}(T) - W_{\mathrm{g,intrinsic}}(0\ \mathrm{K})$ is the energy shift of the band gap with respect to the value at 0 K, S_{OC} is a dimensionless coupling constant indicating the strength of the electron–phonon coupling, and $\langle \hbar\omega \rangle$ is an average phonon energy. Fitting the data of the undoped single QDs in Figure 2.2 (a) to eq. (2.1) yields S_{OC} = 2.05 and $\langle \hbar\omega \rangle$ = 14.2 meV. These values are slightly smaller than those found in literature for bulk CdSe ($S_{\mathrm{OC,ref}}$ = 2.5 ± 0.4, $\langle \hbar\omega \rangle_{\mathrm{ref}}$ = 16.7 ± 4.4 meV, averaged over all CdSe values in ref. [72]), but are in good agreement with the trend discussed in ref. [73] for CdSe QDs coated with large CdS shells.

$\Delta E_{\mathrm{PL}}(T)$ of QD #1 is strikingly different from the behavior observed for undoped QDs, with an energy blue shift of 17 meV between 4 K and 40 K (see red dots in Fig. 2.2 (a)), clearly deviating from the intrinsic red shift of the band gap with increasing temperature (see gray dots in Fig. 2.2 (a)). After a turnover between 40 K and 70 K, the energy shift of the PL maximum of QD #1 starts to follow the red shift observed in the undoped analogue. Similar results in colloidal Mn^{2+}:CdSe nanocrystal ensembles have been interpreted as evidence of EMP formation.[31,32,35] In EMPs, the Mn^{2+} magnetic moments couple with the exciton spin *via sp-d* exchange interactions, represented by the exchange field B_{exc}. Under the influence of B_{exc}, the Mn^{2+} spin ensemble is aligned with the exciton spin, leading to a spontaneous magnetization M_{Mn}, thus reducing the system's energy by the polaron energy E_{EMP}. As the temperature rises, thermal disorder and magnetic ordering compete against each other, weakening the magnetization and decreasing E_{EMP}, leading to a blue shift of the PL energy as observed here between 4 K and 40 K.

The overall temperature dependent energy shift of the PL maximum of the single Mn^{2+}:CdSe/CdS QD emission can thus be written as:

$$\begin{aligned} \Delta E_{\mathrm{PL}}(B,T) &= \Delta W_{\mathrm{g,intrinsic}}(T) + E_{\mathrm{EMP}}(B,T) \\ &= \Delta W_{\mathrm{g,intrinsic}}(T) - V_{\mathrm{eff}} \cdot M_{\mathrm{Mn}}(B,T) \cdot B_{\mathrm{exc}} \end{aligned} \tag{2.2}$$

with V_{eff} as the effective volume occupied by the exciton. The magnetization can be described with a modified Brillouin function for a paramagnetic spin ensemble and reads as:

$$M_{\mathrm{Mn}}(B,T) = x_{\mathrm{Mn}} \cdot N_0 \cdot \mu_{\mathrm{B}} \cdot g_{\mathrm{Mn}} \cdot S_{\mathrm{eff}} \cdot \mathcal{B}_{5/2}\left(\frac{5\mu_{\mathrm{B}} g_{\mathrm{Mn}}(B+B_{\mathrm{exc}})}{2k_{\mathrm{B}}(T_{\mathrm{s}}+T_0)}\right) \tag{2.3}$$

Here, x_{Mn} is the dopant concentration, N_0 the number of cations per volume, $\mathcal{B}_{5/2}$ the Brillouin function for the Mn^{2+} S = 5/2 system, T_0 and $S_{\mathrm{eff}} \leq 2.5$ the antiferromagnetic temperature and the effective manganese spin, respectively, μ_{B} the Bohr magneton, k_{B} the Boltzmann constant and g_{Mn} = 2 the gyromagnetic ratio of Mn^{2+}. B and T are the experimentally controlled magnetic field and bath temperature, respectively. The spin temperature entering the magnetization is approximated by $T_{\mathrm{s}} = T + \Delta T_{\mathrm{s}}$, where ΔT_{s} is a zeroth order correction accounting for the difference between the Mn^{2+} spin temperature and the bath temperature of the crystal. ΔT_{s} stems from heating of the Mn^{2+} spin ensemble, *e.g.*, due to spin–flip scattering between the optically generated electron–hole pairs and the Mn^{2+} spin system.[60,61] Using the commonly applied "exchange box" model, the exchange field can be written as:[61,74]

$$B_{\mathrm{exc}} = B_{\mathrm{exc}}^{\mathrm{el}} + B_{\mathrm{exc}}^{\mathrm{h}} = \frac{N_0\alpha - N_0\beta}{2V_{\mathrm{eff}} N_0 g_{\mathrm{Mn}} \mu_{\mathrm{B}}} \tag{2.4}$$

$N_0\alpha$ ($N_0\beta$) is the electron-dopant (hole-dopant) exchange constant and $B_{\mathrm{exc}}^{\mathrm{el}}$ ($B_{\mathrm{exc}}^{\mathrm{h}}$) the electron-dopant (hole-dopant) exchange field. Thus, inserting eq. (2.3) and (2.4) into eq. (2.2), and using the parameters obtained from fitting the data of undoped QDs, the temperature dependence of ΔE_{PL} can be simulated, using V_{eff}, x_{Mn}, and ΔT_{s} as fit parameters.

In Figure 2.2 (a), the simulated data using the parameters x_{Mn} = 1.73%, V_{eff} = 30.4 nm^3 (corresponding to an effective spherical exciton diameter of 3.9 nm), and ΔT_{s} = 4.3 K are shown (red dashed curve). T_0 = 1.1 K and S_{eff} = 2.3 are obtained from interpolating data from ref. [75]. The calculations reproduce the experimental data (red symbols) very well. For clarity, the green dashed curve plots the EMP energy contribution to eq. (2.2), with respect to the value at T = 0 K. The value of x_{Mn} = 1.73% is reasonable as an overall manganese concentration of 0.9% of the doped core-shell QDs has been measured *via* inductively coupled plasma atomic emission spectroscopy (ICP-AES), and the Mn^{2+} concentration varies statistically from dot to dot. Due to strong confinement of the hole wavefunction, the effective exciton volume should be approximately 36% of the core volume,[34] corresponding to $V_{\mathrm{eff,expected}}$ = 35 nm^3, in very good agreement with the value used in the simulation. From eq. (2.4), these results yield an exchange field of B_{exc} = 11.9 T, which falls in the range (between 8 T and 17 T) of values reported for similar Mn^{2+}:CdSe QDs.[31,32,34,35] The additional spin heating ΔT_{s} = 4.3 K also closely resembles values found in literature (*e.g.*, 4.4 K for self-assembled CdMnSe QDs[61] and 8 K – 14.5 K for self-assembled CdMnTe QDs[60]). For simplicity we assume an overlap between the carrier wave functions with

the doped regions equal to unity, which may result in a slight overestimation of the effective exciton volume, since the electron wave function is delocalized into the undoped CdS shell. Because the contribution of the *s-d* exchange interaction is only about 15% of the total *sp-d* exchange interaction, we estimate the error introduced by neglecting the finite overlap of the electron wavefunction with the magnetic dopants in deriving V_{eff} to be ≤ 10%. From this analysis, we conclude that $\Delta E_{\mathrm{PL}}(T)$ of QD #1 is unambiguously correlated with the formation of an EMP. These results represent the first observation of an EMP in a single colloidal QD.

In Figure 2.2 (b), the extracted temperature dependent FWHM of the undoped reference QD (gray dots) and QD #1 (red dots) are depicted. Again, the undoped reference is analyzed first to distinguish intrinsic line broadening effects from the contributions introduced by the dopants. Commonly, the change of the FWHM with temperature in undoped semiconductors is related to homogeneous broadening due to dephasing of the exciton by phonon scattering, as described by equation (2.5):[76]

$$FWHM_{\mathrm{intrinsic}}(T) = \Gamma_0 + \Gamma_{\mathrm{AC}} \cdot T + \Gamma_{\mathrm{LO}} \cdot \frac{1}{\exp\left(\frac{\hbar\omega_{\mathrm{LO}}}{k_{\mathrm{B}}T}\right)-1} \qquad (2.5)$$

Here, Γ_0 is an inhomogeneous offset, *e.g.*, caused by a finite resolution of the experimental setup or by charge fluctuations, Γ_{AC} is a constant related to the coupling of the exciton to acoustic phonons, and Γ_{LO} describes coupling to the longitudinal optical phonons with energy $\hbar\omega_{\mathrm{LO}}$. Because $\hbar\omega_{\mathrm{LO}}$ = 26.5 meV is extracted directly from Figure 2.1, $FWHM_{\mathrm{intrinsic}}(T)$ of the undoped QD can be fitted with the remaining three parameters (see black dashed curve in Fig. 2.2b), yielding Γ_0 = 0.98 meV, Γ_{AC} = 49 µeV/K, and Γ_{LO} = 26.1 meV. These values are close to values found in literature for experiments on an ensemble of colloidal CdSe QDs (Γ_{AC} = 20 µeV/K and Γ_{LO} = 30 meV).[77] To the best of our knowledge, these parameters have not been reported for single colloidal CdSe QDs.

Turning to the line broadening of QD #1, we find a distinct difference to the undoped reference, namely an enhanced emission linewidth and a strong increase of the broadening with temperature (see red dots in Fig. 2.2 (b)). More specifically, even at the lowest temperature (T = 4 K) the FWHM of QD #1 (~ 6.3 meV) exceeds the FWHM of the undoped reference (1.1 meV) considerably and increases very steeply with an anomalous negative curvature up to a FWHM of 17 meV at 40 K. In this temperature regime, the major contribution to the increase in FWHM for the undoped QDs is due to acoustic phonon scattering, leading to a linewidth

broadening of just 1.7 meV with respect to the value measured at 4 K. For temperatures above 40 K, the slope of the FWHM(T) curve of QD #1 decreases, while even at 100 K its FWHM still exceeds the undoped reference by almost a factor of 3.

Previously, a broadening of the ZPL linewidth in magnetically doped QDs grown by epitaxy has been correlated to statistical spin fluctuations within the Mn^{2+} ensemble.[63] These fluctuations stem from the statistically varying occupation of the six possible spin projections $s_{\mathrm{Mn,z}}$ = ±5/2, ±3/2, ±1/2 of each individual Mn^{2+} ion, leading to fluctuations of the magnetization with variance $\langle M_{\mathrm{Mn}}^2 \rangle$. Considering the EMP equilibrium state and making use of the fluctuation dissipation theorem,[78] these fluctuations induce a broadening of the luminescence linewidth:[63]

$$FWHM_{\mathrm{fluct}}(B,T) = \sqrt{8\ln(2)} \cdot \sqrt{k_{\mathrm{B}} T_{\mathrm{s}} \cdot B_{\mathrm{exc}}^2 \cdot V_{\mathrm{eff}} \left| \frac{dM_{\mathrm{Mn}}(B,T)}{dB} \right|_{\substack{B_{\mathrm{exc}}+B \\ T_{\mathrm{s}}+T_0}}} \qquad (2.6)$$

The total temperature dependence of the FWHM is now calculated in a first approximation by summing up the intrinsic contribution $FWHM_{\mathrm{intrinsic}}(T)$ due to phonon broadening (obtained by fitting the data from the undoped reference to eq. (2.5)) and the contributions of spin fluctuations $FWHM_{\mathrm{fluct}}(B,T)$:

$$FWHM(B,T) = FWHM_{\mathrm{intrinsic}}(T) + FWHM_{\mathrm{fluct}}(B,T) \qquad (2.7)$$

Importantly, no new parameters are introduced to describe the linewidth broadening of QD #1 with temperature. The red dashed curve in Figure 2.2 (b) shows the result of simulating the linewidth according to eq. (2.7) for QD #1 using the same parameters as for the simulation of $\Delta E_{\mathrm{PL}}(T)$ (see Fig. 2.2 (a)), while the green and gray dashed curves show the contributions of $FWHM_{\mathrm{fluct}}(T)$ and $FWHM_{\mathrm{intrinsic}}(T)$, respectively. The precise measurement of $\Delta E_{\mathrm{PL}}(T)$ and $FWHM(T)$ in single Mn^{2+}-doped QDs makes it possible to use one parameter set to fit both energy shift and linewidth broadening over a large temperature range simultaneously with V_{eff}, x_{Mn}, and ΔT_{s} as the only fit parameters. An excellent agreement with experiment is obtained, including the steep increase of the FWHM up to 40 K due to spin fluctuations. Note, that in contrast to $\Delta E_{\mathrm{PL}}(T)$, $FWHM(T)$ is very sensitive to the parameter ΔT_{s}, essentially offsetting $FWHM$ at 4 K. The observed negative curvature of $FWHM(T)$ is revealed to be caused by the contribution of the Mn^{2+} magnetization fluctuations (green dashed curve), converging towards a value of 16.5 meV for temperatures above 80 K, where EMP formation is more and more suppressed by the thermal energy. The impact of

statistical magnetic fluctuations on emission linewidths in the absence of EMP formation – which can be caused either by too weak exchange interactions (*i.e.*, low exchange fields, high temperatures) or by too fast exciton recombination – has been described for self-assembled QDs exhibiting small confinement and weak *sp-d* exchange interactions.[79] In this case, the exciton recombination probes the instantaneous magnetization of the Mn^{2+} ensemble at the moment of photo-excitation. Since all possible spin projections $s_{\mathrm{Mn,z}}$ = ±5/2, ±3/2, ±1/2 for each Mn^{2+} ion are probed with the same probability, the time average of the expectation value $\langle M_{\mathrm{Mn}} \rangle$ is zero. However, the variance of the spin projections is non-zero with $\langle s_{\mathrm{Mn,z}}^2 \rangle$ = 35 / 12 for each Mn^{2+}. This variance leads to a finite variance $\langle M_{\mathrm{Mn}}^2 \rangle$ and therefore to a fluctuation broadening of the PL linewidth in the absence of EMP formation:[79]

$$FWHM_{\mathrm{high-T}} = \sqrt{8\ln(2)} \cdot \frac{1}{N_0 V_{\mathrm{eff}}} \cdot \sqrt{\frac{35}{12} x_{\mathrm{Mn}} N_0 V_{\mathrm{eff}}} \cdot \left(\frac{1}{2} N_0 \alpha - \frac{1}{2} N_0 \beta \right) \tag{2.8}$$

The black dotted line in Figure 2.2 (b) represents the value calculated using eq. (2.8) with the same parameters used in the simulations discussed above. Importantly, this formula implies no temperature dependence and can be regarded as the high temperature limit of eq. (2.6).[80] At lower temperatures, the magnetic polaron in fact suppresses the fluctuation broadening due to spin alignment driven by the large exchange field B_{exc}.

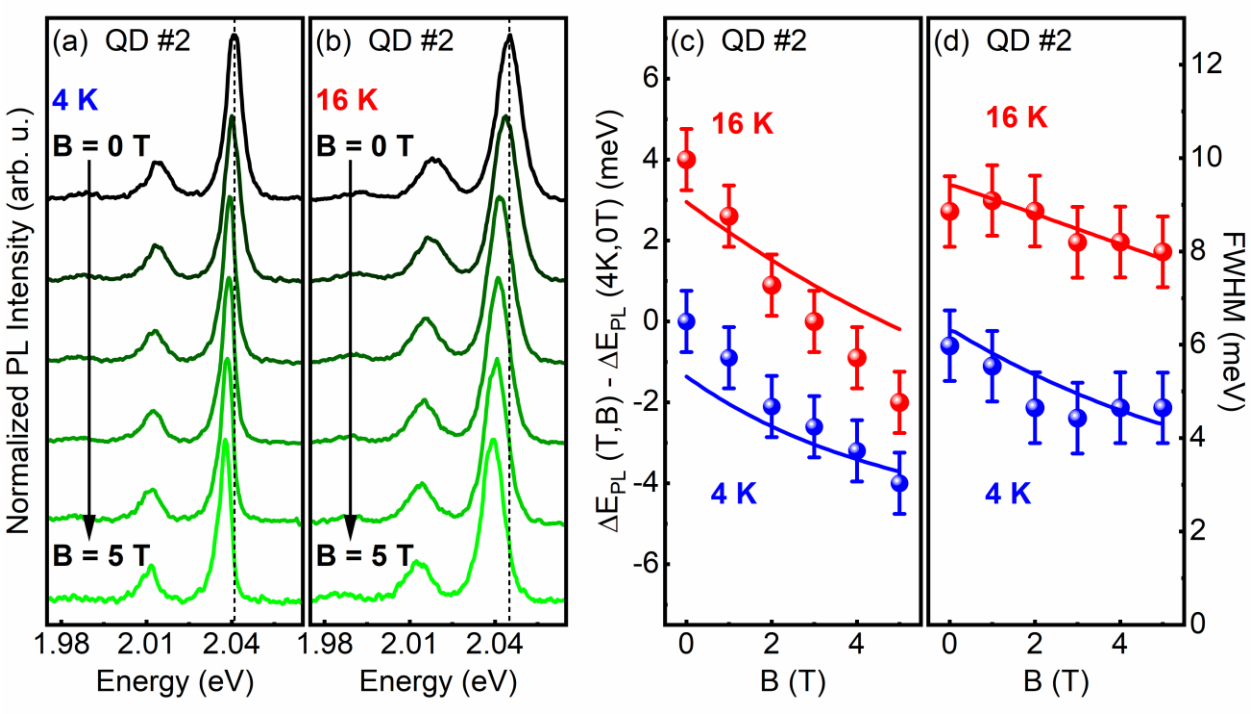

Figure 2.3 Field dependent single particle photoluminescence collected at 4 K and 16 K. (a) Magnetic field dependent PL spectra of QD #2 at (a) $\boldsymbol{T}$ = 4 K and (b) $\boldsymbol{T}$ = 16 K. The dashed lines are guides to the eye and mark the ZPL position at $\boldsymbol{B}$ = 0 T while the magnetic field is varied up to $\boldsymbol{B}$ = 5 T in Faraday geometry. (c) Magnetic field dependent energy shift $\boldsymbol{\Delta E_{PL}(B,T)}$ with respect to the ZPL position at $\boldsymbol{B}$ = 0 T and $\boldsymbol{T}$ = 4 K and (d) magnetic field dependent FWHM extracted from (a) and (b). Dots represent experimental data at $\boldsymbol{T}$ = 4 K (blue) and $\boldsymbol{T}$ = 16 K (red), solid lines show results of a simultaneous fit of all four curves, using eqs. (2.2) and (2.7).

To complete our picture of EMP formation and magnetization fluctuations in individual transition metal doped nanocrystals, single QD PL studies in an external magnetic field of variable strength and orientation have been performed. In Figure 2.3 (a) and (b) magnetic field dependent PL spectra of a second nanocrystal (QD #2) are shown for T = 4 K and T = 16 K, respectively. Similar to QD #1, the ZPL of QD #2 also exhibits an energy blue shift and an increase in FWHM with rising temperature, indicating the observation of EMP formation. For both temperatures, the ZPL shifts to lower energies under the influence of a magnetic field, as highlighted by the dashed lines. The changes in energy and FWHM of the ZPL with magnetic field are extracted from the spectra and shown in Figures 2.3 (c) and (d) as blue and red dots for T = 4 K and T = 16 K, respectively. At B = 0 T, the blue shift ΔE_{PL} (~ 4.0 meV) and the linewidth increase $\Delta FWHM$

(~ 2.9 meV) between T = 4 K and T = 16 K are smaller than observed in QD #1. This comparison emphasizes the uniqueness of each individual QD with respect to, *e.g.*, dopant concentration and exciton volume (and thus exchange field).

Under the influence of an external magnetic field of B = 5 T in Faraday geometry, $E_{\mathrm{PL}}(B)$ exhibits a red shift of $\Delta E_{\mathrm{PL}}(B) \sim$ - 4 meV with respect to the B = 0 T value due to magnetic field induced spin ordering.[58] This result indicates that in QD #2 the EMP exchange field is not strong enough to completely saturate M_{Mn} even at T = 4 K, because in the case of an extremely strong exchange field the magnetization would be saturated and E_{EMP} would not depend on B. At T = 16 K, $E_{\mathrm{PL}}(B)$ exhibits an enhanced red shift of $\Delta E_{\mathrm{PL}}(B)$ = - 6 meV between B = 0 T and B = 5 T, since a higher temperature drives the magnetization further away from saturation, where the influence of the magnetic field on the spin ordering is larger. For the FWHM, a decrease with applied magnetic field is observed for both temperatures, which is consistent with partial suppression of spin fluctuations by increased magnetic order.

The data of $\Delta E_{\mathrm{PL}}(B)$ and $FWHM(B)$ can be fit to eqs. (2.2) and (2.7) for both temperatures. Figures 2.3 (c) and (d) show the result of the simultaneous fit of all four curves, yielding x_{Mn} = 0.8%, ΔT_{s} = 5.8 K, and V_{eff} = 49 nm^3, corresponding to an effective spherical exciton diameter of 4.6 nm and B_{exc} = 7.3 T. It should be noted that not only the magnetic field dependence, but - by considering the offset between the T = 4 K and T = 16 K curves - also the temperature dependence of $\Delta E_{\mathrm{PL}}(B,T)$ and $FWHM(B,T)$ is implicitly fitted as well. With these results, we demonstrate how an external magnetic field stabilizes EMP formation against thermal disorder, as reflected in the energy gain (red shift) and the narrowing of the FWHM.

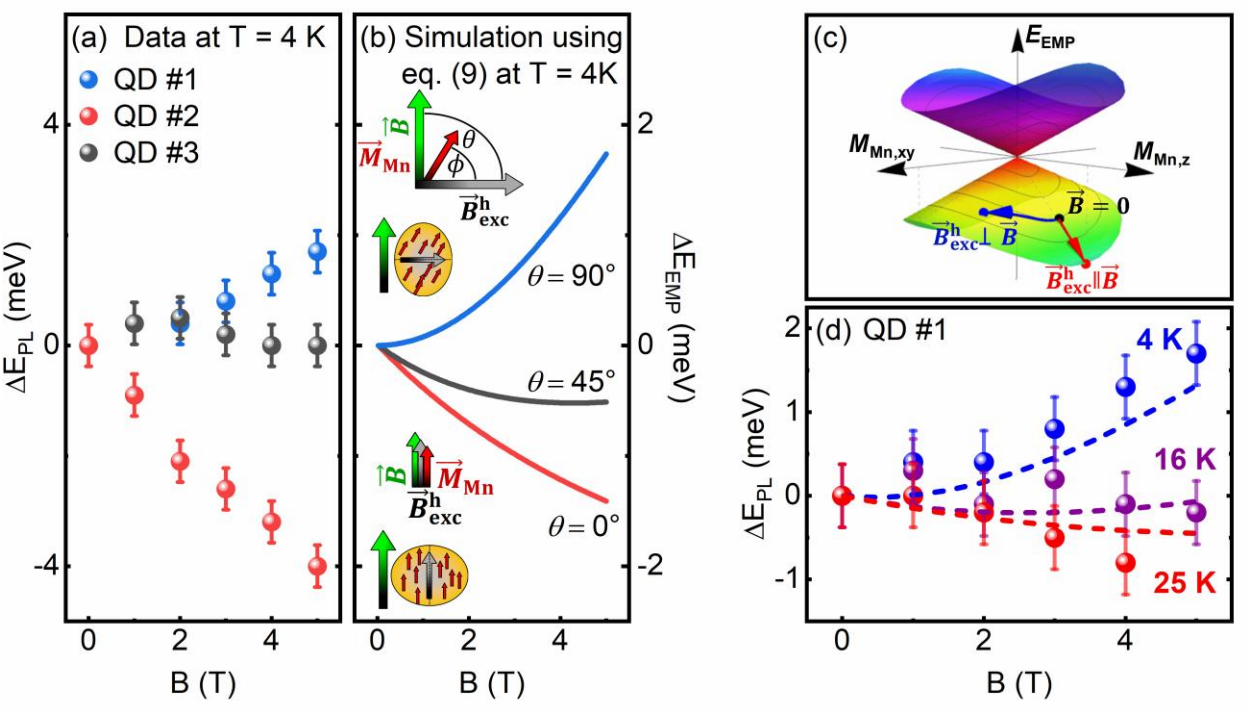

Figure 2.4 Selected magnetic field and temperature dependent photoluminescence maxima of sinlge particles displaying different EMP behavior. (a) PL energy shift with magnetic field in Faraday geometry for QDs #1, #2 and #3 at 4 K. (b) Simulation of the influence of the angle $\boldsymbol{\theta}$ between the hole exchange field $\vec{\boldsymbol{B}}^{\mathbf{h}}_{\mathbf{exc}}$ and the external magnetic field $\vec{\boldsymbol{B}}$ using eq. (2.9). The schematics illustrate the two limiting cases of a QD exhibiting a hole exchange field parallel (*i.e.* $\boldsymbol{\theta}$ = 0°) and perpendicular (*i.e.* $\boldsymbol{\theta}$ = 90°) to $\vec{\boldsymbol{B}}$. In the latter case, the Mn^{2+} magnetization is directed along $\vec{\boldsymbol{B}}^{\mathbf{h}}_{\mathbf{exc}} + \vec{\boldsymbol{B}}$. (c) Schematic of the EMP energy surface, warped by an axial asymmetry into the z-direction, where contour lines represent lines of equal Mn^{2+} magnetization. Starting from the EMP equilibrium energy at $\vec{\boldsymbol{B}}$ = 0 T (black dot), the influence of applying $\vec{\boldsymbol{B}}$ parallel (red arrow) and perpendicular to the anisotropy axis (blue arrow) on the equilibrium EMP energy are illustrated. (d) ZPL energy shift between $\boldsymbol{B}$ = 0 T and $\boldsymbol{B}$ = 5 T in Faraday geometry for QD #1 (dots) at three different temperatures. Corresponding simulations are added (dashed lines) with the same fit parameters as extracted from Fig. 2.2, now using eq. (2.9) with $\boldsymbol{\theta}$ = 80°.

Performing magneto-PL studies on several individual QDs reveals a surprising finding: Although usually a red shift with magnetic field is obtained at low temperatures, in some cases the magnetic field has no effect or even causes a blue shift of the ZPL energy (see Appendix A, Figure

A5 for statistics). Figure 2.4 (a) shows $\Delta E_{\mathrm{PL}}(B)$ for three different single QDs, measured at 4 K. Two of the QDs (QD #1 and QD #2) have already been discussed. While QD #2 shows a red shift, *i.e.*, a stabilization of its EMP with magnetic field (increased E_{EMP}), QD #3 shows no net shift between B = 0 and B = 5 T, and QD #1 shows a distinct blue shift, *i.e.*, a destabilization of the EMP in an external magnetic field (decreased E_{EMP}). Note that in the absence of EMP formation, increasing the magnetic field always leads to a red shift of the ZPL. Such red shifts stem from the giant Zeeman effect and are commonly observed in diluted magnetic semiconductors.[70]

The puzzling blue shift of the ZPL in Figure 2.4 (a) cannot be explained with the theory presented so far. To resolve this discrepancy, the theoretical description needs to be generalized as follows. The magnetic moments of the Mn^{2+} ions can be aligned by both an external magnetic field $\vec{B}$ and the exchange field $\vec{B}_{\mathrm{exc}} = \vec{B}_{\mathrm{exc}}^{\mathrm{el}} + \vec{B}_{\mathrm{exc}}^{\mathrm{h}}$ (see eq (2.3)). The direction of $\vec{M}_{\mathrm{Mn}}$ is then given by the direction of the total field $\vec{B}_{\Sigma} = \vec{B} + \vec{B}_{\mathrm{exc}}$. In the isotropic case, it is usually assumed that electron and hole spin align along the direction determined by the instantaneous direction of the randomly fluctuating Mn^{2+} magnetization – which can be directed by an external magnetic field – and EMP formation occurs. Then, the directions of $\vec{M}_{\mathrm{Mn}}$, $\vec{B}_{\mathrm{exc}}^{\mathrm{el}}$ and $\vec{B}_{\mathrm{exc}}^{\mathrm{h}}$ are expected to be colinear and given by the direction of $\vec{B}$ in the experimental situation, where the PL data are recorded by averaging over lots of excitation events. In that case, magnetic field, magnetization, and exchange field can be considered as scalars (eqs. (2.2-2.4) and (2.6-2.7)).

If, however, exchange field and magnetization are not colinear, the full vector form of the above-mentioned equations needs to be used. This would imply an anisotropy in the nanocrystals, constraining, *e.g.*, the wavefunction of the hole, which is dominated by its anisotropic p – character. If a magnetic field $\vec{B} \perp \vec{B}_{\mathrm{exc}}^{\mathrm{h}}$ is applied, a strict constraining of the hole wavefunction in the direction of the anisotropy axis would result in $g_{\perp}$ = 0. Such a behavior is *e.g.*, known for the heavy hole in bulk CdSe in the wurtzite crystal structure,[69] where the c-axis forms the anisotropy axis. In literature, similar arguments have been used to explain the dependence of the PL polarization degree in undoped CdSe QDs on magnetic fields up to 60 T.[81,82] Under this assumption, the hole total angular momentum and thus the hole exchange field $\vec{B}_{\mathrm{exc}}^{\mathrm{h}}$ are not necessarily aligned along $\vec{B}$, and $\vec{M}_{\mathrm{Mn}}$ is neither directed parallel to $\vec{B}_{\mathrm{exc}}^{\mathrm{h}}$ nor parallel to $\vec{\mathrm{B}}$, but instead oriented along $\vec{B}_{\Sigma}$ (see cartoon in Figure 2.4 (b)). Since the electron wavefunction is

dominated by its isotropic *s* – character, we assume $\vec{B}_{\mathrm{exc}}^{\mathrm{el}} \parallel \vec{B}_{\Sigma}$. Then, the sum of $\vec{B}$ and $\vec{B}_{\mathrm{exc}}^{\mathrm{h}}$ dictates the direction of $\vec{B}_{\Sigma}$ and the modified EMP energy is given by:[61]

$$E_{\mathrm{EMP}}(\vec{B},T) = -\vec{M}_{\mathrm{Mn}} \cdot \left(\vec{B}_{\mathrm{exc}}^{\mathrm{el}} + \vec{B}_{\mathrm{exc}}^{\mathrm{h}}\right) \cdot V_{\mathrm{eff}} = -V_{\mathrm{eff}} \cdot \left|\vec{M}_{\mathrm{Mn}}\right| \cdot \left(\left|\vec{B}_{\mathrm{exc}}^{\mathrm{el}}\right| + \cos(\phi) \cdot \left|\vec{B}_{\mathrm{exc}}^{\mathrm{h}}\right|\right) \tag{2.9}$$

Here, $\vec{M}_{\mathrm{Mn}}(\vec{B},T) = \vec{B}_{\Sigma}/B_{\Sigma} \cdot M_{\mathrm{Mn}}(|\vec{B}_{\Sigma}|,T)$ is the modified version of eq. (2.3) and ϕ the angle between $\vec{B}_{\mathrm{exc}}^{\mathrm{h}}$ and $\vec{M}_{\mathrm{Mn}}$. Note, that ϕ changes monotonically with increasing magnetic field strength if $\vec{B} \nparallel \vec{B}_{\mathrm{exc}}^{\mathrm{h}}$ and is therefore not easily accessible in an experiment. Therefore, in order to be compatible with the experimental situation, we define an angle θ between the external magnetic field $\vec{B}$ and the hole exchange field $\vec{B}_{\mathrm{exc}}^{\mathrm{h}}$ which does not change if the magnitude of the external field is varied.

Figure 2.4 (b) shows a simulation using the parameters previously extracted by fitting the temperature series of the emission of QD #1 (see Fig. 2.2) for three different angles θ = 0°, 45° and 90°, *i.e.* different orientations of the QD anisotropy axis with respect to the external magnetic field. For the simulations, x_{Mn}, ΔT_{s}, and V_{eff} as extracted for QD #1 (see Fig. 2.2) are used. The simulation of $\Delta E_{PL}(B)$ in fact displays fundamental differences for different θ, namely a blue shift for θ = 90°, no significant shift for θ = 45° and a red shift for θ = 0°, in qualitative agreement with the data shown in Figure 2.4 (a). In contrast to the magnetic field induced red shift of the ZPL energy explained above, a blue shift, *i.e.* a *decrease* of the EMP binding energy, can only take place if $\vec{B}$ and $\vec{B}_{\mathrm{exc}}^{\mathrm{h}}$ are not collinear. Considering the angle dependence of eq. (2.9), such a blue shift can be ascribed to the monotonic increase of ϕ with $|\vec{B}|$ (largest for θ = 90°, *i.e.* $\vec{B} \perp \vec{B}_{\mathrm{exc}}^{\mathrm{h}}$), leading to a decreased projection of $\vec{B}_{\mathrm{exc}}^{\mathrm{h}}$ onto $\vec{M}_{\mathrm{Mn}}$ (decrease of $\cos(\phi)$) and thus a decrease of the EMP binding energy E_{EMP} with $|\vec{B}|$.

Figure 2.4 (c) illustrates the dependence of the EMP potential energy surface on $\vec{M}_{\mathrm{Mn}}$, warped by an axial asymmetry, where, as an example, the anisotropy axis is chosen to be directed along the spatial z direction. In this example, the magnetization is not fully saturated at $\vec{B}$ = 0 T after EMP formation, *i.e.* the corresponding EMP equilibrium state (black dot) is not located on the outermost contour line. Applying a magnetic field $\vec{B}$ into the direction of the anisotropy axis enhances the magnetization $|\vec{M}_{\mathrm{Mn}}|$ and thus causes the EMP equilibrium state to move *downhill*

along the red arrow. Thus, a stabilization of the EMP state occurs due to an increase of the EMP binding energy by the applied field. While applying a magnetic field $\vec{B}$ perpendicular to the anisotropy axis also slightly enhances the magnetization, $\vec{M}_{\mathrm{Mn}}$ is now directed along $\vec{B}_{\Sigma}$ and therefore displaced away from the anisotropy axis when $|\vec{B}|$ is increased. This causes the EMP equilibrium state to move uphill along the trace of the blue arrow, *i.e.* a destabilization of the EMP state occurs due a reduction of the EMP binding energy. The observation of a magnetic field induced blue shift, a missing energy shift and a red shift of the ZPL energy in cases of QD #1, QD #2 and QD #3, respectively, may thus be assigned to the three cases of the individual QDs, having their anisotropy axes differently oriented with respect to the magnetic field direction. In colloidal QDs, a preferential axis for EMP formation has, to the best of our knowledge, not been observed so far, even though it has long been hypothesized to explain the EMP formation dynamics in Mn^{2+}-doped CdSe QDs.[31,32]

A second fundamental consequence of the directional dependence of eq. (2.9) is the influence of temperature on the results of a magnetic field series. Recall that in the case of QD #2, where $\vec{B}_{\mathrm{exc}}^{\mathrm{h}}$ is parallel to $\vec{B}$ (or close to), $d|\Delta E_{\mathrm{PL}}|/dB$ increases with temperature (see Figure 2.3 (c)) due to the fact that the increase in temperature drives the magnetization away from saturation, increasing the possible magnetization gain by application of $\vec{B}$. In contrast, in the case of QD #1, where $\vec{B}_{\mathrm{exc}}^{\mathrm{h}}$ is apparently almost perpendicular to $\vec{B}$, we find a fundamentally different behavior as shown in Figure 2.4 (c). Here, the blue shift with magnetic field observed at T = 4 K decreases with increasing temperature, and turns into a red shift for $T \geq 25$ K. While, as discussed above, the influence of $\vec{B}$ onto the magnetization gain (*i.e.* E_{EMP} gain) is temperature dependent, the evolution of ϕ and thus the projection term $|\vec{B}_{\mathrm{exc}}^{\mathrm{h}}|\cos(\phi)$ of $\vec{B}_{\mathrm{exc}}^{\mathrm{h}}$ onto $\vec{M}_{\mathrm{Mn}}$ in eq. (2.9) is temperature independent. Therefore, at low temperatures, where the magnetization is almost saturated, the projection term $|\vec{B}_{\mathrm{exc}}^{\mathrm{h}}|\cos(\phi)$ causes a destabilization of the EMP (blue shift) with external magnetic field. At higher temperatures, *e.g.* T > 25 K, the projection term is overcompensated by the magnetization gain and $\vec{B}$ thus causes a net stabilization (red shift) of the EMP. In the picture of a warped potential energy surface (Figure 2.4 (c)), the influence of a temperature increase is equivalent to moving the $\vec{B}$ = 0 T equilibrium state (black dot) uphill into the direction of the $|\vec{M}_{\mathrm{Mn}}|$ = 0 origin. While the direction of $\vec{M}_{\mathrm{Mn}}$ is still displaced away from the

anisotropy axis, the application of $\vec{B}$ perpendicular to the anisotropy axis increases $|\vec{M}_{\mathrm{Mn}}|$ and causes a net gain in E_{EMP}, *i.e.* a downhill movement.

Using eq. (2.9) with the same parameters for x_{Mn}, V_{eff} and ΔT_{s} as extracted from the temperature series depicted in Figure 2.2, we simulated the theoretical behavior of QD #1 in a magnetic field at three different temperatures using $\theta = 80°$. The results, displayed as dashed lines in Figure 2.4 (c), resemble the trend of the data very well, demonstrating the strength of the model and underlining the physical considerations about the origin of this effect.

To directly test our hypothesis of an anisotropy axis constraining the direction of the hole exchange field in the nanocrystals, we use the possibility of our experimental setup to apply a rotating (3D) magnetic field with $|\vec{B}| = 2$ T in any direction with respect to the substrate surface. In the case of a uniaxial anisotropy, a red shift (stabilization) and a blue shift (destabilization) would be expected if the magnetic field is aligned parallel and perpendicular to the axis of anisotropy, respectively. In this case, the full 3D dependence of EMP formation on the direction of the magnetic field is characterized by the projection angle ϕ of $\vec{M}_{\mathrm{Mn}}$ onto $\vec{B}^{\mathrm{h}}_{\mathrm{exc}}$, or equivalently, by the angle θ between $\vec{B}^{\mathrm{h}}_{\mathrm{exc}}$ and $\vec{B}$, as introduced above. For these experiments we define a plane given by the direction of the anisotropy axis (*i.e.* direction of the maximum red shift) and the direction where the maximum blue shift is observed (*i.e.* a direction perpendicular to the anisotropy axis), and we then rotate $\vec{B}$ within this plane. Figure 2.5 illustrates the rotating magnetic field experiment for single QD #4 (see Appendix A, Figure A6, for more statistics). As depicted in Figure 2.5 (a), the maximum blue and red shift of the ZPL position with respect to $|\vec{B}| = 0$ T were found when the magnetic field was applied close to the [$x_{\mathrm{lab}} = 0$, $y_{\mathrm{lab}} = 0$, $z_{\mathrm{lab}} = 1$] and [1,1,0] directions, respectively, for QD #4. These directions were used to define the plane in which the magnetic field with $|\vec{B}| = 2$ T was rotated (green shaded plane in Figure 2.5 (b)).

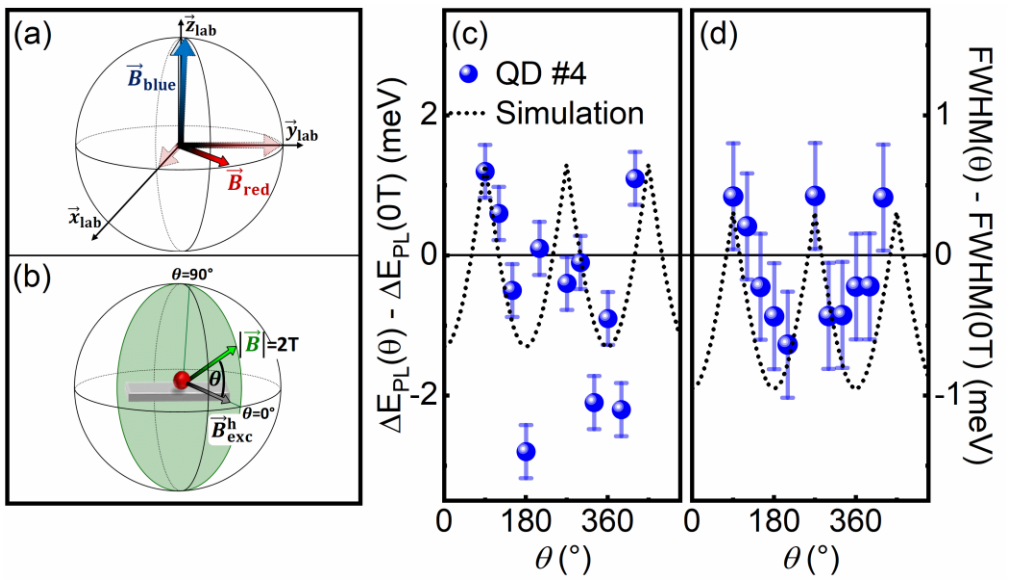

Figure 2.5 Photoluminescence maxima as a function of the angle of the applied magnetic field. (a) Illustration of the rotating magnetic field experiment on QD #4. The QD ZPL energy shows a maximum blue shift with respect to $|\vec{B}|$ = 0 T when applying a magnetic field $\vec{B}$ close to the [x = 0,y = 0, z = 1] direction in lab coordinates. Rotating the magnetic field perpendicular to [0,0,1] leads to a red shift of the ZPL energy with respect to $|\vec{B}|$ = 0 T, which is maximized for the [1,1,0] direction. (b) Schematic of the angle dependent magneto PL measurement on a single anisotropic QD (red dot). The previously found directions of maximum red ([1,1,0]) and blue shift ([0,0,1]) are used to span the plane (green shaded) in which the magnetic field with $|\vec{B}|$ = 2 T is rotated. The rotation is characterized by the angle θ between $\vec{B}$ and the [1,1,0] direction. (c) ZPL energy shift and (d) change of FWHM of QD #4 with respect to $|\vec{B}|$ = 0 T when rotating $\vec{B}(\theta)$ in the plane spanned by the lab [1,1,0] and [0,0,1] directions. $|\vec{B}|$ = 2 T and T = 4 K are kept constant during the experiment. Dotted black lines show simulations using eqs. (2.9) and (2.10) with x_{Mn} = 2%, V_{eff} = 58 nm^3 and ΔT_s = 0 K.

Figures 2.5 (c) and (d) show the evolution of the ZPL shift $\Delta E_{PL}(\theta)$ and the change in linewidth $\Delta FWHM(\theta)$ with respect to $|\vec{B}|$ = 0 T as the magnetic field is rotated. Starting from θ = 90°, the energy shift $\Delta E_{PL}(\theta)$ follows the progression blue – red – blue with rising θ with a periodicity of $\Delta\theta$ = 180°. With the same periodicity, the change in FWHM evolves from a broadening to a narrowing to a broadening and so forth. We interpret these findings as an angle

dependent stabilization and destabilization of EMP formation. Hereby, the stabilization, *i.e.* an enhancement of the EMP binding energy and a suppression of the magnetic fluctuations, is maximized if the magnetic field is coaxial with the anisotropy axis (θ = 0° or 180°). A destabilization, *i.e.* a reduced EMP binding energy and an enhanced fluctuation broadening, occurs if the magnetic field and anisotropy axes are perpendicular. Interestingly, the 180° periodicity implies an abrupt reorientation of the direction of the hole exchange field by 180°, and thus a change in EMP formation direction, as soon as the projection of $\vec{B}$ on the anisotropy axis changes its sign, *i.e.* at θ = 90° and 270°.

To model this behavior we use eq. (2.9) and a generalized version of eq. (2.6), including the influence of transverse and longitudinal magnetization fluctuations with respect to the exchange field:[61]

$$FWHM_{\mathrm{fluct}}(\vec{B},T) = \sqrt{8\ln(2)}\sqrt{V_{\mathrm{eff}}\left[\left(\left|\vec{B}_{\mathrm{exc}}^{\mathrm{el}}\right| + \left|\vec{B}_{\mathrm{exc}}^{\mathrm{h}}\right|\cos(\phi)\right)^2\langle\delta M_{\parallel}^2\rangle + \left(\left|\vec{B}_{\mathrm{exc}}^{\mathrm{h}}\right|\sin(\phi)\right)^2\langle\delta M_{\perp}^2\rangle\right]} \tag{2.10}$$

The longitudinal and transverse fluctuations of the magnetization are given by:[61]

$$\langle\delta M_{\parallel}^2\rangle = \left|\frac{dM_{\mathrm{Mn},\parallel}(\vec{B},T)}{dB_{\parallel}}\right|_{\vec{B}_{\Sigma}} \cdot k_{\mathrm{B}}T_{\mathrm{s}} = \left|\frac{dM_{\mathrm{Mn}}(B,T)}{dB}\right|_{|\vec{B}_{\Sigma}|} \cdot k_{\mathrm{B}}T_{\mathrm{s}}$$

$$\langle\delta M_{\perp}^2\rangle = \left|\frac{dM_{\mathrm{Mn},\perp}(\vec{B},T)}{dB_{\perp}}\right|_{\vec{B}_{\Sigma}} \cdot k_{\mathrm{B}}T_{\mathrm{s}} = \frac{|\vec{M}_{\mathrm{Mn}}(\vec{B})|}{|\vec{B}_{\Sigma}|} \cdot k_{\mathrm{B}}T_{\mathrm{s}} \tag{2.11}$$

Figures 2.5 (c) and (d) exhibit the simulations of $\Delta E_{\mathrm{PL}}(\theta)$ and $\Delta FWHM(\theta)$ for QD #4 as dotted lines using x_{Mn} = 2%, ΔT_{s} = 0 K, V_{eff} = 58 nm^3 (corresponding to an effective spherical exciton diameter of 4.8 nm and $|\vec{B}_{\mathrm{exc}}|$ = 6.3 T at $\vec{B}$ = 0 T). Note that at θ = 90° and 270° this corresponds to a maximum angle of ϕ = 20° between $\vec{M}$ and $\vec{B}_{\mathrm{exc}}^{\mathrm{h}}$. The simulations show good qualitative agreement with the experimental data and reproduce well the trend of switching between EMP stabilization and EMP destabilization *via* the angle of the external magnetic field with respect to the anisotropy axis of the QD. Apparently, EMP formation can be directed by a magnetic field much smaller than the exchange field.

The conclusion from this analysis of an anisotropy axis constraining the direction of the hole wavefunction is consistent with previous work[81,82], where *e.g.* in undoped CdSe QDs,

magnetic fields up to 60 T were found to be insufficient to reach a PL polarization degree higher than 75%.[81] The results presented here unambiguously prove the existence of an anisotropy axis in our doped colloidal QDs, and they highlight the major importance of this anisotropy for EMP formation. Such anisotropy has been invoked to explain EMP formation-reorientation dynamics[31] and the finite maximum PL polarization[32] of colloidal magnetically doped QDs, but has never previously been identified experimentally. The most prominent sources of such an anisotropy are the one introduced by the wurtzite crystal lattice with an energy splitting $\Delta_{\mathrm{int}} \approx 24$ meV[83] and the shape anisotropy due to distortions of the spherical QD shape with an energy splitting Δ_{sh}. While the former is a uniaxial anisotropy, the latter may include more than one symmetry axes, and is dependent on the magnitude of the distortion (i.e. the ellipticity in the case of a uniaxial distortion) and the QD size. In our case, the Mn^{2+}:CdSe cores are only slightly ellipsoidal (see Appendix A Figure A1), so that we expect $\Delta_{\mathrm{int}} > \Delta_{\mathrm{sh}}$ for the investigated QDs with core diameter of 5.9 nm.[83] Additionally, the magnetic field dependent PL energy shift shown in Figure 2.5 hints towards a periodicity of $\Delta\theta = 180°$, i.e. a uniaxial symmetry rather than a triangular ($\Delta\theta = 120°$) or multi axial symmetry. Although we cannot reliably identify the main source of the anisotropy, we therefore hypothesize the crystal asymmetry of the wurtzite lattice to be the main source for constraining the direction of the hole wavefunction.

2.4 Conclusion

In summary, temperature and magnetic field dependent confocal PL spectroscopy was used to unravel the formation of EMPs in single colloidal QDs for the first time. The absence of a statistical variation of size, shape and crystal orientation - typical in an ensemble of nanocrystals – provides unique insights into the role of anisotropy in EMP formation and magnetic fluctuations. The single QD PL linewidth is strongly influenced by fluctuations of the Mn^{2+} spin ensemble, leading to an unusually steep increase of the FWHM with temperature. Detailed modeling of the temperature dependent ZPL energy shifts and the corresponding linewidth broadening allows extraction of key parameters including V_{eff}, x_{Mn}, and spin heating ΔT_{s} for single QDs. Experiments in a 3D vector magnetic field reveal both stabilization and destabilization of the EMP that are unique for each single QD, and that are reflected by a corresponding change in energy and FWHM of the ZPL depending on the direction of the applied magnetic field. QD anisotropy was identified as the source of this behavior, constraining the direction of the hole exchange field within the QD and consequently directing the orientation of EMP formation. Our findings not only demonstrate

the fundamental impact of anisotropy on the physical properties of doped colloidal nanocrystals, but in addition indicate a promising pathway to control the directionality of optically generated magnetism in colloidal nanocrystals.

2.5 Methods

µ-PL spectra were recorded using a confocal microscopy setup (Attocube attoCFM I, microscope LT-APO-Vis, NA: 0.82), inserted into a closed cycle cryostat (T_{sample} = 4.0 K) with the option to apply magnetic fields up to 5 T in Faraday geometry or, alternatively, up to 2 T in any arbitrary direction. The sample is surrounded by He exchange gas, ensuring the thermal coupling between the QDs and the environment. Optical excitation was conducted with a 532 nm solid-state laser (Laserglow LRS-0532 DPSS) in combination with a laser clean up filter (Thorlabs FLH532-10) and an ultra-steep long-pass edge filter (Razor Edge 532-RU), using excitation power densities of less than 10 W / cm^{-2}. Spectra were recorded using a liquid nitrogen-cooled charge coupled device (CCD) camera (Horiba Symphony II, back illuminated deep depletion 1-LS) in combination with monochromator setup (Horiba Triax 550), equipped with a 600 mm^{-1} grating. Integration time for all measurements was held constant at 300 s.

2.6 References

1. Kovalenko, M. V.; Manna, L.; Cabot, A.; Hens, Z.; Talapin, D. V.; Kagan, C. R.; Klimov, V. I.; Rogach, A. L.; Reiss, P.; Milliron, D. J.; et al. Prospects of Nanoscience with Nanocrystals. *ACS Nano* **2015**, *9*, 1012–1057.
2. Pietryga, J. M.; Park, Y.-S.; Lim, J.; Fidler, A. F.; Bae, W. K.; Brovelli, S.; Klimov, V. I. Spectroscopic and Device Aspects of Nanocrystal Quantum Dots. *Chem. Rev.* **2016**, *116*, 10513–10622.
3. Erwin, S. C.; Zu, L.; Haftel, M. I.; Efros, A. L.; Kennedy, T. A; Norris, D. J. Doping Semiconductor Nanocrystals. *Nature* **2005**, *436*, 91–94.
4. Norris, D. J.; Efros, A. L.; Erwin, S. C. Doped Nanocrystals. *Science* **2008**, *319*, 1776–1779.
5. Beaulac, R.; Ochsenbein, S. T.; Gamelin, D. R. Colloidal Transition-Metal-Doped Quantum Dots. In *Nanocrystal Quantum Dots*; Klimov, V. I., Ed.; CRC Press: Boca Raton, FL, 2010; pp 397–453.
6. Vlaskin, V. A.; Barrows, C. J.; Erickson, C. S.; Gamelin, D. R. Nanocrystal Diffusion Doping. *J. Am. Chem. Soc.* **2013**, *135*, 14380–14389.
7. Suyver, J. F.; Wuister, S. F.; Kelly, J. J.; Meijerink, A. Luminescence of Nanocrystalline ZnSe:Mn^{2+}. *Phys. Chem. Chem. Phys.* **2000**, *2*, 5445–5448.
8. Beaulac, R.; Archer, P. I.; Gamelin, D. R. Luminescence in Colloidal Mn^{2+}-Doped Semiconductor Nanocrystals. *J. Solid State Chem.* **2008**, *181*, 1582–1589.
9. Karan, N. S.; Sarma, D. D.; Kadam, R. M.; Pradhan, N. Doping Transition Metal (Mn or Cu) Ions in Semiconductor Nanocrystals. *J. Phys. Chem. Lett.* **2010**, *1*, 2863–2866.
10. Erickson, C. S.; Bradshaw, L. R.; McDowall, S.; Gilbertson, J. D.; Gamelin, D. R.; Patrick, D. L. Zero-Reabsorption Doped-Nanocrystal Luminescent Solar Concentrators. *ACS Nano* **2014**, *8*, 3461–3467.
11. Knowles, K. E.; Nelson, H. D.; Kilburn, T. B.; Gamelin, D. R. Singlet–Triplet Splittings in the Luminescent Excited States of Colloidal Cu^+:CdSe, Cu^+:InP, and $CuInS_2$ Nanocrystals: Charge-Transfer Configurations and Self-Trapped Excitons. *J. Am. Chem. Soc.* **2015**, *137*, 13138–13147.
12. Parobek, D.; Roman, B. J.; Dong, Y.; Jin, H.; Lee, E.; Sheldon, M.; Son, D. H. Exciton-to-Dopant Energy Transfer in Mn-Doped Cesium Lead Halide Perovskite Nanocrystals. *Nano Lett.* **2016**, *16*, 7376–7380.
13. Pu, C.; Ma, J.; Qin, H.; Yan, M.; Fu, T.; Niu, Y.; Yang, X.; Huang, Y.; Zhao, F.; Peng, X. Doped Semiconductor-Nanocrystal Emitters with Optimal Photoluminescence Decay Dynamics in Microsecond to Millisecond Range: Synthesis and Applications. *ACS Cent. Sci.* **2016**, *2*, 32–39.
14. Liu, W.; Lin, Q.; Li, H.; Wu, K.; Robel, I.; Pietryga, J. M.; Klimov, V. I. Mn^{2+}-Doped Lead Halide Perovskite Nanocrystals with Dual-Color Emission Controlled by Halide Content. *J. Am. Chem. Soc.* **2016**, *138*, 14954–14961.
15. Sharma, M.; Gungor, K.; Yeltik, A.; Olutas, M.; Guzelturk, B.; Kelestemur, Y.; Erdem, T.; Delikanli, S.; McBride, J. R.; Demir, H. V. Near-Unity Emitting Copper-Doped Colloidal Semiconductor Quantum Wells for Luminescent Solar Concentrators. *Adv. Mater.* **2017**, *29*, 1700821.
16. Nelson, H. D.; Hinterding, S. O. M.; Fainblat, R.; Creutz, S. E.; Li, X.; Gamelin, D. R. Mid-Gap States and Normal vs Inverted Bonding in Luminescent Cu^+- and Ag^+-Doped CdSe Nanocrystals. *J. Am. Chem. Soc.* **2017**, *139*, 6411–6421.

17. Norris, D. J.; Yao, N.; Charnock, F. T.; Kennedy, T. A. High-Quality Manganese-Doped ZnSe Nanocrystals. *Nano Lett.* **2001**, *1*, 3–7.
18. Beaulac, R.; Archer, P. I.; Ochsenbein, S. T.; Gamelin, D. R. Mn^{2+}-Doped CdSe Quantum Dots: New Inorganic Materials for Spin-Electronics and Spin-Photonics. *Adv. Funct. Mater.* **2008**, *18*, 3873–3891.
19. Bussian, D. A.; Crooker, S. A.; Yin, M.; Brynda, M.; Efros, A. L.; Klimov, V. I. Tunable Magnetic Exchange Interactions in Manganese-Doped Inverted Core–Shell ZnSe–CdSe Nanocrystals. *Nat. Mater.* **2009**, *8*, 35–40.
20. Barrows, C. J.; Vlaskin, V. A.; Gamelin, D. R. Absorption and Magnetic Circular Dichroism Analyses of "Giant" Zeeman Splittings in Diffusion-Doped Colloidal $Cd_{1-x}Mn_xSe$ Quantum Dots. *J. Phys. Chem. Lett.* **2015**, *6*, 3076–3081.
21. Yang, J.; Fainblat, R.; Kwon, S. G.; Muckel, F.; Yu, J. H.; Terlinden, H.; Kim, B. H.; Iavarone, D.; Choi, M. K.; Kim, I. Y.; et al. Route to the Smallest Doped Semiconductor: Mn^{2+}-Doped $(CdSe)_{13}$ Clusters. *J. Am. Chem. Soc.* **2015**, *137*, 12776–12779.
22. Delikanli, S.; Akgul, M. Z.; Murphy, J. R.; Barman, B.; Tsai, Y.; Scrace, T.; Zhang, P.; Bozok, B.; Hernández-Martínez, P. L.; Christodoulides, J.; et al. Mn^{2+}-Doped CdSe/CdS Core/Multishell Colloidal Quantum Wells Enabling Tunable Carrier–Dopant Exchange Interactions. *ACS Nano* **2015**, *9*, 12473–12479.
23. Yang, J.; Muckel, F.; Baek, W.; Fainblat, R.; Chang, H.; Bacher, G.; Hyeon, T. Chemical Synthesis, Doping, and Transformation of Magic-Sized Semiconductor Alloy Nanoclusters. *J. Am. Chem. Soc.* **2017**, *139*, 6761–6770.
24. Yang, J.; Muckel, F.; Choi, B. K.; Lorenz, S.; Kim, I. Y.; Ackermann, J.; Chang, H.; Czerney, T.; Kale, V. S.; Hwang, S. J.; et al. Co^{2+}-Doping of Magic-Sized CdSe Clusters: Structural Insights via Ligand Field Transitions. *Nano Lett.* **2018**, *18*, 7350–7357.
25. Muckel, F.; Delikanli, S.; Hernández-Martínez, P. L.; Priesner, T.; Lorenz, S.; Ackermann, J.; Sharma, M.; Demir, H. V.; Bacher, G. Sp–d Exchange Interactions in Wave Function Engineered Colloidal CdSe/Mn:CdS Hetero-Nanoplatelets. *Nano Lett.* **2018**, *18*, 2047–2053.
26. Furdyna, J. K. Diluted Magnetic Semiconductors. *J. Appl. Phys.* **1988**, *64*, R29–R64.
27. Gaj, J. A. Semiconductors and Semimetals. In *Semiconductors and Semimetals*; Furdyna, J.K., Kossut, J., Ed.; Academic Press, Inc.: San Diego, 1972; Vol. 25, pp xi–xiii.
28. Hoffman, D. M.; Meyer, B. K.; Ekimov, A. I.; Merkulov, I. A.; Efros, A. L.; Rosen, M.; Couino, G.; Gacoin, T.; Boilot, J. P. Giant Internal Magnetic Fields in Mn Doped Nanocrystal Quantum Dots. *Solid State Commun.* **2000**, *114*, 547–550.
29. Fainblat, R.; Frohleiks, J.; Muckel, F.; Yu, J. H.; Yang, J.; Hyeon, T.; Bacher, G. Quantum Confinement-Controlled Exchange Coupling in Manganese(II)-Doped CdSe Two-Dimensional Quantum Well Nanoribbons. *Nano Lett.* **2012**, *12*, 5311–5317.
30. Muckel, F.; Yang, J.; Lorenz, S.; Baek, W.; Chang, H.; Hyeon, T.; Bacher, G.; Fainblat, R. Digital Doping in Magic-Sized CdSe Clusters. *ACS Nano* **2016**, *10*, 7135–7141.
31. Beaulac, R.; Schneider, L.; Archer, P. I.; Bacher, G.; Gamelin, D. R. Light-Induced Spontaneous Magnetization in Doped Colloidal Quantum Dots. *Science* **2009**, *325*, 973–976.
32. Nelson, H. D.; Bradshaw, L. R.; Barrows, C. J.; Vlaskin, V. A.; Gamelin, D. R. Picosecond Dynamics of Excitonic Magnetic Polarons in Colloidal Diffusion-Doped $Cd_{1-x}Mn_xSe$ Quantum Dots. *ACS Nano* **2015**, *9*, 11177–11191.
33. Rice, W. D.; Liu, W.; Baker, T. A.; Sinitsyn, N. A.; Klimov, V. I.; Crooker, S. A. Revealing

Giant Internal Magnetic Fields Due to Spin Fluctuations in Magnetically Doped Colloidal Nanocrystals. *Nat. Nanotechnol.* **2016**, *11*, 137–142.
34. Rice, W. D.; Liu, W.; Pinchetti, V.; Yakovlev, D. R.; Klimov, V. I.; Crooker, S. A. Direct Measurements of Magnetic Polarons in $Cd_{1-x}Mn_xSe$ Nanocrystals from Resonant Photoluminescence. *Nano Lett.* **2017**, *17*, 3068–3075.
35. Muckel, F.; Barrows, C. J.; Graf, A.; Schmitz, A.; Erickson, C. S.; Gamelin, D. R.; Bacher, G. Current-Induced Magnetic Polarons in a Colloidal Quantum-Dot Device. *Nano Lett.* **2017**, *17*, 4768–4773.
36. Bhattacharjee, A. K. Crystal-Field Model for Acceptor-Associated Bound Magnetic Polarons in Wurtzite Semiconductors. *Phys. Rev. B* **1987**, *35*, 9108–9111.
37. Peng, B.; May, J. W.; Gamelin, D. R.; Li, X. Effects of Crystallographic and Shape Anisotropies on Dopant-Carrier Exchange Interactions in Magnetic Semiconductor Quantum Dots. *J. Phys. Chem. C* **2014**, *118*, 7630–7636.
38. Hazarika, A.; Layek, A.; De, S.; Nag, A.; Debnath, S.; Mahadevan, P.; Chowdhury, A.; Sarma, D. D. Ultranarrow and Widely Tunable Mn^{2+}-Induced Photoluminescence from Single Mn-Doped Nanocrystals of ZnS-CdS Alloys. *Phys. Rev. Lett.* **2013**, *110*, 267401.
39. Ishizumi, A.; Kanemitsu, Y. Blinking Behavior of Surface-Defect and Impurity Luminescence in Nondoped and Mn^{2+}-Doped CdS Nanocrystals. *J. Phys. Soc. Japan* **2009**, *78*, 83705.
40. Zhang, Y.; Gan, C.; Muhammad, J.; Battaglia, D.; Peng, X.; Xiao, M. Enhanced Fluorescence Intermittency in Mn-Doped Single ZnSe Quantum Dots. *J. Phys. Chem. C* **2008**, *112*, 20200–20205.
41. Whitham, P. J.; Knowles, K. E.; Reid, P. J.; Gamelin, D. R. Photoluminescence Blinking and Reversible Electron Trapping in Copper-Doped CdSe Nanocrystals. *Nano Lett.* **2015**, *15*, 4045–4051.
42. Fainblat, R.; Barrows, C. J.; Hopmann, E.; Siebeneicher, S.; Vlaskin, V. A.; Gamelin, D. R.; Bacher, G. Giant Excitonic Exchange Splittings at Zero Field in Single Colloidal CdSe Quantum Dots Doped with Individual Mn^{2+} Impurities. *Nano Lett.* **2016**, *16*, 6371–6377.
43. Nirmal, M.; Dabbousi, B. O.; Bawendi, M. G.; Macklin, J. J.; Trautman, J. K.; Harris, T. D.; Brus, L. E. Fluorescence Intermittency in Single Cadmium Selenide Nanocrystals. *Nature* **1996**, *383*, 802–804.
44. Chen, Y.; Vela, J.; Htoon, H.; Casson, J. L.; Werder, D. J.; Bussian, D. A.; Klimov, V. I.; Hollingsworth, J. A. "Giant" Multishell CdSe Nanocrystal Quantum Dots with Suppressed Blinking. *J. Am. Chem. Soc.* **2008**, *130*, 5026–5027.
45. Schlegel, G.; Bohnenberger, J.; Potapova, I.; Mews, A. Fluorescence Decay Time of Single Semiconductor Nanocrystals. *Phys. Rev. Lett.* **2002**, *88*, 137401.
46. Neuhauser, R. G.; Shimizu, K. T.; Woo, W. K.; Empedocles, S. A.; Bawendi, M. G. Correlation between Fluorescence Intermittency and Spectral Diffusion. *Phys. Rev. Lett.* **2000**, *85*, 3301–3304.
47. Efros, A. L.; Nesbitt, D. J. Origin and Control of Blinking in Quantum Dots. *Nat. Nanotechnol.* **2016**, *11*, 661–671.
48. Empedocles, S. A. Quantum-Confined Stark Effect in Single CdSe Nanocrystallite Quantum Dots. *Science* **1997**, *278*, 2114–2117.
49. Fernée, M. J.; Sinito, C.; Tamarat, P.; Lounis, B. State Selective Pumping Reveals Spin-Relaxation Pathways in CdSe Quantum Dots. *Nano Lett.* **2014**, *14*, 4480–4485.
50. Sinito, C.; Fernée, M. J.; Goupalov, S. V.; Mulvaney, P.; Tamarat, P.; Lounis, B. Tailoring

the Exciton Fine Structure of Cadmium Selenide Nanocrystals with Shape Anisotropy and Magnetic Field. *ACS Nano* **2014**, *8*, 11651–11656.
51. Osovsky, R.; Cheskis, D.; Kloper, V.; Sashchiuk, A.; Kroner, M.; Lifshitz, E. Continuous-Wave Pumping of Multiexciton Bands in the Photoluminescence Spectrum of a Single CdTe-CdSe Core-Shell Colloidal Quantum Dot. *Phys. Rev. Lett.* **2009**, *102*, 197401.
52. Shulenberger, K. E.; Bischof, T. S.; Caram, J. R.; Utzat, H.; Coropceanu, I.; Nienhaus, L.; Bawendi, M. G. Multiexciton Lifetimes Reveal Triexciton Emission Pathway in CdSe Nanocrystals. *Nano Lett.* **2018**, *18*, 5153–5158.
53. Besombes, L.; Léger, Y.; Maingault, L.; Ferrand, D.; Mariette, H.; Cibert, J. Probing the Spin State of a Single Magnetic Ion in an Individual Quantum Dot. *Phys. Rev. Lett.* **2004**, *93*, 207403.
54. Léger, Y.; Besombes, L.; Maingault, L.; Mariette, H. Valence-Band Mixing in Neutral, Charged, and Mn-Doped Self-Assembled Quantum Dots. *Phys. Rev. B* **2007**, *76*, 045331.
55. Kobak, J.; Smoleński, T.; Goryca, M.; Papaj, M.; Gietka, K.; Bogucki, A.; Koperski, M.; Rousset, J. G.; Suffczyński, J.; Janik, E.; et al. Designing Quantum Dots for Solotronics. *Nat. Commun.* **2014**, *5*, 3191.
56. Smoleński, T.; Kazimierczuk, T.; Kobak, J.; Goryca, M.; Golnik, A.; Kossacki, P.; Pacuski, W. Magnetic Ground State of an Individual Fe^{2+} Ion in Strained Semiconductor Nanostructure. *Nat. Commun.* **2016**, *7*, 10484.
57. Maksimov, A. A.; Bacher, G.; McDonald, A.; Kulakovskii, V. D.; Forchel, A.; Becker, C. R.; Landwehr, G.; Molenkamp, L. W. Magnetic Polarons in a Single Diluted Magnetic Semiconductor Quantum Dot. *Phys. Rev. B* **2000**, *62*, R7767–R7770.
58. Bacher, G.; Schömig, H.; Scheibner, M.; Forchel, A.; Maksimov, A. A.; Chernenko, A. V.; Dorozhkin, P. S.; Kulakovskii, V. D.; Kennedy, T.; Reinecke, T. L. Spin–Spin Interaction in Magnetic Semiconductor Quantum Dots. *Phys. E Low-dimensional Syst. Nanostructures* **2005**, *26*, 37–44.
59. Kłopotowski, Ł.; Cywiński, Ł.; Wojnar, P.; Voliotis, V.; Fronc, K.; Kazimierczuk, T.; Golnik, A.; Ravaro, M.; Grousson, R.; Karczewski, G.; et al. Magnetic Polaron Formation and Exciton Spin Relaxation in Single $Cd_{1-x}Mn_xTe$ Quantum Dots. *Phys. Rev. B* **2011**, *83*, 081306.
60. Kłopotowski, L.; Cywiński, L.; Szymura, M.; Voliotis, V.; Grousson, R.; Wojnar, P.; Fronc, K.; Kazimierczuk, T.; Golnik, A.; Karczewski, G.; et al. Influence of Exciton Spin Relaxation on the Photoluminescence Spectra of Semimagnetic Quantum Dots. *Phys. Rev. B - Condens. Matter Mater. Phys.* **2013**, *87*, 1–12.
61. Dorozhkin, P. S.; Chernenko, A. V.; Kulakovskii, V. D.; Brichkin, A. S.; Maksimov, A. A.; Schoemig, H.; Bacher, G.; Forchel, A.; Lee, S.; Dobrowolska, M.; et al. Longitudinal and Transverse Fluctuations of Magnetization of the Excitonic Magnetic Polaron in a Semimagnetic Single Quantum Dot. *Phys. Rev. B* **2003**, *68*, 195313.
62. Dorozhkin, P. S.; Kulakovskii, V. D.; Chernenko, A. V.; Brichkin, A. S.; Ivanov, S. V.; Toropov, A. A. Controlling Magnetic Moment and Its Fluctuations in Individual Semimagnetic Quantum Dots with Different Exchange Interactions. *Appl. Phys. Lett.* **2005**, *86*, 062507.
63. Bacher, G.; Maksimov, A. A.; Schömig, H.; Kulakovskii, V. D.; Welsch, M. K.; Forchel, A.; Dorozhkin, P. S.; Chernenko, A. V.; Lee, S.; Dobrowolska, M.; et al. Monitoring Statistical Magnetic Fluctuations on the Nanometer Scale. *Phys. Rev. Lett.* **2002**, *89*, 1272011–1272014.

64. Mahler, B.; Spinicelli, P.; Buil, S.; Quelin, X.; Hermier, J.-P.; Dubertret, B. Toward Non-Blinking Quantum Dots: The Effect of Thick Shell. In *Colloidal Quantum Dots for Biomedical Applications IV*; Osinski, M., Jovin, T. M., Yamamoto, K., Eds.; International Society for Optics and Photonics, 2009; Vol. 7189, p 718903.
65. Empedocles, S. A.; Bawendi, M. G. Influence of Spectral Diffusion on the Line Shapes of Single CdSe Nanocrystallite Quantum Dots. *J. Phys. Chem. B* **1999**, *103*, 1826–1830.
66. Empedocles, S. A.; Norris, D. J.; Bawendi, M. G. Photoluminescence Spectroscopy of Single CdSe Nanocrystallite Quantum Dots. *Phys. Rev. Lett.* **1996**, *77*, 3873–3876.
67. Fernée, M. J.; Littleton, B. N.; Cooper, S.; Rubinsztein-Dunlop, H.; Gómez, D. E.; Mulvaney, P. Acoustic Phonon Contributions to the Emission Spectrum of Single CdSe Nanocrystals. *J. Phys. Chem. C* **2008**, *112*, 1878–1884.
68. Varshni, Y. P. Temperature Dependence of the Energy Gap in Semiconductors. *Physica* **1967**, *34*, 149–154.
69. Madelung, O. *Semiconductors: Data Handbook*, 3rd ed.; Springer: Berlin (U.A.), 2003.
70. Furdyna, J. K.; Kossut, K. Dilute Magnetic Semiconductors. In *Semiconductors and Semimetals*; Furdyna, J. K., Kossut, J., Ed.; Academic Press, Inc.: New York, 1988; Vol. 25.
71. O'Donnell, K. P.; Chen, X. Temperature Dependence of Semiconductor Band Gaps. *Appl. Phys. Lett.* **1991**, *58*, 2924–2926.
72. Hernandez-Calderon, I. Optical Properties and Electronic Structure of Wide Band Gap II-VI Semiconductors. In *II-VI Semiconductor Materials and Their Applications*; Tamargo, M. C., Ed.; Taylor and Francis: New York, 2002; pp 113–170.
73. Scott, R.; Prudnikau, A. V.; Antanovich, A.; Christodoulou, S.; Riedl, T.; Bertrand, G. H. V.; Owschimikow, N.; Lindner, J. K. N.; Hens, Z.; Moreels, I.; et al. A Comparative Study Demonstrates Strong Size Tunability of Carrier–Phonon Coupling in CdSe-Based 2D and 0D Nanocrystals. *Nanoscale* **2019**, *11*, 3958–3967.
74. Yakovlev, D. R.; Ossau, W. Magnetic Polarons. In *Introduction to the Physics of Diluted Magnetic Semiconductors*; Gaj, J. A., Kossut, J., Eds.; Springer Series in Materials Science; Springer Berlin Heidelberg: Berlin, Heidelberg, 2010; pp 221–262.
75. Heiman, D.; Shapira, Y.; Foner, S.; Khazai, B.; Kershaw, R.; Dwight, K.; Wold, A. Exchange Energy, Magnetization, and Raman Scattering of (Cd,Mn)Se. *Phys. Rev. B* **1984**, *29*, 5634–5640.
76. Rudin, S.; Reinecke, T. L.; Segall, B. Temperature-Dependent Exciton Linewidths in Semiconductor Quantum Wells. *Phys. Rev. B* **1990**, *41*, 3017–3027.
77. Al Salman, A.; Tortschanoff, A.; Mohamed, M. B.; Tonti, D.; van Mourik, F.; Chergui, M. Temperature Effects on the Spectral Properties of Colloidal CdSe Nanodots, Nanorods, and Tetrapods. *Appl. Phys. Lett.* **2007**, *90*, 093104.
78. Landau, L.; Lifshitz, E. M. *Statistical Physics*; Pergamon: New York, 1983.
79. Hundt, A.; Puls, J.; Henneberger, F. Spin Properties of Self-Organized Diluted Magnetic $Cd_{1-x}Mn_xSe$ Quantum Dots. *Phys. Rev. B* **2004**, *69*, 121309.
80. Henneberger, F.; Puls, J. Diluted Magnetic Quantum Dots. In *Introduction to the Physics of Diluted Magnetic Semiconductors*; Kossut, K., Gaj, J. A., Eds.; Springer: Heidelberg, 2010.
81. Johnston-Halperin, E.; Awschalom, D. D.; Crooker, S. A.; Efros, A. L.; Rosen, M.; Peng, X.; Alivisatos, A. P. Spin Spectroscopy of Dark Excitons in CdSe Quantum Dots to 60 T. *Phys. Rev. B* **2001**, *63*, 205309.

82. Furis, M.; Hollingsworth, J. A.; Klimov, V. I.; Crooker, S. A. Time- and Polarization-Resolved Optical Spectroscopy of Colloidal CdSe Nanocrystal Quantum Dots in High Magnetic Fields. *J. Phys. Chem. B* **2005**, *109*, 15332–15338.
83. Efros, A.; Rosen, M.; Kuno, M.; Nirmal, M.; Norris, D.; Bawendi, M. Band-Edge Exciton in Quantum Dots of Semiconductors with a Degenerate Valence Band: Dark and Bright Exciton States. *Phys. Rev. B* **1996**, *54*, 4843–4856.

Chapter 3: Orientation of Individual Anisotropic Nanocrystals Identified by Polarization Fingerprint

Reproduced with permission from Lorenz, S.; Bieniek, J.; Erickson, C. S.; Gamelin, D. R.; Fainblat, R.; Bacher, G.; *ACS Nano* **2021**, *Submitted*.

3.1 Overview

The polarization of photoluminescence emitted from anisotropic nanocrystals directly reflects the symmetry of the eigenstates involved in the recombination process and can thus be considered as a specific fingerprint of a nanocrystal. We performed polarization resolved magneto-photoluminescence spectroscopy on single colloidal Mn^{2+}:CdSe/CdS core shell quantum dots of wurtzite crystal symmetry. At zero magnetic field, a distinct linear polarization pattern is observed while applying a magnetic field enforces circularly polarized emission with a characteristic saturation value below 100%. These polarization features are shown to act as a specific fingerprint of each individual nanocrystal. A model considering the orientation of the crystal $\vec{c}$ axis with respect to the optical axis and the magnetic field and taking into account the impact of magnetic doping is introduced and quantitatively explains our findings. We demonstrate that a careful analysis of the polarization state of single nanocrystal emission using the full set of Stokes parameters allows for identification of the complete 3D orientation of the crystal anisotropy axis of an individual nanoobject in lab coordinates.

3.2 Introduction

The information carried by the polarization state of light is harnessed in a wide variety of applications, ranging from emerging modern technologies such as quantum information technology[1–6] or spintronics[7–9] to material characterization of organic[10,11] or inorganic matter.[12] A particularly intriguing aspect is the use in optical spectroscopy of nanoscale materials, such as 2D transition-metal dichalcogenides,[13–15] 1D nanowires[16] and 0D quantum dots (QDs),[17–19] because the polarization encodes the fingerprint of the electronic eigenstate symmetry.[20] A prominent example is the emergence of linearly polarized photoluminescence (PL), e.g. induced by a break of rotational symmetry in colloidal QDs (cQDs),[21] by strong shape anisotropies in quantum rods[22] or by the crystal structure in lead halide perovskites.[23,24] Circularly polarized PL, on the other hand,

is widely used to access the magnetic-field-dependent state splitting in undoped,[23,25–32] as well as in doped QDs.[33–40] This state splitting is evidenced by a spectral shift of the right circularly polarized (σ^+) and the left circularly polarized (σ^-) PL and causes an increase of the degree of circular polarization with magnetic field because of the resulting state occupation. Thus, circularly polarized PL is considered as a particularly effective tool for probing magnetic-field-dependent changes of the eigenstate symmetry.[41]

In undoped cQDs, however, large magnetic fields are typically necessary to reach polarization saturation even at low temperatures because of the small g-factors. Magnetically doped cQDs like Mn^{2+}:CdSe cQDs, in contrast, exhibit huge effective g-factors[42–44] due to the *sp-d* exchange interactions between the delocalized charge carriers of the host material (*s*-type electrons and *p*-type holes) and the localized magnetic moments of the dopants' *d* electrons. These exchange interactions lead to giant magneto-optical responses[42,45] and strong circularly polarized emission even at small magnetic fields,[46] opening a pathway to giant Zeeman splittings up to room temperature.[43,47,48] In case of a careful adjustment of the bandgap with respect to the internal $^4T_1 - {}^6A_1$ Mn^{2+} transition,[49] such materials can exhibit the formation of a spontaneous collective magnetization of the dopant magnetic moments in the presence of an electron-hole pair, mediated by the exchange field between the dopant magnetic moments and the host charge carriers. This so called exciton magnetic polaron (EMP) formation has been observed in a variety of DMS systems, ranging from quantum wells[50–53] and self-assembled QDs[54,55] to cQDs.[35,56–58] While it is commonly agreed that the exchange field is strong enough to drive the Mn^{2+} magnetization close to saturation at cryogenic temperatures, magnetic fluctuations inhibit the saturation of the degree of circular polarization at small magnetic fields.[35,58]

Saturation values of the degree of circular polarization of 100% are usually found for epitaxially grown samples exhibiting EMP formation such as quantum wells[50–53] and self-assembled QDs.[54,55] Surprisingly, for colloidal nanostructures, such as nanoplatelets[36,38,59] and cQDs with wurtzite crystal structure, saturation values below 100% are consistently found.[35,57] Similarly, saturation values of the degree of circular polarization below 100% have been observed in undoped CdSe cQDs,[60–62] and were attributed to the anisotropy of the cQDs induced by the wurtzite $\vec{c}$ axis. Reports to date are restricted to ensemble investigations on colloidal nanostructures, which leads to an averaging of nanocrystal orientation, thus hiding polarization fingerprints of individual species.

Here we report on polarization resolved magneto–PL spectroscopy of single wurtzite Mn^{2+}:CdSe/CdS core/shell cQDs. We find a distinct linear polarization pattern at zero magnetic field typical for each nanocrystal and circularly polarized PL evolving in a magnetic field with a characteristic saturation of the degree of circular polarization below 100%. Model calculations evidence how the orientation of the crystal $\vec{c}$ axis plays a crucial role for the polarization emitted from each single cQD. We demonstrate the need to measure the full set of Stokes parameters for describing the complete polarization state of the single cQD PL and show how these parameters can be used to determine the 3D orientation of a single nanoobject in the fixed lab reference frame.

3.2 Results and Discussion

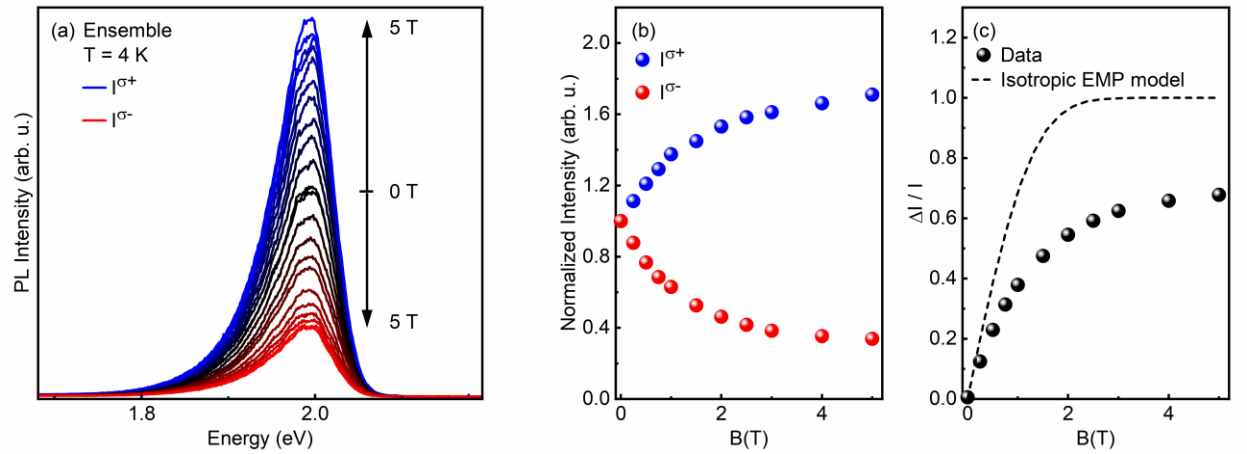

Figure 3. 1 Field dependent circularly polarized photoluminescence of an ensemble of EMP NCs collected at 4 K. (a) Magneto-photoluminescence spectra of $\boldsymbol{\sigma^+}$ (black to blue) and $\boldsymbol{\sigma^-}$ (black to red) polarized ensemble PL, collected at 4 K. (b) Integrated intensity of right circularly polarized emission ($\boldsymbol{I^{\sigma+}}$, blue) and left circularly polarized emission ($\boldsymbol{I^{\sigma-}}$, red) normalized to the corresponding value at $B = 0$ T, and (c) $\boldsymbol{\Delta I/I}$ as a function of the applied magnetic field. The dashed line shows the result for a simulation using a model of isotropic EMP formation.[35]

3.2.1 Ensemble of cQDs. 3% Mn^{2+}:CdSe/CdS cQDs were synthesized by diffusion doping methods detailed previously (see section B.1 of the Appendix B for general sample analysis).[35,43,44,58] Figure 3.1 (a) depicts the polarization resolved magneto-PL spectra of an ensemble of Mn^{2+}:CdSe/CdS cQDs dropcast onto a silicon substrate at $T = 4$ K. These cQDs exhibit strong EMP formation, as shown in Figure B.2 of Appendix B. Starting from $B = 0$ T, where the right circularly polarized (σ^+) and left circularly polarized (σ^-) PL intensities are

identical, $I^{\sigma+}$ (black to blue) continuously increases with B, while $I^{\sigma-}$ (black to red) decreases. Even at B = 5 T, however, $I^{\sigma-}$ does not vanish. Interestingly, we find no energy splitting between the σ^+ and σ^- components of the PL spectra in Figure 3.1 (a) within the resolution of the experiment. This observation is in pronounced contrast to the oppositely directed energy shift for σ^+ and σ^- polarized PL typically observed in epitaxially grown QDs, which is usually explained by two involved states of opposite spin orientation, leading to two Zeeman split branches.[46,51,63–65]

Plotting the integrated intensities normalized to B = 0 T (Figure 3.1 (b)) reveals a saturation of $I^{\sigma+}$ and $I^{\sigma-}$ at 170% and 30% of their starting values, respectively. Note that the sum of $I^{\sigma+}$ and $I^{\sigma-}$ is constant, hinting towards a magnetic field-induced redistribution of populations between two emissive states of different symmetry. From the integrated intensities we determine the degree of circular polarization, $\Delta I/I = (I^{\sigma+} - I^{\sigma-})/(I^{\sigma+} + I^{\sigma-})$, plotted in Figure 3.1 (c). For small magnetic field strengths (B < 1 T), $\Delta I/I$ (B) increases steeply, followed by a saturation behavior at about 70% for high magnetic fields. In literature, saturation values of 100% have been reported in DMSs with EMP formation such as quantum wells[50–53] or self-assembled QDs[54,55] and even in epitaxially grown DMS QDs in the absence of EMP formation.[46] On the other hand, finite saturation values between 50% and 80% have been published for colloidal DMS nanoplatelets,[36,38,59] as well as for wurtzite cQDs with EMP formation.[35,57] One similarity between all these systems is the presence of an axis of anisotropy, which is either introduced by the growth mechanism or by the crystal structure. A major difference, however, is the orientation of this axis of anisotropy: it is pre-defined by the growth mechanism in epitaxial quantum wells and self-assembled QDs but randomly oriented in ensembles of cQDs and colloidal nanoplatelets. Thus far, for colloidal DMS nanocrystals no conclusive explanation has been given for the saturation of $\Delta I/I < 100\,\%$. It has, however, been hypothesized,[35,57] that anisotropy effects, which are averaged due to the random orientation of the crystal $\vec{c}$, may play a role in determining $\Delta I/I$, similar to the case of undoped cQDs.[60–62]

3.2.2 Single cQDs. Acknowledging that the individual anisotropy axes, caused, e.g., by crystal and/or shape anisotropy, are oriented arbitrarily in an ensemble of cQDs, we conducted confocal polarization-resolved micro-PL spectroscopy on selected single Mn^{2+}:CdSe/CdS core/shell cQDs at 4 K. Figure 3.2 (a) plots the PL of a single cQD (cQD #1) in absence and presence of a magnetic field of 5 T. The spectra exhibit a dominant feature at 1.982 eV and a

weaker one, shifted by 26 meV to lower energies. These features are unambiguously assigned to the zero phonon line (ZPL) and its first phonon replica due to the simultaneous emission of a photon and a longitudinal optical phonon (1-LO).[66,67] The broad FWHM of about 8.5 meV is caused by magnetic fluctuations and has been discussed elsewhere.[58] The energetic position of the ZPL at 5 T shows a clear red shift of 7 meV with respect to its position at 0 T. Surprisingly, and in accordance with our observations in the ensemble PL, we find no spectral shift between the σ^+ and σ^- polarized PL components at 5 T (see Figure 3.2 (b)), although the ratio $I^{\sigma+} / I^{\sigma-} \sim 10$, i.e., the PL emission at 5 T is strongly circularly polarized.

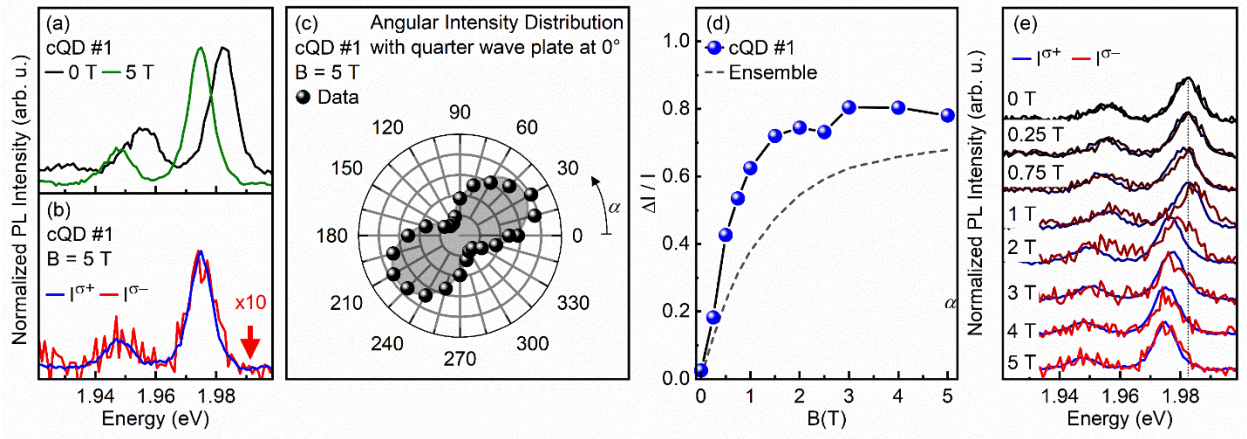

Figure 3.2 Magnetic field and polarization dependent photoluminescence of a single particle. PL of a single cQD at 4 K. (a) Normalized PL spectra (without polarization resolution) in the presence and absence of a magnetic field of 5 T. (b) Normalized PL spectra for $\boldsymbol{\sigma^+}$ and $\boldsymbol{\sigma^-}$ polarization at 5 T. (c) Integrated PL intensity $\boldsymbol{I(\alpha)}$ of cQD #1 using a quarter wave plate with its fast axis horizontal to the table (defined as angle $\boldsymbol{\alpha = 0°}$) and a rotatable linear polarizer with transmission axis at an angle $\boldsymbol{\alpha}$. Each radial tick equals an intensity step of 0.25. The shaded area serves as a guide to the eye. (d) $\boldsymbol{\Delta I / I(B)}$ for cQD #1 (symbols, line is a guide to the eye) compared to the ensemble data (dashed line). (e) Normalized magnetic field dependent spectra of $\boldsymbol{\sigma^+}$-polarized (black to blue) and $\boldsymbol{\sigma^-}$- polarized (black to red) PL of cQD #1. Spectra have been stacked along the y axis for clarity.

To verify the strong circular polarization, a combination of a quarter wave plate with its fast axis oriented horizontally relative to the table (defined as $\alpha = 0°$) and a rotatable analyzing linear polarizer was used. Figure 3.2 (c) plots the corresponding normalized angular dependence

$I(\alpha)$ of the integrated spectral intensity, where α is the angle of the analyzer transmission axis with respect to the table plane. In this configuration, the quarter wave plate converts σ^+ (σ^-) polarized light into linearly polarized light, detected at an angle of +45° (315°, i.e. -45°). $I(\alpha)$ exhibits the dumbbell-shaped profile expected for dominantly linearly polarized light and thus demonstrates the strong circularly polarized character of the PL before passing the quarter wave plate. Identifying $I^{\sigma+} = I(45°)$ and $I^{\sigma-} = I(135°)$, we find a value for the circular polarization degree of $\Delta I/I = 78$ % at 5 T. Figure 3.2 (d) compares $\Delta I/I\,(B)$ for cQD #1 and the ensemble. $\Delta I/I\,(B)$ rises much steeper for cQD #1 than for the ensemble and saturates at higher values. This result suggests that the slope and the saturation value are unique signatures of a cQD and its particular orientation on the substrate.

We emphasize that the lack of an energetic splitting between the σ^+ and σ^- polarized components of the PL (see Figure 3.2 (b)) is quite surprising. In fact, in self-assembled single DMS QDs both with and without EMP formation, a large energetic splitting between the σ^+ and σ^- ZPL have been observed. In the absence of EMP formation, the large energy splitting of 20 meV/T has been attributed to the giant Zeeman splitting induced by the magnetic field due to strong *sp-d* exchange interactions between the dopant *d* electrons and the host charge carriers.[46] In the case of EMP formation, the smaller energy splitting of 3 meV/T has been attributed to EMPs, formed either parallel or antiparallel to the magnetic field direction.[65] A similar energy splitting between $I^{\sigma+}$ and $I^{\sigma-}$ is observed below 2 T and even a slight blueshift of $I^{\sigma-}$ with B is obtained (see Figure 3.2 (e)), suggesting that in this regime the PL stems from the two EMP states as discussed above. For higher magnetic fields, the red shift observed for both, $I^{\sigma+}$ and $I^{\sigma-}$ with respect to B = 0 T is similar, although the intensity is quite different (see Figure 3.2 (b)). We therefore hypothesize that at high magnetic fields, σ^+ as well as σ^- components of the PL are actually emitted from one and the same EMP state (see Appendix B section B.4.5. for a detailed discussion). This is quite surprising as a magnetic field of 5 T is expected to lead to a complete depopulation of the upper Zeeman branch and the PL should be fully circular polarized.

To explain the unsual polarization properties of the PL in Mn^{2+}-doped single nanocrystals, it is therefore necessary to consider the state occupation due to the Zeeman splitting of the contributing states, the magnetic doping, and the crystal anisotropy. It is instructive to start by subsequently describing the magnetic-field-dependent state occupation for undoped cQDs, the

impact of magnetic doping and magnetic fluctuations, and the consequence of EMP formation on the polarization state of the emission in wurtzite cQDs.

3.2.3 Degree of polarization for undoped CdSe cQDs. For undoped CdSe cQDs the relevant optically active excitonic states for the PL emission are the ones dominated by their heavy hole (HH) $|\pm 3/2\rangle$ and electron $|\mp 1/2\rangle$ states. Here, the excitonic states are split in a magnetic field by the intrinsic Zeeman splitting $\Delta E_{\mathrm{Z,int}}$, which is on the order of 0.1 meV/T.[60] As the magnetic field increases, the energy splitting between the two spin split branches with opposite symmetry increases, leading to a change in state occupation. In case the spin flip rate between these states exceeds the recombination rate, the relative contributions of these states to the PL signal can be deduced assuming thermal equilibrium at the moment of exciton recombination, described by a Boltzmann distribution with $\Delta E_{\mathrm{Z,int}}$ as the energetic separation of the states. For undoped cQDs with wurtzite symmetry, the total angular momentum of the HH state is constrained parallel to the crystal $\vec{c}$ axis with opposite projections corresponding to the $|\pm 3/2\rangle$ states. As a consequence, the emitted light from excitons including these states have opposite helicity, depending on the angle θ between the crystal $\vec{c}$ axis and the direction of observation $\vec{k}$. The relative intensities of σ^+ and σ^- emitted light are then given by:[60–62]

$$I^{\sigma^\pm}_{|+3/2,-1/2\rangle} \propto (1 \pm \cos(\theta))^2 \tag{3.1a}$$

$$I^{\sigma^\pm}_{|-3/2,+1/2\rangle} \propto (1 \mp \cos(\theta))^2 \tag{3.1b}$$

where we imply recombination of holes in the $|\pm 3/2\rangle$ states with electrons in the $|\mp 1/2\rangle$ states. Combined with the occupation of the Zeeman split states due to the Boltzmann distribution, the ensemble average over all possible angles of crystal orientation with respect to the observation axis theoretically yields a saturation value of $\Delta I/I \sim 75\%$, which, depending on the cQD size and material, can only be reached at extremely high magnetic fields on the order of 50 T or higher.[60] It should be noted that here the direction of the charge carrier's angular momentum at the moment of radiative recombination is of fundamental importance for the PL polarization.

3.2.4 The case of magnetically doped cQDs. In magnetically doped cQDs exhibiting *sp-d* exchange, an analogous approach can be used by replacing the intrinsic Zeeman splitting with the giant Zeeman splitting, which can be written as $\Delta E_{\mathrm{sp-d}} = g_{\mathrm{eff}}\mu_{\mathrm{B}}B$.[42–44] Here, all exchange effects are included in the effective gyromagnetic ratio g_{eff}, which can reach values up to 1180 at low temperatures and small magnetic fields.[43,44] Such large exchange interactions yield Zeeman

splittings up to several tens of meV / T. Due to the very effective ordering of the Mn^{2+} spins in a magnetic field at low temperatures, the giant Zeeman splitting increases rapidly with B (paramagnetic behavior) leading to a much more sensitive change in state occupation with B and therefore to a steeper increase of $\Delta I/I$ (B) compared to the undoped (diamagnetic) case.[46] Note that the state occupation, and thus the degree of circular polarization, in undoped and doped cQDs is determined by the Zeeman splitting at the moment of radiative recombination, which is usually described by a thermal equilibrium Boltzmann distribution in cases where the spin relaxation rate exceeds the recombination rate.

3.2.5 Magnetically doped cQDs with EMP formation – isotropic case. To derive the polarization degree of cQDs with EMP formation, one must consider the complete formation process, including its direction. In case of EMP formation, the collective alignment of the Mn^{2+} magnetic moments inside the effective exciton volume V_{eff} is driven by the internal exchange field $\vec{B}_{\mathrm{exc}} = \vec{B}_{\mathrm{exc}}^{\mathrm{el}} + \vec{B}_{\mathrm{exc}}^{\mathrm{h}}$ with orientations given by the direction of the charge carriers' total angular momentum (see Appendix B section B.3.1. for details). In Mn^{+2}-doped II-VI QDs it is commonly assumed that the instantaneous direction of $\vec{M}_{\mathrm{f}} = \vec{M}_{\mathrm{Mn}}(t = 0)$ at the moment of exciton creation determines the direction of EMP formation, leading to an isotropic model of EMP formation. Due to the quantum mechanical nature, the Mn^{2+} magnetization is subject to fluctuations in magnitude and direction, and has to be described by the joint probability distribution function $\Phi(\vec{M}_{\mathrm{Mn}})$ (see Appendix B section B.3.2. for details), describing the chance to find a certain value for $\vec{M}_{\mathrm{Mn}}$. Using this framework, the PL polarization can be calculated using eq. (3.1), where the angle θ is now given by the angle between the EMP direction and the magnetic field direction. In Faraday geometry, i.e. light direction $\vec{k}$ and magnetic field $\vec{B}$ are parallel, $\Delta I/I$ can then be calculated by:[35]

$$\Delta I/I = \frac{\int \mathrm{d}M_{\mathrm{x}}\, dM_{\mathrm{y}}\, dM_{\mathrm{z}} (I^{\sigma+} - I^{\sigma-}) \Phi(M_{\mathrm{x}}, M_{\mathrm{y}}, M_{\mathrm{z}})}{\int \mathrm{d}M_{\mathrm{x}}\, dM_{\mathrm{y}}\, dM_{\mathrm{z}} (I^{\sigma+} + I^{\sigma-}) \Phi(M_{\mathrm{x}}, M_{\mathrm{y}}, M_{\mathrm{z}})} \tag{3.2}$$

The dashed line in Figure 3.1 (c) shows the result for a simulation using literature parameters for similar cQDs (see Appendix B section B.3.3. for details). Apparently, this model of isotropic EMP formation consequently overestimates the increase of $\Delta I/I$ for small magnetic fields and cannot explain the saturation $\Delta I/I < 100\%$ at high magnetic fields in cQDs.[35] Therefore, a model explicitly incorporating anisotropy effects needs to be developed.

3.2.6 Magnetically doped cQDs with anisotropic EMP formation – case of zero magnetic field. We therefore establish a model for describing the PL polarization considering

anisotropy effects. Note that the direction of any axis of anisotropy is by default specific to each single cQD in lab coordinates. It is therefore necessary to start the description at a single particle level and move towards an ensemble by averaging afterwards. $\vec{B}_{\mathrm{exc}}^{\mathrm{el}}$ is commonly assumed to be directed by $\vec{M}_{\mathrm{Mn}}$ due to the isotropic orbital *s* character of the electron wavefunction.[68] However, even in the fully formed EMP state, $\vec{B}_{\mathrm{exc}}^{\mathrm{h}}$ can be constrained by an axis of anisotropy in wurtzite cQDs.[58] This constraint is thought to be caused by the strong anisotropic orbital *p* character of the hole wavefunction. The consequences of this strong anisotropic behavior of the hole exchange field for the initial mechanism of EMP formation – and ultimately the PL polarization degree - are therefore discussed in the following.

As $\vec{B}_{\mathrm{exc}}^{\mathrm{h}}$ is constrained by the cQD anisotropy axis, it is reasonable to assume that this constraint is already established at the moment of exciton generation, i.e. at $t \approx 0$. A plausible source of the dominant anisotropy axis in wurtzite cQDs is the crystal $\vec{c}$ axis (see Appendix B section B.4.1. for discussion of relevant energy scales). Then, the direction of the hole exchange field is respectively given by $\vec{B}_{\mathrm{exc}}^{\mathrm{h}} \parallel \vec{c}$ and $\vec{B}_{\mathrm{exc}}^{\mathrm{h}} \parallel -\vec{c}$. This first order criterion is then superimposed with the second order influence of minimizing the *p-d* exchange energy for the hole $E_{\mathrm{p-d}}(t \approx 0) = -V_{\mathrm{eff}}\vec{M}_{\mathrm{f}} \cdot \vec{B}_{\mathrm{exc}}^{\mathrm{h}}$. It is therefore energetically favorable for the hole to align its exchange field in the direction that yields an energy gain $\Delta E_{\mathrm{p-d}} < 0$, i.e. the direction with positive projection $\left(\vec{M}_{\mathrm{f}} \cdot \vec{B}_{\mathrm{exc}}^{\mathrm{h}}\right) > 0$. In other words, while the crystal $\vec{c}$ axis predefines two possible directions of $\vec{B}_{\mathrm{exc}}^{\mathrm{h}}$, the initial direction of the fluctuating magnetization $\vec{M}_{\mathrm{f}}$ at the moment of exciton generation determines the preferred case out of those two.

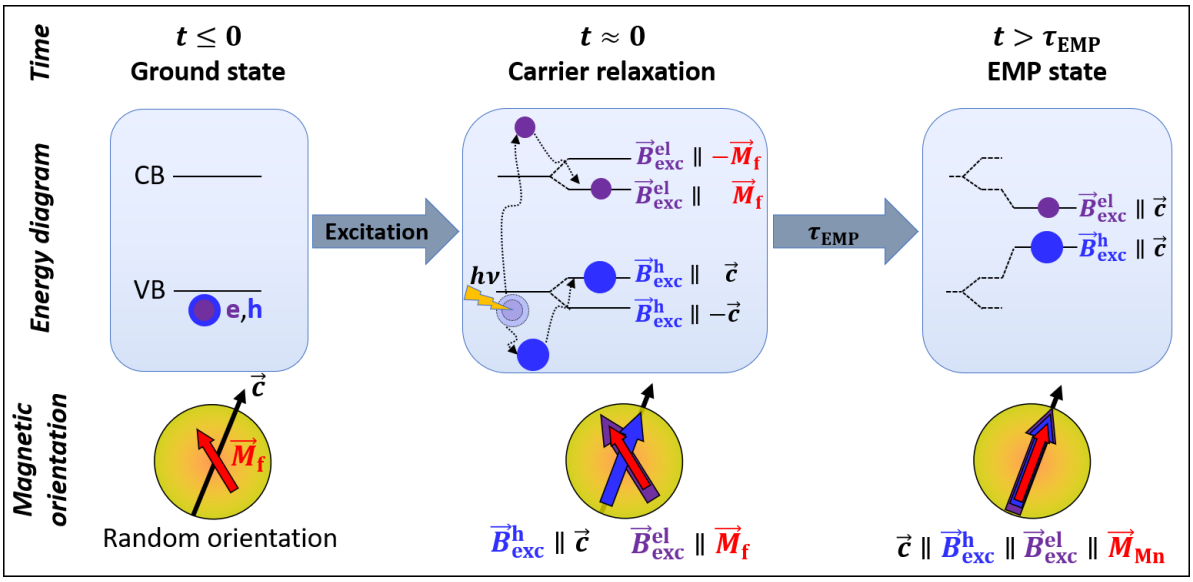

Scheme 3. 1 Illustration of EMP formation. Illustration of the suggested EMP formation process for a single excitation event at $\boldsymbol{B}$ = 0. This schematic depicts the EMP formation for a randomly chosen case of $\boldsymbol{M_c = \vec{M}_f \cdot \vec{c} > 0}$ at the moment of photo-excitation ($\boldsymbol{t = 0}$).

Scheme 3.1 illustrates the suggested EMP formation process for one photoexcitation event. In the case depicted here, the instantaneous magnetization $\vec{M}_f$ is oriented towards the top-left at the moment of photoexcitation and $\vec{c}$ is oriented to the top right. Then the magnetization component in the direction of $\vec{c}$, $M_c = \vec{M}_f \cdot \vec{c}$, is positive. Therefore, the state with $\vec{B}^{h}_{exc}$ parallel to $\vec{c}$ is energetically favored and the subsequent HH relaxation leads to $\vec{B}^{h}_{exc}$ parallel to $\vec{c}$. Note that for another excitation event, where M_c is negative, the relaxation would occur into the state with $\vec{B}^{h}_{exc}$ antiparallel to $\vec{c}$. The electron, on the other hand, has an isotropic character and can either relax into the direction of $\vec{M}_f$ to maximize the energy gain by magnetic *s–d* exchange interaction, or (if $|\vec{M}_f|$ is small) relax into the direction of $\vec{B}^{h}_{exc}$ to maximize the energy gain due to the electron-hole *s–p* exchange interaction. After the hole is relaxed with $\vec{B}^{h}_{exc} \parallel \vec{c}$ or $\vec{B}^{h}_{exc} \parallel -\vec{c}$, the Mn^{2+} spins align into the direction of $\vec{B}^{h}_{exc}$, and the EMP is formed. During the EMP formation, the magnetization reaches saturation and the energy of the electron-hole pair is lowered by the EMP binding energy, splitting the $|\pm 3/2\rangle$ states substantially in energy and preventing thermal occupation of the upper state. Therefore, the problem of predicting EMPs formed with either the $|+3/2\rangle$ or $|-3/2\rangle$ HH state - from which finally the PL polarization can be derived - is reduced to determining the probability for $M_c > 0$ based on the statistics given above.

3.2.7 Magnetically doped cQDs with anisotropic EMP formation – case of finite magnetic field. With $\vec{B} \parallel \vec{z}$, the orientation of a single cQD with crystal axis $\vec{c}$ with respect to $\vec{z}$ is characterized by its polar angle θ between $\vec{c}$ and $\vec{z}$. The above framework can then be used to determine the number of EMPs formed in either the $\vec{c}$ or $-\vec{c}$ direction by determining the probability of $M_\mathrm{c} > 0$ and the probability of $M_\mathrm{c} < 0$. It is instructive to first consider the special case of $\vec{c} \parallel \vec{z}$, i.e. $\theta = 0°$. Then M_c is given by M_z and the task is simply to determine the probability of finding $\vec{M}_\mathrm{f}$ with positive component M_z along $\vec{z}$, using the probability distribution $P(M_\mathrm{z})$, which describes only the z component of $\vec{M}_\mathrm{f}$ instead of the full joint probability distribution $\Phi(M_\mathrm{x}, M_\mathrm{y}, M_\mathrm{z})$:

$$P(M_\mathrm{z}) = \frac{1}{\sqrt{2\pi\langle\delta M_\mathrm{z}^2\rangle}} \exp\left(-\frac{(M_\mathrm{z}-\langle M_\mathrm{z}\rangle)^2}{2\langle\delta M_\mathrm{z}^2\rangle}\right) \quad (3.3)$$

Then, the portion of HH relaxation with $\vec{B}_\mathrm{exc}^\mathrm{h}$ pointing to the positive $\vec{z}$ direction - and hence subsequent EMP formation in this direction - is obtained by summing the probability K for $M_\mathrm{z} > 0$, i.e.:

$$K = \int_0^\infty P(M_\mathrm{z})\mathrm{d}M_\mathrm{z} = \frac{1}{2}\left[1 - \mathrm{erf}\left(-\frac{\langle M_\mathrm{z}\rangle}{\sqrt{2\langle\delta M_\mathrm{z}^2\rangle}}\right)\right] \quad (3.4)$$

The corresponding portion of HH relaxation with $\vec{B}_\mathrm{exc}^\mathrm{h}$ pointing in the negative z direction and subsequent EMP formation in this direction is given by the integral with limits $(-\infty, 0)$, or, since $P(M_\mathrm{z})$ is normalized, simply by $(1 - K)$. Figure 3.3 (a) plots $P(M_\mathrm{c}) = P(M_\mathrm{z})$ for $\theta = 0°$ at $B = 0.5$ T and $T = 4$ K. The red and blue shaded areas nicely visualize $P(M_\mathrm{c} > 0)$ and $P(M_\mathrm{c} < 0)$ and thus the relaxation probability for the HH with $\vec{B}_\mathrm{exc}^\mathrm{h} \parallel \vec{c}$ and $\vec{B}_\mathrm{exc}^\mathrm{h} \parallel -\vec{c}$, respectively. The inset schematically shows the donut-like shape of the heavy hole wavefunction with total orbital momentum projections $J_\mathrm{z} = \pm 3\hbar/2$.

To visualize, the influence of the magnetic field, Figure 3.3 (b) depicts $P(M_\mathrm{c})$ for different magnetic fields applied in the $\vec{z}$-direction. With increasing magnetic field, the distribution is shifted towards positive values of M_z and narrowed. The shift indicates an increase in the time averaged expectation value of the magnetization $\langle M_\mathrm{c}\rangle = \langle M_\mathrm{z}\rangle$ and the decrease of the FWHM corresponds

to a suppression of fluctuations $\langle \delta M_c^2 \rangle = \langle \delta M_z^2 \rangle$. From Figure 3.3 (b) it becomes obvious, that the probability that $M_c > 0$ grows with applied magnetic field, making relaxation into the HH state $|+3/2\rangle$ with $\vec{B}_{exc}^{h} \parallel \vec{c}$ increasingly likely. For magnetic fields larger than 2 T, practically all EMPs are formed along the positive $\vec{z}$-direction, which, as we will discuss below, corresponds to a saturation of the PL polarization.

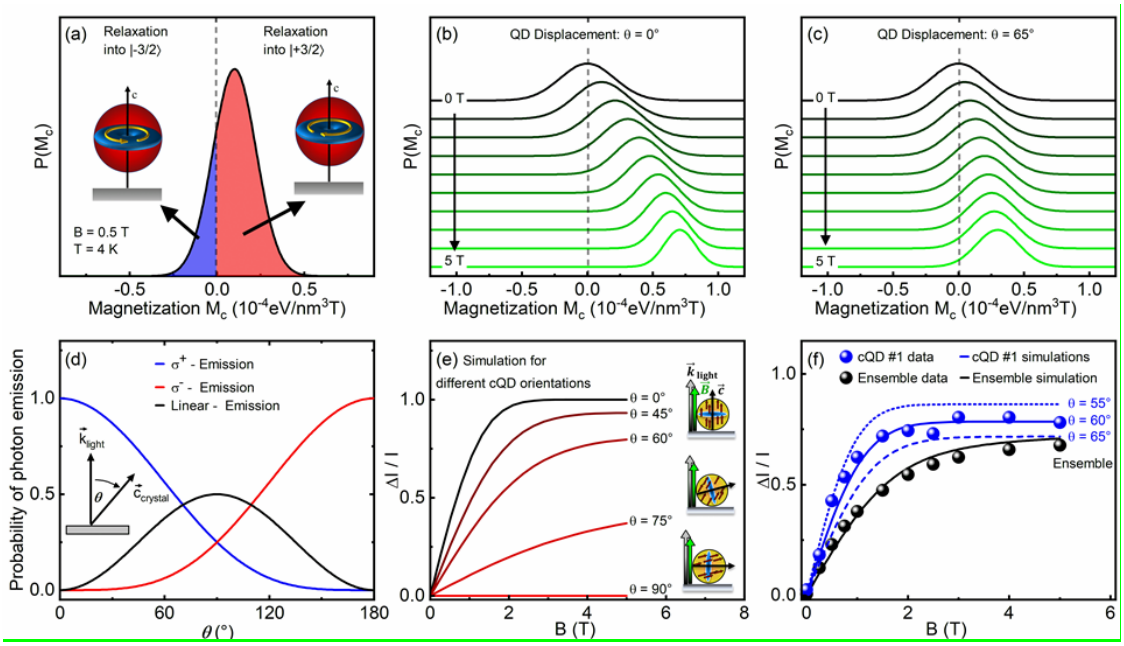

Figure 3. 3 Theoretical description of the photoluminescence polarization ratio based on the orientation of the NC. (a) Probability distribution $\boldsymbol{P(M_c)}$ of the magnetization along the $\vec{\boldsymbol{c}}$-direction at B = 0.5 T. The blue and red shaded areas correspond the probabilities of HH relaxation into the $|\boldsymbol{-3/2}\rangle$ and $|\boldsymbol{+3/2}\rangle$ states, respectively. (b) Calculated change of the probability distribution $\boldsymbol{P(M_c)}$ in a magnetic field applied along $\vec{\boldsymbol{z}}$ for $\boldsymbol{\theta}$ = 0° and (c) $\boldsymbol{\theta}$ = 65° at different magnetic field strengths. (d) Probability of detecting different PL polarization from recombination of a $|\boldsymbol{+3/2}\rangle$ hole and a $|\boldsymbol{-1/2}\rangle$ electron for a cQD with its $\vec{\boldsymbol{c}}$ axis displaced by an angle $\boldsymbol{\theta}$ from the light direction $\vec{\boldsymbol{k}}$ ($\vec{\boldsymbol{k}} || \vec{\boldsymbol{z}}$). (e) Simulated $\boldsymbol{\Delta I / I}$ $\boldsymbol{(B)}$ for five differently oriented cQDs. (f) Comparison of $\boldsymbol{\Delta I / I}$ vs $\boldsymbol{B}$ for cQD #1 (blue symbols) with three different simulations for a single cQD using $\boldsymbol{\theta}$ = 55°(blue dotted line), 60°(blue solid line) and 65° (blue dashed line), as well as ensemble data shown in Figure 3.1 (black symbols) in comparison with a simulation for the whole ensemble of cQDs (black line). For parameters used in the simulations, see Appendix B.

Before the consequences for the PL polarization are considered, the general case of a cQD with crystal orientation $\vec{c} \nparallel \vec{z}$, i.e. $\theta \neq 0°$ needs to be discussed. In this case, $M_c = \cos(\theta)\, M_z$ and the probability to find $\vec{M}_f$ with positive component along $\vec{c}$ can be found in a similar way as before, but with a modified version of eqs. (3.3) and (3.4). Without an electron-hole pair present, the axial anisotropy splitting for the Mn^{2+} spins in wurtzite CdSe cQDs has previously been determined by means of electron paramagnetic resonance spectroscopy.[69] The axial zero-field splitting parameter D was found to be smaller than 0.01 cm^{-1}. Therefore the total the Mn^{2+} ground state zero-field splitting of $6D$ is in the order of only a few percent of $k_B T$ at 4 K and thus the Mn^{2+} spin orientation at 4 K is not influenced by the crystal anisotropy. Hence, the joint probability distribution $\Phi(M_x, M_y, M_z)$ is independent of θ and describes a 3D gaussian distribution, which, in the presence of a magnetic field, is displaced along $\vec{z}$ and narrowed. In analogy to the approach above, the probability of finding $M_c > 0$ for $\vec{c} \nparallel \vec{z}$ is described by a 1D probability distribution $P(M_c)$, reflecting the probability of magnetization along $\vec{c}$. The modified version of eq. (3.4) describing the probability of EMP formation in the direction of $\vec{c}$ is then given by (see Appendix B section B.4.2. for details):

$$K = \frac{1}{2}\left[1 - \mathrm{erf}\left(-\frac{\langle M_z \rangle \cos(\theta)}{\sqrt{2}\cos(\theta)\sqrt{\langle \delta M_{\parallel}^2 \rangle} + \sqrt{2}\sin(\theta)\sqrt{\langle \delta M_{\perp}^2 \rangle}}\right)\right] \tag{3.5}$$

Here, $\langle \delta M_{\parallel}^2 \rangle$ and $\langle \delta M_{\parallel}^2 \rangle$ are the magnetic fluctuations parallel and perpendicular to the magnetic field. To demonstrate the consequences of a finite angle $\theta \neq 0°$, Figure 3.3 (c) plots $P(M_c)$ for an angle of $\theta = 65°$ with the same parameters as used for the case of $\theta = 0°$ in Figure 3.3 (b). The reduced shift of $P(M_c)$ as well as the reduced narrowing with magnetic field are clearly visible, leading to a significant change in the probabilities of HH relaxation with $\vec{B}_{exc}^{h}$ directed along $\vec{c}$ and thus a reduced probability of EMP formation in this direction. This results in a finite probability of EMP formation along $-\vec{c}$ even at 5 T. Thus, increasing the angle θ mitigates the influence of the external magnetic field, leading to a weaker dependence of the probability of EMPs formed along $\vec{c}$, and thus to a more gradual increase of $\Delta I/I\,(B)$.

We note the similarity between this model of constrained EMP orientation to the case of undoped cQDs, where the direction of the total angular momentum during HH relaxation is also determined by the crystal $\vec{c}$ axis. In this latter case, the probability of excitons with total angular momentum along $\vec{c}$ or $-\vec{c}$ is given by the thermal occupation of the Zeeman split electronic states

$|\pm 3/2\rangle$ and described by the equilibrium Boltzmann distribution. Such a thermal occupation cannot be used for the fully formed EMP state because of the very large energies involved. Instead, eq. (3.5) must be used to give the magnetic field dependent relative intensities of PL emitted from EMPs oriented along $\vec{c}$ or $-\vec{c}$ for any given cQD orientation, characterized by its polar angle θ.

It is commonly recognized that the helicity of emitted photons during the recombination process is a direct result of the preservation of angular momentum. For example, recombination of a hole in the $|+3/2\rangle$ state with total angular momentum projection $J_z = +3\hbar/2$ and an electron in the $|-1/2\rangle$ state with total angular momentum projection $-\hbar/2$ yields a photon with angular momentum $+\hbar$, i.e., a σ^+ polarized photon. Due to the conservation of angular momentum, the reference axis of this photon, however, is given by the reference axis of the recombining electron-hole pair, in our case the crystal $\vec{c}$ axis of the cQDs. As a a consequence, the observation of the photon yields an elliptical polarization that depends on the angle between $\vec{c}$ and the observation direction $\vec{k}$. Since all experiments are conducted in Faraday geometry, i.e., $\vec{k} \parallel \vec{B} \parallel \vec{z}$, this angle is given by the polar angle of the crystal c axis, θ. Figure 3.3 (d) plots the angle dependence of the PL polarization for the recombination of a $|+3/2\rangle$ HH with a $|-1/2\rangle$ electron. While for $\theta = 0°$ the emission is purely σ^+ polarized, it becomes completely σ^- polarized for $\theta = 180°$. For intermediate angles, the polarization becomes elliptical and even dominantly linear for $\theta = 90°$.

Similar to the case of undoped cQDs, we therefore expect the PL polarization degree after EMP formation along the $+\vec{c}$ axis, i.e., after relaxation of the HH into the $|+3/2\rangle$ state, to exhibit the same angle dependence as given by eqs. (3.1). Then, the total intensities for σ^+ and σ^- polarized light have contributions from EMPs formed along $\vec{c}$ (called $I_{\uparrow\uparrow}^{\sigma\pm}$) as well as from EMPs formed along $-\vec{c}$ (called $I_{\uparrow\downarrow}^{\sigma\pm}$), i.e. $I^{\sigma+} = I_{\uparrow\uparrow}^{\sigma+} + I_{\uparrow\downarrow}^{\sigma+}$ and $I^{\sigma-} = I_{\uparrow\uparrow}^{\sigma-} + I_{\uparrow\downarrow}^{\sigma-}$. The PL intensity $I_{\uparrow\uparrow}$ emitted from EMPs is proportional to the probability of EMP formation parallel to $\vec{c}$ and therefore given by K, and it has contributions from both helicities $I_{\uparrow\uparrow}^{\sigma+}$ and $I_{\uparrow\uparrow}^{\sigma-}$, while the intensity $I_{\uparrow\downarrow}$ is proportional to $(1-K)$ with contributions from $I_{\uparrow\downarrow}^{\sigma+}$ and $I_{\uparrow\downarrow}^{\sigma-}$. Collecting all contributions and weighting them with the probability of EMP formation in the corresponding direction gives the intensities $I^{\sigma+}(\theta)$ and $I^{\sigma-}(\theta)$ emitted from a single cQD:

$$I^{\sigma+}(\theta) = I_{\uparrow\uparrow}^{\sigma+} + I_{\uparrow\downarrow}^{\sigma+} = A\big[K(B,\theta)(1+\cos(\theta))^2 + \big(1-K(B,\theta)\big)(1-\cos(\theta))^2\big] \tag{3.6a}$$

$$I^{\sigma-}(\theta) = I_{\uparrow\uparrow}^{\sigma-} + I_{\uparrow\downarrow}^{\sigma-} = A\big[K(B,\theta)(1-\cos(\theta))^2 + \big(1-K(B,\theta)\big)(1+\cos(\theta))^2\big] \tag{3.6b}$$

where A is a constant. Using eqs. (3.6), the magnetic field dependence of $\Delta I/I$ can be calculated for a single cQD with orientation θ of the $\vec{c}$-axis with respect to the laboratory $\vec{z}$-axis. Figure 3.3 (e) plots simulated $\Delta I/I\,(B)$ curves for five differently oriented single cQDs as illustrated by the inset scheme. Comparison of the five curves yields two major features: First, only cQDs with $\theta = 0°$ yield a saturation value of $\Delta I/I$ =100%, while for those with θ between 0° and 90°, a saturation value between 100% and 0% can be achieved. This result is a direct consequence of the mixed σ^+ and σ^- emission from each state. In the limit of high magnetic fields and for $0° < \theta° < 90°$, where only EMPs with $\vec{B}^{\mathrm{h}}_{\mathrm{exc}} \parallel \vec{c}$ are formed, the PL intensity is given by $I_{\uparrow\uparrow}$ with right and left circularly polarized contributions $I^{\sigma+}_{\uparrow\uparrow}$ and $I^{\sigma-}_{\uparrow\uparrow}$ dependening on the polar angle θ. This situation leads to saturation values of $\Delta I/I < 100\%$. Therefore, the saturation value of $\Delta I/I\,(B)$ purely depends on the polar angle θ, i.e., the orientation of the $\vec{c}$ axis of the cQD with respect to the $\vec{z}$ direction but not on any other specifics of the material system such as cQD size, dopant concentration, shape anisotropy, etc. The second important observation relates to the changing slope $\Delta I/I\,(B)$ with θ. This flattening is a direct consequence of the mitigated influence of the magnetic field onto the magnetization components along $\vec{c}$, leading to a slow increase of $\langle M_{\mathrm{c}}\rangle = \cos(\theta)\,\langle M_{\mathrm{z}}\rangle$ and a reduced suppresion of fluctuations $\langle \delta M_{\mathrm{c}}^2\rangle$, as discussed in Appendix B section B.4.2. Therefore, much stronger magnetic fields are needed to reach polarization saturation for large polar angles θ than for small values of θ. Note that the finite saturation value, as well as the reduced slope for low magnetic fields differs for each single cQD orientation. Averaging over all possible directions thus enables the simulation of the expected $\Delta I/I\,(B)$ curve for the ensemble. The black solid line in Figure 3.3 (f) depicts such a simulation and shows extremely good agreement with the ensemble data (black symbols) presented in Figure 3.1 (see Appendix B section B.4.3. for details).

As noted above, once polarization saturation is reached by a sufficiently strong magnetic field, the saturation value of $\Delta I/I$ of a cQD only depends on the polar angle θ. Thus, the simulated $\Delta I/I\,(B)$ traces can be used to determine the polar angle θ of a real cQD with respect to the lab $\vec{z}$ direction on the substrate surface. Figure 3.3 (f) compares the data of cQD #1 (blue symbols) with three simulated $\Delta I/I\,(B)$ traces (blue lines) for single cQDs with θ = 55° (dotted), θ = 60° (solid) and θ = 65° (dashed) (see Appendix B section B. 4.4. for detailed simulation parameters). We find very good agreement between the experimental data of cQD #1 and the simulation of $\Delta I/I\,(B)$ for θ = 60°. Additionally, the simulated saturation value strongly depends on the polar angle θ. This result demonstrates how the saturation value of $\Delta I/I\,(B)$ can be used as an elegant and relieable

tool to determine the orientation of a single cQD on a substrate with respect to the optical axis. Note, that this idea is not limited to the special case of cQDs with EMP formation but rather can be used to determine the orientation of any anisotropic cQD or similar nanostructure with appropriate electronic structure. Magnetically doped cQDs are just a particularly attractive model system because of the comparably small magnetic fields needed to achieve saturation.

Figure 3.4 (a) shows $\Delta I/I\ (B)$ of four different single cQDs. First, the curves exhibit different saturation values for high magnetic fields between 60% and 80%, suggesting different polar angles θ for each of these cQD's crystal orientations, in agreement with the model above. Interestingly, within a data set of 17 single cQDs, no cQDs with a saturation value below 50% was found (see inset in Figure 3.4 (a)). This result could be a consequence of preferred cQD orientation due to the single cQD sample preparation, where each single cQD is in contact with the substrate surface, in contrast to the ensemble, where nearly all cQDs are surrounded by other cQDs and a matrix of organic ligands. Because the CdS shell is strongly faceted (see TEM image in Figure B1 of Appendix B), a true random orientation of the cQD crystal orientation is therefore likely inhibited.

The second important feature of the $\Delta I/I\ (B)$ traces is the fact that at zero magnetic field non-zero $\Delta I/I$ values varying between $+5\%$ and -5% are observed. This deviation from zero is found to be unique for each individual cQD, suggesting a hidden influence, which to the best of our knowledge has not been addressed in literature so far. Following the argumentation given above, the observation of a circularly polarized photon with its angular momentum direction tilted by an angle θ from the observation direction can be either detected as being σ^+, σ^- or linearly polarized (π). Our experiments are conducted in Faraday geometry. This suggests that the single cQD emission - in addition to the above discussed circular polarized contributions - also comprise a linearly polarized PL component I^{π}. An analogue consideration is known for the emission from the exciton fine structure state $\pm 1^{\mathrm{L}}$ in wurtzite cQDs, where a linearly polarized PL component with an angular dependence $I^{\pi}_{\pm 1^{\mathrm{L}}}(\theta) \propto \sin^2(\theta)$ was found.[20]

Figure 3.3 (d) shows the dependence of the π polarized PL component, which is zero at $\theta = 0°$ and 180° and has its maximum value at $\theta = 90°$. This behavior can be understood by recognizing that the electric field of circularly polarized PL emitted from the EMP state rotates in the plane perpendicular to $\vec{c}$. For $\theta = 90°$, i.e., $\vec{k} \perp \vec{c}$, the far field thus appears partly linearly polarized. Thus, we can give eq. (3.7) to complement eqs. (3.6a,b) above:

$$I^{\pi}(\theta) = I^{\pi}_{\uparrow\uparrow} + I^{\pi}_{\uparrow\downarrow} = 2A\left[K(B,\theta)\sin^2(\theta) + \left(1 - K(B,\theta)\right)\sin^2(\theta)\right] = 2A\sin^2(\theta) \qquad (3.7)$$

This consideration results in a PL signal consisting of σ^+, σ^- and π components. Noticeably, because $I^{\pi}_{\uparrow\uparrow} = I^{\pi}_{\uparrow\downarrow}$, the overall component I^{π} is expected to be independent of magnetic field. We measure the π polarized PL emission by measuring $I(\alpha)$ with no quarter wave plate inserted into the optical beam. Without a quarter wave plate, circularly polarized components pass the analyzing linear polarizer by 50%, independent of the analyzer angular position α. Therefore, any intensity change in the angular profile is due to a π polarized PL component. Figure 3.4 (b) plots the angular dependence $I(\alpha)$ of the integrated PL intensity for cQD #1 in presence and absence of a magnetic field.

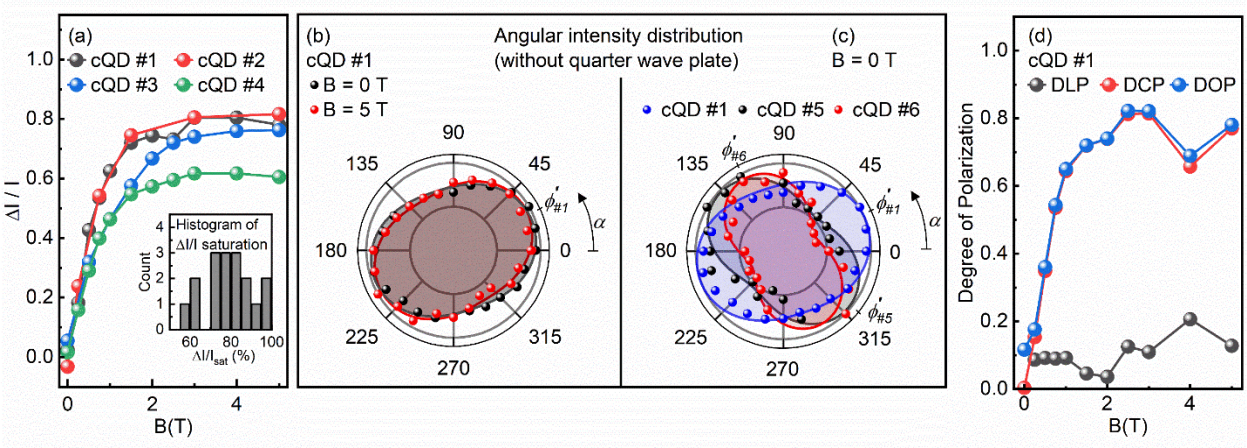

Figure 3.4 Select single particle photolumionescence polarization data. (a) $\boldsymbol{\Delta I/I\,(B)}$ of four different single cQDs at 4 K. The inset shows a histogram of $\boldsymbol{\Delta I/I}$ saturation values for several single cQDs. (b) Integrated intensity $\boldsymbol{I(\alpha)}$ for cQD #1 at $\boldsymbol{B}$ = 0 T (black) and $\boldsymbol{B}$ = 5 T (red). (c) Comparison of $\boldsymbol{I(\alpha)}$ for three single cQDs at $\boldsymbol{B}$ = 0 T. $\boldsymbol{\phi'}$ marks the linear polarization orientation angle for the corresponding single cQD. Shaded areas in (b) and (c) serve as guides to the eye. (d) Degree of linear polarization (black), degree of circular polarization (red) and total degree of polarization (blue) for single cQD #1 obtained from measurements of the full Stokes parameters at each magnetic field strength.

With no external magnetic field applied (black dots), $I(\alpha)$ exhibits an elongated shape with its maximum and minimum values at analyzer positions of $\alpha = 25°$ and 115°. The elongated shape is characteristic of the angular distribution of PL comprising a weak π polarized component superposed with a stronger circular polarized component. The angular intensity dependence $I(\alpha)$ at $B = 5$ T matches the intensity dependence at $B = 0$ T very nicely in shape as well as in

orientation suggesting no change of the linear polarized PL component with magnetic field. This result shows that the π – polarized component of the PL is independent of the distribution of EMPs formed along $\vec{c}$ or $-\vec{c}$.

The degree of linear polarization is defined from the half axes a and b of the polarization ellipse as $\Delta I_{\mathrm{lin}}/I_{\mathrm{lin}} = (I_{\mathrm{a}} - I_{\mathrm{b}})/(I_{\mathrm{a}} + I_{\mathrm{b}})$. From the minimal and maximal values of $I(\alpha)$ we estimate the degree of linear polarization as $\Delta I_{\mathrm{lin}}/I_{\mathrm{lin}} = 15\%$, clearly proving the partly π polarized character of the PL from cQD #1. The orientation angle ϕ' of the polarization ellipse with respect to $\alpha = 0°$ is given by an angle of maximum intensity, i.e. $\phi'_{\#1} = 25°$ in case of cQD #1. To test whether the angle of $\phi'_{\#1}$ is unique for cQD #1, Figure 3.4 (c) compares $I(\alpha)$ for three single cQDs at $B = 0$ T. We find intensity profiles $I(\alpha)$ with individual strengths of the linear polarization contributions, $\Delta I_{\mathrm{lin}}/I_{\mathrm{lin}} = 15\%$, 29% and 42% for cQDs #1, #5 and #6, respectively. From eq. (7) the strength of linearly polarized contributions is expected to depend on the polar angle θ between the crystal $\vec{c}$ axis and the light propagation direction $\vec{k}||\vec{z}$. Therefore, the different strength of π polarized PL components, i.e. the different $\Delta I_{\mathrm{lin}}/I_{\mathrm{lin}}$, is a direct consequence of the individual polar angle θ between the crystal axis $\vec{c}$ and the $\vec{z}$ direction for each single cQD. The intensity profiles $I(\alpha)$ exhibit different linear polarization angles $\phi'_{\#1} = 25°$, $\phi'_{\#5} = 135°$ and $\phi'_{\#6} = 115°$ for cQDs #1, #5 and #6. Thus, every cQD seems to exhibit a unique orientation of its linear polarized PL, which explains the characteristic deviation of $\Delta I/I$ from zero at $B = 0$ (see Figure 3.4 (a) and discussion of Figure B3 in Appendix B).

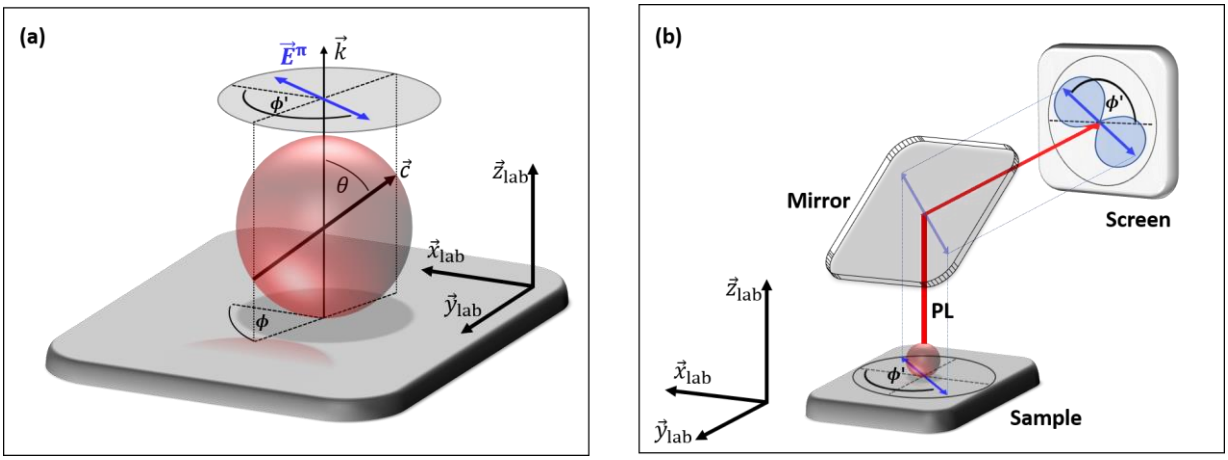

Scheme 3. 2 Illustration of the NC orientation and polarization axes. (a) Illustration of the cQD $\vec{c}$ axis orientation, described by the polar angle θ and azimuthal angle ϕ, and its impact on the electric field orientation of emitted linearly polarized light. Note that the polarization angle ϕ' of

the electric field vector $\vec{\boldsymbol{E}}$ in the *xy* plane is perpendicular to the azimuthal angle $\boldsymbol{\phi}$, describing the direction of $\vec{\boldsymbol{c}}$ in the *xy* plane. (b) Illustration of the correlation between the sample orientation in $\vec{\boldsymbol{x}}$, $\vec{\boldsymbol{y}}$ and $\vec{\boldsymbol{z}}$ lab coordinates and the intensity pattern during the measurement.

One elegant way to get the complete polarization state of the emission is to measure the full Stokes parameters (S_0, S_1, S_2, S_3), defined by $S_0 = E_{\mathrm{x}}E_{\mathrm{x}}^* + E_{\mathrm{y}}E_{\mathrm{y}}^*$, $S_1 = E_{\mathrm{x}}E_{\mathrm{x}}^* - E_{\mathrm{y}}E_{\mathrm{y}}^*$, $S_2 = E_{\mathrm{x}}E_{\mathrm{y}}^* + E_yE_x^*$, $S_3 = i\left(E_{\mathrm{x}}E_{\mathrm{y}}^* + E_{\mathrm{y}}E_{\mathrm{x}}^*\right)$.[70] Here $E_{\mathrm{x,y}}^*$ are the complex conjugates of the complex electric field amplitudes $E_{\mathrm{x,y}}$ in $\vec{x}$ and $\vec{y}$ directions. From the Stokes parameters the exact degree of linear polarization (DLP), degree of circular polarization (DCP) and degree of total polarization (DOP) can be calculated by $DLP = \sqrt{S_1^2 + S_2^2}/S_0$, $DCP = S_3/S_0$, $DOP = \sqrt{S_1^2 + S_2^2 + S_3^2}/S_0$. Additionally, the polarization angle ϕ' is given by $\phi' = 0.5\,\mathrm{atan}(S_2/S_1)$, offering very convenient access to ϕ'.

We therefore set up the appropriate Mueller matrices describing our experiment and measured the Stokes parameters as described in literature.[70] Figure 3.4 (d) plots the DLP, DCP and DOP for single cQD #1. We first note that in case of cQD #1 the DCP trace is very similar to the trace of $\Delta I/I$. The DCP, however, starts exactly at zero for B = 0 T, while $\Delta I/I$ has a value of 2.5% at B = 0 T. This finding demonstrates the advantage of using the DCP derived from the Stokes parameters as compared to simply using $\Delta I/I$. We additionally find that the DLP does not significantly change with B, in agreement with our conclusions earlier. The DOP on the other hand changes from being dominated by the DLP at zero field to being controlled by the DCP at high magnetic fields. Determining ϕ' from the Stokes parameters yields $\phi'_{\#1}$ = 30°, in close agreement with the value found from measuring the full angular intensity distribution $I(\alpha)$. Note that for the measurement of the Stokes parameters merely four measurements are needed, significantly improving the efficiency of the experiment. These results represent the first measurement of the complete polarization state for single cQD emission and showcase a robust method to characterize the polarization state for mixed polarization emission in (single) colloidal nanostructures that has, to the best of our knowledge, not been employed thus far.

The full 3D orientation of the crystal $\vec{c}$ axis is given by its polar angle θ with respect to the lab $\vec{z}$ direction and by the azimuthal angle ϕ describing the angle between the projection of $\vec{c}$ onto the *xy* plane and the $\vec{x}$ direction of the substrate (see Scheme 2). The polar angle θ can be extracted from the measured DCP at high magnetic fields, while the azimuthal angle ϕ can be derived from

the linear polarization angle ϕ' using $\phi = \phi' - 90°$. Thus, the complete crystal 3D orientation of a single cQD in the lab coordinates can now be determined to a high degree of accuracy by accessing the full polarization state of QD emission and extracting θ and ϕ. Using the above given values of $\theta = 60°$ from Figure 3.3 (f) and $\phi' = 25°$ from Figure 3.4 (b), we can calculate the normalized vector describing the $\vec{c}$ axis of cQD #1 as:

$$\vec{c}_{\mathrm{QD\#1}} = (\sin(\theta)\cos(\phi), \sin(\theta)\sin(\phi), \cos(\theta))^{\mathrm{T}} = (0.36, -0.78, 0.50) \quad (3.8)$$

Therefore, the measurement of the polarization angle ϕ' can directly be used to calculate the lab x and y coordinates of the cQD $\vec{c}$ axis on the substrate. This strategy can in principle be used to determine the crystal orientation in the lab reference frame for any anisotropic cQD, where one of the charge carriers' wavefunctions exhibits strong anisotropic character and the axis of anisotropy has sufficiently strong influence to constrain this charge carriers' wavefunction. The example of magnetically doped cQD provides a powerful illustration of this methodology due to the small magnetic fields needed to reach polarization saturation.

3.4 Conclusion:

Single colloidal Mn^{2+}-doped CdSe/CdS cQDs exhibiting EMP formation were investigated using polarization resolved magneto–PL spectroscopy. At zero field, a distinct linear polarization pattern is found while applying a magnetic field, the circular polarization degree of the PL is demonstrated to change characteristically for each single cQD, saturating at values < 100%. A model based on the interplay between crystal anisotropy and magnetic exchange energy, including magnetic fluctuations, was developed to explain our findings. As a direct consequence of a dominant anisotropy axis, we found a mixed polarization of the PL with significant linearly polarized contributions even at high magnetic fields. From a measurement of the magnetic field dependent full Stokes parameters, the full polarization state of single cQD emission is extracted and the degree of circular, linear and total polarization is derived. Most important, we demonstrate that the full polarization state of single cQD emission can be used as a precise method to directly determine the crystal $\vec{c}$ axis of the cQD in lab coordinates – to our knowledge the first demonstration for extracting the exact 3D crystal orientation of a single anisotropic nanostructure by optical means. While cQDs with EMP formation are a nice material system to showcase this strategy, our approach is not exclusive to this material system, but is transferable to a variety of doped and undoped anisotropic colloidal semiconductor nanostructures.

3.5 Methods:

Sample preparation. Mn^{2+}:CdSe/CdS cQDs were synthesized as reported previously.[35,43,44,58] For single single particle spectroscopy, the Mn^{2+}:CdSe/CdS cQDs were dispersed in toluene, highly diluted and spin cast onto a SiO_2/Si substrate (oxide thickness: 270 nm), pre-patterned with cross markers. Patterning of the substrate was done *via* electron beam lithography and thermal evapoaration of Ti/Au and served as a tool to reliable mark the position of single cQDs on the substrate, making it possible to find the same individual cQD several times. The dilution ($1{:}5\cdot 10^5$) was optimized to yield approximately one cQD per several μm^2 to enable addressing single cQDs.

Photoluminescence (PL) spectroscopy. Micro-PL spectra were collected using a confocal microscope setup (Attocube atto CFM I) with a high numeric aperture objective (Attocube LT APO-Vis, NA: 0.82) inside a closed cycle cryostat ($T_{\mathrm{sample}} = 4.0$ K) with the option to apply magnetic fields up to 5 T in Faraday geometry. To assure thermal contact to the reservoir, the samples were surrounded by Helium exchange gas. For the PL experiments, a 532 nm solid-state laser (Laserglow LRS-0532 DPSS) was used as excitation source (power density < 10 W / cm^{-2}, laser spot size on the sample: 700 nm) in combination with a laser clean up filter (Thorlabs FLH 532-10) and an ultrasteep long-pass edge filter (Razor Edge 532-RU). The spectra were recorded with a liquid nitrogen-cooled charge coupled device (CCD) camera (Horiba Symphony, back illuminated deep depletion 1-LS) in combination with a monochromator (Horiba Triax 550) equipped with a 150 mm^{-1} grating.

Polarization resolved PL measurements. For polarization resolved PL experiments, a combination of a quarter wave plate (Thorlabs AQWP05M-580) and a rotatable linear polarizer (Thorlabs LPVISC050) were placed into the detection beam. The fast axis of the quarter wave plate was aligned horizontally (defined as $\alpha = 0°$) with respect to the optical table and σ^+ and σ^- intensities were recorded with the linear polarizer at +45° and -45°, respectively. Gauging of the measurement setup was done by sending unpolarized light through the detection path (sample to detector).

For measurement of the Stokes parameters, the Mueller matrices of all optical components were determined by appropriate test measurements.[70] In addition to $I_{\mathrm{wp}}(45°)$ (with quarter wave plate), three measurements $I(0°)$, $I(45°)$ and $I(90°)$ were recorded without quarter wave plate. According to the Mueller matrix describing our measurement setup, $S_0 = 1.18\big(I(0°) + I(90°)\big)$,

$S_1 = 1.18\big(I(0°) - I(90°)\big)$, $S_2 = 2.35I(45°) - S_0$ and $S_3 = 2.47I_{\mathrm{wp}}(45°) - 0.33I(45°) - 1.03\big(I(0°) - I(90°)\big)$.

3.6 References

1. Pirandola, S.; Eisert, J.; Weedbrook, C.; Furusawa, A.; Braunstein, S. L. Advances in Quantum Teleportation. *Nat. Photonics* **2015**, *9* (10), 641–652.
2. Sherson, J. F.; Krauter, H.; Olsson, R. K.; Julsgaard, B.; Hammerer, K.; Cirac, I.; Polzik, E. S. Quantum Teleportation between Light and Matter. *Nature* **2006**, *443* (7111), 557–560.
3. Togan, E.; Chu, Y.; Trifonov, A. S.; Jiang, L.; Maze, J.; Childress, L.; Dutt, M. V. G.; Sørensen, A. S.; Hemmer, P. R.; Zibrov, A. S.; et al. Quantum Entanglement between an Optical Photon and a Solid-State Spin Qubit. *Nature* **2010**, *466* (7307), 730–734.
4. Wagenknecht, C.; Li, C. M.; Reingruber, A.; Bao, X. H.; Goebel, A.; Chen, Y. A.; Zhang, Q.; Chen, K.; Pan, J. W. Experimental Demonstration of a Heralded Entanglement Source. *Nat. Photonics* **2010**, *4* (8), 549–552.
5. Degen, C. L.; Reinhard, F.; Cappellaro, P. Quantum Sensing. *Rev. Mod. Phys.* **2017**, *89* (3), 035002.
6. Gisin, N.; Ribordy, G.; Tittel, W.; Zbinden, H. Quantum Cryptography. *Rev. Mod. Phys.* **2002**, *74* (1), 145–195.
7. Žutić, I.; Fabian, J.; Sarma, S. Das. Spintronics: Fundamentals and Applications. *Rev. Mod. Phys.* **2004**, *76* (2), 323–410.
8. Awschalom, D. D.; Flatté, M. E. Challenges for Semiconductor Spintronics. *Nat. Phys.* **2007**, *3* (3), 153–159.
9. Wolf, S. a; Awschalom, D. D.; Buhrman, R. a; Daughton, J. M.; von Molnár, S.; Roukes, M. L.; Chtchelkanova, a Y.; Treger, D. M. Spintronics: A Spin-Based Electronics Vision for the Future. *Science* **2001**, *294* (5546), 1488–1495.
10. Ranjbar, B.; Gill, P. Circular Dichroism Techniques: Biomolecular and Nanostructural Analyses- A Review. *Chem. Biol. Drug Des.* **2009**, *74* (2), 101–120.
11. Longhi, G.; Castiglioni, E.; Koshoubu, J.; Mazzeo, G.; Abbate, S. Circularly Polarized Luminescence: A Review of Experimental and Theoretical Aspects. *Chirality* **2016**, *28* (10), 696–707.
12. Safronova, M. S.; Budker, D.; Demille, D.; Kimball, D. F. J.; Derevianko, A.; Clark, C. W. Search for New Physics with Atoms and Molecules. *Rev. Mod. Phys.* **2018**, *90* (2), 025008.
13. Tebyetekerwa, M.; Zhang, J.; Xu, Z.; Truong, T. N.; Yin, Z.; Lu, Y.; Ramakrishna, S.; Macdonald, D.; Nguyen, H. T. Mechanisms and Applications of Steady-State Photoluminescence Spectroscopy in Two-Dimensional Transition-Metal Dichalcogenides. *ACS Nano* **2020**, *14* (11), 14579–14604.
14. Chen, X.; Yan, T.; Zhu, B.; Yang, S.; Cui, X. Optical Control of Spin Polarization in Monolayer Transition Metal Dichalcogenides. *ACS Nano* **2017**, *11* (2), 1581–1587.
15. Zhao, Y.; Zhang, S.; Shi, Y.; Zhang, Y.; Saito, R.; Zhang, J.; Tong, L. Characterization of Excitonic Nature in Raman Spectra Using Circularly Polarized Light. *ACS Nano* **2020**, *14* (8), 10527–10535.
16. De Luca, M.; Polimeni, A.; Capizzi, M.; Meaney, A. J.; Christianen, P. C. M.; Maan, J. K.; Mura, F.; Rubini, S.; Martelli, F. Determination of Exciton Reduced Mass and Gyromagnetic Factor of Wurtzite (Inga)as Nanowires by Photoluminescence Spectroscopy under High Magnetic Fields. *ACS Nano* **2013**, *7* (12), 10717–10725.
17. Adhikari, S.; Spaeth, P.; Kar, A.; Baaske, M. D.; Khatua, S.; Orrit, M. Photothermal Microscopy: Imaging the Optical Absorption of Single Nanoparticles and Single Molecules. *ACS Nano* **2020**, *14* (12), 16414–16445.

18. Ghali, M.; Ohtani, K.; Ohno, Y.; Ohno, H. Generation and Control of Polarization-Entangled Photons from GaAs Island Quantum Dots by an Electric Field. *Nat. Commun.* **2012**, *3* (1), 1–6.
19. Fujita, T.; Morimoto, K.; Kiyama, H.; Allison, G.; Larsson, M.; Ludwig, A.; Valentin, S. R.; Wieck, A. D.; Oiwa, A.; Tarucha, S. Angular Momentum Transfer from Photon Polarization to an Electron Spin in a Gate-Defined Quantum Dot. *Nat. Commun.* **2019**, *10* (1), 1–6.
20. Efros, A. L. Fine Structure and Polarization Properties of Band-Edge Excitons in Semiconductor Nanocrystals. In *Nanocrystal Quantum Dots*; Klimov, V. I., Ed.; CRC Press: Boca Raton (U.A.), 2010.
21. Htoon, H.; Furis, M.; Crooker, S. A.; Jeong, S.; Klimov, V. I. Linearly Polarized "fine Structure" of the Bright Exciton State in Individual CdSe Nanocrystal Quantum Dots. *Phys. Rev. B - Condens. Matter Mater. Phys.* **2008**, *77* (3), 035328.
22. Hu, J.; Li Ls; Yang, W.; Manna, L.; Wang Lw; Alivisatos, A. P. Linearly Polarized Emission from Colloidal Semiconductor Quantum Rods. *Science* **2001**, *292* (5524), 2060–2063.
23. Isarov, M.; Tan, L. Z.; Bodnarchuk, M. I.; Kovalenko, M. V.; Rappe, A. M.; Lifshitz, E. Rashba Effect in a Single Colloidal $CsPbBr_3$ Perovskite Nanocrystal Detected by Magneto-Optical Measurements. *Nano Lett.* **2017**, *17* (8), 5020–5026.
24. Becker, M. A.; Vaxenburg, R.; Nedelcu, G.; Sercel, P. C.; Shabaev, A.; Mehl, M. J.; Michopoulos, J. G.; Lambrakos, S. G.; Bernstein, N.; Lyons, J. L.; et al. Bright Triplet Excitons in Caesium Lead Halide Perovskites. *Nature* **2018**, *553* (7687), 189–193.
25. Efros, A.; Rosen, M.; Kuno, M.; Nirmal, M.; Norris, D.; Bawendi, M. Band-Edge Exciton in Quantum Dots of Semiconductors with a Degenerate Valence Band: Dark and Bright Exciton States. *Phys. Rev. B* **1996**, *54* (7), 4843–4856.
26. Furis, M.; Hollingsworth, J. A.; Klimov, V. I.; Crooker, S. A. Time- And Polarization-Resolved Optical Spectroscopy of Colloidal CdSe Nanocrystal Quantum Dots in High Magnetic Fields. *J. Phys. Chem. B* **2005**, *109* (32), 15332–15338.
27. Htoon, H.; Crooker, S. A.; Furis, M.; Jeong, S.; Efros, A. L.; Klimov, V. I. Anomalous Circular Polarization of Photoluminescence Spectra of Individual CdSe Nanocrystals in an Applied Magnetic Field. *Phys. Rev. Lett.* **2009**, *102* (1), 017402.
28. Rice, W. D.; McDaniel, H.; Klimov, V. I.; Crooker, S. A. Magneto-Optical Properties of CuInS2 Nanocrystals. *J. Phys. Chem. Lett.* **2014**, *5* (23), 4105–4109.
29. Fu, M.; Tamarat, P.; Huang, H.; Even, J.; Rogach, A. L.; Lounis, B. Neutral and Charged Exciton Fine Structure in Single Lead Halide Perovskite Nanocrystals Revealed by Magneto-Optical Spectroscopy. *Nano Lett.* **2017**, *17* (5), 2895–2901.
30. Shornikova, E. V.; Biadala, L.; Yakovlev, D. R.; Feng, D.; Sapega, V. F.; Flipo, N.; Golovatenko, A. A.; Semina, M. A.; Rodina, A. V.; Mitioglu, A. A.; et al. Electron and Hole G-Factors and Spin Dynamics of Negatively Charged Excitons in CdSe/CdS Colloidal Nanoplatelets with Thick Shells. *Nano Lett.* **2018**, *18* (1), 373–380.
31. Tamarat, P.; Bodnarchuk, M. I.; Trebbia, J. B.; Erni, R.; Kovalenko, M. V.; Even, J.; Lounis, B. The Ground Exciton State of Formamidinium Lead Bromide Perovskite Nanocrystals Is a Singlet Dark State. *Nat. Mater.* **2019**, *18* (7), 717–724.
32. Pandya, R.; Steinmetz, V.; Puttisong, Y.; Dufour, M.; Chen, W. M.; Chen, R. Y. S.; Barisien, T.; Sharma, A.; Lakhwani, G.; Mitioglu, A.; et al. Fine Structure and Spin Dynamics of Linearly Polarized Indirect Excitons in Two-Dimensional CdSe/CdTe

Colloidal Heterostructures. *ACS Nano* **2019**, *13* (9), 10140–10153.
33. Furdyna, J. K.; Kossut, K. Dilute Magnetic Semiconductors. In *Semiconductors and Semimetals*; Furdyna, J. K., Kossut, J., Ed.; Academic Press, Inc.: New York, 1988; Vol. 25, pp R29–R64.
34. Knowles, K. E.; Nelson, H. D.; Kilburn, T. B.; Gamelin, D. R. Singlet–Triplet Splittings in the Luminescent Excited States of Colloidal Cu^+:CdSe, Cu^+:InP, and $CuInS_2$ Nanocrystals: Charge-Transfer Configurations and Self-Trapped Excitons. *J. Am. Chem. Soc.* **2015**, *137* (40), 13138–13147.
35. Nelson, H. D.; Bradshaw, L. R.; Barrows, C. J.; Vlaskin, V. A.; Gamelin, D. R. Picosecond Dynamics of Excitonic Magnetic Polarons in Colloidal Diffusion-Doped $Cd_{1-x}Mn_xSe$ Quantum Dots. *ACS Nano* **2015**, *9* (11), 11177–11191.
36. Delikanli, S.; Akgul, M. Z.; Murphy, J. R.; Barman, B.; Tsai, Y.; Scrace, T.; Zhang, P.; Bozok, B.; Hernández-Martínez, P. L.; Christodoulides, J.; et al. Mn 2+ -Doped CdSe/CdS Core/Multishell Colloidal Quantum Wells Enabling Tunable Carrier–Dopant Exchange Interactions. *ACS Nano* **2015**, *9* (12), 12473–12479.
37. Nelson, H. D.; Hinterding, S. O. M.; Fainblat, R.; Creutz, S. E.; Li, X.; Gamelin, D. R. Mid-Gap States and Normal vs Inverted Bonding in Luminescent Cu^+- and Ag^+-Doped CdSe Nanocrystals. *J. Am. Chem. Soc.* **2017**, *139* (18), 6411–6421.
38. Shornikova, E. V.; Yakovlev, D. R.; Tolmachev, D. O.; Ivanov, V. Y.; Kalitukha, I. V.; Sapega, V. F.; Kudlacik, D.; Kusrayev, Y. G.; Golovatenko, A. A.; Shendre, S.; et al. Magneto-Optics of Excitons Interacting with Magnetic Ions in CdSe/CdMnS Colloidal Nanoplatelets. *ACS Nano* **2020**, *14* (7), 9032–9041.
39. Kłopotowski; Mikulski, J.; Szymura, M.; Minikayev, R.; Parlińska-Wojtan, M.; Kazimierczuk, T.; Kossut, J. Ultraslow Spin Relaxation Dynamics in Colloidal Copper-Doped CdSe Quantum Dots. *J. Phys. Chem. C* **2020**, *124*, 1042–1052.
40. Najafi, A.; Sharma, M.; Delikanli, S.; Bhattacharya, A.; Murphy, J. R.; Pientka, J.; Sharma, A.; Quinn, A. P.; Erdem, O.; Kattel, S.; et al. Light-Induced Paramagnetism in Colloidal Ag+-Doped CdSe Nanoplatelets. *J. Phys. Chem. Lett.* **2021**, *12*, 2892–2899.
41. Henneberger, F.; Puls, J. Diluted Magnetic Quantum Dots. In *Introduction to the Physics of Diluted Magnetic Semiconductors*; Kossut, K., Gaj, J. A., Eds.; Springer: Heidelberg, 2010.
42. Furdyna, J. K. Diluted Magnetic Semiconductors. *J. Appl. Phys.* **1988**, *64* (4), R29.
43. Vlaskin, V. A.; Barrows, C. J.; Erickson, C. S.; Gamelin, D. R. Nanocrystal Diffusion Doping. *J. Am. Chem. Soc.* **2013**, *135* (38), 14380–14389.
44. Barrows, C. J.; Vlaskin, V. A.; Gamelin, D. R. Absorption and Magnetic Circular Dichroism Analyses of Giant Zeeman Splittings in Diffusion-Doped Colloidal $Cd_{1-x}Mn_xSe$ Quantum Dots. *J. Phys. Chem. Lett.* **2015**, *6* (15), 3076–3081.
45. Gaj, J. A. *Semiconductors and Semimetals*, Vol. 25.; Furdyna, J. K., Kossut, J., Ed.; Academic Press: San Diego, CA, USA, 1988.
46. Hundt, A.; Puls, J.; Henneberger, F. Spin Properties of Self-Organized Diluted Magnetic $Cd_{1-x}Mn_x$ Quantum Dots. *Phys. Rev. B* **2004**, *69* (12), 121309.
47. Fainblat, R.; Frohleiks, J.; Muckel, F.; Yu, J. H.; Yang, J.; Hyeon, T.; Bacher, G. Quantum Confinement-Controlled Exchange Coupling in Manganese(II)-Doped CdSe Two-Dimensional Quantum Well Nanoribbons. *Nano Lett.* **2012**, *12* (10), 5311–5317.
48. Muckel, F.; Yang, J.; Lorenz, S.; Baek, W.; Chang, H.; Hyeon, T.; Bacher, G.; Fainblat, R. Digital Doping in Magic-Sized CdSe Clusters. *ACS Nano* **2016**, *10* (7), 7135–7141.

49. Beaulac, R.; Ochsenbein, S. T.; Gamelin, D. R. Colloidal Transition-Metal-Doped Quantum Dots. In *Nanocrystal Quantum Dots*; Klimov, V. I., Ed.; CRC Press: Boca Raton, FL, 2010; pp 397–453.
50. Merkulov, I. A.; Kavokin, K. V.; Mackh, G.; Kuhn-Heinrich, B.; Ossau, W.; Waag, A.; Landwehr, G.; Yakovlev, D. R. Luminescence Polarization and Spontaneous Lowering of Symmetry Caused by Magnetic-Polaron Formation in Semimagnetic-Semiconductor Quantum Wells. *Phys. Solid State* **1997**, *39* (11), 1859–1863.
51. Keller, D.; Yakovlev, D. R.; König, B.; Ossau, W.; Gruber, T.; Waag, A.; Molenkamp, L. W.; Scherbakov, A. V. Heating of the Magnetic Ion System in (Zn, Mn)Se/(Zn, Be)Se Semimagnetic Quantum Wells by Means of Photoexcitation. *Phys. Rev. B* **2001**, *65* (3), 035313.
52. (52) Reshina, I. I.; Ivanov, S. V. Magnetooptical Properties of a Single CdMnSe/CdMgSe Quantum Well. *Semiconductors* **2008**, *42* (11), 1318–1322.
53. Akimov, I. A.; Godde, T.; Kavokin, K. V.; Yakovlev, D. R.; Reshina, I. I.; Sedova, I. V.; Sorokin, S. V.; Ivanov, S. V.; Kusrayev, Y. G.; Bayer, M. Dynamics of Exciton Magnetic Polarons in CdMnSe/CdMgSe Quantum Wells: Effect of Self-Localization. *Phys. Rev. B* **2017**, *95* (15), 155303.
54. Merkulov, I. A.; Yakovlev, D. R.; Kavokin, K. V; Mackh, G.; Ossau, W.; Waag, A.; Landwehr, G. Hierarchy of Relaxation Times in the Formation of an Excitonic Magnetic Polaron in (CdMn)Te. *JETP Letters*. 1995, p 335.
55. Merkulov, I.; Pozina, G.; Coquillat, D.; Paganotto, N.; Siviniant, J.; Lascaray, J. Parameters of the Magnetic Polaron State in Diluted Magnetic Semiconductors Cd-Mn-Te with Low Manganese Concentration. *Phys. Rev. B - Condens. Matter Mater. Phys.* **1996**, *54* (8), 5727–5731.
56. Beaulac, R.; Schneider, L.; Archer, P. I.; Bacher, G.; Gamelin, D. R. Light-Induced Spontaneous Magnetization in Doped Colloidal Quantum Dots. *Science* **2009**, *325* (5943), 973–976.
57. Rice, W. D.; Liu, W.; Pinchetti, V.; Yakovlev, D. R.; Klimov, V. I.; Crooker, S. A. Direct Measurements of Magnetic Polarons in $Cd_{1-x}Mn_xSe$ Nanocrystals from Resonant Photoluminescence. *Nano Lett.* **2017**, *17* (5), 3068–3075.
58. Lorenz, S.; Erickson, C. S.; Riesner, M.; Gamelin, D. R.; Fainblat, R.; Bacher, G. Directed Exciton Magnetic Polaron Formation in a Single Colloidal Mn^{2+}:CdSe/CdS Quantum Dot. *Nano Lett.* **2020**, *20* (3), 1896–1906.
59. Najafi, A.; Tarasek, S.; Delikanli, S.; Zhang, P.; Norden, T.; Shendre, S.; Sharma, M.; Bhattacharya, A.; Taghipour, N.; Pientka, J.; et al. CdSe/CdMnS Nanoplatelets with Bilayer Core and Magnetically Doped Shell Exhibit Switchable Excitonic Circular Polarization: Implications for Lasers and Light-Emitting Diodes. *ACS Appl. Nano Mater.* **2020**, *3* (4), 3151–3156.
60. Johnston-Halperin, E.; Awschalom, D. D.; Crooker, S. A.; Efros, A. L.; Rosen, M.; Peng, X.; Alivisatos, A. P. Spin Spectroscopy of Dark Excitons in CdSe Quantum Dots to 60 T. *Phys. Rev. B* **2001**, *63* (20), 205309.
61. Furis, M.; Hollingsworth, J. A.; Klimov, V. I.; Crooker, S. A. Time- and Polarization-Resolved Optical Spectroscopy of Colloidal CdSe Nanocrystal Quantum Dots in High Magnetic Fields. *J. Phys. Chem. B* **2005**, *109* (32), 15332–15338.
62. Granados Del Águila, A.; Pettinari, G.; Groeneveld, E.; De Mello Donegá, C.; Vanmaekelbergh, D.; Maan, J. C.; Christianen, P. C. M. Optical Spectroscopy of Dark and

Bright Excitons in CdSe Nanocrystals in High Magnetic Fields. *J. Phys. Chem. C* **2017**, *121* (42), 23693–23704.
63. Yakovlev, D. R.; Ossau, W.; Landwehr, G.; Bicknell-Tassius, R. N.; Waag, A.; Uraltsev, I. N. First Observation and Experimental Proof of Free Magnetic Polaron Formation in CdTe/(Cd, Mn)Te Quantum Wells. *Solid State Commun.* **1990**, *76* (3), 325–329.
64. Yakovlev, D. R. Exciton Magnetic Polarons in Semimagnetic Quantum Wells and Superlattices. *J. Phys. IV JP* **1993**, *3* (5), 67–74.
65. Maksimov, A. A.; Bacher, G.; McDonald, A.; Kulakovskii, V. D.; Forchel, A.; Becker, C. R.; Landwehr, G.; Molenkamp, L. W. Magnetic Polarons in a Single Diluted Magnetic Semiconductor Quantum Dot. *Phys. Rev. B* **2000**, *62* (12), R7767–R7770.
66. Empedocles, S. A.; Norris, D. J.; Bawendi, M. G. Photoluminescence Spectroscopy of Single CdSe Nanocrystallite Quantum Dots. *Phys. Rev. Lett.* **1996**, *77* (18), 3873–3876.
67. Fernée, M. J.; Littleton, B. N.; Cooper, S.; Rubinsztein-Dunlop, H.; Gómez, D. E.; Mulvaney, P. Acoustic Phonon Contributions to the Emission Spectrum of Single CdSe Nanocrystals. *J. Phys. Chem. C* **2008**, *112*, 1878–1884.
68. Dorozhkin, P. S.; Chernenko, A. V.; Kulakovskii, V. D.; Brichkin, A. S.; Maksimov, A. A.; Schoemig, H.; Bacher, G.; Forchel, A.; Lee, S.; Dobrowolska, M.; et al. Longitudinal and Transverse Fluctuations of Magnetization of the Excitonic Magnetic Polaron in a Semimagnetic Single Quantum Dot. *Phys. Rev. B* **2003**, *68* (19), 195313.
69. Archer, P. I.; Santangelo, S. a; Gamelin, D. R. Direct Observation of Sp−d Exchange Interactions in Colloidal Mn 2+ - and Co 2+ -Doped CdSe Quantum Dots. *Nano Lett.* **2007**, *7* (4), 1037–1043.
70. Goldstein, D. H. *Polarized Light*, 3rd ed.; CRC Press: Boca Raton, 2011.

Chapter 4: Photoluminescence Saturation in Quantum-Cutting Yb^{3+}-Doped $CsPb(Cl_{1-x}Br_x)_3$ Nanocrystals: Implications for Solar Downconversion

4.1 Overview

Yb^{3+}-doped halide perovskites have recently emerged as extraordinarily promising materials for solar spectral downconversion applications because of their extremely high photoluminescence quantum yields of nearly 200%, attributable to a highly efficient picosecond quantum-cutting process. One of the major roadblocks to widespread application of these materials is their photoluminescence saturation under modest photoexcitation fluences. In this study, we examine the excitation-fluence dependence of Yb^{3+}-doped $CsPb(Cl_{1-x}Br_x)_3$ nanocrystal photoluminescence to develop a quantitative understanding of this saturation. Facile saturation is observed across a multitude of halide and Yb^{3+} compositions, with specific trends that provide insight into the microscopic mechanism behind this saturation. We show that the data can be simulated well by a kinetic model that introduces a specific new Auger-type cross-relaxation process involving nonradiative energy transfer from photoexcited nanocrystals to Yb^{3+} ions that are already in their luminescent $^2F_{5/2}$ excited state from a previous photoexcitation event. This cross relaxation occurs with a sub-nanosecond rate constant, allowing it to compete with picosecond quantum cutting when excited-state Yb^{3+} is accumulated. These results point to specific strategies for ameliorating photoluminescence saturation in this class of materials, one of which is demonstrated experimentally. The proposed strategies provide guidance for future materials development and application efforts involving these materials.

4.2 Introduction

Quantum-cutting phosphors can absorb single high-energy photons and release that energy by emitting *two* or more lower-energy photons, *i.e.*, they show photoluminescence quantum yields (PLQYs) exceeding 100%. Such materials have been proposed as spectral converters for increasing the solar power-conversion efficiencies of single-junction photovoltaics beyond their thermodynamic limits,[1,2] and they offer new opportunities for photonic energy conversion in photodetection and other novel technologies. Quantum cutters additionally show unique non-

statistical correlations among emitted photons, which could be valuable for quantum information technologies.[3] Originally conceived by Dexter in 1957,[4] quantum cutting requires an unusual combination of electronic and photophysical characteristics that few materials display. Most reports of quantum cutting have involved pairs of lanthanide ions within insulating inorganic matrices, in which one lanthanide (the sensitizer) is used to absorb photons and sensitize the luminescence of the other (the activator).[2] Yb^{3+} is a particularly attractive activator for this purpose because of its lack of upper excited states in the visible/ultraviolet range that could interfere with quantum cutting, and because its ~980 nm $^2F_{5/2} \rightarrow {}^2F_{7/2}$ PL is well matched to the absorption onset of silicon. PLQYs as high as 188% in Tb^{3+}/Yb^{3+}-doped YPO_4,[5] 187% in Tm^{3+}/Yb^{3+}-doped oxyfluoride aluminosilicates,[6] and 167% in Pr^{3+}/Yb^{3+}-doped $GdAl_3(PO_3)_4$,[7] have been measured. Although excellent emitters, such lanthanide ion pairs absorb only weakly because their *f-f* transitions are formally electric-dipole forbidden, making practical solar applications challenging. Introduction of other (non-*f-f*) sensitizers such as Ce^{3+} or organic dyes has improved solar absorption, but at the expense of quantum-cutting efficiency.[8-11]

Recently, this challenge of limited absorption was solved by pairing Yb^{3+} ions with halide perovskite semiconductors in the family of Yb^{3+}-doped $CsPb(Cl_{1-x}Br_x)_3$ nanocrystals (NCs) and thin films.[12-16] As direct-bandgap semiconductors, such halide perovskites have very large absorption cross sections across broad spectral windows,[17-19] making them excellent solar harvesters. Extremely rapid (ps) quantum cutting has been demonstrated in these materials.[13, 14] PLQYs very close to 200% have been measured in both Yb^{3+}-doped $CsPb(Cl_{1-x}Br_x)_3$ NCs and thin films,[13, 14, 16] showing that the effect is a bulk property of this composition. Continuous energy-gap tuning by anion exchange has also been demonstrated in high-PLQY samples, allowing experimental quantum-cutting energy efficiencies to reach nearly their theoretical maximum (unity) at room temperature.[16] For the first time, materials now exist that have suitable absorption and emission characteristics for truly effective solar quantum cutting.

This very strong absorption does come at a cost, however; we have recently noted facile PL power saturation in Yb^{3+}:$CsPb(Cl_{1-x}Br_x)_3$ NCs and thin films.[13, 14] Specifically, a substantial reduction in PLQY is observed under even modest excitation fluences, including at excitation rates relevant to AM1.5 solar irradiation. Power saturation has also been reported for some quantum-cutting materials involving Tb^{3+}/Yb^{3+} pairs, where it has been attributed to a change in the quantum-cutting mechanism itself between low- and high-power regimes.[20-22] Specifically,

predominant participation of an additional virtual excited state at high powers has been invoked to explain the sub-linear power dependence in this regime, but no corroborating evidence for the participation of such a state exists. Collectively, such observations raise fundamental questions about the microscopic origins of the PL power saturation observed in Yb^{3+}:$CsPb(Cl_{1-x}Br_x)_3$ NCs and thin films, as well as practical questions about potential limitations that such saturation may pose for real device applications of these materials. To date, this saturation effect in Yb^{3+}:$CsPb(Cl_{1-x}Br_x)_3$ has not been investigated quantitatively and its microscopic origins remain unexplained. A solid fundamental understanding of its origins and characteristics is needed if the practical challenges to future solar technologies posed by such saturation are to be overcome.

Here, we present results from experiments and kinetic modeling aimed at clarifying the origins of the power saturation observed in Yb^{3+}:$CsPb(Cl_{1-x}Br_x)_3$ NCs. Quantitative PL power-dependence measurements show highly reproducible saturation characteristics across numerous Yb^{3+}:$CsPb(Cl_{1-x}Br_x)_3$ NC compositions, and further demonstrate that these results are essentially indistinguishable from those reported recently for Yb^{3+}:$CsPb(Cl_{1-x}Br_x)_3$ thin films. A novel two-pulse photoexcitation scheme is used to conclusively link this PL saturation with the long excited-state lifetime of Yb^{3+}. These data are then simulated using a kinetic model that includes not just the photoexcitation, quantum-cutting, and PL dynamics quantified in previous experiments,[13, 14] but also two new Auger-type nonradiative cross-relaxation processes that only occur in the scenario of multiple photoexcitations. These simulations allow differentiation between the two cross-relaxation processes and indicate that the active cross-relaxation process specifically involves picosecond energy transfer from a photoexcited NC to an already excited Yb^{3+} dopant to generate a highly excited Yb^{3+} ion that loses its excess energy by phonon emission. Microscopic details of this rapid cross-relaxation process are discussed in relation to the lowest-energy halide-to-metal charge-transfer (LMCT) excited states of Yb^{3+}, which appear to serve as the final state of the cross relaxation. The model further predicts that saturation can be partially ameliorated by increasing the Yb^{3+} concentration, a prediction that is tested and borne out quantitatively by experiment. Finally, general strategies for overcoming power saturation in solar applications of quantum-cutting Yb^{3+}:$CsPb(Cl_{1-x}Br_x)_3$ are proposed and discussed.

4.3 Methods

4.3.1 Materials. Lead acetate trihydrate [$Pb(OAc)_2 \cdot 3H_2O$] (99.9%) was purchased from Baker Chemical; ytterbium acetate hydrate [$Yb(OAc)_3 \cdot xH_2O$] (99.9%) was purchased from Strem

Chemical; Cesium acetate [CsOAc] (99.9%) was purchased Alfa Aesar; anhydrous ethanol (200 proof) was purchased from Decon Laboratories, Inc.; chlorotrimethylsilane (TMS-Cl) (98%) and 1-octadecene (ODE) (90%) were purchased from Acros Organics; bromotrimethylsilane (TMS-Br) (97%), olyelamine (OAm) (70%), oleic acid (OA) (90%), hexanes (99%), and anhydrous ethyl acetate (99%) were purchased from Sigma Aldrich. All chemicals were used as received unless otherwise noted.

4.3.2 Nanocrystal synthesis. Yb^{3+}-doped $CsPbCl_3$ NCs were synthesized according to previously reported procedures.[13, 23] Briefly, 10 mL ODE, 1 mL OAm, 2 mL OA, 0.4 mmol $Pb(OAc)_2 \cdot 3H_2O$, 560 μL of 1 M CsOAc in ethanol, and 0.32 mmol $Yb(OAc)_3 \cdot 3H_2O$ were added to a 100 mL round bottom flask. This solution was stirred and degassed at room temperature for 5 min before heating to 110 °C and degassing for 1 hr. The reaction vessel was then heated to 240 °C under N_2. Upon reaching this temperature, 0.4 mL of TMS-Cl in 1 mL ODE was swiftly injected and the flask was rapidly cooled to room temperature. The crude NC solution was centrifuged for 15 min. The supernatant was discarded and the pellet was resuspended in hexanes. The NCs were then washed with ethyl acetate, resuspended in hexanes, allowed to settle overnight, and then filtered through a 0.2 μm PTFE filter. Undoped $CsPbCl_3$ NCs were synthesized following the procedure reported above except without adding $Yb(OAc)_3 \cdot xH_2O$ to the reaction flask.

Yb^{3+}-doped and undoped $CsPb(Cl_{1-x}Br_x)_3$ NCs were prepared using procedures adapted from our previous reports.[16, 24] Solutions of Yb^{3+}-doped $CsPbCl_3$ NCs were dried, moved into a glovebox, then resuspended in hexanes. Various amounts of 0.1 M TMS-Br in hexanes were added to the NC solutions and left to react overnight. Excess TMS-halide and hexanes were removed by vacuum and the NCs were resuspended in hexane.

4.3.3 General nanocrystal characterization. Absorption spectra were collected with an Agilent Cary 60 spectrometer. Steady-state room-temperature photoluminescence (PL) data were measured using a 5 mW 375 nm laser for excitation and a LN_2-cooled silicon CCD for detection. All spectra were corrected for instrument response. NC TEM images were obtained using an FEI TECNAI F20 microscope operating at 200 kV. Samples for TEM were prepared by dropcasting NC suspensions onto carbon-coated copper grids from TED Pella, Inc. Elemental composition was determined by inductively coupled plasma – atomic emission spectroscopy (ICP-AES, PerkinElmer 8300). Samples were prepared by digesting the NCs in concentrated nitric acid

overnight with sonication. Powder X-ray diffraction of samples dried on Si substrates was measured using a Bruker D8 Advance irradiated using Cu Kα radiation (50 W).

Absolute PLQY measurements were performed on dilute colloidal NC samples dispersed in hexane within a teflon-based integrating sphere. Samples were excited with a 5 mW, 375 nm laser, emitted light was fiber coupled to a spectrometer and detected using a LN_2-cooled silicon CCD. All spectra were corrected for integrating sphere, fiber, lens, grating, and detector spectral response using a radiometric calibration lamp (Ocean Optics, LS-1-Cal).

4.3.4 Time-resolved photoluminescence (TRPL) spectroscopy. For time-resolved NIR luminescence, colloidal NCs in hexane were irradiated with modulated square-wave pulses of 405 nm light so that the NCs were excited continuously for 5 ms followed by a 45 ms off time to ensure complete relaxation of the Yb^{3+} excited state. The NIR luminescence was detected using an InGaAs/InP PMT and a multichannel scalar.

4.3.5 Two-pulse photoluminescence. In the two-pulse experiment, identical NC solutions from the PL power dependence were excited by a pulsed 405 nm laser diode. Two function generators were used to vary the delay time between 100 ns pulses while keeping the time-averaged irradiance constant at 1.6 mW/cm^2. PL intensities were quantified by integrating for 5 s, and the delay time was randomly varied to avoid artifacts.

4.3.6 Photoluminescence power dependence. NC solutions suspended in hexanes at RT were placed in a sealed 1 mm quartz cuvette. NC concentrations were adjusted so that the optical density was ~0.25 at the excitation wavelength. A brass foil plate with a 500 μm pinhole was mounted on the outside of the cuvette. Excitation and PL collection were both performed through the pinhole to ensure a uniform excitation rate across the excited area and to reduce the effects of scattering. A 405 nm laser diode was used for photoexcitation. The excitation beam was collimated to a diameter of ~3 mm and directed to the sample at an angle of ~20˚ from the collection axis. Irradiance was adjusted by passing the excitation beam through a variable neutral density filter wheel and additional neutral density filters as needed. Laser power densities between 0.01 and 3000 mW/cm^2 were measured with a Coherent Lab-max power meter using an LM-2 Vis head. Powers were then converted to a photon flux, f_{ex}, and these were used to calculate the NC excitation rates, $k_{ex} = \sigma f_{ex}$, using the $CsPbCl_3$ NC absorption cross section, σ, at 405 nm. Absorption cross sections were determined using the ratio of the absorption at 405 and 365 nm along with the previously reported[13] $CsPbCl_3$ cross section of 4.20 x 10^{-14} cm^2 at 365 nm. $CsPb(Cl_{1-x}Br_x)_3$ NC

absorption cross sections at 405 nm were determined by extrapolating the cross section of the pure $CsPbCl_3$ NCs *via* the absorption spectra taken of $CsPb(Cl_{1-x}Br_x)_3$ NCs during a continuous anion exchange from $CsPbCl_3$ to $CsPbBr_3$.[16] All variable-power measurements reported here were performed by increasing the laser power across the full power range and then returning to the low-power regime to confirm that no laser degradation had occurred. As a cross-check, power dependence measurements were also made using dropcast thin films of Yb^{3+}-doped $CsPbCl_3$ NCs with a smaller optical density. These measurements are shown in Figure C3.

4.3.7 Modeling and simulation. Data simulations were performed by solving simultaneous differential equations used to quantify the population distributions among ground and various electronic excited states, as detailed in the Appendix C.

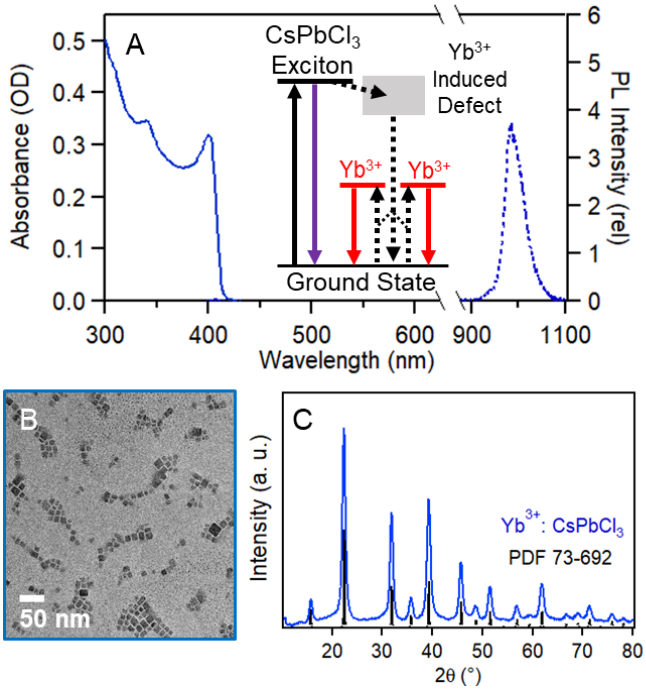

Figure 4.1 Physical characterization and energy level diagram of Yb^{3+} doped $CsPbCl_3$ NCs. (A) Room-temperature absorption (solid) and photoluminescence (dashed) spectra of 1.4% Yb^{3+}:$CsPbCl_3$ NCs suspended in hexane. Inset: Energy level diagram depicting the processes involved in Yb^{3+} sensitization. (B) TEM image of the Yb^{3+}:$CsPbCl_3$ NCs from panel A. (C) Powder XRD data for the same Yb^{3+}:$CsPbCl_3$ NCs. A reference $CsPbCl_3$ diffraction pattern is included for comparison.

4.4 Results

Following our previous reports,[13, 16] colloidal Yb^{3+}:$CsPbCl_3$ NCs were prepared that display PLQYs as high as ~175% without further processing, and as high as ~200% following post-synthetic optimization. Figure 4.1A shows room-temperature absorption and PL spectra of a representative sample of colloidal 1.4% Yb^{3+}:$CsPbCl_3$ NCs suspended in hexane. The PL spectrum is dominated by an intense NIR feature centered at ~980 nm, corresponding to the $^2F_{5/2} \rightarrow {}^2F_{7/2}$ *f-f* emission of Yb^{3+}. The PLQY of this sample was 146%, measured at an excitation rate of 150 photons NC^{-1} s^{-1}. Very weak band-edge excitonic luminescence at 410 nm is also observed. Figures 4.1B and C show transmission electron microscopy (TEM) images and X-ray diffraction (XRD) data collected for the same NCs. The NCs are cube-like crystallites with average edge lengths of ~11 nm, and they show XRD features consistent with the perovskite crystal structure. Although some NCs appear to be much larger than the average size, we note that the optical characteristics of these NCs are not size dependent in this size regime because the Bohr exciton radius of $CsPbCl_3$ NCs is ~2.5 nm.[25] For example, essentially indistinguishable results are obtained from bulk films with much larger grain sizes.[14]

Figure 4.2 summarizes the photoexcitation power dependence of the Yb^{3+} PL intensity from the Yb^{3+}:$CsPbCl_3$ NC sample described by Figure 4.1. Figure 4.2A shows the NIR PL spectra measured at several CW photoexcitation powers. Figure 4.2B plots the integrated Yb^{3+} PL intensities *vs* NC excitation rate constant, defined as $k_{ex} = \sigma f_{ex}$, where σ is the NC absorption cross section at the excitation wavelength and f_{ex} is the photon flux. A value of $\sigma \sim 4.3 \times 10^{-14}$ cm^2 at 405 nm was determined from the absorption cross section at 365 nm for similar undoped $CsPbCl_3$ NCs.[13] At small k_{ex} (inset), I_{Yb} increases linearly with increasing k_{ex}. At larger k_{ex}, however, I_{Yb} begins to saturate and its dependence on k_{ex} becomes sub-linear.

Figure 4.2C presents the same data as a log-log plot. At low k_{ex}, the slope of this curve is close to unity, but at $k_{ex} \sim 10^3$ s^{-1} this slope decreases markedly. Figure 4.2D presents the same data as a semi-log plot. Although absolute PLQYs weren't measured for every excitation rate, the PLQY is proportional to I_{Yb}/k_{ex}, allowing the same data to be plotted as PLQYs *vs* k_{ex}, normalized to the PLQY at k_{ex} = 0-10 s^{-1}. Varying the excitation rate over several orders of magnitude shows that the Yb^{3+} PLQY changes continuously from its maximum value in the low-power limit to its minimum value at $k_{ex} > 10^5$ s^{-1}. At the highest excitation rates measured here, the PLQY is only ~5% of its initial value. These data agree well with our previously published PLQY power-

dependence data, some of which are reproduced in Figure 4.2D for comparison.

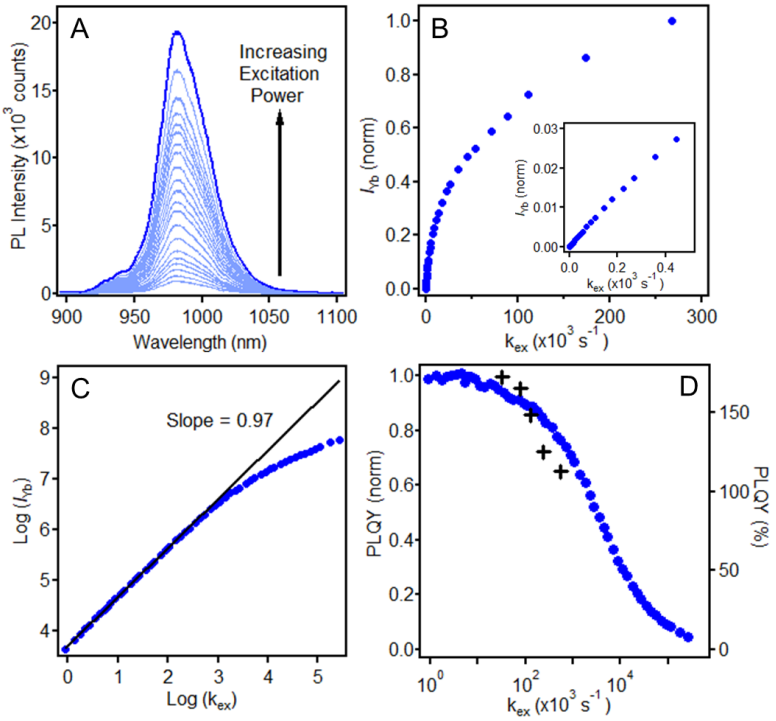

Figure 4.2 Excitation power depenedence of the Yb^{3+} NIR emission. (A) Room-temperature PL spectra of the Yb^{3+}:$CsPbCl_3$ NCs from Figure 4.1, collected as a function of increasing photoexcitation power from a 405 nm CW laser diode. (B) Integrated Yb^{3+} PL intensities (I_{Yb}) from the data in panel A, plotted as function of the NC photoexcitation rate constant (k_{ex}). Inset: Expanded view of the same data between k_{ex} = 0 and 500 s^{-1}. (C) Log-log plot of I_{Yb} from Figure 4.2B. The solid line shows a fit of the data at small k_{ex} to a straight line. (D) Semi–log plot of the normalized PLQY, obtained by dividing I_{Yb} by k_{ex} and normalizing in the low-power limit (blue symbols, left axis). For reference, the *absolute* PLQYs of Yb^{3+}:$CsPbCl_3$ NCs measured as a function of k_{ex}, taken from ref. [13], are also included (black symbols, right axis).

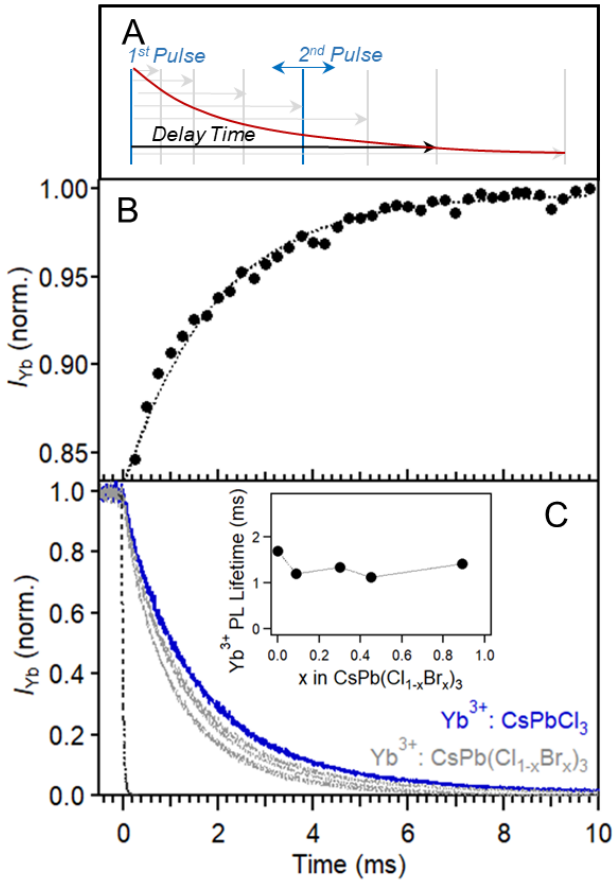

Figure 4.3 Variable delay two-pulse photoluminesence of Yb^{3+} doped $CsPbCl_3$ NCs. (A) Schematic of the variable-delay two-pulse PL experiment. The first pulse excites the NCs and establishes a decaying excited-state population. The second pulse photoexcites already-excited NCs, which leads to a reduced PLQY. The pairs of pulses are separated by long dark times (> 10 ms), and the time-averaged excitation power density is held constant, independent of inter-pulse delay. Variation of the inter-pulse delay time allows the lifetime of the relevant intermediate state to be identified. (B) Results from the variable-delay two-pulse PL experiment depicted in panel A. I_{Yb} from Yb^{3+}:$CsPbCl_3$ NCs was measured at a constant time-averaged excitation power density of 1.6 mW/cm^2, but with different delay times between 150 fs excitation pulses. The time between pulses was varied between 0.1 and 10 ms. The circles plot I_{Yb} *vs* the inter-pulse delay time. The dashed curve shows a fit of these data to a single-exponential function, yielding τ = 1.9 ms. (C) Yb^{3+} $^2F_{5/2} \rightarrow {}^2F_{7/2}$ PL decay dynamics measured for several Yb^{3+}:$CsPb(Cl_{1-x}Br_x)_3$ NCs with different x values, including Yb^{3+}:$CsPbCl_3$ NCs (blue). Inset: Average Yb^{3+} PL decay times obtained from fitting of the decay data in the main panel to a bi-exponential function, plotted *vs* the halide composition parameter, x.

As mentioned above, sub-linear power dependence has been observed previously in Tb^{3+}/Yb^{3+} quantum-cutting pairs at high excitation rates and explained in terms of a quantum-cutting mechanism involving population of a short-lived virtual excited state of Tb^{3+},[20-22] but independent corroboration of this mechanism is lacking. It is also difficult to reconcile the very short lifetimes of virtual states with the small multi-polar energy-transfer rates between trivalent lanthanides. To explain the PL saturation observed in Figure 4.2, we instead propose that at large k_{ex} values there is a substantial probability of photoexciting NCs that already contain Yb^{3+} ions in their $^2F_{5/2}$ electronic excited state from a previous photoabsorption event, and that this second photoexcitation does not generate further Yb^{3+} excitation because of an efficient non-radiative deactivation mechanism involving this excited-state Yb^{3+}. This proposal comes from an experiment we performed involving pairs of excitation pulses delivered to Yb^{3+}:$CsPbCl_3$ NCs with tunable inter-pulse delays, as illustrated schematically in Figure 4.3A. The first pulse establishes a population of photoexcited NCs, and some fraction of the photons from the second pulse excite NCs that are already in an electronic excited state from the first pulse. Keeping the time-averaged power constant while varying the inter-pulse delay allows the relevant lifetime associated with PL saturation to be identified. Figure 4.3B plots I_{Yb} as a function of the delay time between excitation pulses. When the pulses are separated by long times, *e.g.,* 9 ms, there is little dependence of I_{Yb} on the inter-pulse delay time. As the inter-pulse delay is shortened, I_{Yb} decreases. The dependence of I_{Yb} on the inter-pulse delay time can be fit to a single exponential with a time constant of ~1.9 ms. These dynamics are essentially identical to those measured for the Yb^{3+} PL decay of these and related Yb^{3+}:$CsPb(Cl_{1-x}Br_x)_3$ NCs, all of which show similar lifetimes (Figure 4.3C). The agreement between these two dynamics indicates that the saturation of I_{Yb} with increasing k_{ex} stems from photoexcitation of NCs that already possess Yb^{3+} ions in their emissive $^2F_{5/2}$ *f-f* excited state, and it rules out other potential explanations of these data such as a high-power mechanism involving short-lived virtual excited states like that postulated for Tb^{3+}/Yb^{3+} quantum-cutting pairs,[20-22] or participation of metastable charge-separated states such as those responsible for delayed luminescence and blinking in halide perovskite and many similar semiconductor NCs.[26-29] We thus conclude that the power saturation observed in the PL of quantum-cutting Yb^{3+}:$CsPb(Cl_{1-x}Br_x)_3$ NCs stems directly from the long lifetime of the emissive Yb^{3+} $^2F_{5/2}$ excited state.

Figure 4.4A plots absorption and normalized PL spectra of 1.4% Yb^{3+}:$CsPb(Cl_{1-x}Br_x)_3$ NCs at several values of *x*. This entire series of compositions was made by partial anion exchange from the same starting Yb^{3+}:$CsPbCl_3$ NCs, and ICP experiments show that the Yb^{3+} concentration doesn't change during this anion exchange.[16] Figure 4B plots power saturation data for each of the samples shown in Figure 4.4A. Each data set is normalized to its value of I_{Yb} at $k_{ex} = 2x10^5$ s^{-1}. Figure 4.4C shows a semi-log plot of the same data. Notably, all Yb^{3+}:$CsPb(Cl_{1-x}Br_x)_3$ NCs show very similar power dependence. The power saturation is almost independent of the anion composition, *x*, including for the weak PL of the Yb^{3+}:$CsPbBr_3$ NCs that is not generated by quantum cutting. This result is consistent with the observations from Figure 4.3 that saturation is determined by the long Yb^{3+} lifetime (Figure 3B), and that the Yb^{3+} lifetime varies little with anion composition (Figure 4.3C).

The data above demonstrate facile saturation of the Yb^{3+} PL in quantum-cutting Yb^{3+}:$CsPb(Cl_{1-x}Br_x)_3$ NCs. For this power saturation to be so pronounced, photoexcitation of NCs that already possess photoexcited Yb^{3+} must introduce an efficient nonradiative relaxation pathway that does not exist in the same NC when excited only once. Such nonradiative decay can occur *via* an Auger-type cross relaxation. To examine this scenario quantitatively, a kinetic model was developed based upon a similar model that was used to describe PL saturation in Mn^{2+}-doped chalcogenide NCs.[30] Figure 4.5A illustrates a general kinetic scheme that describes the quantum cutting dynamics reported for these NCs previously.[13] Here, photoexcitation (k_{ex}) of a NC containing *n* Yb^{3+} dopants leads to rapid (ps) formation of two excited Yb^{3+} ions *via* quantum cutting (k_{QC}). These Yb^{3+} ions relax back to the ground state *via* luminescence (k_{Yb}) with ms time constants. Quantum cutting competes with direct relaxation of the NC back to the ground state (k_{NC}, both radiative and nonradiative), which occurs with ps to ns time constants. All of these processes have been characterized experimentally.[13,14]

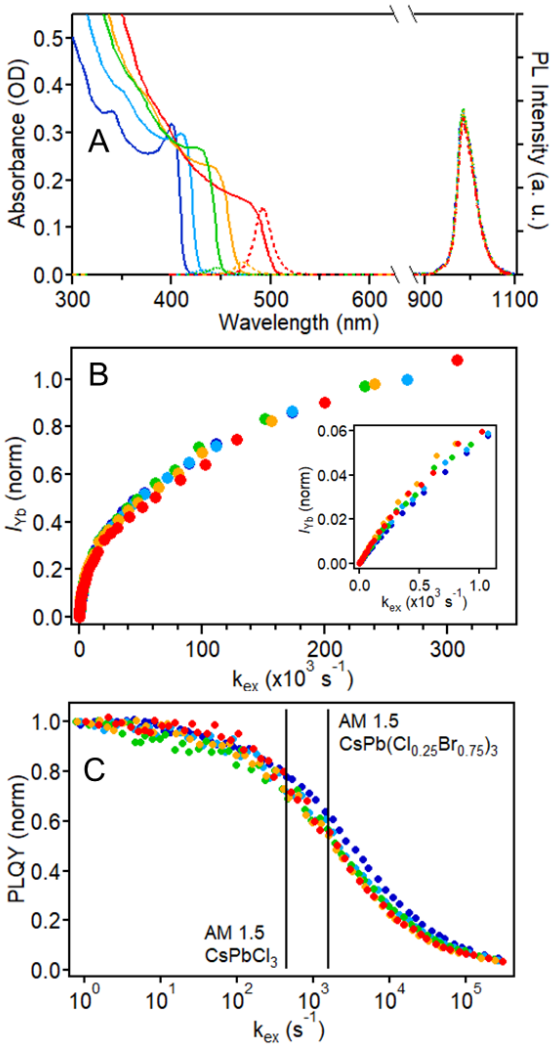

Figure 4.4 Absorption, steady-state photoluminescence, and power dependent photoluminescence of a series of Yb^{3+} doped $CsPb(Cl_{1-x}Br_x)_3$ NCs. (A) Absorption (solid) and PL (dashed) spectra of Yb^{3+}:$CsPbCl_3$ (dark blue) and Yb^{3+}:$CsPb(Cl_{1-x}Br_x)_3$ NCs (colors). The latter were synthesized *via* anion exchange of the Yb^{3+}:$CsPbCl_3$ NCs. For each sample presented, all PL intensities are normalized to the Yb^{3+} PL intensity at 985 nm and low photoexcitation power. Excitonic PL is observed for all Yb^{3+}:$CsPb(Cl_{1-x}Br_x)_3$ NCs, but it is weaker at smaller x. (B) I_{Yb} plotted *vs* k_{ex} for the samples shown in panel A. Inset: Expanded view of the data and simulation for k_{ex} between 0 and 1100 s^{-1}. (C) Semi-log plot of the normalized PLQY, obtained by dividing I_{Yb} from panel B (colors) by k_{ex} and normalizing to the average value in the low photoexcitation power limit. AM1.5 photoexcitation rates, determined by integrating the AM 1.5 solar spectrum over the absorption range of $CsPbCl_3$ and $CsPb(Cl_{1-x}Br_x)_3$ NCs, are included for reference.

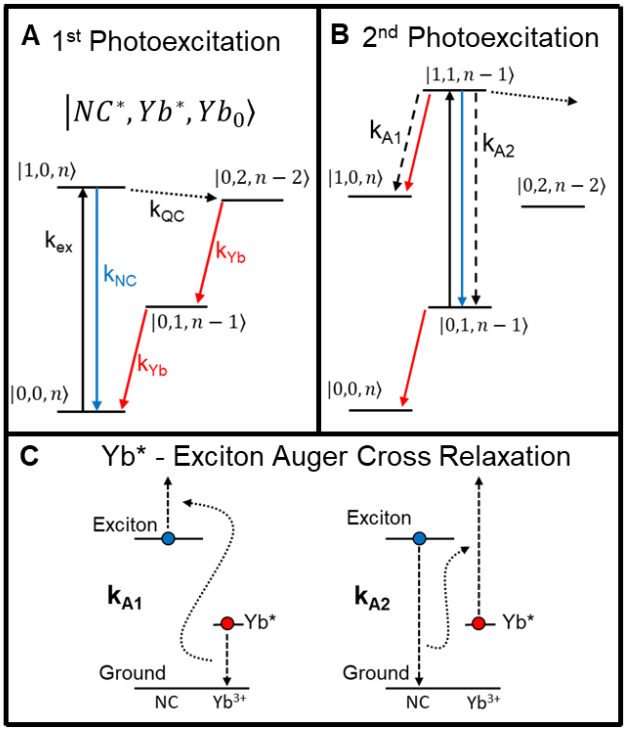

Figure 4.5 Energy level diagram depicting the relevant excitation and decay pathways for low and high power excitation of Yb^{3+} doped NCs. (A) Depiction of the kinetics relevant to low-power photoexcitation of Yb^{3+}:$CsPbCl_3$ NCs. NC photoexcitation generates excitons with a rate constant of k_{ex} (solid black arrow). Following photoexcitation, the NC relaxes by quantum cutting to generate a pair of excited Yb^{3+} ions, described by k_{QC} (dashed black arrow). Excited Yb^{3+} ions then relax to the ground state *via* $^2F_{5/2} \rightarrow {}^2F_{7/5}$ decay, represented by k_{Yb} (red arrow). The photoexcited NCs can also relax directly to the ground state (k_{NC}, blue arrow). (B) Depiction of photoexcitation of an Yb^{3+}:$CsPbCl_3$ NC that already contains an excited Yb^{3+} ion. In addition to the processes described in panel A, two new Auger cross-relaxation processes are now possible, described by k_{A1} or k_{A2} (dashed arrows). k_{A1} describes energy transfer from the excited Yb^{3+} ion to the NC to generate a hot exciton, and k_{A2} describes energy transfer from the NC to the Yb^{3+} ion to generate Yb^{3+} in an upper excited state. (C) Schematic illustrations of the two Auger cross-relaxation processes, described by k_{A1} and k_{A2}. NC excitation levels are parameterized by the populations of excitons (NC*), excited-state Yb^{3+} (Yb*), and ground-state Yb^{3+} (Yb_0), $|\boldsymbol{NC^*, Yb^*, Yb_0}\rangle = |\boldsymbol{N_1, y_1, y_0}\rangle$, where Yb* + Yb_0 = y_1 + y_0 = n.

The data in Figure 4.3 demonstrate that saturation is associated with photoexcitation of NCs that already possess excited-state Yb^{3+} ions from a previous photoexcitation event, and Figure 4.5B depicts the various processes that can occur in this situation. When the second photon is absorbed by the NC, the excited NC may still relax *via* the processes outlined in Figure 4.5A (k_{NC} or k_{QC}), but these processes must now compete with the two new Auger cross-relaxation processes depicted in Figure 4.5C. In the first, the excited Yb^{3+} ion transfers its energy to the NC to generate a hot exciton and the ground-state Yb^{3+}. The hot exciton can then cool to the band edge and relax *via* the processes described in Figure 4.5A, including *via* quantum cutting to yield two excited Yb^{3+} ions. In the second, the energy of the exciton is instead transferred non-radiatively to the excited Yb^{3+} dopant to generate the ground-state NC and a highly excited Yb^{3+} ion. This highly excited Yb^{3+} can then relax back to its $^2F_{5/2}$ excited state *via* internal conversion and phonon emission, from which it can emit a photon. These cross-relaxation processes only occur when the excitation rate is large enough that the NC absorbs a photon within the excited-state lifetime of the Yb^{3+} dopant (Figure 4.3). It is conceivable that the non-radiative process could instead be initiated by excited-state absorption promoting Yb^{3+} directly from its $^2F_{5/2}$ state into an LMCT state, but the molar extinction of such a localized transition (~160 M^{-1} cm^{-1})[31] is several orders of magnitude smaller than that of the $CsPb(Cl_{1-x}Br_x)_3$ NC band-to-band transition (~10^5 M^{-1} cm^{-1})[19] at the same energy, allowing this process to be ruled out.

Eqs 4.1 and 4.2 provide generalized descriptions of the population dynamics for individual NCs in terms of coupled differential equations describing the Yb* population (y_1) and the excited-state NC population, NC*, in terms of their generation and loss rates. Here, k_{ex} is the excitation rate constant, k_{QC} is the fundamental quantum-cutting rate constant, and k_{NC} is the rate constant for NC relaxation. The NC contains n Yb^{3+} dopants, with $y_1 = 0, 1, 2, \ldots, n$ in their excited ($^2F_{5/2}$) state and $y_0 = n, n\text{-}1, n\text{-}2, \ldots, 0$ in their ground ($^2F_{7/2}$) state depending on k_{ex} and the values of the other rate constants. The number of excitons per NC equals 0 or 1 for all conditions examined here, indicated as N_0 or N_1, respectively. Because of the long Yb^{3+} excited-state lifetime, continuous photoexcitation can in principle generate NCs with multiple excited Yb^{3+} ions, and eqs 4.1 and 4.2 describe this "staircase" of doped-NC excitation levels, each defined by its respective dopant and NC excited-state populations, *i.e.*, $|NC^*, Yb^*, Yb_0\rangle = |N_1, y_1, y_0\rangle$. As the Yb* population increases, the rate of quantum cutting is reduced and cross relaxation accelerates, reducing the quantum-cutting efficiency. Solving eqs 4.1 and 4.2 for continuous photoexcitation provides the

steady-state populations of each level in the excitation "staircase". Complete details of the modeling are provided in Appendix C.

$$\frac{dy_1}{dt} = k_{QC}N_1\frac{y_0}{2} - k_{A1}y_1N_1 - k_{Yb}y_1 \quad (4.1)$$

$$\frac{dN_1}{dt} = k_{ex}N_0 - k_{QC}N_1\frac{y_0}{2} - k_{NC}N_1 - k_{A2}y_1N_1 \quad (4.2)$$

In formulating the above model, we have assumed that thermalization is rapid relative to PL, quantum cutting, or cross relaxation, that k_{ex} does not depend on y_1 or y_0, and that Yb^{3+} concentration quenching and Yb*-Yb* annihilation are negligible. All three assumptions appear reasonable based on available data. For example, Yb^{3+} PL decay times are not concentration dependent over the range studied here,[13] or dependent on anion composition (Figure 4.3C, inset). Less obvious is how to treat the ensemble of Yb^{3+} activator ions in this model, because this quantum cutting involves simultaneous energy transfer to two Yb^{3+} ions but it is not clear *a priori* whether those two ions have any special relationship to one another. Previously, we proposed[13] that the microscopic quantum-cutting mechanism here involves shallow trapping by charge-neutral Yb^{3+}-V_{Pb}-Yb^{3+} defect clusters that promote fast energy transfer to the two Yb^{3+} ions in the cluster, but it is also conceivable that quantum cutting could involve *any* two Yb^{3+} ions within a given Yb^{3+}:$CsPbX_3$ NC. We therefore explicitly modeled these two different quantum-cutting scenarios to attempt to differentiate them. In the former scenario, the effective quantum-cutting rate constant is proportional to the number of ground-state Yb^{3+} ions: $k'_{QC} = (y_0/2)k_{QC}$. In the latter scenario, there are many more possible pairwise combinations, and $k'_{QC} = y_0!/(2(y_0\text{-}2)!)k_{QC}$. These two scenarios are clearly differentiated by the much stronger and nonlinear Yb^{3+} concentration dependence of the latter, which contradicts the weaker and linear Yb^{3+} concentration dependence observed experimentally,[13, 14] allowing that second scenario to be ruled out (see Appendix C, Figure C2). The full model is described in detail in Appendix C.

The data in Figure 4.2 were simulated using this kinetic model, for NCs with $n = 100$ Yb^{3+} ions/NC. Using the experimentally determined rate constants of $k_{Yb} = 500$ s^{-1}, $k_{NC} = 10^8$ s^{-1}, and $k'_{QC} = (y_0/2)k_{QC} = 10^{10}$ s^{-1}, and introducing either k_{A1} or k_{A2} as the only unknown, saturation curves were calculated and compared with the experimental data. Note that the experimental picosecond quantum-cutting dynamics reflect the *effective* rate constant defined above, k'_{QC}. Figures 4.6A,B

plot calculated curves over broad ranges of the ratios k_{A1}/k_{QC} and k_{A2}/k_{QC}, respectively. Both sets of simulations show that increasing power increases the Yb* population per NC. In the absence of cross relaxation (k_{A1}/k_{QC} and k_{A2}/k_{QC} equal zero), the Yb* population would continue to increase until all Yb^{3+} ions are in the $^2F_{5/2}$ excited state and no more can be excited. Under realistic conditions, however, the Yb* population is always limited to much smaller values because of cross relaxation, which makes the PL saturate when only a subset of Yb^{3+} ions are in their excited state. Interestingly, the power dependence predicted with a non-zero k_{A1} is significantly different from that predicted with a non-zero k_{A2}; whereas simulations with non-zero k_{A2} reproduce the experimental observation of gradually increasing PL intensity even at high excitation rates, simulations using k_{A1} show abrupt saturation at high power. This difference arises from the competition between Auger and quantum-cutting processes. For k_{A1}, each Auger cross relaxation eliminates one Yb*, decreasing y_1. As y_1 increases with increasing k_{ex}, cross relaxation accelerates relative to quantum cutting until the rates of these two processes become equal, causing the Yb^* population to plateau. For k_{A2}, however, cross relaxation does not directly affect y_1 but only reduces the probability of further quantum cutting; quantum cutting becomes increasingly unlikely at high excitation rates, but it is still possible, and consequently a slow buildup of Yb* is still observed. We cannot categorically rule out *any* cross relaxation following the A1 pathway, but comparison of the simulated curves with the experimental data allows the conclusion that PL saturation in Yb^{3+}:$CsPbX_3$ NCs proceeds predominantly by process A2.

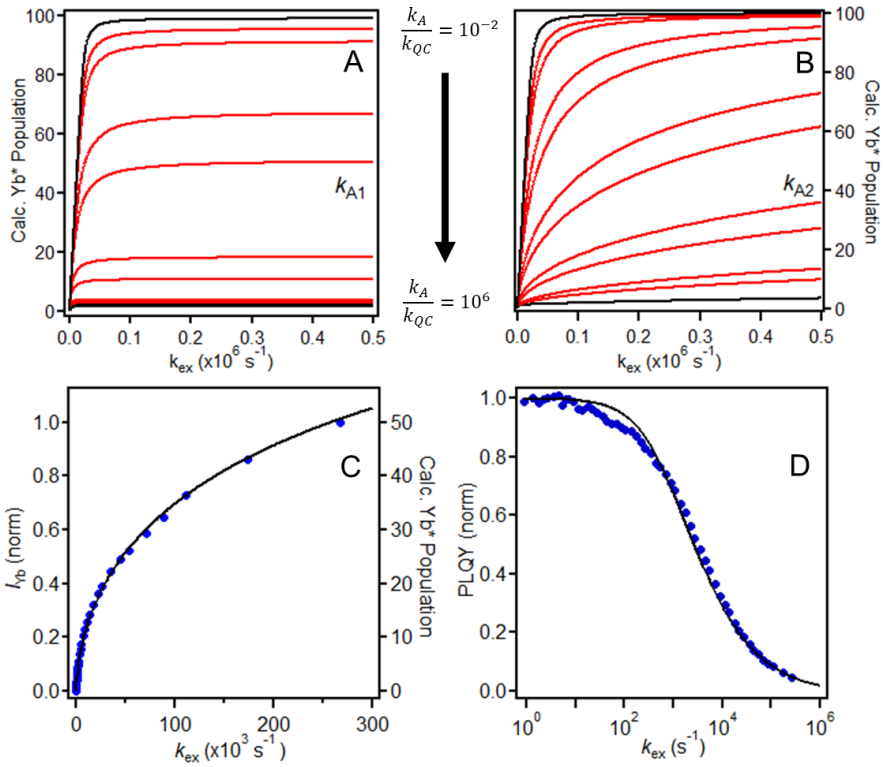

Figure 4.6 Simulated power dependence based on model described in text with experimental photoluminescence power dependence. Simulations of NC power dependence using the kinetic model described in Figure 4.5 and the SI, and parameters n = 100 Yb^{3+} dopants, k_{Yb} = 500 s^{-1}, k_{NC} = 10^8 s^{-1}, and k_{QC} = 10^8 s^{-1}, with either k_{A1} or $k_{A2} \neq 0$. (A) Simulations using k_{A2} = 0 and k_{A1}/k_{QC} varying from < 0.01 to > 10^6. (B) Simulations using k_{A2}/k_{QC} varying from < 0.01 to > 10^6 and k_{A1} = 0. (C) Simulated experimental power dependence, using the data from Figure 4.2 plotted on linear axes using the parameters above and k_{A2} = 10^{10} s^{-1} (k_{A2}/k_{QC} = 100). (D) Simulated experimental power dependence using the same data plotted with a logarithmic x axis and a power-normalized y axis.

Figure 4.6C,D compares the PL power dependence simulated using the above experimental parameters plus k_{A2} = 10^{10} s^{-1} with the experimental results from Figure 4.2, plotted in two different representations. The simulations reproduce the data very well in both the low- and high-power regimes, and in both the linear and semi-log representations. From these simulations we can conclude that at saturation, cross relaxation must be substantially more rapid than quantum cutting,

such that further photoexcitation has a small probability of generating additional Yb*. We also find that the cross-relaxation rate does not exceed the quantum-cutting rate for these NCs until ~20% of the Yb^{3+} ions are in their $^2F_{5/2}$ excited state, meaning that quantum cutting is in fact reasonably competitive with cross relaxation. This conclusion is one of the major new microscopic insights drawn from these simulations.

In light of the above conclusion, we hypothesized that it should be possible to shift the competition between cross relaxation and quantum cutting by increasing the Yb^{3+} concentration, because the model predicts that higher Yb^{3+} concentrations should selectively accelerate quantum cutting without affecting the other processes. To test this hypothesis, power saturation data were collected for a series of Yb^{3+}:$CsPbCl_3$ NCs with different Yb^{3+} dopant concentrations. Figure 4.7A plots I_{Yb} as a function of k_{ex} for this series. As the Yb^{3+} concentration is increased, a larger value of k_{ex} is required to observe to same degree of saturation. For ease of comparison, Figure 4.7B plots the value of k_{ex} required to reduce the normalized PLQY to 75% of its value at low power ($I_{3/4}$). Increasing the Yb^{3+} concentration gradually increases k_{ex} at $I_{3/4}$, roughly doubling the excitation rate required to achieve the same level of saturation upon increasing from 0.7 to 5.7% Yb^{3+}. This experimental trend is almost exactly predicted by the kinetic model (Figure 4.6B).

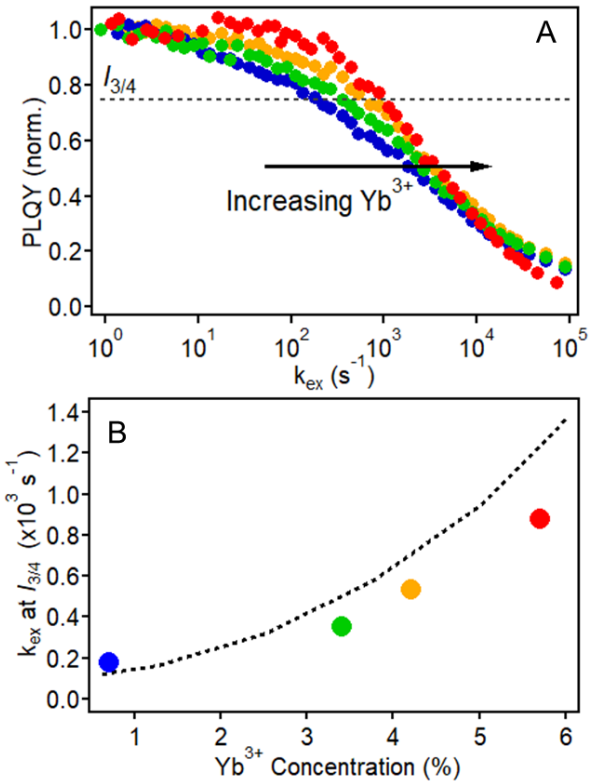

Figure 4.7 Power dependent photoluminescence of a series of Yb^{3+} doped $CsPb(Cl_{1-x}Br_x)_3$ NCs. (A) Semi-log plot of the normalized PLQY plotted *vs* k_{ex} for four Yb^{3+}-doped $CsPbCl_3$ NC samples with different Yb^{3+} concentrations: 0.7% (blue), 3.4 % (green), 4.2% (orange), and 5.7% (red), all normalized at the lowest excitation rate. The black dashed line depicts a normalized PLQY of 0.75, denoted $I_{3/4}$. (B) Plot of k_{ex} at $I_{3/4}$ *vs* Yb^{3+} concentration for the four samples shown in panel A. The dashed curve plots the trend predicted from the kinetic model using the same parameters as used in Figure 4.6 and varying only the Yb^{3+} concentration.

4.5 Discussion

4.5.1 Fast Auger cross relaxation. Luminescence saturation phenomena have posed serious challenges for many practical applications of bulk phosphors for decades.[32] Most classic phosphors used in display and lighting technologies show luminescence saturation under high rates of photo-, cathode-ray, or electrical excitation.[32-34] Efficiency droop in light-emitting diodes is another a well-known example. Luminescence saturation is frequently associated with either energy migration among phosphor activators (A) followed by nonradiative A*−A* cross relaxation, or with A*−carrier Auger-type cross relaxation. Such processes are exacerbated by the

long excited-state lifetimes of many phosphors.

The data and analysis presented above demonstrate the existence of an efficient non-radiative deactivation process that causes photoluminescence saturation in Yb^{3+}:$CsPb(Cl_{1-x}Br_x)_3$ NCs at relatively low excitation rates. A*−A* cross relaxation can be ruled out as the cause because the Yb^{3+} excited-state lifetime shows no concentration dependence over the experimental concentration range.[13] Instead, the analysis here specifically points to a cross-relaxation process involving energy transfer from photoexcited NCs (NC*) to Yb^{3+} ions that are already in their luminescent $^2F_{5/2}$ excited state (Yb*), thereby intercepting NC* before quantum cutting can occur. For such NC*-Yb* cross relaxation to cause luminescence saturation, the cross-relaxation rate must rival or exceed the quantum-cutting rate, *i.e.*, surprisingly large given that quantum cutting in this system has a fundamental rate constant of ~10^8 s^{-1}. The model can account for both the variable-photoexcitation-rate data and Yb^{3+} concentration effects using a fundamental cross-relaxation rate constant of $k_{A2} = 10^{10}$ s^{-1} ($k_{A2}/k_{QC} = 100$). This cross-relaxation rate constant is very similar in magnitude to those deduced previously for CB electron-Mn* cross relaxation in doped II-VI semiconductors,[30] as well as for biexciton, trion, and trap-assisted Auger recombination in colloidal quantum dots of various types.[35-39] NC*-Yb* cross relaxation differs from these other cases in that the spectroscopically active *f* orbitals are highly shielded, and NC-Yb^{3+} electronic coupling is therefore expected to be small. Additionally, the Yb^{3+} *f-f* transitions are electric-dipole forbidden to first order, possessing very small transition probabilities, which should slow any cross-relaxation process involving those transitions.

The question then arises: *why* is this NC*-Yb* Auger-type cross relaxation so fast? The answer to this question is revealed by the differences between simulations using the A1 and A2 cross-relaxation channels, which show that A2 is dominant. The A2 cross relaxation involves transfer of NC* energy *to* Yb*, rather than the other direction. We postulate that the dominance of this pathway stems in large part in the fact that for all halide compositions, the $CsPb(Cl_{1-x}Br_x)_3$ band-gap energy is almost perfectly matched with the halide-to-Yb^{3+} charge-transfer transition energy when starting from the $^2F_{5/2}$ excited state of Yb^{3+}, *i.e.*, $E_g + E_{5/2} = E_{LMCT}$ (Figure 4.8 A-C). For example, a broad and intense LMCT absorption band is observed in bulk $YbCl_3$ centered around E_{LMCT} ~ 36,000 cm^{-1} (width of ~4,800 cm^{-1}).[31, 40] A very similar E_{LMCT} is anticipated in Yb^{3+}:$CsPbCl_3$. As illustrated in Figure 4.8C, energy transfer from the $CsPbCl_3$ absorption edge to an excited Yb^{3+} ion would place the system squarely within such an LMCT band, *i.e.*, 24,350 cm^{-}

^{1} + 10,200 cm^{-1} ≈ 36,000 cm^{-1}. The LMCT band thus provides a high density of resonant final states for energy-conserving A2 cross relaxation. Similarly, broad LMCT absorption is observed in bulk Yb^{3+}:$CsCdBr_3$ between ~27,500 cm^{-1} and ~35,000 cm^{-1},[41] with its maximum at E_{LMCT} ~ 29,000 cm^{-1}. A very similar E_{LMCT} is also observed[42] in other hexabromides and is anticipated in Yb^{3+}:$CsPbBr_3$. Thus, although E_g decreases by ~5,300 cm^{-1} going from Yb^{3+}:$CsCdCl_3$ to Yb^{3+}:$CsCdBr_3$, E_{LMCT} also decreases by a similar amount and the resonance is retained (Figure 4.8C, 19,050 cm^{-1} + 10,200 cm^{-1} ≈ 29,000 cm^{-1}). Excellent energy matching is therefore expected for all Yb^{3+}:$CsPb(Cl_{1-x}Br_x)_3$ compositions, providing a large density of final states for cross relaxation in each composition.

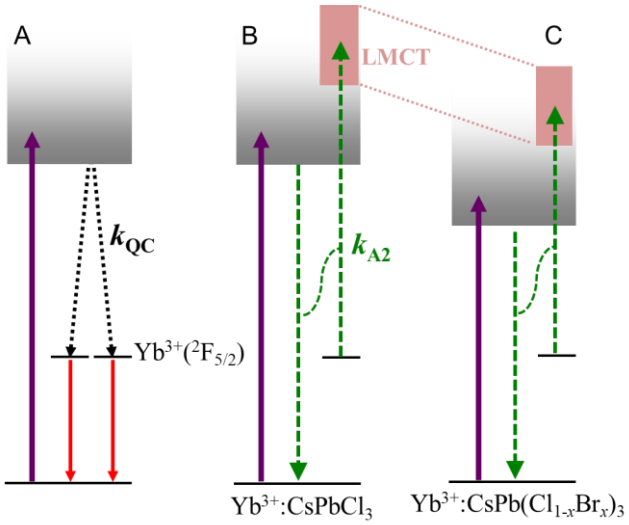

Figure 4.8 Summary of the contributions to PL power saturation in Yb^{3+}:$CsPb(Cl_{1-x}Br_x)_3$. (a) Quantum cutting in Yb^{3+}:$CsPbCl_3$ NCs, in which Yb^{3+}:$CsPbCl_3$ excitation (purple arrow) is followed by simultaneous energy transfer to two Yb^{3+} ions (black arrows), exciting them to their $^2F_{5/2}$ excited states, which return to the ground state radiatively (red arrows). (b) Nonradiative Auger-type cross relaxation in Yb^{3+}:$CsPbCl_3$ NCs that already contain excited-state Yb^{3+} upon photoexcitation (green arrows). The Yb^{3+} $^2F_{5/2}$ → LMCT transition energy equals E_g of the $CsPbCl_3$ host NC. (c) Anion alloying to form Yb^{3+}:$CsPb(Cl_{1-x}Br_x)_3$ reduces both E_g and the $^2F_{5/2}$ → LMCT transition energy, allowing retention of energy resonance for the cross-relaxation process.

In addition to good energy matching, the A2 cross relaxation may be dominant because it couples two fairly strongly allowed individual transitions, the semiconductor band-to-band transition and the Yb^{3+} LMCT transition (dashed arrows in Figures 4.8B,C). The allowedness of

these individual transitions contributes to the cross-relaxation rate if energy transfer proceeds by a multipolar coupling mechanism. In this case, the rate of the A2 cross relaxation involving an electric-dipole allowed Yb^{3+} LMCT transition should greatly exceed that of the A1 cross-relaxation pathway, which involves an electric-dipole forbidden Yb^{3+} *f-f* transition. It is also possible that this cross relaxation is mediated by exchange, however. Overall, we conclude that the good energy match and possibly also the allowedness of the participating donor and acceptor transitions in the A2 cross relaxation, in conjunction with the long $Yb^{3+}(^2F_{5/2})$ radiative lifetime and negligible nonradiative decay by other routes, combine to yield the power saturation observed in Yb^{3+}:$CsPb(Cl_{1-x}Br_x)_3$ NCs and related materials.

4.5.2 Implications for solar applications. The power saturation reported here has major implications for the utility of these materials in solar downconversion schemes.[12, 43, 44] Despite having similar saturation curves when plotting I_{Yb} *vs* k_{ex}, each composition in the Yb^{3+}:$CsPb(Cl_{1-x}Br_x)_3$ series has a different absorption onset and hence a different k_{ex} under AM1.5 solar irradiation. The vertical lines in Figure 4.4C illustrate these values of k_{ex} for Yb^{3+}:$CsPbCl_3$ and Yb^{3+}:$CsPb(Cl_{0.25}Br_{0.75})_3$ compositions, and indicate that both will show saturation under direct AM1.5 illumination, with the PLQY of the latter reduced from 200% down to as little as ~120%. Power saturation in these materials is therefore a serious liability for practical solar applications and it must be overcome.

From the analysis presented above, we suggest that there are in principle at least 3 general routes for engineering quantum-cutting perovskites and related materials to reduce saturation: (*i*) shorten the Yb^{3+} lifetime, (*ii*) decrease the photoexcitation rate per Yb^{3+}, and (*iii*) reduce the cross-relaxation rate. For (*i*), the saturation is unfortunately largely defined by the long $^2F_{5/2}$ excited-state lifetime of Yb^{3+}, which appears to be essentially independent of the halide composition (Figure 4.3C) or the Yb^{3+} concentration[13] in these materials over the composition ranges investigated. It is not likely that the intrinsic Yb^{3+} radiative lifetime itself can be shortened to any sufficient extent, but it is conceivable that the excited-state lifetime could be shortened *non*-radiatively without performance losses by coupling Yb^{3+} to energy acceptors, for example to the Si PV itself in a layered QC/PV device. Non-radiative energy transfer from Yb^{3+} to the energy acceptor would retain the high quantum-cutting efficiency and reduce population accumulation in the Yb^{3+} $^2F_{5/2}$ excited state. Proof of concept for route (*ii*) is already illustrated in Figure 4.7, in which increasing the Yb^{3+} concentration reduces saturation by improving the competition between

quantum cutting and Auger cross relaxation. It is conceivable that materials with even greater Yb^{3+} concentrations than those explored here could perform even better, but at some high Yb^{3+} concentration deleterious energy migration to traps or concentration quenching will begin to reduce efficiency. A related tactic could be to diminish the absorption cross section of the sensitizing host lattice, thereby decreasing the excitation rate per Yb^{3+}, and numerous specific approaches for doing this can be conceived. A less obvious strategy for decreasing the photoexcitation rate per Yb^{3+} would be to stack Yb^{3+}:$CsPb(Cl_{1-x}Br_x)_3$ layers with different E_g values such that the solar flux hitting any given lower layer is filtered by the upper layers to limit k_{ex} in each layer, hence reducing saturation. Route (*iii*) could possibly be achieved by altering the host-lattice composition to detune the LMCT-E_g resonance that is critical to the large k_{A2} as described above (Figure 4.8). Other routes for circumventing saturation may also exist, and further research is needed to identify the most promising. Such efforts are presently underway in our laboratories.

4.6 Conclusion

In summary, facile PL power saturation is observed in quantum-cutting Yb^{3+}:$CsPb(Cl_{1-x}Br_x)_3$ NCs and related materials. This saturation poses a major challenge for the anticipated practical application of these quantum-cutting materials as solar spectral-downconversion phosphors. It will also influence the behavior of these materials in other photonics applications or experiments, for example in single-NC PL studies or as sensitizers for photodetectors. In the present study, spectroscopic measurements coupled with synthetic variation of NC composition and kinetic modeling of power saturation curves have provided a detailed quantitative description of the key characteristics of PL saturation in quantum-cutting Yb^{3+}:$CsPb(Cl_{1-x}Br_x)_3$ NCs and, by extension, other morphologies of similar composition. In particular, data simulation has yielded fundamental insights into the dynamical and electronic-structure origins of this saturation, allowing the conclusion that it arises from a rapid non-radiative Auger-type cross-relaxation process that involves transfer of energy from photoexcited NCs to Yb^{3+} ions that are already in their $^2F_{5/2}$ excited state from a previous photoexcitation event. The presence of an electric-dipole-allowed LMCT excitation in resonance with the NC-to-Yb^{3+} energy transfer contributes to the efficacy of this cross relaxation. Although several Yb^{3+} ions can be elevated to the $^2F_{5/2}$ excited state of a given NC under continuous photoexcitation, the cross-relaxation process accelerates as the $Yb^{3+}(^2F_{5/2})$ population grows, and eventually it outpaces quantum cutting to become the

dominant channel for exciton relaxation after photoexcitation. In so doing, the NC PLQY decreases from ~200% observed in the low-power limit to values as low as ~10% at the highest excitation rates explored here.

The mechanistic understanding developed here has allowed a set of specific strategies for circumventing this saturation to be proposed. One of these strategies involves increasing the Yb^{3+} concentration within the lattice and has been successfully demonstrated in experiment; several other feasible strategies have also been described, and it is anticipated that one or a combination of these strategies will ultimately be required to fully capitalize on the remarkable quantum-cutting properties of these materials. Overall, these results highlight both the general scope and specific characteristics of the saturation challenge posed by these materials, as well as possible routes to solving this challenge, and as such this work is expected to provide valuable guidance to future development of quantum-cutting phosphors for solar downconversion and related applications.

4.7 References

1. Trupke, T.; Green, M. A.; Würfel, P., Improving Solar Cell Efficiencies by Down-Conversion of High-Energy Photons. *Journal of Applied Physics* **2002,** *92*, 1668-1674.
2. van der Ende, B. M.; Aarts, L.; Meijerink, A., Lanthanide Ions as Spectral Converters for Solar Cells. *Phys. Chem. Chem. Phys.* **2009,** *11*, 11081-11095.
3. de Jong, M.; Meijerink, A.; Rabouw, F. T., Non-Poissonian Photon Statistics from Macroscopic Photon Cutting Materials. *Nat. Commun.* **2017,** *8*, 15537.
4. Dexter, D. L., Possibility of Luminescent Quantum Yields Greater than Unity. *Phys. Rev.* **1957,** *108*, 630-635.
5. Vergeer, P.; Vlugt, T. J. H.; Kox, M. H. F.; den Hertog, M. I.; van der Eerden, J. P. J. M.; Meijerink, A., Quantum Cutting by Cooperative Energy Transfer in $Yb_xY_{1-x}PO_4$: Tb^{3+}. *Phys. Rev. B* **2005,** *71*, 014119.
6. Lakshminarayana, G.; Yang, H.; Ye, S.; Liu, Y.; Qiu, J., Co-operative Downconversion Luminescence in Tm^{3+}/Yb^{3+}: SiO_2–Al_2O_3–LiF–GdF_3 Glasses. *J. Phys. D: Appl. Phys.* **2008,** *41*, 175111.
7. Zhang, Q. Y.; Yang, G. F.; Jiang, Z. H., Cooperative Downconversion in $GdAl_3(BO_3)_4$:RE^{3+},Yb^{3+} (RE=Pr, Tb, and Tm). *Appl. Phys. Lett.* **2007,** *91*, 051903.
8. D'Aléo, A.; Picot, A.; Beeby, A.; Gareth Williams, J. A.; Le Guennic, B.; Andraud, C.; Maury, O., Efficient Sensitization of Europium, Ytterbium, and Neodymium Functionalized Tris-Dipicolinate Lanthanide Complexes through Tunable Charge-Transfer Excited States. *Inorg. Chem.* **2008,** *47*, 10258-10268.
9. Wang, Z.; Meijerink, A., Dye-Sensitized Downconversion. *J. Phys. Chem. Lett.* **2018,** *9*, 1522-1526.
10. Shao, W.; Lim, C.-K.; Li, Q.; Swihart, M. T.; Prasad, P. N., Dramatic Enhancement of Quantum Cutting in Lanthanide-Doped Nanocrystals Photosensitized with an Aggregation-Induced Enhanced Emission Dye. *Nano Lett.* **2018,** *18*, 4922-4926.
11. Wu, D.; Dong, X.; Xiao, W.; Hao, Z.; Zhang, J., Efficient Visible-to-NIR Spectral Conversion for Polycrystalline Si Solar Cells and Revisiting the Energy Transfer Mechanism from Ce^{3+} to Yb^{3+} in $Lu_3Al_5O_{12}$ Host. *Inorg. Chem.* **2019,** *58*, 234-242.
12. Zhou, D.; Liu, D.; Pan, G.; Chen, X.; Li, D.; Xu, W.; Bai, X.; Song, H., Cerium and Ytterbium Codoped Halide Perovskite Quantum Dots: A Novel and Efficient Downconverter for Improving the Performance of Silicon Solar Cells. *Adv. Mater.* **2017,** *29*, 1704149.
13. Milstein, T. J.; Kroupa, D. M.; Gamelin, D. R., Picosecond Quantum Cutting Generates Photoluminescence Quantum Yields Over 100% in Ytterbium-Doped $CsPbCl_3$ Nanocrystals. *Nano Lett.* **2018,** *18*, 3792-3799.
14. Kroupa, D. M.; Roh, J. Y.; Milstein, T. J.; Creutz, S. E.; Gamelin, D. R., Quantum-Cutting Ytterbium-Doped $CsPb(Cl_{1-x}Br_x)_3$ Perovskite Thin Films with Photoluminescence Quantum Yields over 190%. *ACS Energy Lett.* **2018,** *3*, 2390-2395.
15. Mir, W. J.; Mahor, Y.; Lohar, A.; Jagadeeswararao, M.; Das, S.; Mahamuni, S.; Nag, A., Postsynthesis Doping of Mn and Yb into $CsPbX_3$ (X = Cl, Br, or I) Perovskite Nanocrystals for Downconversion Emission. *Chem. Mater.* **2018,** *30*, 8170-8178.
16. Milstein, T. J.; Kluherz, K. T.; Kroupa, D. M.; Erickson, C. S.; De Yoreo, J. J.; Gamelin, D. R., Anion Exchange and the Quantum-Cutting Energy Threshold in Ytterbium-Doped $CsPb(Cl_{1-x}Br_x)_3$ Perovskite Nanocrystals. *Nano Lett.* **2019,** *19*, 1931-1937.

17. Ravi, V. K.; Markad, G. B.; Nag, A., Band Edge Energies and Excitonic Transition Probabilities of Colloidal $CsPbX_3$ (X = Cl, Br, I) Perovskite Nanocrystals. *ACS Energy Lett.* **2016,** *1*, 665-671.
18. Manser, J. S.; Christians, J. A.; Kamat, P. V., Intriguing Optoelectronic Properties of Metal Halide Perovskites. *Chem. Rev.* **2016,** *116*, 12956-13008.
19. Maes, J.; Balcaen, L.; Drijvers, E.; Zhao, Q.; De Roo, J.; Vantomme, A.; Vanhaecke, F.; Geiregat, P.; Hens, Z., Light Absorption Coefficient of $CsPbBr_3$ Perovskite Nanocrystals. *J. Phys. Chem. Lett.* **2018,** *9*, 3093-3097.
20. de A. Florêncio, L.; Gómez-Malagón, L. A.; Lima, B. C.; Gomes, A. S. L.; Garcia, J. A. M.; Kassab, L. R. P., Efficiency Enhancement in Solar Cells Using Photon Down-Conversion in Tb/Yb-Doped Tellurite Glass. *Sol. Energy Mater. Sol. Cells* **2016,** *157*, 468-475.
21. Stręk, W.; Bednarkiewicz, A.; Dereń, P. J., Power Dependence of Luminescence of Tb^{3+}-Doped $KYb(WO_4)_2$ Crystal. *J. Lumin.* **2001,** *92*, 229-235.
22. Duan, Q.; Qin, F.; Zhang, Z.; Cao, W., Quantum Cutting Mechanism in $NaYF_4$:Tb^{3+}, Yb^{3+}. *Opt. Lett., OL* **2012,** *37*, 521-523.
23. Creutz, S. E.; Crites, E. N.; De Siena, M. C.; Gamelin, D. R., Colloidal Nanocrystals of Lead-Free Double-Perovskite (Elpasolite) Semiconductors: Synthesis and Anion Exchange To Access New Materials. *Nano Lett.* **2018,** *18*, 1118-1123.
24. Creutz, S. E.; Crites, E. N.; De Siena, M. C.; Gamelin, D. R., Anion Exchange in Cesium Lead Halide Perovskite Nanocrystals and Thin Films using Trimethylsilyl Halide Reagents. *Chem. Mater.* **2018,** *30*, 4887–4891.
25. Protesescu, L.; Yakunin, S.; Bodnarchuk, M. I.; Krieg, F.; Caputo, R.; Hendon, C. H.; Yang, R. X.; Walsh, A.; Kovalenko, M. V., Nanocrystals of Cesium Lead Halide Perovskites ($CsPbX_3$, X = Cl, Br, and I): Novel Optoelectronic Materials Showing Bright Emission with Wide Color Gamut. *Nano Lett.* **2015,** *15*, 3692-3696.
26. Sher, P. H.; Smith, J. M.; Dalgarno, P. A.; Warburton, R. J.; Chen, X.; Dobson, P. J.; Daniels, S. M.; Pickett, N. L.; O'Brien, P., Power Law Carrier Dynamics in Semiconductor Nanocrystals at Nanosecond Timescales. *Appl. Phys. Lett.* **2008,** *92*, 101111.
27. Rabouw, F. T.; Kamp, M.; van Dijk-Moes, R. J. A.; Gamelin, D. R.; Koenderink, A. F.; Meijerink, A.; Vanmaekelbergh, D., Delayed Exciton Emission and its Relation to Blinking in CdSe Quantum Dots. *Nano Lett.* **2015,** *15*, 7718–7725.
28. Whitham, P. J.; Marchioro, A.; Knowles, K. E.; Kilburn, T. B.; Reid, P. J.; Gamelin, D. R., Single-Particle Photoluminescence Spectra, Blinking, and Delayed Luminescence of Colloidal CuInS2 Nanocrystals. *J. Phys. Chem. C* **2016,** *120*, 17136–17142.
29. Chirvony, V. S.; González-Carrero, S.; Suárez, I.; Galian, R. E.; Sessolo, M.; Bolink, H. J.; Martínez-Pastor, J. P.; Pérez-Prieto, J., Delayed Luminescence in Lead Halide Perovskite Nanocrystals. *J. Phys. Chem. C* **2017,** *121*, 13381-13390.
30. Bradshaw, L. R.; Hauser, A.; McLaurin, E. J.; Gamelin, D. R., Luminescence Saturation via Mn^{2+}–Exciton Cross Relaxation in Colloidal Doped Semiconductor Nanocrystals. *J. Phys. Chem. C* **2012,** *116*, 9300-9310.
31. Ryan, J. L.; Jørgensen, C. K., Absorption Spectra of Octahedral Lanthanide Hexahalides. *J. Phys. Chem.* **1966,** *70*, 2845-2857.
32. Yen, W. M.; Shionoya, S.; Yamamoto, H., *Fundamentals of Phosphors*. Eds ed.; CRC Press: Boca Raton, FL, 2006.

33. Mikoshiba, S.; Shirai, S.; Shinada, S.; Fukushima, M., Saturation of $Zn_2SiO_4:Mn$ Luminescence Under Intense VUV Excitation. *Journal of Applied Physics* **1979,** *50*, 1088-1090.
34. de Leeuw, D. M.; 't Hooft, G. W., Method for the Analysis of Saturation Effects of Cathodoluminescence in Phosphors; Applied to Zn_2SiO_4:Mn and $Y_3Al_5O_{12}$:Tb. *J. Lumin.* **1983,** *28*, 275-300.
35. Klimov, V. I.; Mikhailovsky, A. A.; McBranch, D. W.; Leatherdale, C. A.; Bawendi, M. G., Quantization of Multiparticle Auger Rates in Semiconductor Quantum Dots. *Science* **2000,** *287*, 1011-1013.
36. Jha, P. P.; Guyot-Sionnest, P., Trion Decay in Colloidal Quantum Dots. *ACS Nano* **2009,** *3*, 1011–1015.
37. Cohn, A. W.; Schimpf, A. M.; Gunthardt, C. E.; Gamelin, D. R., Size-Dependent Trap-Assisted Auger Recombination in Semiconductor Nanocrystals. *Nano Lett.* **2013,** *13*, 1810−1815.
38. Cohn, A. W.; Rinehart, J. D.; Schimpf, A. M.; Weaver, A. L.; Gamelin, D. R., Size Dependence of Negative Trion Auger Recombination in Photodoped CdSe Nanocrystals. *Nano Lett.* **2014,** *14*, 353−358.
39. Canneson, D.; Shornikova, E. V.; Yakovlev, D. R.; Rogge, T.; Mitioglu, A. A.; Ballottin, M. V.; Christianen, P. C. M.; Lhuillier, E.; Bayer, M.; Biadala, L., Negatively Charged and Dark Excitons in $CsPbBr_3$ Perovskite Nanocrystals Revealed by High Magnetic Fields. *Nano Lett.* **2017,** *17*, 6177-6183.
40. Dorenbos, P.; Josef, A.; de Haas, J. T. M.; Krämer, K. W., Vacuum Referred Binding Energies of the Lanthanides in Chloride, Bromide, and Iodide Compounds. *J. Lumin.* **2019,** *208*, 463-467.
41. Demirbilek, R.; Heber, J.; Nikitin, S. I., Charge Transfer and $4f^n$-$4f^{n-1}$ 5d Transitions of Trivalent Rare-Earch Ions in $CsCdBr_3$. In *XI Feofilov Symposium on Spectroscopy of Crystals Activated by Rare-Earth and Transition Metal Ions*, SPIE: Kazan, Russian Federation, 2002; Vol. 4766, pp 47-50.
42. Jørgensen, C. K., Electron Transfer Spectra. In *Progress in Inorganic Chemistry*, Lippard, S. J., Ed. New York, 1970; Vol. 12.
43. Cohen, T. A.; Milstein, T. J.; Kroupa, D. M.; MacKenzie, J. D.; Luscombe, C.; Gamelin, D. R., Quantum-Cutting Yb^{3+}-Doped Perovskite Nanocrystals for Monolithic Bilayer Luminescent Solar Concentrators. *J. Mater. Chem. A* **2019**, in press.
44. Luo, X.; Ding, T.; Liu, X.; Liu, Y.; Wu, K., Quantum-Cutting Luminescent Solar Concentrators Using Ytterbium-Doped Perovskite Nanocrystals. *Nano Letters* **2019,** *19*, 338-341.

Appendix A: Directed Exciton Magnetic Polaron Formation in a Single Colloidal Mn^{2+}:CdSe/CdS Quantum Dot

A.1 Quantum dot synthesis and shell growth

Colloidal wurtzite-structured Mn^{2+} doped CdSe quantum dots were prepared by nanocrystal diffusion doping as detailed previously.[1,2] In a typical synthesis, pre-prepared CdSe nanocrystals, synthesized following literature methods,[3] (~0.13 mmol, d = 5.8 nm) were dried and added to 8 mg (0.10 mmol) of selenium, 1 mL of 1-octadecene (ODE), and 1 mL of tributylphosphine in a septum-capped 5 mL round-bottom flask in a nitrogen-atmosphere glovebox. Separately, 12 g of ODE, 0.5 g of oleic acid, and 1.0 g of hexadecylamine (HDA) were added to a 100 mL three-neck round-bottom flask and heated for 60 min at 100 ˚C under vacuum. Then 25 mg (0.10 mmol) of $Mn(OAc)_2 \cdot 4H_2O$ was added against a nitrogen overpressure. The flask was then placed under vacuum to remove acetic acid and water and then heated under nitrogen to 300 ˚C, at which point the CdSe/selenide solution was rapidly injected and held at 300 ˚C for 20 h. As the solution was cooled to room temperature, 3 mL of toluene was added at ~110 ˚C. The nanocrystals were then washed by repeated flocculation with ethanol and re-suspensions in toluene.

CdS shells (~10 monolayers, d = 12 nm) were grown onto the Mn^{2+} doped CdSe cores following previous literature methods.[4] In a typical synthesis, the doped cores (~0.10 mmol) were dried and added to 4 g ODE and 2 g HDA in a 100 mL three-neck round-bottom flask and heated for 2 h at 100 °C under vacuum. Then the reaction flask was heated to 300 °C under nitrogen and pre-prepared 0.10 M shell precursor solutions of cadmium oleate and octanethiol in ODE were added dropwise at a rate of 2.5 mL/h. Once all the shell precursors solutions were added the reaction solution was allowed to cool to room temperature. 3 mL of toluene was added at ~110 ˚C and the nanocrystals were then washed by repeated flocculation with ethanol and re-suspensions in toluene. Undoped CdSe/CdS core/shell quantum dots (d = 11 nm) were prepared following the same shelling procedure using pre-prepared undoped CdSe quantum dots following literature methods.[3,4]

A.2 Quantum dot analysis

Relative elemental compositions were obtained by analysis of dried nanocrystals digested overnight with sonication in ultrapure nitric acid using inductively coupled plasma atomic emission spectrometry (ICP-AES; PerkinElmer 8300). Transmission electron microscope (TEM) samples were prepared by dip coating Cu grids (200 mesh, Ted Pella, Inc.) into dilute colloidal suspensions of QDs in toluene. TEM images were obtained on a FEI TECNAI F20, 200 kV microscope at the UW Molecular Analysis Facility. QD sizes were determined from analysis of ≥100 individual QDs in TEM images using the ImageJ64 software.

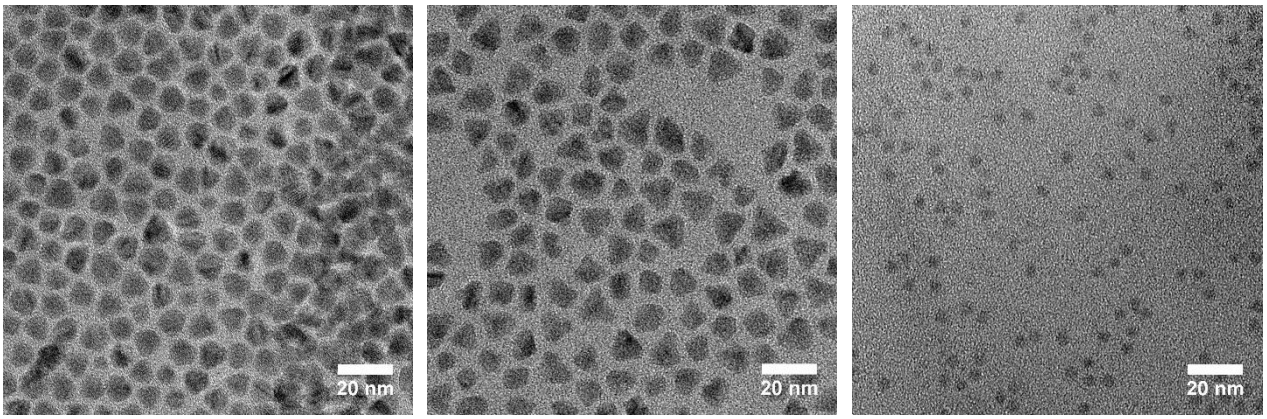

Figure A.1 NC TEM images. Transmission electron microscopy image of the undoped reference (left), the Mn^{2+}:CdSe/CdS sample (middle), and the Mn^{2+}:CdSe cores before shelling (right).

Powder X-ray diffraction data were collected from evaporated nanocrystal films on silicon substrates using a Bruker D8 Advance irradiated sing Cu Kα radiation (50000 mW).

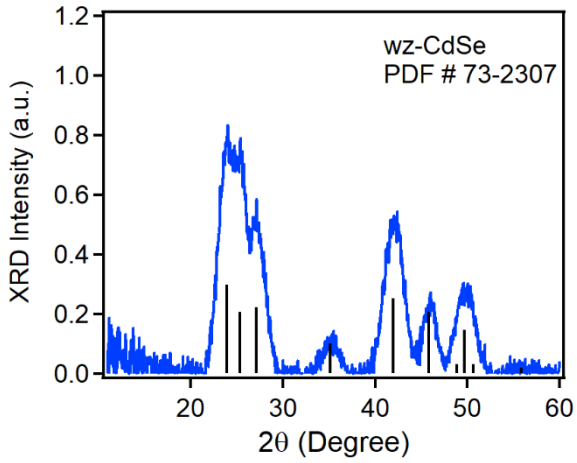

Figure A.2 X-ray diffraction pattern of the Mn^{2+}:CdSe/CdS sample.

A.3 Single QD sample preparation:

Single QD samples for confocal photoluminescence (PL) investigations with high spatial resolution were prepared by diluting the Mn^{2+}:CdSe/CdS QDs in toluene to a concentration of ~500 nMol / L. The diluted dispersion was spin cast onto a SiO_2 (90 nm) / Si substrate, which was pre-structured with marker crosses by means of electron beam lithography. Using this way of marking the QD position on the substrate, the reliable relocation of each single QD was enabled, even after changing the sample temperature or magnetic field strength.

A.4 Addition to Figure 2.4

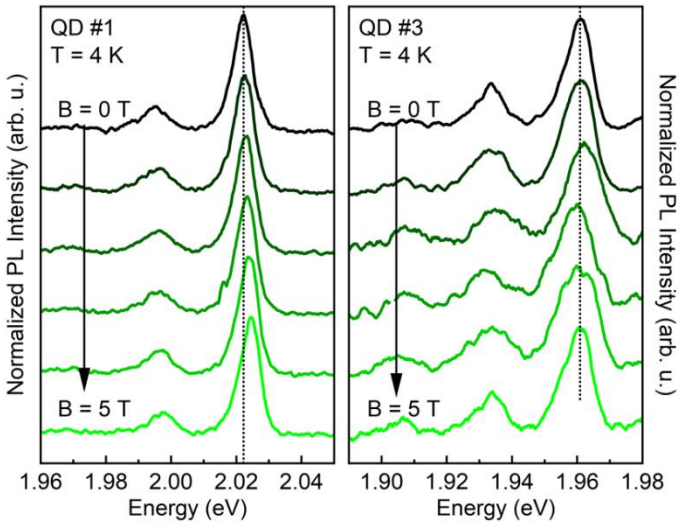

Figure A.3 Magnetic field dependent photoluminescence spectra from selected NCs collected at 4 K. Magnetic field dependent PL spectra of QD #1 and QD #3 as used to extract the data plotted in Figure 3.4 (a) (data of QD #2 were already shown in Figure 2.3 (a)).

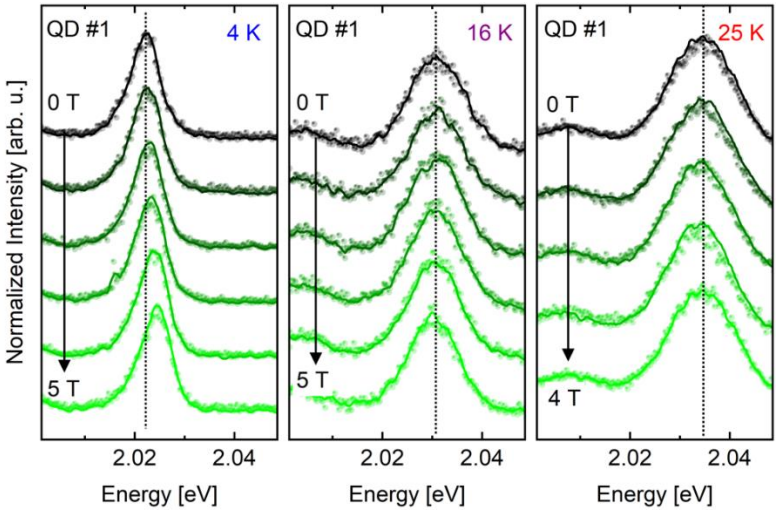

Figure A.4 Magnetic field dependent photoluminescence spectra of QD used in Figure 2.4C. Magnetic field dependent PL spectra of QD #1 at 4 K, 16 K and 25 K.

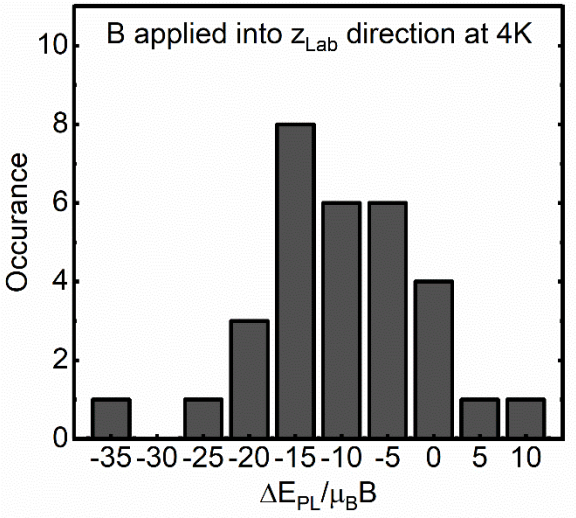

Figure A.5 Single NC statistics. Histogram depicting the energy shift of the ZPL ($\boldsymbol{\Delta E_{PL}}$) normalized by $\boldsymbol{\mu_B B}$ of 31 single Mn:CdSe/CdS QDs, when the magnetic field is applied in the $\boldsymbol{z_{Lab}}$ direction (i.e. in Faraday geometry) at 4 K. An energy redshift is represented by a negative value, while a blueshift is represented by a positive value along the x-axis.

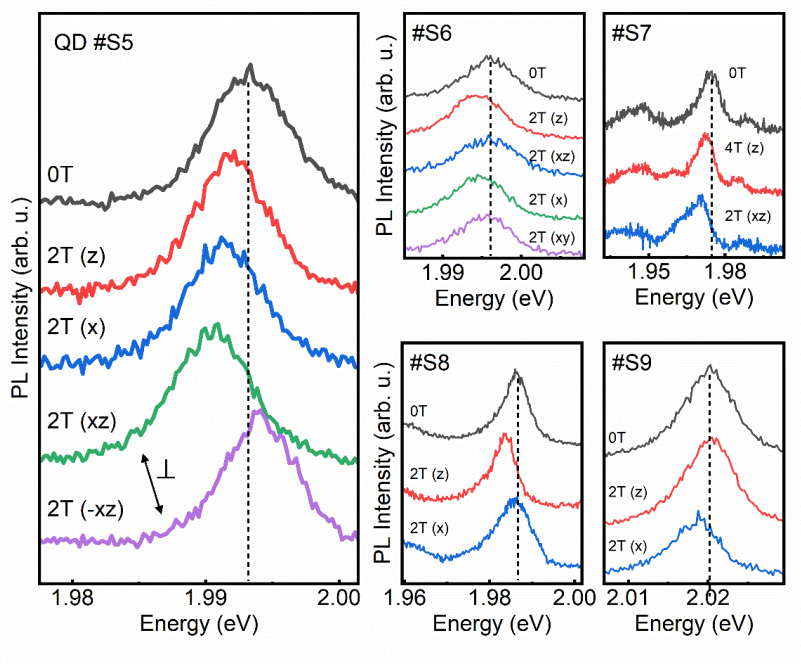

Figure A.6. Photoluminescence spectra of several individual QDs with the magnetic field directed along various lab axes. Change of the ZPL emission for different single QDs in a rotating vector magnetic field. $|\vec{B}|$ and the direction of the magnetic field with respect to the lab axes x, y and z are given in the captions.

A.5 Addition to Figure 2.5

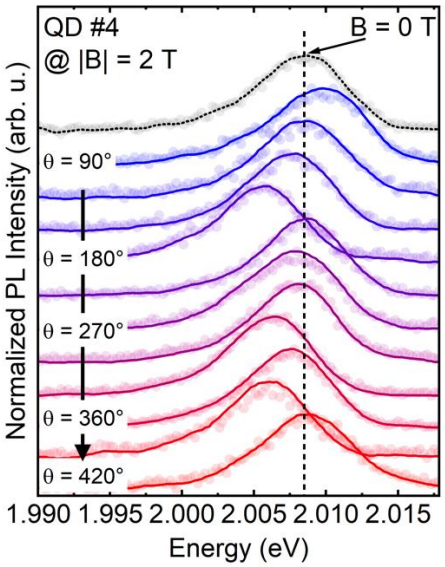

Figure A.7. Photoluminescence spectra of the QD used in Figure 2.5. PL spectra of QD #4 as used to extract the data plotted in Figure 3.5 of the main paper. Dotted black line shows the PL spectrum at $|\vec{B}| = 0$ T, colored spectra have been collected at $|\vec{B}| = 2$ T for different angles θ between the axis of anisotropy and the external magnetic field $\vec{B}$.

A.6 References

1. Vlaskin, V. A.; Barrows, C. J.; Erickson, C. S.; Gamelin, D. R. Nanocrystal Diffusion Doping. *J. Am. Chem. Soc.* **2013**, *135*, 14380–14389.
2. Barrows, C. J.; Chakraborty, P.; Kornowske, L. M.; Gamelin, D. R. Tuning Equilibrium Compositions in Colloidal Cd 1– x Mn x Se Nanocrystals Using Diffusion Doping and Cation Exchange. *ACS Nano* **2016**, *10*, 910–918.
3. Qu, L.; Peng, X. Control of Photoluminescence Properties of CdSe Nanocrystals in Growth. *J. Am. Chem. Soc.* **2002**, *124*, 2049–2055.
4. Coropceanu, I.; Bawendi, M. G. Core/Shell Quantum Dot Based Luminescent Solar Concentrators with Reduced Reabsorption and Enhanced Efficiency. *Nano Lett.* **2014**, *14*, 4097–4101.

Appendix B: Orientation of Individual Anisotropic Nanocrystals Identified by Polarization Fingerprint

B.1 Quantum dot analysis

Relative elemental compositions were determined by means of inductively coupled plasma atomic emission spectrometry (ICP-AES; PerkinElmer 8300) after sonicating in ultrapure nitric acid and drying over night. Transmission electron microscopy (TEM) images were collected at the UW Molecular Analysis Facility using a FEI TEXNAI F20, 200kV microscope. TEM samples were prepared by dip coating of Cu grids (200 mesh) into a diluted suspension of colloidal QDs in toluene. For the QD size determination, ≥100 individual QDs in TEM images were analyzed using the ImageJ64 software. Powder X-ray diffractograms were collected from evaporated nanocrystal films on silicon using a Bruker D8 Discover with a high-efficiency IμS microfocus x-ray source for Cu Kα radiation (50 kV, 1 mA).

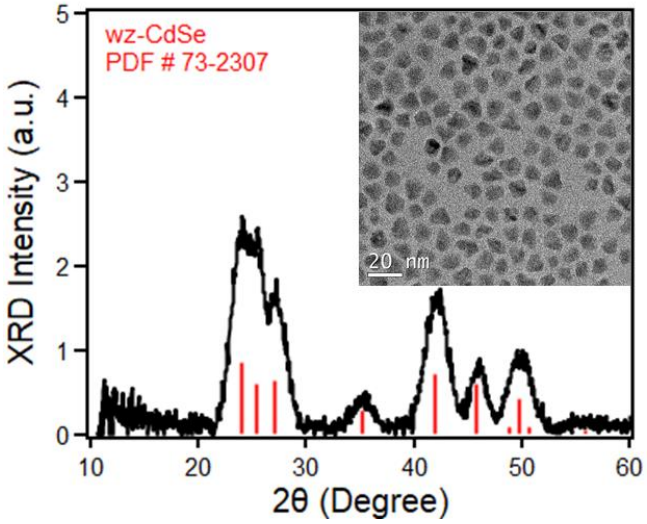

Figure B.1. XRD data and TEM image of NCs used in Chapter 3. X-ray diffraction pattern of the Mn^{2+}:CdSe/CdS sample. Inset: Transmission electron microscopy image of the Mn^{2+}:CdSe/CdS sample. XRD data adapted from previous report on these NCs.[4]

B.2 Photoluminescence spectra

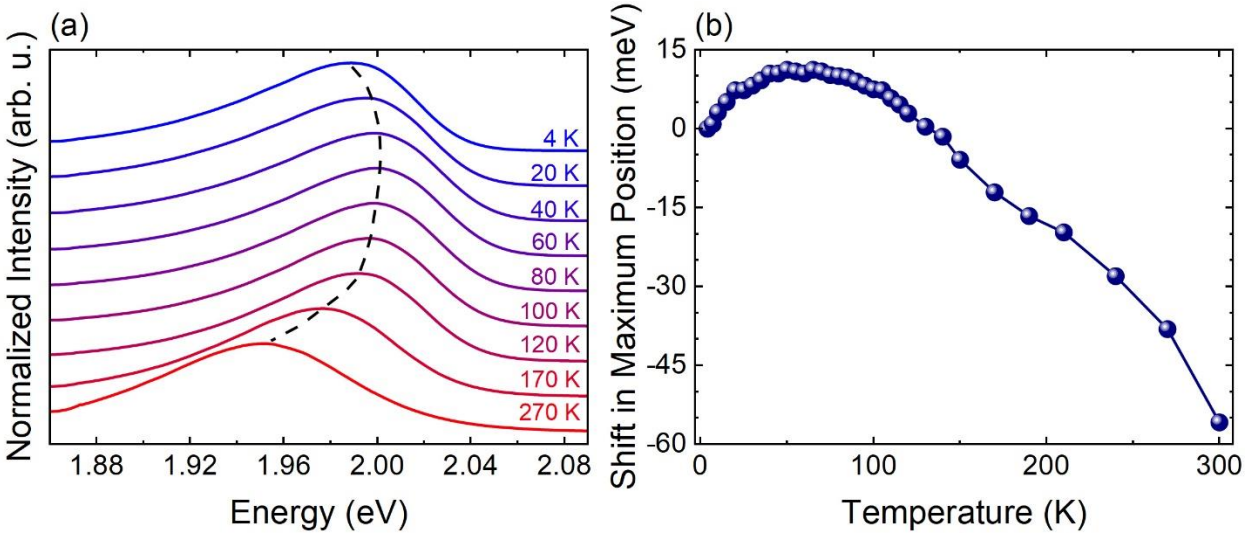

Figure B.2. Ensemble variable temperature photoluminescence. Temperature dependent PL spectra (a) and maximum position shift (b) of an ensemble of Mn^{2+}:CdSe/CdS cQDs, dropcast on a SiO_2 substrate. The blue shift with $\boldsymbol{T}$ for temperatures up to 50 K, followed by the typical Varshni-like behavior for higher temperatures unambiguously indicates EMP formation.

B.3 Isotropic EMP formation mechanism

B.3.1. Exchange field and magnetization During EMP formation, which takes place on the time scale τ_{EMP} of a few tens or hundreds ps,[1–3] the internal exchange field B_{exc} between the host charge carriers and the magnetic dopants leads to a spontaneous alignment of the dopant spins. In turn, this magnetization increases the *sp-d* exchange energy of the exciton and results in a giant Zeeman splitting in the order of 80 meV at 4 K,[4] with no external magnetic field. As in DMS cQDs, the exciton lifetime τ_{r} is on the order of several tens of ns,[3,4] and it can be assumed that the PL contributions for $t < \tau_{\mathrm{EMP}}$ can be neglected in a continuous wave PL experiment. The energy gain of the excitonic state with respect to the energy without EMP formation is called the EMP binding energy.

The derivation of the PL polarization degree is fundamentally different in Mn^{2+}-doped nanomaterials exhibiting EMP formation. It is instructive to write the *sp-d* exchange energy in the general form of $E_{\mathrm{sp-d}} = -V_{\mathrm{eff}}\,\vec{M}_{\mathrm{Mn}} \cdot \vec{B}_{\mathrm{exc}}$, where V_{eff} is the effective exciton volume and $\vec{B}_{\mathrm{exc}}$ the exchange field given by:[5,6]

$$\vec{B}_{\mathrm{exc}} = \vec{B}^{\mathrm{el}}_{\mathrm{exc}} + \vec{B}^{\mathrm{h}}_{\mathrm{exc}} = \frac{N_0\alpha}{V_{\mathrm{eff}}N_0 g_{\mathrm{Mn}}\mu_{\mathrm{B}}}\,\vec{J}_{\mathrm{el}} \; - \frac{N_0\beta}{3V_{\mathrm{eff}}N_0 g_{\mathrm{Mn}}\mu_{\mathrm{B}}}\,\vec{J}_{\mathrm{h}} \qquad \text{Eq. B.1}$$

where N_0 is the cation density per unit volume. Note that the directions of the exchange fields are given by the directions of the total angular momenta $\vec{J}_{\mathrm{el}}$ and $\vec{J}_{\mathrm{h}}$. In case of EMP formation it is usually assumed that immediately after excitation ($t = 0$) the optically generated charge carriers relax to the band edge quickly and interact with the dopant spins. During this stage, the electron-hole pair aligns its exchange field along the direction that maximizes the energy gain due to the strong *sp-d* exchange interactions.[5] This orientation is given by the instantaneous direction of the fluctuating magnetization $\vec{M}_{\mathrm{f}} = \vec{M}_{\mathrm{Mn}}(t \approx 0)$ and thus the EMP can be formed into an arbitrary direction if no magnetic field is applied. As in a typical single cQD experiment, averaging occurs over a large variety of recombination events, and unpolarized emission is expected even though the exchange field leads to a strong spin splitting of the exciton states. If an external magnetic field $\vec{B}$ is applied, the time average of the magnetization is given by:

$$\left\langle \vec{M}_{\mathrm{Mn}}\left(|\vec{B}_{\Sigma}|, T\right)\right\rangle = x_{\mathrm{Mn}} N_0 \mu_{\mathrm{B}} g_{\mathrm{Mn}} S_{\mathrm{eff}} \mathcal{B}_{5/2}\left(\frac{5\mu_{\mathrm{B}} g_{\mathrm{Mn}} |B_{\Sigma}|}{2k_{\mathrm{B}}(T_{\mathrm{s}}+T_0)}\right)\frac{\vec{B}_{\Sigma}}{|\vec{B}_{\Sigma}|} \qquad \text{Eq. B.2}$$

Here, $\vec{B}_{\Sigma}$ is the total magnetic field, which is equal to $\vec{B}$ at $t \leq 0$ and equal to the sum $\vec{B} + \vec{B}_{\mathrm{exc}}$ in the presence of an electron-hole pair, representing the ordering character of both, external field and exchange field, i.e. *sp-d* exchange interaction, onto the Mn^{2+} spins. In the time average, the orientation of EMP formation is random at $\vec{B} = 0$, but can be guided by the direction of the net magnetization evolving in an external magnetic field at $t \leq 0$. Hence, the application of a magnetic field influences the predominant direction of EMP formation and thus controls the degree of polarization of emitted photons in the time average.[3] Note the fundamental difference to the situation described above, where the PL polarization degree is derived from the occupation of the Zeeman split states at the time of radiative recombination. Here, the decisive element for the state occupation and thus the PL polarization is the initial state of the magnetization at $t \leq 0$, i.e. before optical excitation.

B.3.2. Magnetization fluctuation distribution. The initial magnetization can be described by the probability of finding a certain $\vec{M}_{\mathrm{f}} = \left(M_{\mathrm{x}}, M_{\mathrm{y}}, M_{\mathrm{z}}\right)$ at a defined magnetic field B and temperature T_{s}, which is given by the joint probability distribution:[7]

$$\Phi\left(M_{\mathrm{x}}, M_{\mathrm{y}}, M_{\mathrm{z}}\right) = \frac{1}{\sqrt{2\pi\langle\delta M_{\mathrm{z}}^2\rangle}}\exp\left(-\frac{(M_z-\langle M_z\rangle)^2}{2\langle\delta M_{\parallel}^2\rangle}\right)\frac{1}{2\pi\langle\delta M_{\perp}^2\rangle}\exp\left(-\frac{\left(M_{\mathrm{x}}^2+M_{\mathrm{y}}^2\right)}{2\langle\delta M_{\perp}^2\rangle}\right) \qquad \text{Eq. B.3}$$

For simplicity, it is assumed that $\vec{B}$ is directed along the positive z direction. Then, the fluctuations along the z direction are called the longitudinal fluctuations $\langle \delta M_{\parallel}^2 \rangle$ and the fluctuations along x and y are equal and are called transverse fluctuations $\langle \delta M_{\perp}^2 \rangle$, respectively given by:[6]

$$\langle \delta M_{\parallel}^2 \rangle = \left| \frac{\mathrm{d}M_{\mathrm{Mn}}(B,T)}{\mathrm{d}B} \right|_{|\vec{B}_{\Sigma}|} k_{\mathrm{B}} T_{\mathrm{s}} = \langle \delta M_{\mathrm{z}}^2 \rangle \qquad \text{Eq. B.4a}$$

$$\langle \delta M_{\perp}^2 \rangle = \frac{|\vec{M}_{\mathrm{Mn}}(\vec{B})|}{|\vec{B}_{\Sigma}|} k_{\mathrm{B}} T_{\mathrm{s}} = \langle \delta M_{\mathrm{x}}^2 \rangle = \langle \delta M_{\mathrm{y}}^2 \rangle \qquad \text{Eq. B.4b}$$

The time averaged expectation values $\langle M_{\mathrm{x}} \rangle$ and $\langle M_{\mathrm{y}} \rangle$ vanish, while the expectation value for $\langle M_z \rangle$ is the scalar given by the magnitude of eq. (E3) with $B_{\Sigma} = B$.

B.3.3. Simulation of isotropic case (Figure 3.1 (c)): For the simulation of $\Delta I/I$ in Figure 3.1 (c), eqs. (Eq B.1-Eq B.4) were inserted into eq. (3.2), using the following parameters: N_0 = 17.82 nm^3,[8] $N_0\alpha$ = 0.23 eV,[9] $N_0\beta$ = - 1.27 eV,[9] x_{Mn} = 1.7%,[4] d_{QD} = 3.6 nm,[4] B_{exc} = 10 T, T_{s} = 6 K,[4] T_0 = 1 K, S_{eff} = 2.3.

B.4 Anisotropic EMP formation

B.4.1. Energy cross check. To cross-check whether the energy gain of the HH by aligning along the crystal $\vec{c}$ axis is larger than aligning it along the direction of instantaneous magnetization, we compare the characteristic energy scale for both cases. A hole with total angular momentum $J = 3\hbar/2$ can have projections $J_{\mathrm{z}} = \pm 3\hbar/2$ or $\pm 3/2$ with respect to the $\vec{c}$ axis, separated by the crystal field energy Δ_{cf} = 25 meV for CdSe.[10] This can be considered as a characteristic energy cost in case the total angular momentum of the hole and the $\vec{c}$ axis are misaligned. In comparison, the characteristic energy gain for the hole to align $\vec{B}_{\mathrm{exc}}^{\mathrm{h}}$ along $\vec{M}_{\mathrm{f}}$ is given by $\Delta_{\mathrm{p-d}} = V_{\mathrm{eff}} B_{\mathrm{exc}}^{\mathrm{h}} \sqrt{\langle \delta M^2 \rangle}$, which is typically on the order of 5 meV, as calculated with the following parameters reported in literature for similar cQDs: V_{eff} = 30 nm^3, $B_{\mathrm{exc}}^{\mathrm{h}}$ = 10 T, T_{s} = 4 K, x_{Mn} = 1.73%.[4] Therefore we assume that during the stage of EMP formation the hole can only relax with its total angular moment projection parallel or antiparallel to the $\vec{c}$ axis, corresponding to the $|+3/2\rangle$ and $|-3/2\rangle$ HH states, respectively.

B.4.2. Derivation of K for $\boldsymbol{\theta \neq 0°}$. As discussed in Chapter 3, $\Phi(M_{\mathrm{x}}, M_{\mathrm{y}}, M_{\mathrm{z}})$ is independent of the direction of $\vec{c}$. This has two immediate effects on the 1D probability distribution $P(M_{\mathrm{c}})$ along $\vec{c} \nparallel \vec{z}$: First, because the magnetic field increases the average magnetization $\langle M_{\mathrm{z}} \rangle$ in the direction of $\vec{B} \parallel \vec{z}$, the corresponding increase of average magnetization along $\vec{c}$ changes as

$\langle M_c \rangle = \cos(\theta)\langle M_z \rangle$. Second, if a magnetic field is applied, the longitudinal fluctuations $\langle \delta M_{\parallel}^2 \rangle$ of the magnetization along the magnetic field are suppressed more efficiently by the magnetic field than the transverse fluctuations $\langle \delta M_{\perp}^2 \rangle$ in the xy plane.[6] Therefore, the fluctuations along $\vec{c}$ differ from the fluctuations $\langle \delta M_{\parallel}^2 \rangle$ or $\langle \delta M_{\perp}^2 \rangle$. Then, $P(M_c)$ is given by a gaussian distribution centered around $\langle M_c \rangle$, with a standard deviation of $\sqrt{\langle \delta M_c^2 \rangle}$. This standard deviation is given by $\sqrt{\langle \delta M_c^2 \rangle} = \cos(\theta)\sqrt{\langle \delta M_{\parallel}^2 \rangle} + \sin(\theta)\sqrt{\langle \delta M_{\perp}^2 \rangle}$, i.e. $P(M_c)$ is obtained from a coordinate transformation in (M_x, M_y, M_z) space by rotating $\vec{z}$ to $\vec{c}$ around the axis perpendicular to $\vec{z}$ and $\vec{c}$, i.e. $\vec{z} \times \vec{c}$. $P(M_c)$ is then given by:

$$P(M_c) = \frac{1}{\sqrt{2\pi\langle \delta M_c^2 \rangle}} \exp\left(-\frac{(M_c - \langle M_c \rangle)^2}{2\langle \delta M_c^2 \rangle}\right) \qquad \text{Eq. B.5}$$

Inserting $\langle \delta M_c^2 \rangle$ and $\langle M_c \rangle$ and integrating over $(0, \infty)$ yields eq. 3.5 in Chapter 3.

B.4.3. Ensemble average. Using the framework presented here, the magnetic field dependence of the PL polarization of the ensemble can be simulated by summing the $\sigma^{\pm}$ contributions for each uniquely oriented cQD. For ensembles like those studied experimentally, $i \to \infty$ and assuming the cQDs are randomly oriented on the substrate we find:

$$\Delta I/I_{\text{ensemble}} = \frac{\int_0^{\pi} \left(I^{\sigma+}(\theta) - I^{\sigma-}(\theta)\right) \sin(\theta) \mathrm{d}\theta}{\int_0^{\pi} \left(I^{\sigma+}(\theta) + I^{\sigma-}(\theta)\right) \sin(\theta) \mathrm{d}\theta} \qquad \text{Eq. B.6}$$

The black solid line in Figure 3.3 (f) compares the simulation of $\Delta I/I\ (B)$ using eq. (E7) with the ensemble data presented in Figure 3.1. For the simulation we use the same parameters as for cQD #1. Notably, the slow increase of $\Delta I/I$ as well as the near saturation value of $\Delta I/I\ (B) \sim 70\%$ at $B = 5$ T are reproduced very well by the simulation. Averaging over an ensemble of cQDs with random displacement angles θ thus leads to the slow increase of $\Delta I/I\ (B)$ observed experimentally due to the mitigated impact of the field onto the projected magnetization distribution $P(M_c)$ as discussed above. Additionally, the ensemble average leads to a saturation value below 100% due to mixed σ^+ and σ^- PL contributions from each individual cQD. These results explain why for the ensemble data reported here and in literature,[3] $\Delta I/I$ saturates at values < 100%. While the ensembles average in Eq. B.6 suggests a saturation value of 75% for $B \to \infty$, this exact value is only achieved for a true isotropic distribution of cQD crystal axes. If, for any reason, e.g. by a self organization of a QD film or due to steric reasons related to cQD shell faceting, no true random crystal orientation is present, the experimental saturation value will differ from 75%.

B.4.4. Simulation parameters for Figure 3.3. Figures 3.3 (a, b, c, e) were simulated using parameters from literature: N_0 = 17.82 nm^3,[8] $N_0\alpha$ = 0.23 eV,[9] $N_0\beta$ = - 1.27 eV[9], x_{Mn} = 1.7%,[4] d_{QD} =3.6 nm,[4] B_{exc} = 10 T, T_{s} = 6 K,[4] T_0 = 1 K, S_{eff} = 2.3. For Figure 3 (f) specific parameters for single QD #1 were used: x_{Mn} = 3%, d_{QD} = 4.2 nm, B_{exc} = 9.3 T and T_{s} = 4 K were used, which are similar to the values reported for single cQDs of the same batch previously.[4]

B.4.5. Discussion of the lack of spectral splitting between σ^+ and σ^- PL. The model of constrained EMP formation can also be used to explain the unusual spectral behavior of the polarized emission as discussed in Figure 3.1 and Figure 3.2. Recall, that in the ensemble PL seemingly no energy shift between the spectra of σ^+ and σ^- polarized PL in a magnetic field was observed and only a marginal red shift between 0 T and 5 T was found. Single cQD spectroscopy then revealed a more complex spectral behavior: While the σ^+ component indeed exhibits a red shift increasing with magnetic field, the σ^- polarized PL spectra showed a more complicated behavior, with a blue shift for small magnetic fields followed by a red shift for large ones (see Figure 3.2e).

The model of anisotropic EMP formation can now be used to explain this behavior very nicely: Recall that the intensity of σ^- polarized PL is given by $I^{\sigma-} = I_{\uparrow\uparrow}^{\sigma-} + I_{\uparrow\downarrow}^{\sigma-}$, i.e. it stems from emission from both EMPs directed with $\vec{B}_{\mathrm{exc}}^{\mathrm{h}} \parallel \vec{c}$ as well as EMPs with $\vec{B}_{\mathrm{exc}}^{\mathrm{h}} \parallel -\vec{c}$. The relative intensities K and $(1-K)$, respectively, are given by the probability of $\vec{B}_{\mathrm{exc}}^{\mathrm{h}}$ aligned along the corresponding directions. Let us now discuss cQD #1 (see Figure 3.2 and Figure 3.3) in more detail. From Figure 3.3 (f) it is known that the angle between $\vec{c}$ and $\vec{B}$ is approximately $\theta = 60°$. Using Figure 3.3 (d) we can therefore extract the relative contributions of σ^+ and σ^- polarized components of the PL for both EMP directions. We find that $I_{\uparrow\uparrow}$ comprises 56% σ^+ emission and 6% σ^- emission, while the PL of oppositely oriented EMPs, $I_{\uparrow\downarrow}$, comprises 6% σ^+ and 56% σ^- emission. Therefore, the total σ^- polarized intensity is given by $I^{\sigma-} = I_{\uparrow\uparrow}^{\sigma-} + I_{\uparrow\downarrow}^{\sigma-} = 0.06\,K + 0.56(1-K)$.

For zero magnetic field, where EMPs are formed into both directions equally likely, the σ^- emission is strongly dominated by $I_{\uparrow\downarrow}^{\sigma-}$, i.e., EMPs formed along $-\vec{c}$. As the magnetic field increases, EMPs are also formed with $\vec{B}_{\mathrm{exc}}^{\mathrm{h}} \parallel \vec{c}$, increasing the corresponding intensity $I_{\uparrow\uparrow}$ and thus the σ^- contribution $I_{\uparrow\uparrow}^{\sigma-}$ of these EMPs. Therefore the σ^- PL spectra change their character from

being purely dominated by EMPs directed along $-\vec{c}$ at small magnetic fields to being more and more dominanted by EMPs formed along $\vec{c}$ at high fields.

To explain the observed unusual spectral shift (Figure 3.2 (e)) the influence of the magnetic field on the EMP binding for EMPs formed along $\vec{c}$ and $-\vec{c}$ needs to be considered. It is known in literature that the EMP binding energy can be increased (resulting in a PL red shift) or decreased (leading to a PL blue shift) by application of a suitably directed magnetic field with respect to the crystal $\vec{c}$ axis.[4] In case of cQD #1, the angle between $\vec{B}_{\mathrm{exc}}^{\mathrm{h}}$ and $\vec{B}$ is θ = 60° for EMPs formed along $\vec{c}$, but it is θ = 180° - 60° = 120° for EMPs formed along $-\vec{c}$. Therefore, the blue shift of the σ^- polarized spectra at low magnetic fields can be attributed to the decrease of the EMP binding energy for EMPs formed along $-\vec{c}$, while the red shift at large magnetic fields is caused by the increase of the EMP binding energy for EMPs formed along $\vec{c}$.

Considering θ = 60° for cQD #1, the regimes of "small" and "large" magnetic fields can be specified more precisely: Using the relative σ^+ and σ^- polarized contributions of 56% and 6% for $I_{\uparrow\uparrow}$ as explained above, we find that $I_{\uparrow\uparrow}^{\sigma-} = I_{\uparrow\downarrow}^{\sigma-}$ for K = 0.93. Thus, in the case, where 93% of the EMPs are formed along $\vec{c}$ and 7% are formed along $-\vec{c}$, both EMPs contribute equally to the σ^- polarized PL. Using the simulation parameters for cQD #1, we find $I_{\uparrow\uparrow}^{\sigma-} = I_{\uparrow\downarrow}^{\sigma-}$ at a magnetic field of 1.6 T. This interpretation fits nicely to the observation in Figure 3.2 (e), where we see a change from a blue shift to a red shift of the σ^- polarized spectra between 1 and 2 T. Our findings in addition emphasize the need for a careful consideration of conclusions gained from polarization resolved measurements in anisotropic nanostructures: A spectral splitting (or a lack thereof) between σ^+ and σ^- polarized PL is not a reliable tool to extract the energy splitting between the involved electronic states. Additionally, purely considering the degree of circular polarization for such nanostructures is not a reliable tool to determine the state occupation.

B.5 Discussion of finite $\Delta I/I$ at zero magnetic field

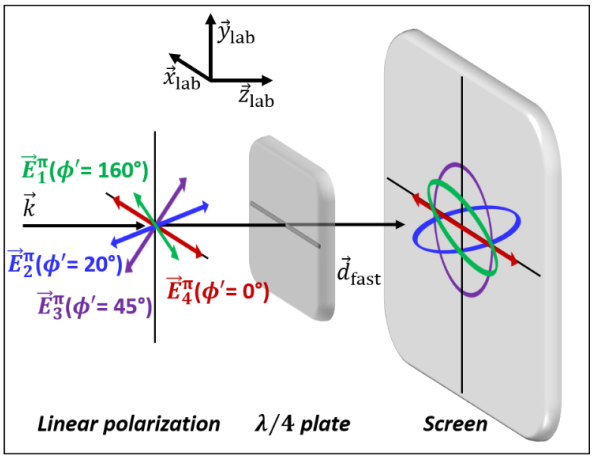

Figure B.3. Drawing showing the projection of the linearly polarized photoluminescence. Schematic of the resulting angular intensity dependence for linearly polarized light with three different linear polarization angles ϕ' after passing a quarter wave plate with horizontal fast axis.

As noted in the Chapter 3, the linearly polarized PL components cause different single cQDs to exhibit different values for $\Delta I/I$ at $B = 0$. Recall, that $\Delta I/I$ is commonly measured by a combination of a quarter wave plate (here parallel to the lab $\vec{x}$ axis) and a linear polarizer. The transmitted intensity $I(\alpha)$ is then recorded, where the angle $\alpha = 0°$ is the direction of the fast axis of the quarter wave plate. The degree of circular polarization is then defined as $\Delta I/I = I(45°) - I(135°)/I(45°) + I(135°)$. When using the combination of a retarder (like a quarter wave plate) and an analyzer (linear polarizer), the identity $I(45°) = I^{\sigma+}$ and $I(135) = I^{\sigma-}$ (with quarter wave plate) is only accurate if no linear polarized PL component is present. In case of single cQDs exhibiting partly π polarized PL, the linear component contributes to the intensities $I(45°)$ and $I(135°)$ differently. As an example, Figure B.4 schematically illustrates the case of individual cQDs exhibiting π polarized PL components with the electric field oriented in different directions, $\phi' = 0°$ (red), 20° (blue), 45° (purple) and 160° (green), with respect to the fast axis of a quarter wave plate (fast axis parallel to the $\vec{x}$ axis). For $\phi' = 20°$ and $\phi' = 160°$, the transmitted light is elliptically polarized and in general does not add equally to $I(45°)$ and $I(135°)$. More precisely, for $0 < \phi' < 90°$ the direction of the transmitted polarization ellipse leads to $I(135°) > I(45°)$, i.e. $\Delta I/I > 0$ at $B = 0$. Similarly, $90 < \phi' < 180°$ leads to $I(135°) < I(45°)$, i.e. $\Delta I/I >$

0 at $B = 0$. As a consequence, a finite offset of $\Delta I/I$ at $B = 0$ T is obtained. Only for the special cases of $\phi' = 45°$ and $\phi' = 0°$, the π PL component contributes equally to $I(45°)$ and $I(135°)$.

B.6 References

1. Merkulov, I. A.; Yakovlev, D. R.; Kavokin, K. V; Mackh, G.; Ossau, W.; Waag, A.; Landwehr, G. Hierarchy of Relaxation Times in the Formation of an Excitonic Magnetic Polaron in (CdMn)Te. *JETP Letters*. 1995, p 335.
2. Beaulac, R.; Schneider, L.; Archer, P. I.; Bacher, G.; Gamelin, D. R. Light-Induced Spontaneous Magnetization in Doped Colloidal Quantum Dots. *Science* **2009**, *325*, 973–976.
3. Nelson, H. D.; Bradshaw, L. R.; Barrows, C. J.; Vlaskin, V. A.; Gamelin, D. R. Picosecond Dynamics of Excitonic Magnetic Polarons in Colloidal Diffusion-Doped $Cd_{1-x}Mn_xSe$ Quantum Dots. *ACS Nano* **2015**, *9*, 11177–11191.
4. Lorenz, S.; Erickson, C. S.; Riesner, M.; Gamelin, D. R.; Fainblat, R.; Bacher, G. Directed Exciton Magnetic Polaron Formation in a Single Colloidal Mn^{2+}:CdSe/CdS Quantum Dot. *Nano Lett.* **2020**, *20*, 1896–1906.
5. Yakovlev, D. R.; Ossau, W. Magnetic Polarons. In *Introduction to the Physics of Diluted Magnetic Semiconductors*; Gaj, J. A., Kossut, J., Eds.; Springer Series in Materials Science; Springer Berlin Heidelberg: Berlin, Heidelberg, 2010; pp 221–262.
6. Dorozhkin, P. S.; Chernenko, A. V.; Kulakovskii, V. D.; Brichkin, A. S.; Maksimov, A. A.; Schoemig, H.; Bacher, G.; Forchel, A.; Lee, S.; Dobrowolska, M.; et al. Longitudinal and Transverse Fluctuations of Magnetization of the Excitonic Magnetic Polaron in a Semimagnetic Single Quantum Dot. *Phys. Rev. B* **2003**, *68*, 195313.
7. Merkulov, I.; Pozina, G.; Coquillat, D.; Paganotto, N.; Siviniant, J.; Lascaray, J. Parameters of the Magnetic Polaron State in Diluted Magnetic Semiconductors Cd-Mn-Te with Low Manganese Concentration. *Phys. Rev. B - Condens. Matter Mater. Phys.* **1996**, *54*, 5727–5731.
8. Madelung, O. *Semiconductors: Data Handbook*, 3rd ed.; Springer: Berlin (U.A.), 2003.
9. Furdyna, J. K.; Kossut, K. Dilute Magnetic Semiconductors. In *Semiconductors and Semimetals*; Furdyna, J. K., Kossut, J., Ed.; Academic Press, Inc.: New York, 1988; Vol. 25, pp R29–R64.
10. Efros, A.; Rosen, M.; Kuno, M.; Nirmal, M.; Norris, D.; Bawendi, M. Band-Edge Exciton in Quantum Dots of Semiconductors with a Degenerate Valence Band: Dark and Bright Exciton States. *Phys. Rev. B* **1996**, *54*, 4843–4856.

Appendix C: Photoluminescence Saturation in Quantum-Cutting Yb^{3+}-Doped $CsPb(Cl_{1-x}Br_x)_3$ Nanocrystals: Implications for Solar Downconversion

C.1 Modeling the photoluminescence power dependence

Eq C1a describes the population dynamics for a given excited state in the general case of a Yb^{3+}:$CsPbX_3$ NC with y_1 excited-state Yb^{3+} ions (Yb*), y_0 ground-state Yb^{3+} ions (Yb_0), in the absence of a NC exciton. The number of excitons per NC is either zero or one, indicated by N_0 and N_1, respectively. In the special cases where $y_1 = 0$, 1, or n, the dynamics are described by eq C1b, c, and d, respectively. n describes the total number of Yb^{3+} ions in the NC, *i.e.*, $n = y_0 + y_1$.

$$\frac{d|N_0,y_1,y_0\rangle}{dt} = -(k_{ex} + y_1k_{Yb})|N_0,y_1,y_0\rangle + \frac{(y_0+2)}{2}k_{QC}|N_1,y_1-2,y_0+2\rangle + (k_{NC} + y_1k_{A2})|N_1,y_1,y_0\rangle + (y_1+1)k_{Yb}|N_0,y_1+1,y_0-1\rangle \quad \text{Eq. C.1a}$$

$$\frac{d|N_0,0,n\rangle}{dt} = -k_{ex}|N_0,0,n\rangle + k_{NC}\,|N_1,0,n\rangle + k_{Yb}|N_0,1,n-1\rangle \quad \text{Eq. C.1b}$$

$$\frac{d|N_0,1,n-1\rangle}{dt} = -k_{ex}|N_0,1,n-1\rangle + (k_{NC} + 1k_{A2})\,|N_1,1,n-1\rangle + 2k_{Yb}|N_0,2,n-2\rangle \quad \text{Eq. C.1c}$$

$$\frac{d|N_0,n,0\rangle}{dt} = -(k_{ex} + nk_{Yb})|N_0,n,0\rangle + k_{QC}|N_1,n-2,2\rangle + (k_{NC} + nk_{A2})\,|N_1,n,0\rangle \quad \text{Eq. C.1d}$$

Similarly, Eq. C.2a describes the general excited-state population dynamics for excitons (N_1) in the presence of y_1 and y_0. In the special cases where $y_1 = 0$, n - 1, and n, these dynamics are described by equations C.2b, c, and d respectively.

$$\frac{d|N_1,y_1,y_0\rangle}{dt} = -\left(k_{NC} + y_1k_{Yb} + y_1k_{A1} + y_1k_{A2} + \frac{y_0}{2}k_{QC}\right)|N_1,\ y_1,y_0\rangle + k_{ex}|N_0,\ y_1,y_0\rangle + (y_1+1)(k_{Yb} + k_{A1})|N_1,\ y_1+1,y_0-1\rangle \quad \text{Eq. C.2a}$$

$$\frac{d|N_1,0,n\rangle}{dt} = -\left(k_{NC} + \frac{n}{2}k_{QC}\right)|N_1,0,n\rangle + k_{ex}|N_1,0,n\rangle + (k_{Yb} + k_{A1})|N_1,1,n-1\rangle \quad \text{Eq. C.2b}$$

$$\frac{d|N_1,n-1,1\rangle}{dt} = -\big(k_{NC} + (n-1)(k_{Yb} + k_{A1} + k_{A2})\big)|N_1,n-1,1\rangle + k_{ex}|N_0,n-1,1\rangle + n(k_{Yb} + k_{A1})|N_1,n,0\rangle \quad \text{Eq. C.2c}$$

$$\frac{d|N_1,n,0\rangle}{dt} = -(k_{NC} + nk_{Yb} + nk_{A1} + nk_{A2})|N_1,n,0\rangle + k_{ex}|N_0,n,0\rangle \qquad \text{Eq. C.2d}$$

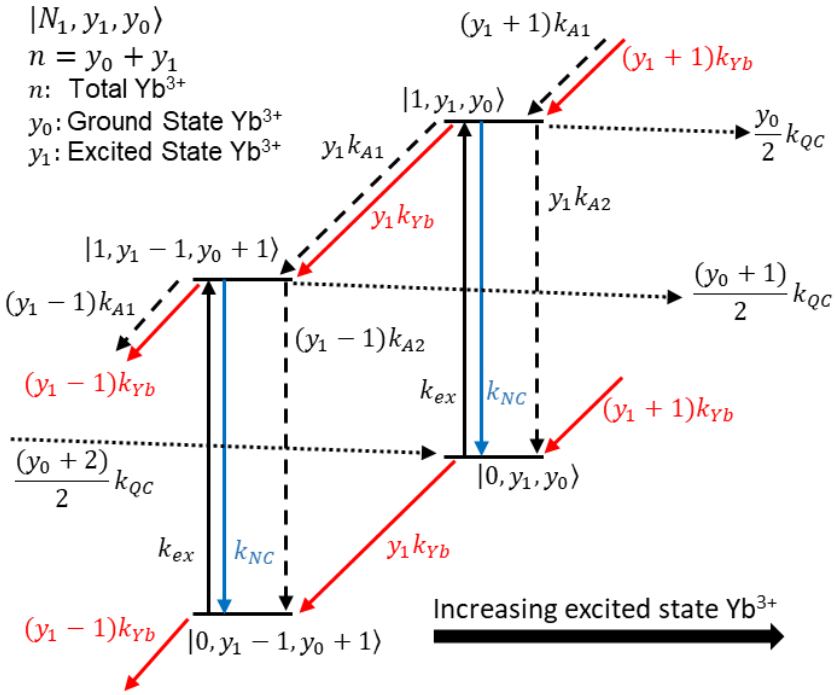

Figure C.1. Schematic depiction of the kinetics relevant to photoexcitation of Yb^{3+}:$CsPbCl_3$ NCs over a broad range of photoexcitation powers. NC photoexcitation is described by the rate constant k_{ex} (solid black arrows). Depending on the number of Yb^{3+} ions already in their $^2F_{5/2}$ excited state at the time of photoexcitation, y_1, the excited NC may relax *via* quantum cutting (k_{QC}, dotted black arrow), Auger cross relaxation (k_{A1} or k_{A2}, dashed black arrows), or direct return to the NC ground state (k_{NC}, blue arrow). Yb^{3+} photoluminescence is described by k_{Yb} (red arrows). As y_1 increases, the number of ground-state Yb^{3+} ions (y_0) available for quantum cutting decreases, making the quantum-cutting rate smaller and Auger rates larger.

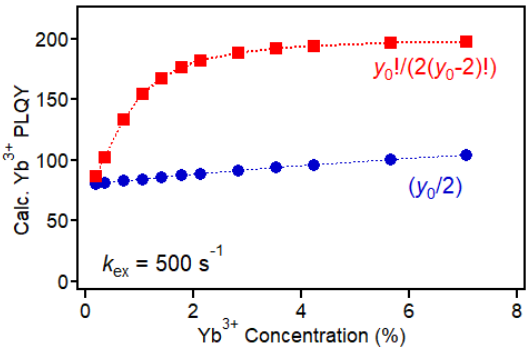

Figure C. 2 Modeled Yb^{3+} PLQYs. Yb^{3+} PLQYs calculated using the kinetic model described in Figure 4.5 and above, for the two different energy-transfer scenarios of (*i*) energy transfer to specific Yb^{3+} dimer pairs (number of eligible pairs per NC = $y_0/2$), or (*ii*) energy transfer to *any* pair of Yb^{3+} dopants (number of eligible pairs per NC = $y_0!/(2(y_0\text{-}2)!)$). For each case the I_{Yb} *vs* k_{ex} data were calculated using the following parameters: n = 100 Yb^{3+} dopants/NC, k_{Yb} = 500 s^{-1}, k_{NC} = 10^8 s^{-1}, and k_{ex} = 500 s^{-1}. k_{QC} and k_{A2} were adjusted to fit the experimental data in the low-fluence limit, such that k'_{QC} (dimer) = k'_{QC} (pairwise) = 10^{10} s^{-1} in this limit.

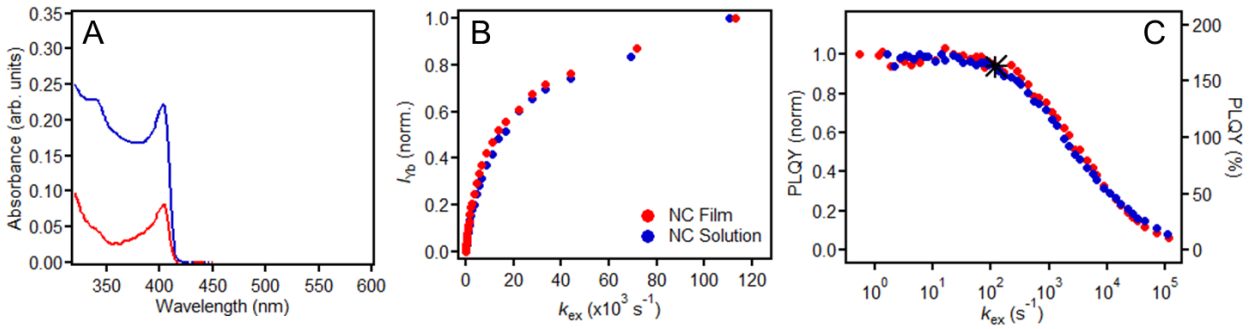

Figure C.3. Photoluminesecnec power dependence comparision between NC solution and thin film. (A) Absorption spectra of a Yb^{3+}:$CsPbCl_3$ NC solution (blue) and dropcast film of NCs (red). (B) Integrated Yb^{3+} PL intensities (I_{Yb}) for the two samples shown in panel A, plotted as function of the NC photoexcitation rate constant (k_{ex}). (C) Normalized PL quantum yields (PLQYs) for the same samples, plotted *vs* excitation rate constant on a logarithmic axis. Normalized PLQYs are obtained by dividing I_{Yb} by k_{ex} and normalizing in the low-power limit. The black symbol indicates the *absolute* PLQY (right axis) of the same NC solution, measured in an integrating sphere at a known excitation rate.

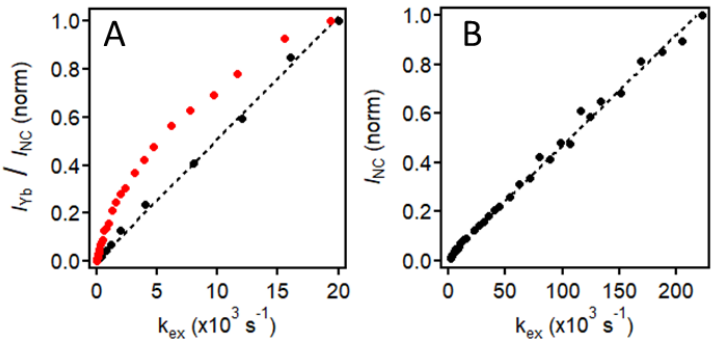

Figure C.4. Excitonic photoluminescence intensities for the NCs used in Figure 4.3. (A) Integrated Yb^{3+} PL intensities (I_{Yb}, red) and NC excitonic PL (I_{NC}, black) measured for the 1.4% Yb^{3+}:$CsPb(Cl_{1-x}Br_x)_3$ NCs shown in Figure 4.3 (green), plotted as a function of the NC photoexcitation rate constant (k_{ex}). The dependence of I_{NC} on k_{ex} is linear across the entire excitation range. (B) Integrated NC excitonic PL intensities measured for undoped $CsPb(Cl_{1-x}Br_x)_3$ NCs, plotted *vs* k_{ex}. I_{NC} again varies linearly with k_{ex} across the entire power range. The dashed black lines show linear fits to I_{NC}.

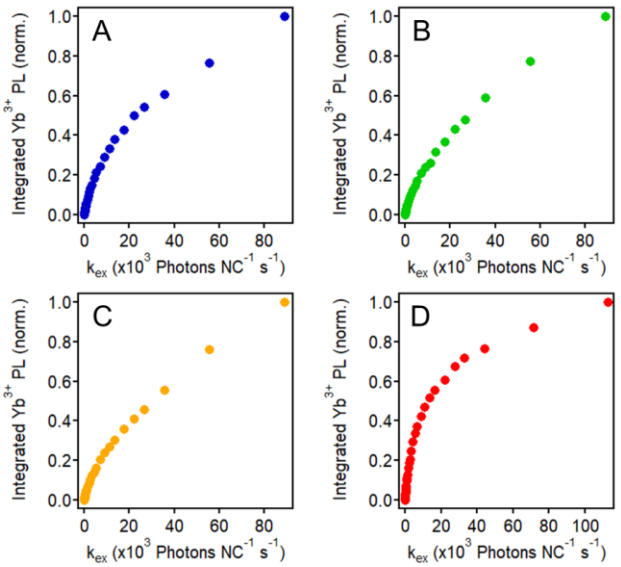

Figure C.5. Integrated Yb^{3+} photoluminescence for the NCs shown in Figure 4.7. (A-D) Integrated Yb^{3+} PL intensities (I_{Yb}, colors) for the four Yb^{3+}:$CsPbCl_3$ NC samples from Figure 4.7, having Yb^{3+} concentrations of 0.7% (blue), 3.4% (green), 4.2% (orange), and 5.7% (red). All data sets have been normalized at their highest excitation rates.